

# **Synthesis and Structural Investigation of Guanine Functionalized Hydrogels and Their Biomedical Applications**

**Ph.D. Thesis**

By  
**SOURAV BHOWMIK**



**DEPARTMENT OF CHEMISTRY  
INDIAN INSTITUTE OF TECHNOLOGY INDORE**

**JULY 2024**



# **Synthesis and Structural Investigation of Guanine Functionalized Hydrogels and Their Biomedical Applications**

**A THESIS**

*Submitted in partial fulfillment of the  
requirements for the award of the degree*

*of*

**DOCTOR OF PHILOSOPHY**

*by*

**SOURAV BHOWMIK**



**DEPARTMENT OF CHEMISTRY  
INDIAN INSTITUTE OF TECHNOLOGY INDORE  
JULY 2024**



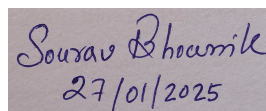




## INDIAN INSTITUTE OF TECHNOLOGY INDORE

I hereby certify that the work which is being presented in the thesis entitled **Synthesis and Structural Investigation of Guanine Functionalized Hydrogels and Their Biomedical Applications** in the partial fulfillment of the requirements for the award of the degree of **DOCTOR OF PHILOSOPHY** and submitted in the **DEPARTMENT OF CHEMISTRY, Indian Institute of Technology Indore**, is an authentic record of my own work carried out during the time period from June 2019 to July 2024 under the supervision of **Prof. APURBA K. DAS**, Professor, Department of Chemistry, Indian Institute of Technology Indore.

The matter presented in this thesis has not been submitted by me for the award of any other degree of this or any other institute.



Signature of the student with date  
(SOURAV BHOWMIK)

-----  
This is to certify that the above statement made by the candidate is correct to the best of my/~~our~~ knowledge.



Signature of Thesis Supervisor with date  
(Prof. APURBA K. DAS)

-----  
**SOURAV BHOWMIK** has successfully given his Ph.D. Oral Examination held on 22/01/2025



Signature of Thesis Supervisor with date  
(Prof. APURBA K. DAS)

-----



## ACKNOWLEDGEMENTS

This work could not have been possible without the guidance and support of so many wonderful people. First, I would like to thank my doctoral research supervisor, Professor Apurba K. Das for giving me the opportunity to work in ‘Supramolecular Organic Chemistry Group’ for the last five years. I have learned many things under his guidance. I am lucky that he has provided me everything to work in cell biology and molecular dynamic simulation area. With out his support it would not be possible. I am eternally grateful for the experience of working in the Prof. Das group. I have learned so much about supramolecular chemistry over the past five years, but working with you has inspired a level of passion for science and research that I did not know I had. Thank you for always being available to discuss on the results and ideas. I would also like to thank my PSPC members Prof. Satya S. Bulusu and Prof Shaibal Mukherjee for their valuable suggestions, guidance and valuable input during the course of my degree. I am grateful to the faculty members in the Department of Chemistry, Prof. Biswarup Pathak (Head, Department of Chemistry), Prof. Satya S. Bulusu, Prof. Anjan Chakraborty, Dr. Tridib K. Sarma, Prof. Rajneesh Misra, Prof. Sampak Samanta, Prof. Suman Mukhopadhyay, Prof. Sanjay K. Singh, Prof. Shaikh M. Mobin, Prof. Chelvam Venkatesh, Dr. Amrendra K Singh, Dr. Abhinav Raghuvanshi, Dr. Umesh A. Kshirsagar, Dr. Dipak K Roy, Dr. Selvakumar Sermadurai, Dr. Debayan Sarkar and Dr. Pravarthana Dhanapal for their guidance and help during various activities. I wish to express my gratitude to Prof. Suhas S. Joshi, Director, IIT Indore, for his continuous encouragement, help, and support in every aspect. I would also like to thank our collaborators Dr. Hem C. Jha, Associate Professor, Department of Bioscience and Bioengineering, IIT Indore for all the insightful conversations and for a fruitful collaboration. Thanks to Dr. Dharmendra Kashyap for guiding me on cell culture experiments. I would also like thank Dr. Shrikant Kunjir for DOSY NMR experiment. I also acknowledge Dr. Ananya Ghosal for correcting English. I am

incredibly appreciative of all the people in the Das group who have helped me along the way. I extend my profound thanks to my past and present group members Dr. Ankan Biswas, Dr. Sayan Maiti, Dr. Pramod K. Gavel, Dr. Rohit G Jadhav, Dr. Tapas Ghosh, Dr. Devraj Singh, Dr. Deepak K. Kori, Ms. Meenu Sharma, Mr. Tanmay Rit, Ms. Lalita Wagh, Ms. Arati Samal, Ms. Anushree Jain, Mr. Arka Acharyya, Mr. Shantanu Paul, Mr. Deepak Pandey, Mr. Mithu Roy, Ms. Nikita Sharma, Ms. Sweta Agarwal, Mr. Sudarshan Majee, Ms. Shruti Ghosh, Mr. Saryu Bhardwaj, Mr. Supratim Ghosh, Mr. Chiranjeeb Kundu, Ms. Shreyashi Sarkar for their generous co-operation and help during my entire Ph.D. time. Once again, thank you Dr. Ankan Biswas, Dr. Pramod K. Gavel, Dr. Sayan Maiti, Mr. Arka Acharyya, for all your hard work and effort during my works. The contributions you have made to my Ph.D. works genuinely took it to another level, and I am so grateful to have gotten to work with you. I am thankful to Mr. Kinney Pandey, Mr. Ghanshyam Bhavsar, Dr. Ravinder, Mr. Ranjeet Raghuwanshi, Mr. Atul Singh, Ms. Kajal Chaudhari, and Mr. Nitin Upadhyay for their help during instrumental analysis. Mr. Manish Kushwaha, Mrs. Vinita Kothari, Mr. Souvik Debnath and Mr. Rameshwar Dauhare are also acknowledged for their technical help and support. I would also like to thank all the funding agencies for providing the financial supports during my Ph.D. works. Furthermore, thank you to the Department of Science and Technology (DST), Government of India for INSPIRE fellowship. I would like to thank my friends for all their help and support throughout this process. Particularly, thanks to Chinmaya K. Patel, Naveen Kumar, Pranit Bagde, Sayan Poddar, Sunanda Samanta for their countless helps and encourage during my Ph.D. Finally, I express my deepest gratitude to my lovable father Mr. Swapan Kumar Bhowmik and mother Mrs. Alpana Bhowmik, and my grandparents and the rest of family members for their encouragement, full support and patience during this tenure. I feel so lucky to have such an amazing, caring family who always supports and loves me, thank you.

Sourav Bhowmik

*Dedicated to*  
*My parents*



## SYNOPSIS

Self-assembly is a process by which components organize themselves into patterns or structures. It is a very effective method for creating a wide range of useful materials. Self-assembly is a valuable technique for creating hydrogels. The use of self-assembly is employed to arrange small molecules to produce hydrogels where the molecules form a network by physical interconnection. These materials are created by the reversible and dynamic bonding of certain components. Self-assembly is a commonly observed phenomenon in the natural systems. Therefore, hydrogels are polymeric three-dimensional networks that can hold a large amount of water molecules. Due to their water absorbing properties, they are biocompatible in nature. In addition to biocompatibility, hydrogels possess exciting properties such as stimuli-responsive, self-healing, and thermoreversibility. Hydrogels are extensively used in the biomedical field for application such as drug delivery, bioimaging, bioactive scaffold, 3D bioprinting, tissue engineering, and regenerative medicine. Peptides have been extensively used as fundamental components in the self-assembly process. However, nucleobase functionalized amino acids/peptides have not been well explored to date. Nucleobases and peptides are the fundamental building blocks of life. Among the purine and pyrimidine nucleobases, guanine has several H-bonding donor and acceptor sides which can contribute to the formation secondary structures of the nucleic acid such as G-quadruplex, G-ribbon, stem-loop structures, double helices, and psuedoknots. Purine and pyrimidine nucleobases are hydrophobic in nature. They are insoluble in water at physiological pH. The formation of the hydrogel depends on achieving the proper balance of hydrophobicity and hydrophilicity of a molecule. Here, we induced the hydrophilicity of guanine by the introduction a long fatty acid chain and amino acid which then went higher-order self-assembly to form the hydrogel.

The primary goals of my current research include

- To design and synthesize guanine functionalized amino acid derivatives by the conventional solution phase peptide synthesis process.
- To induce the gelation property in the synthesized molecules by varying the length of the fatty acid chain as well as the sequence of the amino acids.
- To study their self-assembly by the Molecular dynamic simulation and Diffusion Ordered Spectroscopy (DOSY) NMR.
- To check the biocompatibility of the hydrogel quantitatively by MTT assay and also qualitatively Live/dead cell imaging.
- To use the hydrogel for the pH-responsive release of the drug molecules, and also to study the *in vitro* wound healing.

## **1. Synthesis and Structural Studies of Nucleobase Functionalized Hydrogel for Controlled Release of Vitamins**

In this work, I have synthesized three guanine functionalized phenylalanine derivatives namely **NP1**, **NP2**, and **NP3** using the conventional solution phase peptide synthetic procedure. I have varied the chain length to induce gelation properties in the synthesized **NPs**. Among the synthesized **NPs**, the **NP3** forms the stable hydrogel in the presence of the appropriate monovalent metal ion. The hydrogel is used for the delivery of drug molecules. The presence of the G-quadruplex inside the hydrogel is analyzed by performing spectroscopic experiments. The nanofiber morphology inside the hydrogel is confirmed by microscopic experiments such as SEM, TEM, and AFM. The aggregation propensity of the **NPs** is analyzed by conducting a DOSY NMR experiment. The thixotropic nature of the **NP3** hydrogel is also studied. The injectability of the hydrogel is checked. The biocompatibility of the hydrogel is also checked by performing MTT and live/dead cell assay. MCF7 and HEK 293 cell lines are used for the experiment. The hydrogel is biostable in the presence of proteolytic enzymes, proteinase K, and  $\alpha$ -chymotrypsin. The mechanical strength of the hydrogel is determined by the amplitude sweep and frequency sweep experiments.

## **2. Chemical Reaction Driven Self-assembly of a Nucleobase Functionalized Molecule**



The guanine functionalized amino acids derivatives (**NPs**) are synthesized (**Figure 2a**). The supramolecular order in the synthesized **NPs** is induced by a chemical reaction. Methylation of nucleobases of DNA is a significant metabolic process. Nucleobases are methylated when a methyl group is transferred to a nucleobase by an internal or external methylating agent. Here, the current study demonstrates the use of dimethyl sulfate (DMS) as an external methylating agent (**Figure 2b**). **NP3** forms the hydrogel after the addition of the DMS. However, **NPs** contain several methylating sites. **PDT1** is observed as a major one. The (%) of the conversion is analyzed from HPLC chromatograms (**Figure 2c and 2d**). The dynamic step-strain experiment demonstrates the thixotropic nature of the **NP3** hydrogel. UV-turbidity, fluorescence, viscosity, and CD experiments show the progress of the self-assembly after the addition of the DMS (**Figure 2e, 2f, 2g, and 2h**). SEM and TEM images reveal the presence of nanofiber morphology inside the hydrogel. A live video shows the formation of the nanofiber after the addition of the DMS.

### **3. Design and synthesis of nucleobase functionalized peptide hydrogel: *In vitro* assessment of anti-inflammatory and wound healing effects**

I have functionalized guanine with varying sequences of amino acids (**Figure 3a**). The phenylalanine and tyrosine are attached to the guanine by a six-carbon long fatty acid chain. **NP5**, **NP6**, and **NP7** are synthesized by the solution phase synthetic procedure. I introduce the varying sequence of the amino acid to adjust the hydrophobic and hydrophilic balance which in turn induces the gelation in the synthesized compound (**Figure 3b**). The aggregation behavior of these **NPs** are analyzed using a molecular dynamics simulation study (**Figure 3c and 3d**). The DOSY NMR experiment confirms the higher level of aggregation of the **NP5**. The **NP5** hydrogel is viscoelastic in nature (**Figure 3e**). Furthermore, **NP5** hydrogel is characterized using CD, PXRD, and ThT-dye binding experiments. SEM and TEM experiments reveal the existence of nanofibers within the **NP5** hydrogel. The **NP5**

hydrogel exhibits minimal cytotoxicity, as demonstrated by MTT and cell death studies (**Figure 3f and 3g**). The **NP5** hydrogel is found to be nonhemolytic in nature (**Figure 3h and 3i**). The **NP5** hydrogel is also found to be biostable against the proteolytic enzyme proteinase K and  $\alpha$ -chymotrypsin. Furthermore, the **NP5** hydrogel showed efficacy against *B. subtilis* and *E. Coli* bacteria. It also demonstrates the properties of ROS scavenging, antibacterial, and anti-inflammatory activity in epithelial cells and keratinocytes. Notably, the hydrogel shows enhanced activity in keratinocytes compared to epithelial cells.

#### **4. Enzyme Fueled Reverse Hydrolysis of Guanine Base Functionalized Molecules: Equilibrium Shifts, Dissipative Self-assembly and Cellular Behavior**

I have explored an enzyme-fueled dissipative self-assembly process, which is constructed using nucleobase-functionalized biomaterials. These materials are designed and synthesized to create non-covalent polymers that were readily self-assembled using the G-quadruplex motif (**Figure 4a**). The dissipative self-assembly system shifts the equilibrium in reverse due to morphological transition over time upon treatment with lipase (**Figure 4b**). The ThT dye-binding assay, wide-angle PXRD, and CD experiments are performed to confirm the presence of G-quadruplex endowed with hydrolyzable properties. The biocompatibility experiment was performed on HEK 293 and McCoy cell lines. The potential for **NP10** as wound dressing was evaluated by scratch assay, demonstrating the disappearance of the scratch in 24 h following the cell migration after hydrogel treatment (**Figure 4c**). The hydrogel goes within the cell and binds with the nucleus of the cells (**Figure 4d**).

# LIST OF PUBLICATIONS

## (A) Publications included in Thesis:

### A1. In referred journals

1. **Bhowmik S**, Ghosh T, Sanghvi YS, Das AK Enzyme fueled reverse hydrolysis of guanine base functionalized molecules: Equilibrium shifts, dissipative self-assembly and cellular behavior. *Chem. Eur. J.* **2024**, *30*, e202402687. (I.F. **3.9**) (DOI: 10.1002/chem.202402687)
2. **Bhowmik S**, Baral B, Rit T, et al (2024) Design and synthesis of a nucleobase functionalized peptide hydrogel: in vitro assessment of anti-inflammatory and wound healing effects. *Nanoscale*, **2024** (Just accepted). (I.F. **6.7**) (DOI: 10.1039/D4NR01149J)
3. **Bhowmik S**, Ghosh T, Das AK (2024) Chemical reaction driven self-assembly of a nucleobase functionalized molecule. *Journal of Molecular Liquids* 406:125034. (I.F. **6.0**) (DOI: 10.1016/j.molliq.2024.125034)
4. **Bhowmik S**, Ghosh T, Sanghvi YS, Das AK (2023) Synthesis and Structural Studies of Nucleobase Functionalized Hydrogels for Controlled Release of Vitamins. *ACS Appl Bio Mater* 6:5301–5309. (I.F. **4.6**) (DOI: 10.1021/acsabm.3c00582)

### A2. In referred conferences

**Bhowmik S**, Das AK., Nucleobase Functionalized Peptide Conjugated Injectable Biocompatible Hydrogel for Controlled Release of Vitamins, In-House Chemistry Symposium “CHEM2023” 6<sup>th</sup> March 2023 at Department of Chemistry, Indian Institute of Technology, Indore, India, (Poster Presentation).

## (B) Publications apart from Thesis:

### B1. In referred journals

1. Ghosh T, Biswas A, **Bhowmik S**, Das AK (2021) Pt Nanoparticles Supported on a Dynamic Boronate Ester-Based G-quadruplex Hydrogel as a Nanoreactor. *Chemistry An Asian Journal* 16:215–223. (I.F. **3.5**) (DOI: 10.1002/asia.202001284)

2. Ghosh S, Ghosh T, **Bhowmik S**, Patidar MK, Das AK (2023) Nucleopeptide-Coupled Injectable Bioconjugated Guanosine-Quadruplex Hydrogel with Inherent Antibacterial Activity. *ACS Appl Bio Mater* 6:640–651. (I.F. **4.6**) (DOI: 10.1021/acsabm.2c00912)
3. Rit T, Ghosh T, **Bhowmik S**, Patidar MK, Das AK (2023) Dynamic Multicomponent Reactions-Directed Self-Assembled G-quadruplex Inherent Antibacterial Hydrogel. *Langmuir* 39:6466–6475. (I.F. **3.7**) (DOI: 10.1021/acs.langmuir.3c00392)
4. **Bhowmik S**, Biswas S, Das AK (2023) An efficient enzymatic approach for the detection of glucose and uric acid from blood serum. *Prayogik Rasayan* 7:22-28. (DOI: 10.53023/p.rasayan-20230605)

## **B2. BOOK CHAPTER:**

1. Das AK, Biswas A, **Bhowmik S**, Ghosh, T. (2021) Nucleobase and DNA Functionalized Hydrogels and Their Applications, Invited author of a book chapter for the book, *Molecular Architectonics and Nanoarchitectonics*, (Editors: T. Govindaraju and K. Ariga), Springer Nature, Singapore. (ISBN: 978-981-16-4189-3) (DOI: 10.1007/978-981-16-4189-3\_14)

# TABLE OF CONTENTS

1. LIST OF FIGURES	xviii
2. LIST OF TABLES	xxxvii
3. ACRONYMS	xxxix
4. NOMENCLATURE	xl
<b>Chapter 1: General Introduction</b>	<b>1-82</b>
1.1 Introduction	3
1.1.1 Molecular self-assembly	3
1.1.2 Hydrogels	7
1.1.3 Hydrogel formation	8
1.1.4 Dynamic Covalent Bond-Driven Hydrogel	9
1.1.5 Building blocks of DNA and RNA	22
1.1.6 Nucleotides and Nucleosides	22
1.1.7 Supramolecular assemblies in DNA and RNA	24
1.1.8 G-quartet and G-quadruplex	26
1.1.9 G-quadruplex in the Biological System	28
1.1.10 G4 in the Replications of DNA	28
1.1.11 DNA in the Telomere	29
1.1.12 Role of G-quadruplex in the DNA Transcription	30
1.1.13 Background of G-quadruplex Hydrogels	31
1.1.14 Hydrogel Formed by the Peptide-functionalized Molecules	36
1.1.15 Application of the Hydrogel	45
1.1.15.1 Tissue Engineering	45
1.1.15.2 Wound Healing	49
1.1.15.3 Drug Delivery	50
1.1.15.4 3D Printing	52
1.2 Summary	53

1.3 Thesis Organization	54
1.4 References	55
<b>Chapter 2 Synthesis and Structural Studies of Nucleobase Functionalized Hydrogels for Controlled Release of Vitamins</b>	<b>83-135</b>
2.1 Introduction	85
2.2 Experimental Section	87
2.2.1 Materials and Methods	87
2.2.2 Synthesis of Compounds	88
2.2.2.1 General Procedure for the Synthesis of 2a-c	88
2.2.2.2 Synthesis of 2a	88
2.2.2.3 Synthesis of 2b	90
2.2.2.4 Synthesis of 2c	91
2.2.2.5 General Procedure for the Synthesis of 3a-c	93
2.2.2.6 Compound 3a	93
2.2.2.7 Compound 3b	95
2.2.2.8 Compound 3c	96
2.2.2.9 General Procedure for the Synthesis of Compound NP1-3	98
2.2.2.10 Compound NP1	98
2.2.2.11 Compound NP2	99
2.2.2.12 Compound NP3	101
2.2.3 Preparation of Hydrogel	102
2.2.4 Proteolytic Stability	103
2.2.5 Circular Dichroism Spectroscopy	103
2.2.6 Fluorescence Spectroscopy	103
2.2.7 FT-IR Spectroscopy	103
2.2.8 X-ray Diffraction (XRD) Measurement	104
2.2.9 Rheological Behaviour of the Hydrogel	104
2.2.10 Diffusion Ordered NMR Spectroscopy (DOSY)	104

2.2.11 Morphological Study of the Hydrogel	105
2.2.12 HPLC Analysis	105
2.2.13 Drug Release Study	106
2.2.14 Preparation of Vitamin Loaded Hydrogel	107
2.2.15 Cell Viability	107
2.2.16 Live and Dead Cell Imaging	107
2.2.17 Statistical Analyses	107
2.3 Results and Discussion	108
2.4 Conclusion	125
2.5 Reference	125
<b>Chapter 3 Chemical Reaction Driven Self-assembly of a Nucleobase Functionalized Molecule</b>	<b>136-173</b>
3.1 Introduction	138
3.2 Experimental Section	140
3.2.1 Materials and Methods	140
3.2.2 Synthesis of NP3 and NP4	141
3.2.3 General procedure for the synthesis of 2c,4b	141
3.2.4 Synthesis of 2c	141
3.2.5 Synthesis of 4b	142
3.2.6 General procedure for the synthesis of 3c, 5b	143
3.2.7 Compound 3c	144
3.2.8 Compound 5b	145
3.2.9 General procedure for the synthesis of compound NP3, NP4	147
3.2.10 Compound NP3	147
3.2.11 Compound NP4	148
3.2.12 HPLC Analysis	150
3.2.13 pH	150
3.2.14 Circular Dichroism Spectroscopy	150

3.2.15 FT-IR	150
3.2.16 UV-Vis Spectroscopy	151
3.2.17 Fluorescence Spectroscopy	151
3.2.18 Rheological Behavior of the Hydrogel	151
3.2.19 Morphological Study of the Hydrogel	152
3.2.20 Synthesis of Nucleobase Functionalized Amino Acid Conjugates (NPs)	153
3.2.21 Preparation of Chemical Reaction Driven Hydrogel	153
3.3 Results and Discussion	153
3.4 Conclusion	164
3.5 Reference	164
<b>Chapter 4 Design and Synthesis of a Nucleobase Functionalized Peptide Hydrogel: in vitro Assessment of Anti-inflammatory and Wound Healing Effects</b>	174-231
4.1 Introduction	176
4.2 Experimental Section	178
4.2.1 Materials and Methods	178
4.2.2 Synthesis of NPs	179
4.2.3 General procedure for the synthesis of 6a-c	179
4.2.4 Synthesis of 6a	180
4.2.5 Synthesis of 6b	181
4.2.6 Synthesis of 6c	182
4.2.7 General procedure for the synthesis of 7a-c	183
4.2.8 Synthesis of 7a	183
4.2.9 Synthesis of 7b	184
4.2.10 Synthesis of 7c	185
4.2.11 General procedure for the synthesis of compound NP5-7	186
4.2.12 Synthesis of NP5	187
4.2.13 Synthesis of NP6	188



4.2.14 Synthesis of NP7	190
4.2.15 Molecular Dynamics (MD) Simulation	191
4.2.16 HPLC Analysis	192
4.2.17 CD Spectroscopy	192
4.2.18 FTIR Spectroscopy	192
4.2.19 ThT Dye Binding Assay	193
4.2.20 Rheological Experiment	193
4.2.21 Scanning Electron Microscopy	193
4.2.22 TEM	194
4.2.23 Wound Healing Assay	193
4.2.24 Antibacterial Experiment	194
4.2.24.1 Bacterial Culture	194
4.2.24.2 Culture Media	195
4.2.25 Gelation Method	195
4.2.26 Isolation of Blood	195
4.2.27 Separation of WBCs and Erythrocytes	196
4.2.28 Hemolytic Activity	195
4.2.29 Antibacterial Properties of the Hydrogel	195
4.2.30 Animal Cell Culture	196
4.2.31 Cytotoxicity of the Hydrogel	197
4.2.32 ROS Estimation by DCFDA Assay	197
4.2.33 RNA Isolation and qRT PCR	197
4.2.34 Western Blot	198
4.2.35 Wound Healing Assay	198
4.3 Results and Discussion	199
4.4 Conclusion	220
4.5 References	221

**Chapter 5 Enzyme Fueled Dissipative Self-assembly of Guanine Functionalized Molecules and Their Cellular Behaviour** 232-290

5.1 Introduction	234
5.2 Experimental Section	236
5.2.1 Materials and Methods	236
5.2.2 Synthesis of NPs	237
5.2.3 General procedure for the synthesis of 8a-e	237
5.2.4 Synthesis of 8a	237
5.2.5 Synthesis of 8b	239
5.2.6 Synthesis of 8c	240
5.2.7 Synthesis of 8d	242
5.2.8 Synthesis of 8e	243
5.2.9 General procedure for the synthesis of 9a-e	245
5.2.10 Compound 9a	245
5.2.11 Compound 9b	247
5.2.12 Compound 9c	248
5.2.13 Compound 9d	250
5.2.14 Compound 9e	251
5.2.15 General procedure for the synthesis of compound NPs	253
5.2.16 Compound NP8	253
5.2.17 Compound NP4	255
5.2.18 Compound NP3	256
5.2.19 Compound NP9	258
5.2.20 Compound NP10	259
5.2.15 HPLC Analysis	261
5.2.16 Computational Molecular Docking	261
5.2.17 Circular Dichroism Spectroscopy	261
5.2.18 FT-IR	262

5.2.19 UV-Vis Spectroscopy	262
5.2.20 Fluorescence Spectroscopy	262
5.2.21 ThT Dye Binding Experiment	263
5.2.22 Rheological Behavior of the Hydrogel	263
5.2.23 Morphological Study of the Hydrogel	264
5.2.24 MTT Cell-viability Assay	264
5.2.25 Live/Dead Cell Imaging	265
5.2.26 Scratch Assay	265
5.3 Results and Discussion	266
5.4 Conclusion	281
5.5 References	282
Chapter 6: Conclusions and Future Perspectives	291-296
6.1 Conclusions	293
6.2 Future Perspectives	295

# LIST OF FIGURES

## Chapter 1: General Introduction

**Figure 1.1** Self-assembled nanostructures: (a) micelles, (b) vesicles, (c) cylinder, (d) coacervates, (e) bilayers, (f) nanotubes, (g) host–guest, and (h) nanofiber. 3

**Figure 1.2** Top-down and bottom-up fabrication approach: (a) the formation of nanoparticles from the bulk of the matter and (b) atoms aggregate into clusters to form the nanoparticles. 5

**Figure 1.3** Methods for creating nanoparticles and microparticles with specific sizes and shapes using a top-down approach: (a) Template-based and stamp lithography methods use either disposable templates that can be dissolved or templates that can be used again, (b) Flow-based lithography methods can be used by UV light with photomasks that are precisely made, or two-photon polymerization and (c) Stereolithography or 3D printing can make micro- and nanoparticles in the widest range of shapes, but it might not be as easy to scale up. 5

**Figure 1.4** Bottom-up approaches for the formation of nanoparticles and microparticles that are defined by their size and shape: (a) Emulsion polymerizations and emulsions, with single phases that don't mix, (b) Spontaneous arrangement of chemically different molecules that have both hydrophilic and hydrophobic parts which lead to the formation of nanostructures of different forms and size under certain circumstances and (c) Polymer induced self-assembly (PISA) of molecules that are hydrophilic and hydrophobic, with radical polymerizations that can be activated as well as deactivate, or controlled ring-opening polymerizations. 6

**Figure 1.5** Diagram illustrating the formation of 8  
supramolecular hydrogels via many noncovalent contacts: (a)  
electrostatic interaction, (b) H-bonding interaction, (c)  $\pi$ -  $\pi$   
interaction, and (d) Hydrophobic interaction.

**Figure 1.6** Schematic representation demonstrating the 10  
formation of stimuli-responsive hydrogels by dynamic  
covalent bonding.

**Figure 1.7** Optical photograph shows the formation of the self- 11  
healable hydrogel by the dynamic covalent bond.

**Figure 1.8** PEG-CHO undergoes a reaction with PEG-ADH 11  
and PEG-CDH to create hydrogels that can degrade due to  
reversible hydrazone cross-links. Additionally, PEG-CHO can  
react with PEG-AO to make nonreversible oxime bonds, which  
help stabilize the hydrazone gels.

**Figure 1.9** Graphical abstract representing the pH-responsive 12  
release of Dox to the tumor cells from the self-healable  
hydrogel matrices.

**Figure 1.10** The reversible dynamic disulfide bond formation. 13

**Figure 1.11** The scheme illustrating a hydrogel that responds 14  
to redox reactions. The oxidation and reduction reaction drives  
the sol-gel transformation.

**Figure 1.12** Self-healing hydrogels built on disulfide bonds: (a) 15  
Schematics of hydrogel which was formed by the crosslinking  
of cystamine and bis(phenylboronic acid carbamoyl)  
(BPBAC). Assessment of the self-healing capacity of the  
hydrogel derived from disulfide bonds and (b) The schematic  
representation of the self-repairing hydrogel is composed of  
2,3-dimercapto-1-propanol and meso-2,3-dimercaptosuccinic  
acid. Additionally, this hydrogel exhibits a self-healing  
mechanism.

**Figure 1.13** Construction of photodegradable hydrogels by 16  
chain and step polymerization. CP gels, which are chain-  
polymerized hydrogels, were created by copolymerizing

photolabile PEGA with PEGdiPDA by FRP. This process resulted in the creation of a unique network topology.

**Figure 1.14** The peptide hydrogelator's molecular structure, as well as its monomeric and their respective dimeric forms, Light driven trans to the cis transition of dimeric and monomeric form. 17

**Figure 1.15** The mechanistic steps of the (a) NCL (b) cysteine-free auxiliary mediated NCL. 18

**Figure 1.16** Reaction of diol and boronic acid. 19

**Figure 1.17** The reaction scheme shows the breaking of cross-linking in the presence of the lactic acid which results in the release of the anticancer drug molecules. 20

**Figure 1.18** The diagram illustrates the synthetic procedure for the formation of the  $\beta$ -CD/MPA hydrogel and the related intermolecular connections within the networks. 21

**Figure 1.19** Schematic diagram shows the formation of the boronic acid cross-link hydrogel and its application. 21

**Figure 1.20** Structures of nucleotide, nucleoside, purine, and pyrimidine nucleobases. 23

**Figure 1.21** Structures of nucleoside in DNA and RNA. 24

**Figure 1.22** (a) The double-stranded structure of DNA, whereas the typical single-stranded structure of RNA. (b) RNA can also form a secondary structure by the complementary base pairing. 25

**Figure 1.23** A Few examples of guanine derivatives and Watson-crick and Hoogsteen faces in the guanine molecule. 26

**Figure 1.24** The formation of the G-tetrad in the presence of the suitable monovalent cation. Different topologies of the G-quadruplex. 27

**Figure 1.25** G4 in the DNA replication. 28

**Figure 1.26** (a) Proteins that are capped in G4 structures prevent the erroneous guiding of cellular repair mechanisms when DNA is damaged. (b) The G4 complexes present in the 29

telomere protect nuclease enzymes. (c) Ligand or drug molecule binding assists in the stabilization of G4s.

**Figure 1.27** The graphics demonstrate the role of G-quadruplex in DNA transcription.

**Figure 1.28** The Scheme shows the formation of G-quadruplex hydrogel for the cascade reaction container.

**Figure 1.29** The G-quadruplex hydrogels stabilized by PEI and their putative creation process.

**Figure 1.30** (a) The formation of the G-quadruplex by the antiviral drug entecavir. (b) The cation selectivity of the hydrogel (c) The optimization diagram.

**Figure 1.31** The formation of the gel-immobilized high-internal-phase emulsions (HIPEG) using the G-quadruplex hydrogel.

**Figure 1.32** The scheme illustrates the formation of the G-quadruplex hydrogel and shows the catalytic activity.

**Figure 1.33** Peptides based self-assembling building blocks with N-terminal protective groups.

**Figure 1.34** The diagram illustrates the process of selenoester-mediated native chemical ligation (NCL) reaction which is used to create Nmoc-capped self-assembled peptides.

**Figure 1.35** The chemical structure of 2-naphthylacetyl (2-Naph; 1a–c) and 1-naphthaloyl (1-Nap; 2a, b).

**Figure 1.36** (a) The scheme depicts the molecular composition of the sticky hydrogel. (b) Illustration depicting the use of sticky hydrogel for repairing articular cartilage. (c) Post-treatment magnetic resonance imaging. (d) The scheme shows the step-by-step procedure for making sticky HA-PG patches.

**Figure 1.37** (a) Schematic depicting the Exo-pGel treatment for spinal cord injury. (b) Images depicting the gaits of various animals. (c) Illustrative depiction of the process involved in creating hydrogels made of conducting polymers. Attachment of the hydrogel to (d) skin and (e) spinal cord tissue.

**Figure 1.38** The schematic illustration shows the formation of GP hydrogel and wound healing using mice model. 49

**Figure 1.39** The scheme depicts the formation of the hydrogel and its use in in vivo wound healing. 50

**Figure 1.40** The scheme demonstrates the formation of the G-quadruplex hydrogel and the use of the hydrogel for the delivery of the anticancer drug doxorubicin. 51

**Figure 1.41** The scheme demonstrates the formation of the hydrogel and the use of the hydrogel for the delivery of the vitamin molecules. 52

**Figure 1.42** The scheme illustrates the formation of the G-quadruplex hydrogel and the use of the hydrogel for 3D printing. 53

## **Chapter 2 Synthesis and Structural Studies of Nucleobase Functionalized Hydrogels for Controlled Release of Vitamins**

**Scheme 2.1** Synthetic outline of nucleobase amino acid conjugates. 88

**Figure 2.1**  $^1\text{H}$  NMR (500 MHz,  $\text{DMSO-}d_6$ ) spectrum of compound **2a**. 89

**Figure 2.2**  $^{13}\text{C}$  NMR (125 MHz,  $\text{DMSO-}d_6$ ) spectrum of compound **2a**. 89

**Figure 2.3** ESI-MS spectrum of compound **2a**. 90

**Figure 2.4**  $^1\text{H}$  NMR (500 MHz,  $\text{DMSO-}d_6$ ) spectrum of compound **2b**. 90

**Figure 2.5**  $^{13}\text{C}$  NMR (125 MHz,  $\text{DMSO-}d_6$ ) spectrum of compound **2b**. 91

**Figure 2.6** ESI-MS spectrum of compound **2b**. 91

**Figure 2.7**  $^1\text{H}$  NMR (500 MHz,  $\text{DMSO-}d_6$ ) spectrum of compound **2c**. 92

**Figure 2.8**  $^{13}\text{C}$  NMR (125 MHz,  $\text{DMSO-}d_6$ ) spectrum of **2c**. 92

**Figure 2.9** ESI-MS spectrum of compound **2c**. 92



<b>Figure 2.10</b> $^1\text{H}$ NMR (500 MHz, DMSO- $d_6$ ) spectrum of compound <b>3a</b> .	94
<b>Figure 2.11</b> $^{13}\text{C}$ NMR (125 MHz, DMSO- $d_6$ ) spectrum of compound <b>3a</b> .	94
<b>Figure 2.12</b> ESI-MS spectrum of compound <b>3a</b> .	95
<b>Figure 2.13</b> $^1\text{H}$ NMR (500 MHz, DMSO- $d_6$ ) spectrum of compound <b>3b</b> .	95
<b>Figure 2.14</b> $^{13}\text{C}$ NMR (125 MHz, DMSO- $d_6$ ) spectrum of compound <b>3b</b> .	96
<b>Figure 2.15</b> ESI-MS spectrum of compound <b>3b</b> .	96
<b>Figure 2.16</b> $^1\text{H}$ NMR (500 MHz, DMSO- $d_6$ ) spectrum of compound <b>3c</b> .	97
<b>Figure 2.17</b> $^{13}\text{C}$ NMR (125 MHz, DMSO- $d_6$ ) spectrum of compound <b>3c</b> .	97
<b>Figure 2.18</b> ESI-MS spectrum of compound <b>3c</b> .	97
<b>Figure 2.19</b> $^1\text{H}$ NMR (500 MHz, DMSO- $d_6$ ) spectrum of compound <b>NP1</b> .	98
<b>Figure 2.20</b> $^{13}\text{C}$ NMR (125 MHz, DMSO- $d_6$ ) spectrum of compound <b>NP1</b> .	99
<b>Figure 2.21</b> ESI-MS spectrum of compound <b>NP1</b> .	99
<b>Figure 2.22</b> $^1\text{H}$ NMR (500 MHz, DMSO- $d_6$ ) spectrum of compound <b>NP2</b> .	100
<b>Figure 2.23</b> $^{13}\text{C}$ NMR (125 MHz, DMSO- $d_6$ ) spectrum of compound <b>NP2</b> .	100
<b>Figure 2.24</b> ESI-MS spectrum of compound <b>NP2</b> .	101
<b>Figure 2.25</b> $^1\text{H}$ NMR (500 MHz, DMSO- $d_6$ ) spectrum of compound <b>NP3</b> .	101
<b>Figure 2.26</b> $^{13}\text{C}$ NMR (125 MHz, DMSO- $d_6$ ) spectrum of compound <b>NP3</b> .	102
<b>Figure 2.27</b> ESI-MS spectrum of compound <b>NP3</b> .	102
<b>Figure 2.28</b> (a) The increasing hydrophobicity in the synthesized nucleobase peptide conjugated molecule induces proper hydrophilic and hydrophobic which in turn leads to the	109

formation of the hydrogel. DOSY NMR spectrum of 10 mM (b) **NP1**, (c) **NP2** and, (d) **NP3** in D<sub>2</sub>O at 298K. Optical images of **NP3** hydrogel formed in (e) LiOH and (f) NaOH. (g) Precipitation was observed when prepared with KCl (100 mM) solution.

**Scheme 2.2** Graphical illustration demonstrating the development of **NP3** hydrogel with the support of suitable monovalent alkali metal ion and the utilization of hydrogel to study the release of vitamins from the hydrogel matrices.

**Figure 2.29** (a) Fluorescence spectra of ThT solution (black line), ThT loaded **NP3** without K<sup>+</sup> (blue line) and ThT loaded **NP3** hydrogel (in presence of K<sup>+</sup>) (red line). (b) Optical photographs of ThT loaded **NP3** hydrogel under daylight (left) and under 365 nm UV light (right). (c) Plausible mechanism of enhancement of fluorescence intensity in presence of ThT. (d) Wide angle powder X-ray diffraction pattern of the **NP3** xerogel. (e) Graphical presentation of the G-quadruplex showing the distance between two consecutive stacked G-quartet and the width of the quartet. (f) Wide angle PXRD spectrum of **NP3**.

**Figure 2.30** (a) CD spectrum of the **NP3** hydrogel (0.2 mM). Circular dichroism spectra of the **NP3** hydrogel prepared with (b) NaOH and (c) LiOH. FT-IR spectra of (d) **NP3** compound and (e) xerogel of **NP3**.

**Figure 2.31** (a) TEM image shows the presence of nanofibrillar morphology inside the **NP3** hydrogel. (b) AFM image also reveals nanofibrillar morphology in the hydrogel state. (c) AFM 3D height profile image of **NP3** hydrogel. (d) SEM image of **NP3** hydrogel.

**Figure 2.32** Rheological experiments of **NP3** hydrogel: (a) amplitude strain-sweep experiment where frequency was fixed at 10 rad. s<sup>-1</sup> and (b) the frequency sweep test at fixed strain of 1%. Rheological experiments of **NP3** hydrogel prepared in

NaOH (c) Amplitude sweep experiment. (d) Frequency sweep experiment at a constant strain of 0.5%. Rheological experiments of **NP3** hydrogel prepared in LiOH. (e) Amplitude sweep experiment. (f) Frequency sweep experiment at a constant strain of 0.5%.

**Figure 2.33** (a) Optical photographs demonstrate the 117 Injectability nature of the **NP3** hydrogel. (b) Dynamic step-strain sweep profile of the **NP3** hydrogel at a constant angular frequency of  $10 \text{ rad.s}^{-1}$ . Rheological experiment of vitamin B<sub>2</sub> loaded hydrogel: (c) Amplitude sweep experiment. (d) Frequency sweep experiment. Rheological experiment of vitamin B<sub>12</sub> loaded hydrogel: (e) Amplitude sweep experiment. (f) Frequency sweep experiment.

**Figure 2.34** Cumulative release (%) of vitamins: (a) release 119 profiles of vitamin B<sub>12</sub> and (b) release profiles of vitamin B<sub>2</sub> from the gel matrices at pH = 4.0, 5.5, 7.4. Error bars represent SD, n = 3.

**Figure 2.35** Model fittings of vitamin B<sub>12</sub> release profile with 120 different equations: (1) Zero-order release model at pH (a) 4.0, (b) 5.5 (c) 7.4, (2) first-order release model at pH (d) 4.0, (e) 5.5, (f) 7.4, (3) Higuchi release model at pH (g) 4.0, (h) 5.5 (i) 7.4.

**Figure 2.36** Model fittings of vitamin B<sub>2</sub> release profile with 121 different equations: lease (1) Zero-order release model at pH (a) 4.0, (b) 5.5 (c) 7.4, (2) first-order release model at pH (d) 4.0, (e) 5.5, (f) 7.4, (3) Higuchi release model at pH (g) 4.0, (h) 5.5 (i) 7.4.

**Figure 2.37** Time-dependent progress of digestion of 122 hydrogelator **NP3** by (a) proteinase K and (b) chymotrypsin. Time-dependent HPLC Chromatograms of **NP3** hydrogelator with (c) proteinase K and (d) chymotrypsin.

**Figure 2.38** Concentration dependent (2-0.0078 mM) MTT 123 cell viability experiment of **NP3** hydrogel against (a) HEK 293

and (b) MCF-7 cells. Statistical analysis of data was carried out by one-way ANOVA test. A collection of biological triplicates served as the basis for all the findings. *P* values were calculated using GraphPad Prism software version 9.0. *P* values < 0.05 were considered statistically significant and represented by # increased, the remaining data points show non-significant changes (*N* = 3).

**Figure 2.39** Biocompatibility assessment of **NP3** hydrogels using the MCF-7 cell line. (a) Control, (b) 0.25 mM **NP3** hydrogel, (c) 0.031 mM **NP3** hydrogel (Scale bar 20  $\mu$ m). 124

### **Chapter 3 Chemical Reaction Driven Self-assembly of a Nucleobase Functionalized Molecule**

**Scheme 3.1.** Synthesis of **NP3** and **NP4**. 141

**Figure 3.1**  $^1\text{H}$  NMR (500 MHz,  $\text{DMSO-}d_6$ ) spectrum of compound **2c**. 142

**Figure 3.2** ESI-MS spectrum of compound **2c**. 142

**Figure 3.3**  $^1\text{H}$  NMR (500 MHz,  $\text{DMSO-}d_6$ ) spectrum of compound **4b**. 143

**Figure 3.4** ESI-MS spectrum of compound **4b**. 143

**Figure 3.5**  $^1\text{H}$  NMR (500 MHz,  $\text{DMSO-}d_6$ ) spectrum of compound **3c**. 144

**Figure 3.6**  $^{13}\text{C}$  NMR (125 MHz,  $\text{DMSO-}d_6$ ) spectrum of compound **3c**. 145

**Figure 3.7** ESI-MS spectrum of compound **3c**. 145

**Figure 3.8**  $^1\text{H}$  NMR (500 MHz,  $\text{DMSO-}d_6$ ) spectrum of compound **5b**. 146

**Figure 3.9**  $^{13}\text{C}$  NMR (125 MHz,  $\text{DMSO-}d_6$ ) spectrum of compound **5b**. 146

**Figure 3.10** ESI-MS spectrum of compound **5b**. 146

**Figure 3.11**  $^1\text{H}$  NMR (500 MHz,  $\text{DMSO-}d_6$ ) spectrum of compound **NP3**. 147

**Figure 3.12**  $^{13}\text{C}$  NMR (125 MHz,  $\text{DMSO-}d_6$ ) spectrum of compound **NP3**. 148

**Figure 3.13** ESI-MS spectrum of compound **NP3**. 148

**Figure 3.14**  $^1\text{H}$  NMR (500 MHz,  $\text{DMSO-}d_6$ ) spectrum of compound **NP4**. 149

**Figure 3.15**  $^{13}\text{C}$  NMR (125 MHz,  $\text{DMSO-}d_6$ ) spectrum of compound **NP4**. 149

**Figure 3.16** ESI-MS spectrum of compound **NP4**. 149

**Scheme 3.2.** Graphical representation demonstrates the activation of the non-assembling building blocks by the addition of dimethyl sulphate. 153

**Figure 3.17.** Conversion plot of (a) **NP3** after the addition of DMS, show the formation methylated products. Formation of the hydrogel after the addition of dimethyl sulphate. (b) Formation of the hydrogel after the addition of dimethyl sulphate. The change of the pH of the medium of (c) **NP3** and (d) **NP3** after the addition of 2 and 5 equivalent of DMS. 154

**Figure 3.18.** Conversion plot of (a) **NP4**. No significant change is observed for **NP4** after 4 h. (b) Precipitate formed after the addition of the DMS in **NP4**. (c) The conversion of **NP3** after the addition of 2 equiv DMS (d) The conversion of **NP4** after the addition of 2 equiv DMS. 155

**Figure 3.19.** (a) ESI-MS spectrum after the formation of the **NP3** hydrogel. (b) ESI-MS spectrum of the precipitate of **NP4**. 156

**Figure 3.20.** FT-IR spectra of (a) the **NP3** hydrogel and the gelator precursor **NP3**. (b) Wide angle powder XRD spectrum of **NP3** hydrogel and **NP3**. (c) Fluorescence spectra of **NP3**, ThT and ThT incorporated in **NP3** hydrogel. 157

**Figure 3.21.** Confocal laser scanning microscopy images (DIC, Fluorescence) of (a) **NP3** hydrogel and (b) ThT loaded **NP3** hydrogel (scale bar = 5  $\mu\text{m}$ ). The images were taken after the formation of the **NP3** hydrogel at day 1. Rheological experiments (c) amplitude sweeps experiment (d) frequency 158

sweep experiment. Dynamic step-strain sweep profile of **NP3** hydrogel at a constant angular frequency of  $10 \text{ rad s}^{-1}$ .

**Figure 3.22.** (a) The increase of viscosity with the time demonstrates the formation of the hydrogel after the addition of the DMS. (b) UV turbidity experiment. (c) Time dependent fluorescence spectra (d) time dependent CD spectra of the **NP3** hydrogel after the addition of the DMS.

**Figure 3.23.** Time dependent NMR spectra depicting the formation of active molecules after the addition of dimethyl sulphate. From, the NMR spectrum, it is evident that the addition of DMS activate the precursor molecule which undergo higher order self-assembly to form the hydrogel. The control spectra are taken without DMS.

**Figure 3.24.** (a) CLSM image captured after the addition of the DMS (0 min) (b) CLSM images taken after 15 min from the addition of the DMS at the same region. Morphological assessment: (c) TEM (d) SEM images of the DMS-driven **NP3** hydrogel demonstrate the presence of fiber. The images were taken after the formation of the **NP3** hydrogel at day 1.

#### **Chapter 4 Design and Synthesis of a Nucleobase Functionalized Peptide Hydrogel: in vitro Assessment of Anti-inflammatory and Wound Healing Effects**

**Scheme 4.1** Synthesis of Nucleobase functionalized peptide derivatives (NPs)

**Figure 4.1.**  $^1\text{H}$  NMR (500 MHz,  $\text{DMSO-}d_6$ ) spectrum of **6a**.

**Figure 4.2** ESI-MS spectrum of **6a**.

**Figure 4.3.**  $^1\text{H}$  NMR (500 MHz,  $\text{DMSO-}d_6$ ) spectrum of **6b**.

**Figure 4.4** ESI-MS spectrum of **6b**.

**Figure 4.5.**  $^1\text{H}$  NMR (500 MHz,  $\text{DMSO-}d_6$ ) spectrum of **6c**.

**Figure 4.6** ESI-MS spectrum of **6c**.

**Figure 4.7.**  $^1\text{H}$  NMR (500 MHz,  $\text{DMSO-}d_6$ ) spectrum of **7a**.

**Figure 4.8** ESI-MS spectrum of **7a**.

<b>Figure 4.9.</b> $^1\text{H}$ NMR (500 MHz, $\text{DMSO-}d_6$ ) spectrum of <b>7b</b> .	185
<b>Figure 4.10</b> ESI-MS spectrum of <b>7b</b> .	185
<b>Figure 4.11.</b> $^1\text{H}$ NMR (500 MHz, $\text{DMSO-}d_6$ ) spectrum of <b>7c</b> .	186
<b>Figure 4.12</b> ESI-MS spectrum of <b>7c</b> .	186
<b>Figure 4.13.</b> $^1\text{H}$ NMR (500 MHz, $\text{DMSO-}d_6$ ) spectrum of <b>NP5</b> .	187
<b>Figure 4.14</b> $^{13}\text{C}$ NMR (125 MHz, $\text{DMSO-}d_6$ ) spectrum of <b>NP5</b> .	188
<b>Figure 4.15</b> ESI-MS spectrum of <b>NP5</b> .	188
<b>Figure 4.16.</b> $^1\text{H}$ NMR (500 MHz, $\text{DMSO-}d_6$ ) spectrum of <b>NP6</b> .	189
<b>Figure 4.17</b> $^{13}\text{C}$ NMR (125 MHz, $\text{DMSO-}d_6$ ) spectrum of <b>NP6</b> .	189
<b>Figure 4.18</b> ESI-MS spectrum of <b>NP6</b> .	190
<b>Figure 4.19</b> $^1\text{H}$ NMR (500 MHz, $\text{DMSO-}d_6$ ) spectrum of <b>NP7</b> .	190
<b>Figure 4.20</b> $^{13}\text{C}$ NMR (125 MHz, $\text{DMSO-}d_6$ ) spectrum of <b>NP7</b> .	191
<b>Figure 4.21</b> ESI-MS spectrum of <b>NP7</b> .	191
<b>Figure 4.22</b> The formation of the hydrogel by <b>NP5</b> . The formation of the precipitate in presence of the phosphate buffer pH = 7.4 by <b>NP6</b> and <b>NP7</b> respectively.	199
<b>Scheme 4.2</b> Schematic illustration demonstrates the formation of the <b>NP5</b> hydrogel, which effectively decreases the inflammation, is efficient against bacterial infection and exhibits excellent activity for the invitro wound healing.	200
<b>Figure 4.23</b> (a) Self-aggregation of the synthesized <b>NPs</b> at 0 ns, 50 ns and 100 ns. (b) The decrease of the solvent accessible surface area (SASA) with time.	201
<b>Figure 4.24</b> DOSY NMR spectrum of 10 mM (a) <b>NP5</b> (b) <b>NP6</b> (c) <b>NP7</b> in $\text{D}_2\text{O}$ at 298K.	203
<b>Figure 4.25</b> (a) Circular dichroism spectrum of the <b>NP5</b> hydrogel. (b) Fluorescence spectrum of the ThT solution (blue line), <b>NP5</b> hydrogel (red line) and <b>NP5</b> hydrogel with ThT, the excitation wavelength was 450 nm. (c) CLSM images show non fluorescent supramolecular assemblies ( $\lambda_{\text{ex}} = 488 \text{ nm}$ ) in the <b>NP5</b> hydrogel, upon binding with the ThT, it becomes fluorescent (Scale bar in all images are 5 $\mu\text{m}$ ).	204

**Figure 4.26** PXRD spectrum of (a) **NP5** hydrogel and (b) the synthesized gelator precursor **NP5**. (c) FT-IR spectra of the **NP5** (red line) and **NP5** hydrogel (blue line). (d) Amplitude sweep experiment of the **NP5** hydrogel. (e) Frequency sweep experiment of the **NP5** hydrogel. (f) SEM and (g) TEM images show the presence of the nano-fibrillar morphology in the **NP5** hydrogel.

**Figure 4.27** The MTT assay to check cell viability of **NP5** hydrogel on (a) fibroblasts McCoy cell line and (b) epithelial A549 cell line. Unpaired *t*-tests were conducted for the statistical analysis of the data using graphpad prism trial version. *p*-values of <0.05, <0.001 and <0.0001 were represented with \*, \*\* and \*\*\* respectively as compared to the control. (c) Live-dead cell imaging shows excellent viability of the **NP5** hydrogel towards epithelial A549 cell line. Fluorescein Diacetate (FdA) was used to detect the presence of the live cells after the incubation with different concentration of the **NP5** hydrogel and Propidium iodide (PI) was used for the visualization of the dead cells (scale bar 20  $\mu$ m).

**Figure 4.28** Live-dead cell imaging on the fibroblast McCoy cell by the newly developed **NP5** hydrogel. The scale bar in all the images is 20  $\mu$ m.

**Figure 4.29** (a) Quantitative measurement of the hemolysis by the **NP5** hydrogel (b) optical image shows the hemolytic activity of the **NP5** hydrogel. Unpaired *t*-tests were conducted for the statistical analysis of the data using graphpad prism trial version. *p*-values of <0.05, <0.001 and <0.0001 were represented with \*, \*\* and \*\*\* respectively for significant upregulation and #, ##, and ### for significant downregulation with respect to the control.

**Figure 4.30** HPLC chromatograms depicts the degradation of the **NP5** hydrogel in the presence of the proteolytic enzymes



(a)  $\alpha$ -chymotrypsin (b) proteinase-K. The (%) of the compound remained after the degradation by the proteolytic enzymes (a)  $\alpha$ -chymotrypsin (b) proteinase-K.

**Figure 4.31** The invitro wound healing experiment on the (a) 213 A549 cell 'and' (b) fibroblasts McCoy cell. The quantification of the wound closure by the (c) A549 cell (d) McCoy cell at 0 h, 12 h, 24 h, 36 h, and 48 h. Unpaired *t*-tests were conducted for the statistical analysis of the data using graphpad prism trial version. p-values of <0.05, <0.001 and <0.0001 were represented with \*, \*\* and \*\*\* respectively as compared to the respective 0 h of each group.

**Figure 4.32** DCFDA assay of the **NP5** hydrogel on the (a) 215 epithelial A549 cell line 'and' (b) fibroblasts McCoy cell line. H<sub>2</sub>O<sub>2</sub> was used to create inflammation in the cell. The scale bar in all images is 50  $\mu$ m. The quantification of the inflammation by the (c) A549 'and' (d) McCoy cell with respect to the control was measured with the ImageJ software. Y-axis was broken at 10. Unpaired *t*-tests were conducted for the statistical analysis of the data using graphpad prism trial version. p-values of <0.05, <0.001 and <0.0001 were represented with \*, \*\* and \*\*\* respectively as compared to the control.

**Figure 4.33** Treatment of hydrogel dampens the inflammatory 217 response in lung and fibroblast cells. McCoy and A549 cells were treated with bacterial lipopolysaccharide (LPS) for 12 h to induce inflammation followed by treatment of **NP5** hydrogel for another 12 h (LPS+ **NP5** hydrogel group). Only LPS and gel group cells were treated with LPS and **NP5** hydrogel for 12 and 24 h respectively. After completion of the treatment period cells were harvested and transcript and protein level of inflammatory markers were evaluated. Relative transcript level of inflammatory markers (IL6, TNF $\alpha$  and NF $\kappa$ B) in (a) McCoy 'and' (b) A549 cells. (c) Representative western blot image of NF $\kappa$ B in McCoy (left panel) 'and' A549 (right panel) cells.

Relative NFκB protein level in (d) McCoy 'and' (e) A549 cells. The experiment was performed in triplicates, and the results are shown as the mean ± SD of three data points. Statistical significance was determined by Unpaired *t*-tests with 95% confidence interval. \*/#, \*\*/## and \*\*\*/### denotes p-values of < 0.05, < 0.001 and < 0.0001 respectively as compared to the control for significant up/down regulation.

**Figure 4.34** The antibacterial activity of the synthesized **NP5** hydrogel was investigated against (a) Gram-negative *E. coli* (b) Gram-positive *B. subtilis*. All the results were derived from technical triplicate (N = 3). All the data were statistically analyzed by unpaired t-test using graphpad prism trial version. \*p< 0.05, \*\*p< 0.01 as compared to the control. FE-SEM images of the *E.coli* bacteria (c) control (without **NP5** hydrogel) (d) in the presence of the **NP5** hydrogel.

## Chapter 5 Enzyme Fueled Dissipative Self-assembly of Guanine Functionalized Molecules and Their Cellular Behaviour

**Scheme 5.1** Synthesis of guanine functionalized amino acid derivatives.

<b>Figure 5.1</b> <sup>1</sup> H NMR (500 MHz, CDCl <sub>3</sub> ) spectrum of <b>8a</b> .	238
<b>Figure 5.2</b> <sup>13</sup> C NMR (125 MHz, CDCl <sub>3</sub> ) spectrum of <b>8a</b> .	238
<b>Figure 5.3</b> ESI-MS spectrum of <b>8a</b> .	239
<b>Figure 5.4</b> <sup>1</sup> H NMR (500 MHz, CDCl <sub>3</sub> ) spectrum of <b>8b</b> .	239
<b>Figure 5.5</b> <sup>13</sup> C NMR (125 MHz, CDCl <sub>3</sub> ) spectrum of <b>8b</b> .	240
<b>Figure 5.6</b> ESI-MS spectrum of <b>8b</b> .	240
<b>Figure 5.7</b> <sup>1</sup> H NMR (500 MHz, CDCl <sub>3</sub> ) spectrum of <b>8c</b> .	241
<b>Figure 5.8</b> <sup>13</sup> C NMR (125 MHz, CDCl <sub>3</sub> ) spectrum of <b>8c</b> .	241
<b>Figure 5.9</b> ESI-MS spectrum of <b>8c</b> .	241
<b>Figure 5.10</b> <sup>1</sup> H NMR (500 MHz, CDCl <sub>3</sub> ) spectrum of <b>8d</b> .	242
<b>Figure 5.11</b> <sup>13</sup> C NMR (125 MHz, CDCl <sub>3</sub> ) spectrum of <b>8d</b> .	243
<b>Figure 5.12</b> ESI-MS spectrum of <b>8d</b> .	243

<b>Figure 5.13</b> $^1\text{H}$ NMR (500 MHz, $\text{CDCl}_3$ ) spectrum of <b>8e</b> .	244
<b>Figure 5.14</b> $^{13}\text{C}$ NMR (125 MHz, $\text{CDCl}_3$ ) spectrum of <b>8e</b> .	244
<b>Figure 5.15</b> ESI-MS spectrum of <b>8e</b> .	244
<b>Figure 5.16</b> $^1\text{H}$ NMR (500 MHz, $\text{DMSO}-d_6$ ) spectrum of <b>9a</b> .	246
<b>Figure 5.17</b> $^{13}\text{C}$ NMR (125 MHz, $\text{CDCl}_3$ ) spectrum of <b>9a</b> .	246
<b>Figure 5.18</b> ESI-MS spectrum of <b>9a</b> .	247
<b>Figure 5.19</b> $^1\text{H}$ NMR (500 MHz, $\text{DMSO}-d_6$ ) spectrum of <b>9b</b> .	247
<b>Figure 5.20</b> $^{13}\text{C}$ NMR (125 MHz, $\text{CDCl}_3$ ) spectrum of <b>9b</b> .	248
<b>Figure 5.21</b> ESI-MS spectrum of <b>9b</b> .	248
<b>Figure 5.22</b> $^1\text{H}$ NMR (500 MHz, $\text{DMSO}-d_6$ ) spectrum of <b>9c</b> .	249
<b>Figure 5.23</b> $^{13}\text{C}$ NMR (125 MHz, $\text{CDCl}_3$ ) spectrum of <b>9c</b> .	249
<b>Figure 5.24</b> ESI-MS spectrum of <b>9c</b> .	250
<b>Figure 5.25</b> $^1\text{H}$ NMR (500 MHz, $\text{DMSO}-d_6$ ) spectrum of <b>9d</b> .	250
<b>Figure 5.26</b> $^{13}\text{C}$ NMR (125 MHz, $\text{CDCl}_3$ ) spectrum of <b>9d</b> .	251
<b>Figure 5.27</b> ESI-MS spectrum of <b>9d</b> .	251
<b>Figure 5.28</b> $^1\text{H}$ NMR (500 MHz, $\text{DMSO}-d_6$ ) spectrum of <b>9e</b> .	252
<b>Figure 5.29</b> $^{13}\text{C}$ NMR (125 MHz, $\text{CDCl}_3$ ) spectrum of <b>9e</b> .	252
<b>Figure 5.30</b> ESI-MS spectrum of <b>9e</b> .	252
<b>Figure 5.31</b> $^1\text{H}$ NMR (500 MHz, $\text{DMSO}-d_6$ ) spectrum of <b>NP8</b> .	254
<b>Figure 5.32</b> $^{13}\text{C}$ NMR (125 MHz, $\text{CDCl}_3$ ) spectrum of <b>NP8</b> .	254
<b>Figure 5.33</b> ESI-MS spectrum of <b>NP8</b> .	255
<b>Figure 5.34</b> $^1\text{H}$ NMR (500 MHz, $\text{DMSO}-d_6$ ) spectrum of <b>NP4</b> .	255
<b>Figure 5.35</b> $^{13}\text{C}$ NMR (125 MHz, $\text{CDCl}_3$ ) spectrum of <b>NP4</b> .	256
<b>Figure 5.36</b> ESI-MS spectrum of <b>NP4</b> .	256
<b>Figure 5.37</b> $^1\text{H}$ NMR (500 MHz, $\text{DMSO}-d_6$ ) spectrum of <b>NP3</b> .	257
<b>Figure 5.38</b> $^{13}\text{C}$ NMR (125 MHz, $\text{CDCl}_3$ ) spectrum of <b>NP3</b> .	257
<b>Figure 5.39</b> ESI-MS spectrum of <b>NP3</b> .	258
<b>Figure 5.40</b> $^1\text{H}$ NMR (500 MHz, $\text{DMSO}-d_6$ ) spectrum of <b>NP9</b> .	258
<b>Figure 5.41</b> $^{13}\text{C}$ NMR (125 MHz, $\text{CDCl}_3$ ) spectrum of <b>NP9</b> .	259
<b>Figure 5.42</b> ESI-MS spectrum of <b>NP9</b> .	259
<b>Figure 5.43</b> $^1\text{H}$ NMR (500 MHz, $\text{DMSO}-d_6$ ) spectrum of <b>NP10</b> .	260
<b>Figure 5.44</b> $^{13}\text{C}$ NMR (125 MHz, $\text{CDCl}_3$ ) spectrum of <b>NP10</b> .	260

**Figure 5.42** ESI-MS spectrum of **NP10**. 261

**Scheme 5.2.** Graphical representation demonstrating the biocatalytic dissipative self-assembly. 267

**Figure 5.43** (a) Ester conversion (%) of **NP10** with time (days). 268  
(b) Ester conversion histogram of **NPs** at 55 days by the lipase.  
HPLC chromatograms of (c) **NP8**, (d) **NP4**, (e) **NP3** (f) **NP9**  
(g) **NP10** (blue line) and biocatalytic conversion to ester (red line) at 55 days. (h) Docking image shows the binding region of the **NP10** in lipase. (i) Protein-ligand interaction diagram of 1CRL and **NP10**.

**Figure 5.44** Protein-ligand interaction diagram of 1CRL (a) 269  
**NP8** and (b) **NP4** (c) **NP3** and (d) **NP9**.

**Figure 5.45** ESI-MS analysis for the biocatalytically formed 269  
**NP10** hydrogel. The enzymatic reaction between the synthesized nucleobase amino acid conjugate and *p*-hydroxybenzyl alcohol was used to generate **NP10** hydrogel.

**Figure 5.46** (a) The participation of the aliphatic -OH group of 270  
PHBA in the esterification of **NP10** process is confirmed by the <sup>1</sup>H NMR spectra in DMSO-*d*<sub>6</sub>. (b) FT-IR Spectra of **NP10** xerogel (red line), **NP10** hydrogel (pink line) and **NP10** (blue line). (c) CD spectra of the biocatalytically formed **NP10** hydrogel with time (200 μM). Wide angle PXRD spectrum of **NP10** (red line), **NP10** hydrogel (blue line) and PHBA.

**Figure 5.47** (a) ThT dye binding assay: the excitation spectrum 272  
of ThT (black line), **NP10** hydrogel (pink line) and **NP10** hydrogel+ThT (green line) at 450 nm. ThT dye binding experiment was performed after the formation of the hydrogel at 30 days. (b) Absorbance spectra of the synthesized nucleobase functionalized amino acid conjugate **NP10** hydrogel at 30 day, **NP10** and PHBA. (c) Normalised excitation and (d) emission spectra ( $\lambda_{\text{ex}} = 375$  nm) of the **NP10** hydrogel at 30 day, **NP10** and PHBA. Rheological experiments

(e) amplitude sweeps and (f) frequency sweep experiment of the biocatalytically formed **NP10** hydrogel.

**Figure 5.48** (a) SEM images of nanofiber enclosed sphere, the formation of the fiber enclosed nanosphere on the progress of the reaction has been shown here. (The scale bar in all the images is 1  $\mu\text{m}$ ). (b) TEM image of the biocatalytically formed **NP10** hydrogel at 30 day. The image was taken after the formation of the hydrogel at 30 day.

**Figure 5.49** CLSM images show the formation of the fiber enclose sphere caused by lipase catalyzed esterification of PHBA in **NP10**. (Scale bar in all images are 5  $\mu\text{m}$ ).

**Scheme 5.3** Graphical illustration demonstrating the formation of the bio-catalytically formed **NP10** hydrogel and its use to study cell proliferation and cell migration.

**Figure 5.50** In the cell viability experiment, a range of concentrations (0.00781-1 mM) was applied to check the viability of the cell lines (a) HEK 293 and (b) McCoy.

**Figure 5.51** Live and dead cell images on HEK 293 cell lines of (a) control (buffer treated), (b) 0.25 mM and (c) 0.061 mM **NP10** hydrogel. The images were taken using a 10x objective z1.0 (The scale bar in all images is 20  $\mu\text{m}$ ).

**Figure 5.52** CLSM images (scale bar in all images are 20  $\mu\text{m}$ ) taken after treating of the McCoy cells with **NP10** hydrogel (0.25 mM). The images were taken using 100x objective z1.0.

**Figure 5.53** The scratch wound test was used to evaluate the migratory behavior of McCoy cells after the treatment of 0.5 mM and 0.25 mM of **NP10** hydrogel and control. The migration of the cells was at time 0 h, 12 h and 24 h. (Scale bar in all images are 50  $\mu\text{m}$ ).

**Figure 5.54** Quantification of the wound closure by **NP10** hydrogel after its formation at 30 day with time after 0 h, 12 h and 24 h.



# LIST OF TABLES

## **Chapter 2 Synthesis and Structural Studies of Nucleobase Functionalized Hydrogels for Controlled Release of Vitamins**

<b>Table 2.1</b> Kinetic parameters of vitamin release obtained by fitting in three different release models	120
---	-----





# ACRONYMS

AFM	Atomic Force Microscopy
Boc	<i>tert</i> -butoxycarbonyl
(Boc) <sub>2</sub> O	Di- <i>tert</i> -butyl dicarbonate
CD	Circular Dichroism
DMSO	Dimethyl sulfoxide
DCM	Dichloromethane
DMAP	4-Dimethylaminopyridine
DMF	N,N-dimethylformamide
DCFH-DA	Dichloro-dihydro-fluorescein diacetate
<i>d</i>	Doublet
ESI	Electron spray ionization
FTIR	Fourier Transform Infrared Spectroscopy
HCl	Hydrochloric Acid
HEK	Human embryonic kidney
KOH	Potassium hydroxide
K <sub>2</sub> CO <sub>3</sub>	Potassium carbonate
MeOH	Methanol
MCF-7	Michigan Cancer Foundation-7
NaCl	Sodium Chloride
NaOH	Sodium hydroxide
NaHCO <sub>3</sub>	Sodium bicarbonate
NMR	Nuclear Magnetic Resonance
Na <sub>2</sub> SO <sub>4</sub>	Sodium sulfate
NMM	4-Methylmorpholine
THF	Tetrahydrofuran
TEM	Transmission electron microscopy
t	Triplet
SEM	Scanning Electron Microscope
s	Singlet

# NOMENCLATURE

$\theta$	Angle
$\text{\AA}$	Angstrom
$\omega$	Angular Frequency
$G'$	Storage Modulus
$G''$	Loss Modulus
mM	Millimolar
$\mu\text{M}$	Micromolar
$\mu\text{m}$	Micrometer
nM	Nanometer
$\lambda$	Wavelength





# **Chapter 1**

## **General Introduction**



## 1.1 Introduction

### 1.1.1 Molecular self-assembly

Molecular self-assembly refers to the organization of the molecules in the absence of any external guidance [1,2]. The process of self-assembly involves the formation of organized structures from the disordered structures of the existing molecules. The self-assembly is most commonly observed phenomenon in the natural system. Molecular self-assembly offers several advantages. First, it performs many of the most challenging procedures in nanofabrication (including atomic-level alterations) with highly sophisticated synthetic chemistry techniques. Second, it takes inspiration from the vast array of examples seen in biology, as self-assembly is one of the most significant techniques utilized in biology for the production of intricate functional structures. Third, biological structures can be directly included in the final systems as components [3]. Therefore, scientists have utilized the potent phenomena of molecular self-assembly, which they inherited from nature to create innovative supramolecular structures. The molecular self-assembly is spontaneous and ubiquitous in nature which occurs under thermodynamics equilibrium [4,5]. The molecules under equilibrium spontaneously form supramolecular nanostructures by non-covalent interactions such as pi-pi stacking interaction, H-bonding interactions, hydrophobic interaction, ionic interaction, van der Waals interaction, and dipole-dipole interaction [6-8]. The formation of lipid layers [9], micelle [10], vesicle [11], cylinder [12], nanotube [13], coacervates [14], nanofiber [15] host-guest [16] are instances of the molecular self-assemble system (**Figure 1.1**).

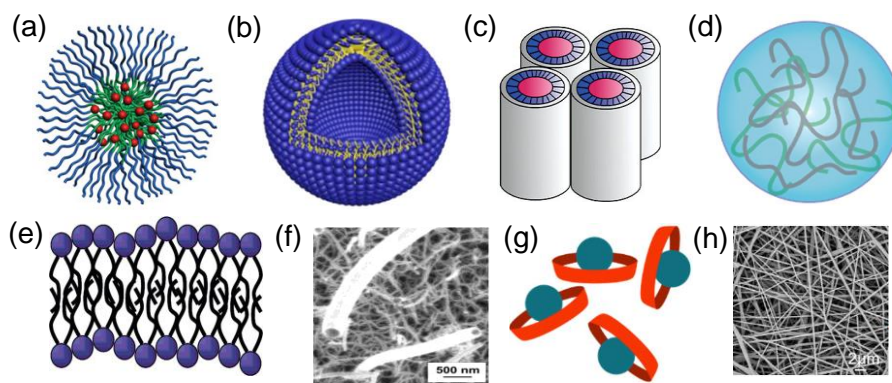


**Figure 1.1** Self-assembled nanostructures: (a) micelles, (b) vesicles, (c) cylinder, (d) coacervates, (e) bilayers, (f) nanotubes, (g) host–guest, and (h) nanofiber. [Recreated from ref. no. 9-16]

In self-assembly, the desired morphology is encrypted in the properties and shape of the molecules which are utilized in comparison to conventional techniques like lithography where the expected morphology is fabricated from the larger matter. For this reason, self-assembly is called as a "bottom-up" manufacturing process, while lithography is called as a "top-down" process [17]. Molecular self-assembly is a form of bottom-up strategy in which molecules adopt a specific layout (**Figure 1.2**).

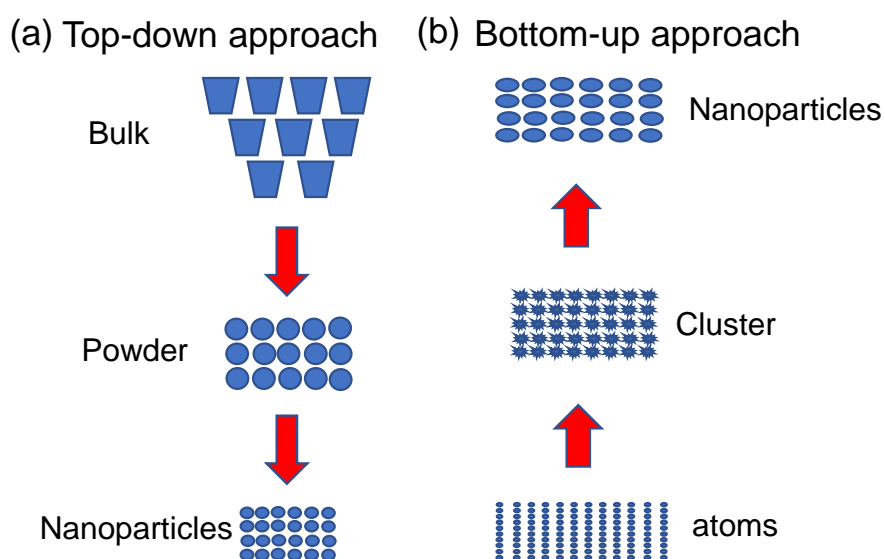




**Figure 1.2** Top-down and bottom-up fabrication approach: (a) the formation of nanoparticles from the bulk of the matter and (b) atoms aggregate into clusters to form the nanoparticles.

In the top-down method, larger components break into smaller parts. The top-down methodology was invented by Alois Asnefeler in 1978 [18]. This approach has now ushered in a new age in the biological and material sciences (**Figure 1.3**). Top-down approaches are employed to create functional nano materials of proteins and peptides [19,20]. Therefore, combining this top-down method with self-assembling materials might provide several options for bioelectronics and micro- or nanofabricated devices.

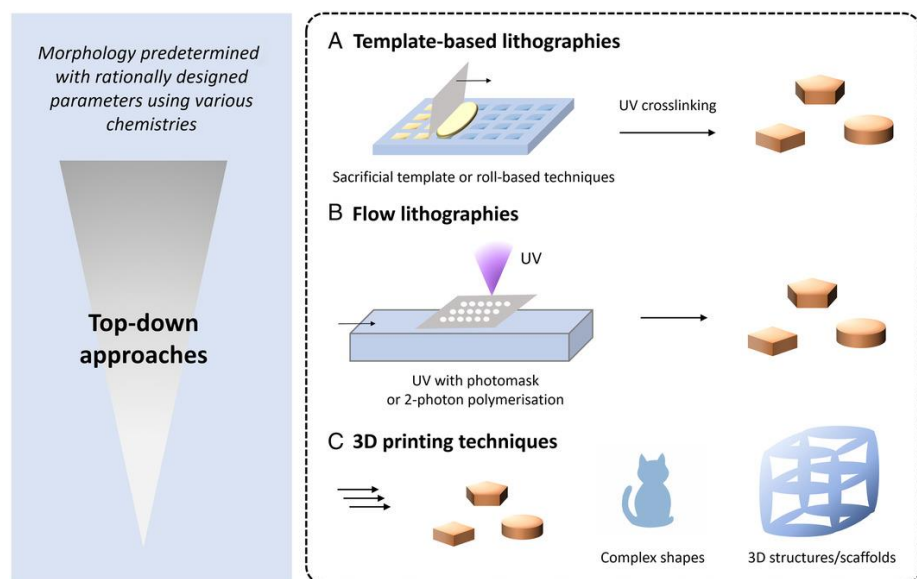


**Figure 1.3** Methods for creating nanoparticles and microparticles with specific sizes and shapes using a top-down approach: (a) Template-based and stamp lithography methods use either disposable templates that can be dissolved or templates that can be used again, (b) Flow-based lithography methods can be used by UV light with photomasks that are precisely made, or two-photon polymerization and (c) Stereolithography or 3D printing can make micro- and nanoparticles in the widest range of shapes, but it might not be as easy to scale up. [Recreated from ref. no. 19]

The idea of bottom-up self-assembly came from a popular quotation given by Richard Feynman at a lecture that there is plenty of room at the bottom [21]. In this approach, the individual molecules and atoms are used as building blocks for the generation of the higher-ordered structure by self-assembly. Specially in supramolecular chemistry, the fabrication of the molecules with a distinct molecular structure has the capability for use in a variety of chemical and material science domains (**Figure 1.4**). Usually, a more sophisticated assembly is often created by arranging smaller components in a bottom-up manner [22].

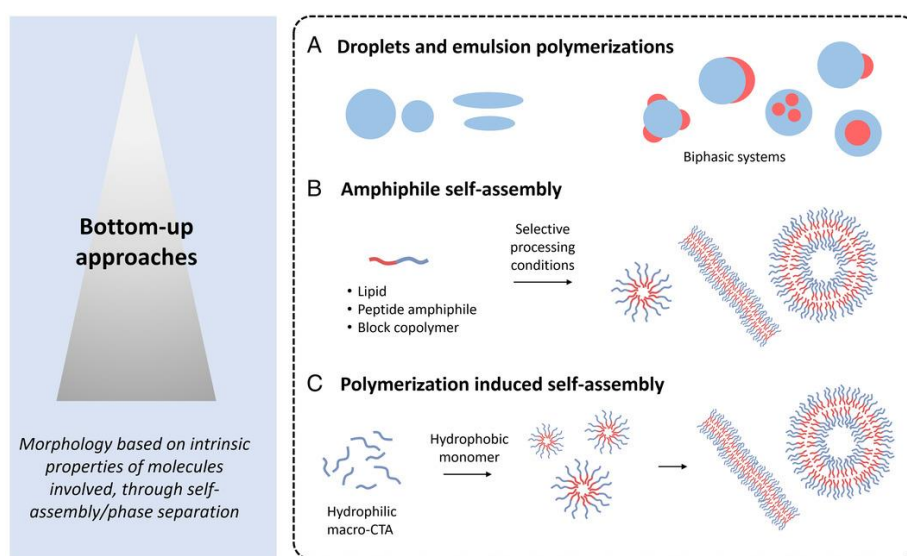


**Figure 1.4** Bottom-up approaches for the formation of nanoparticles and microparticles that are defined by their size and shape: (a) Emulsion polymerizations and emulsions, with single phases that don't mix, (b) Spontaneous arrangement of chemically different molecules that have both hydrophilic and hydrophobic parts which lead to the formation of nanostructures of different forms and size under certain circumstances and (c) Polymer induced self-assembly (PISA) of molecules that are hydrophilic and hydrophobic, with radical polymerizations that can be activated as well as deactivate, or controlled ring-opening polymerizations. [Recreated from ref. no. 19]

These procedures are resemble with the seed model, which begins with small but grows with complexity and completeness. Typically, the methodology for molecular assembly relies on bottom-up approaches to create and assemble highly ordered functional materials [23]. Using bottom-up approaches, naturally occurring bioactive molecules or bio-architectures such as lipids, sugars, amino acids, and nucleic acids are utilized as the precursors for the fabrication of highly ordered self-assembled functional materials. Now, the formation of self-assembled supramolecular nanostructures of proteins, peptides, and other biomolecules includes such as fibers, tapes, tubes, belts, and vesicles [24]. A variety of nanostructures are most effectively prepared using the bottom-up strategy. The top-down method is the process of creating a planned structure by disassembling or moving a system or its parts into a designated spot [25].

### 1.1.2 Hydrogels

In our everyday lives, gels are the most often utilized materials. We used to come into contact with gels-like viscous things in our everyday routine, ranging from hair gel, and toothpaste to food jelly and so on. However, it has proven difficult for academics in the past to precisely characterize such a distinct thing. Thus, materials that primarily absorb solvent (>90% by weight), defy gravity, and have viscoelastic properties akin to solids are the best method to characterize gels. The next question is, "How are the gels formed?" To create gels, two distinct phases must be formed where the substantial volumes of solvent (solution) are held inside the networks, obstructing the flow of liquid, and these networks resemble 3D solid networks built of the gel's ingredients [26,27].

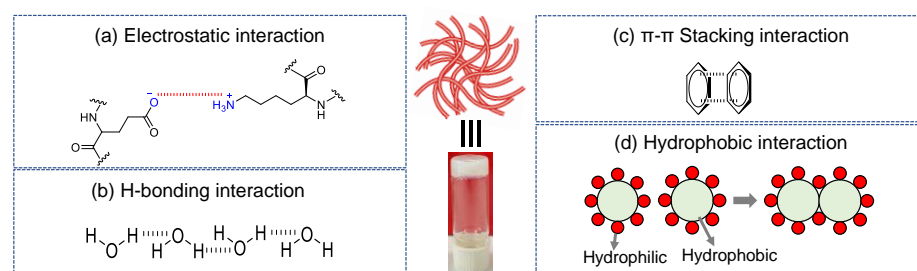


**Figure 1.5** Diagram illustrating the formation of supramolecular hydrogels via many noncovalent contacts: (a) electrostatic interaction, (b) H-bonding interaction, (c)  $\pi$ -  $\pi$  interaction, and (d) Hydrophobic interaction.

### 1.1.3 Hydrogel formation

Gels prepared in an aqueous media are known as hydrogels, and when organic solvents are used, they are referred to as organogels. Because of their high-water content, soft tissue-like properties, biocompatibility, and biodegradability, hydrogels are best known for their vast array of biomedical uses including tissue engineering, contact lenses, wound healing, the release of therapeutic drugs, and tumor treatment. Given their limitations in the biological domain, hydrogels are thus a possible alternative to organogels [28]. Chemical crosslinking or physical crosslinking methods are used to prepare the hydrogel. During the physical process of crosslinking, many non-covalent interactions are considered such as H-bonding,  $\pi$ - $\pi$  interactions, metal-ligand interactions, hydrophobic interactions, host-guest interactions, and Van der Waals interactions (**Figure 1.5**) [29]. The weak and short-range hydrogen bonding interaction occurs when H atoms connect to different functional groups e.g. amine (-NH<sub>2</sub>), hydroxyl (-OH), amide (-CONH) as well as electronegative atoms (O, F, N) containing the lone pairs of electrons. H-bonding interactions are vital for the construction of supramolecular hydrogels which also play an important role in various biological self-assembled systems, such as protein  $\beta$ -sheet structures, DNA, and RNA. Several biomolecules including peptides, polysaccharides, proteins, synthetic polymers, small molecules, and nucleic acid are capable of the formation of hydrogel by the H-bonding interactions [30,31]. Alternatively, the self-healing and shear thinning capabilities of the hydrogels are provided by the easy breaking and reformation capacity of the hydrogen bonds [32].

Hydrophobic interactions are another kind of non-covalent interaction in addition to H-bonding interactions. Hydrophobic interactions also

play a crucial role in the formation of supramolecular hydrogels [33]. Usually, hydrophobic interactions happen between the nonpolar parts to keep the polar water molecules from coming into contact with them. Molecular structures that make gels through hydrophobic interactions usually have hydrophilic as well as hydrophobic parts. When water is present, the molecules self-assemble so that the hydrophobic parts stay at the center and the hydrophilic parts are spread to the water, this creates structures that look like micelles and a hydrogel [34]. Therefore, the length of the hydrophobic chain and the size of the hydrophobic domain have a big effect on the hydrogel's physical features. When hydrogels are involved in these kinds of hydrophobic interactions, they often show bad thermoresponsive behavior. As the temperature rises, the water molecules move around more, which upsets the solvent sphere. As a result, hydrophobic interactions become more important, and this is how the self-assembly hydrogel forms. However, the hydrogen bonds and Van der Waals interactions are not as strong as the hydrophobic interactions [35,36].

One type of non-covalent interaction is the  $\pi$ - $\pi$  stacking interaction, which happens between aromatic rings with  $\pi$ -orbitals. This stacking interaction usually happens between molecules that have a lot of electrons and molecules that don't have many electrons [37]. The stacking interaction has considerable significance. However, the  $\pi$ - $\pi$  stacking interaction plays a crucial role in crystal packing structure, folding of proteins, DNA and RNA base stacking, drug design, and molecular recognition [38-40]. The  $\pi$ - $\pi$  interaction is heavily influenced by size as well as the electron density of the aromatic rings, temperature, and the solvent. The  $\pi$ - $\pi$  stacking of aromatic rings in water is determined by the intermolecular contact, which enhances the stability of the stacked arrangement [41-43].

#### **1.1.4 Dynamic Covalent Bond-Driven Hydrogel**

Dynamic Covalent Chemistry (DCC) has recently emerged as a promising avenue for creating smart materials that possess versatile

characteristics (**Figure 1.6**). The dynamic bonds exhibit reversibility that allowing them to be broken and restored under certain circumstances. This process leads to the creation of novel materials with distinct characteristics and functionalities [44-47]. The stability and functioning of hydrogels are determined by the chemical and physical crosslinking that occurs during self-assembly. Physically cross-linked hydrogels often experience instability due to minor changes in their environment and have limited resilience [44].

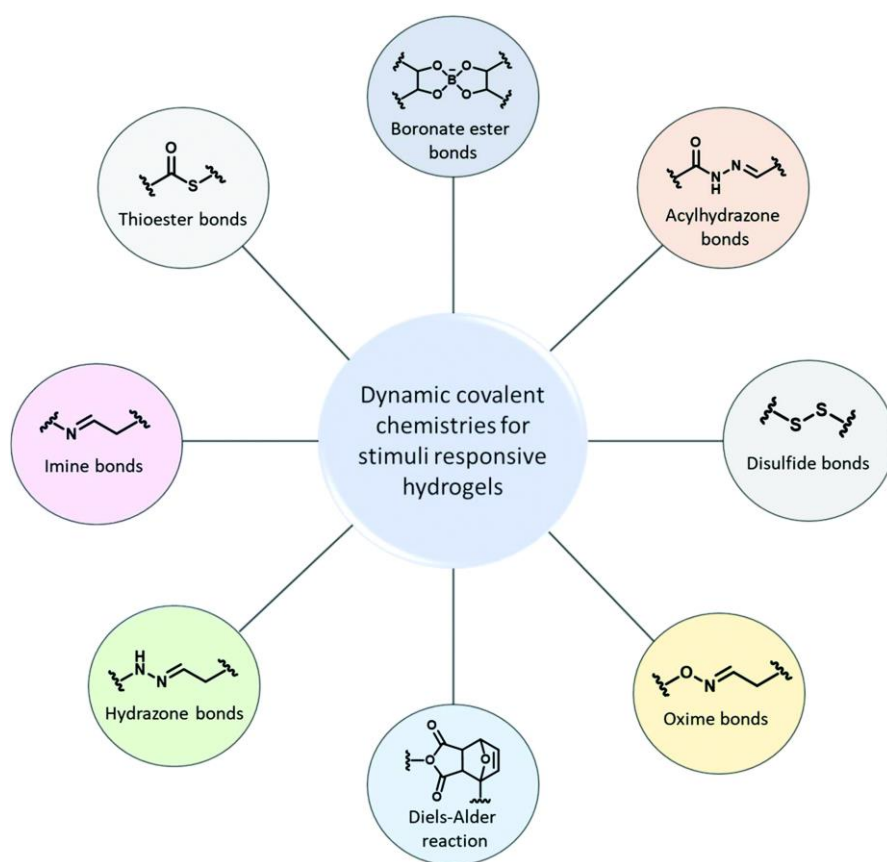


**Figure 1.6** Schematic representation demonstrating the formation of stimuli-responsive hydrogels by dynamic covalent bonding. [Recreated from ref. no. 44]

Reversible chemically cross-linked hydrogels have impressive shear-thinning and self-healing properties (**Figure 1.7**), making them very interesting. Compared to non-covalent interactions such as  $\pi$ - $\pi$  interactions, H-bonding, hydrophobic interactions, metal-ligand interactions, host-guest and Van der Waals interactions, dynamic

covalent chemistry offers more stability, reversibility, and exhibit stimuli responsiveness under certain circumstances [48-50]. A variety of dynamic covalent linkages such as boronate esters bonds, disulfide bonds, imine bonds, and click chemistry are often used in the creation of functional supramolecular hydrogels. The generation of imine bonds are strongly influenced by temperature and pH. The equilibrium shifts more towards imine production at high temperatures and pH values, whereas the reverse happens at low pH values [51].

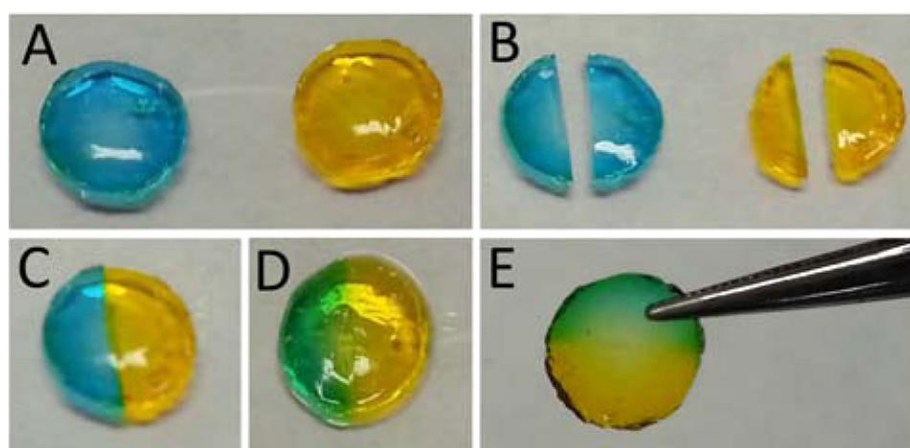


**Figure 1.7** Optical photograph shows the formation of the self-healable hydrogel by the dynamic covalent bond. [Recreated from ref. no. 52]

So, hydrogels based on imines may exhibit self-healing, pH-responsive, and thermoresponsive properties due to the dynamic characteristics of the imine linkages.

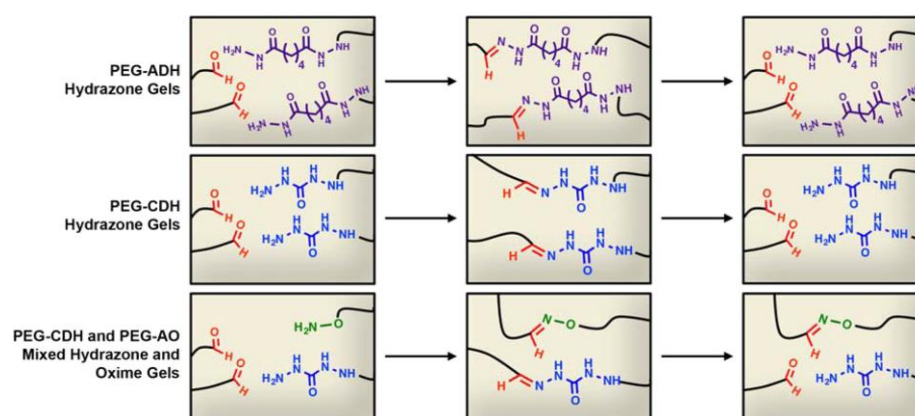




**Figure 1.8** PEG-CHO undergoes a reaction with PEG-ADH and PEG-CDH to create hydrogels that can degrade due to reversible hydrazone cross-links. Additionally, PEG-CHO can react with PEG-AO to make nonreversible oxime bonds, which help stabilize the hydrazone gels. [Recreated from ref. no. 52]

Boehnke *et al.* reported an imine cross-linked gel where dynamic imine cross-link was incorporated for the controllable degradation of the hydrogel. The hydrogel was formed by the reaction of the hydrazide-functionalized poly(ethylene glycol) (PEG) and aldehyde-functionalized PEG (PEG-CHO) which was broken rapidly in the presence of media. It was shown that hydrogel stability may be adjusted from less than 24 hours to more than 7 days by mixing oxime and hydrazone chemistry. Notably, higher cell viability was observed when an RGD peptide was covalently attached [52].

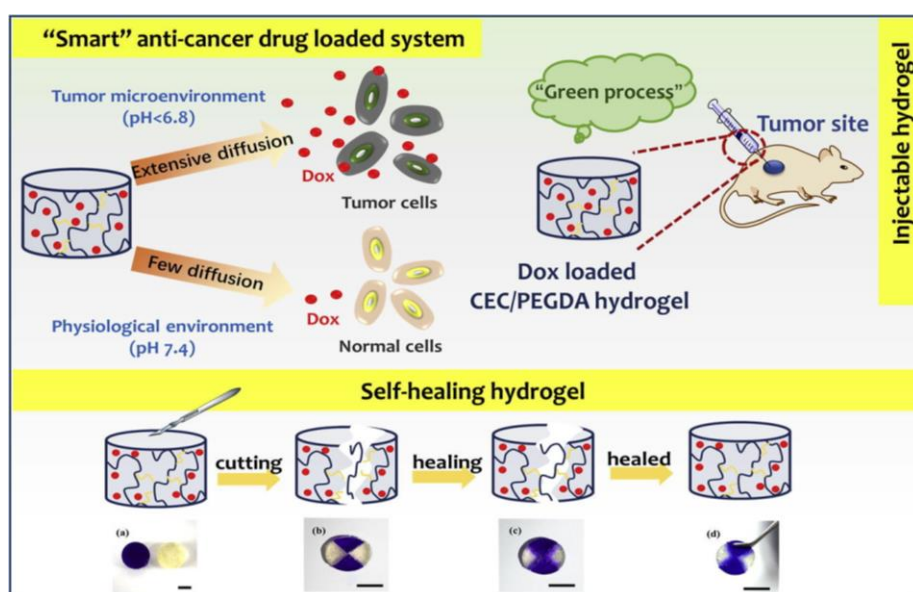


**Figure 1.9** Graphical abstract representing the pH-responsive release of Dox to the tumor cells from the self-healable hydrogel matrices. [Recreated from ref. no. 52]

The resultant hydrogel, which was cross-linked with chitosan and PEG, showed remarkable properties such as being shear-thinning, printable,



injectable, and self-healing. In addition, the biocompatible hydrogel functionalized with dynamic imines was used as an effective drug delivery carrier in the treatment of hepatocellular cancer [53]. Similar to the imine cross-link, hydrazone cross-links are also used for the formation of stable hydrogels. Notably, the hydrazone cross-linking offers more stability than the imine cross-linking [54]. Hydrazone connections are often created by the spontaneous condensation process between a primary amine group and a carbonyl group bonded to a nitrogen atom. Hydrazone crosslinking may be achieved by directly reacting an aldehyde/keto functionalized molecule with a hydrazide-containing moiety. The preparation of hydrazone cross-linked polymeric hydrogels is a straightforward process in the field of polymer chemistry. This is accomplished by combining oxidized polysaccharides with hydrazide-modified polymers [55]. Domingues *et al.* reported an injectable HA-based hydrazone cross-linked hydrogel that was made of aldehyde-modified cellulose and adipic acid dihydrazide HA. The morphology of the hydrogel was compact, and it had a high storage modulus value of 152.4 kPa. Additionally, the cross-linked hydrogel demonstrated a suitable level of biocompatibility with human adipose-derived stem cells [56].

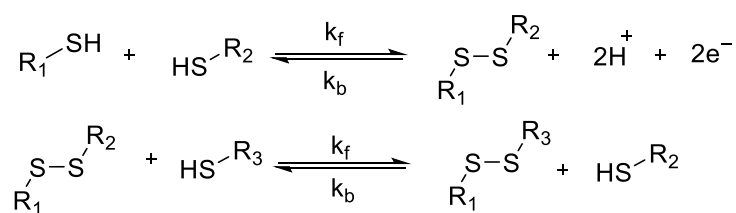


**Figure 1.10** The reversible dynamic disulfide bond formation.

Disulfide bonds, also known as S-S bonds or disulfide bridges, are a kind of covalent link that may quickly break and reform in response to certain external physical or chemical triggers (**Figure 1.10**) [57,58]. Thiols and disulfide bonds play important roles in several biological operations inside living systems, such as protein folding, cell signaling, and protein synthesis [59].

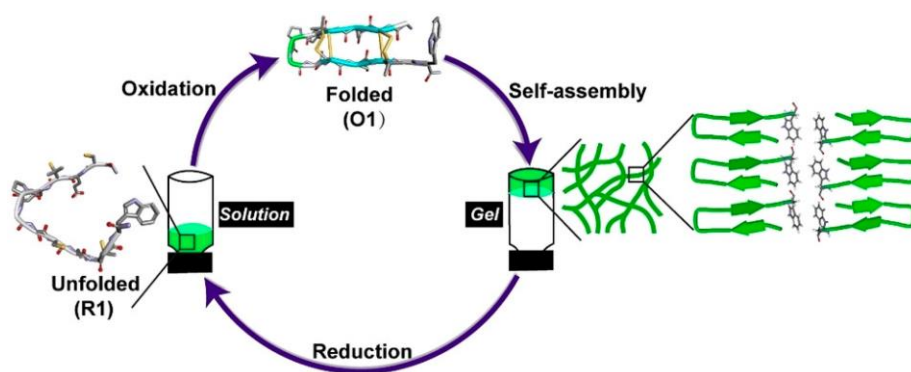


**Figure 1.11** The scheme illustrating a hydrogel that responds to redox reactions. The oxidation and reduction reaction drives the sol-gel transformation. [Recreated from ref. no. 60]

A recent study showed that a peptide with high levels of thiol, consisting of Cys and penicillamine residues, may generate hetero-disulfide bonds. This resulted in the formation of amphipathic  $\beta$ -hairpins gel (**Figure 1.11**). The disulfide bridges collapsed in the presence of dithiothreitol. This caused a conformational flip to a random coil, which then initiates the transition from a gel to a sol state [60].

Hydrogels that rely on disulfide bonds can react to many environmental stimuli by integrating distinct interactions into a single hydrogel structure [61]. In this direction, a hydrogel with multifunctional and multi-sensitive properties is synthesized using reversible cross-linking between the boronic ester and disulfide linkage which shows pH, redox, and glucose-responsive features (**Figure 1.12a**).

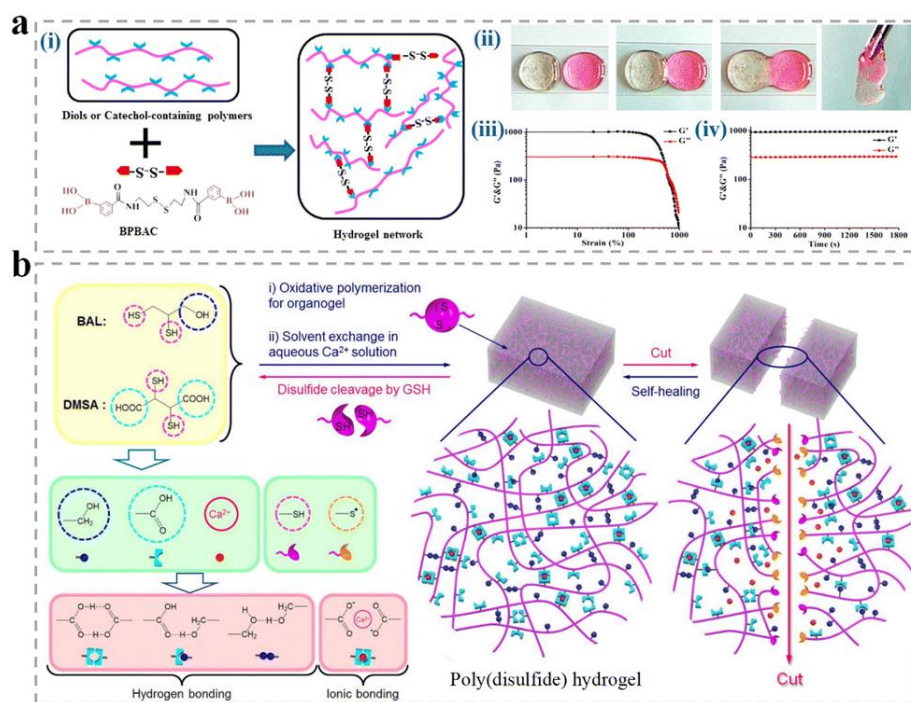


**Figure 1.12** Self-healing hydrogels built on disulfide bonds. (a) Schematics of hydrogel which was formed by the crosslinking of cystamine and bis(phenylboronic acid carbamoyl) (BPBAC). Assessment of the self-healing capacity of the hydrogel derived from disulfide bonds. (b) The schematic representation of the self-repairing hydrogel is composed of 2,3-dimercapto-1-propanol and meso-2,3-dimercaptosuccinic acid. Additionally, this hydrogel exhibits a self-healing mechanism. [Recreated from ref. no. 61, 62]

Although there have been significant advancements in hydrogels that rely on disulfide connections, the poor mechanical characteristics of hydrogels, which are caused by the low density of disulfide links and inefficient energy dissipation processes, might be troublesome for their usage in the biomedical area. To overcome these limitations, Van Tron Tran and his colleagues formed a versatile hydrogel by combining meso-2,3-dimercaptosuccinic acid with 2,3-dimercapto-1-propanol [62]. The hydrogel exhibited quick self-healing capabilities in aqueous media and also showed notable stretchability, and compatibility (**Figure 1.12b**). This approach offers a novel pathway for using dynamic hydrogels based on disulfide bonds in biological and engineering contexts.

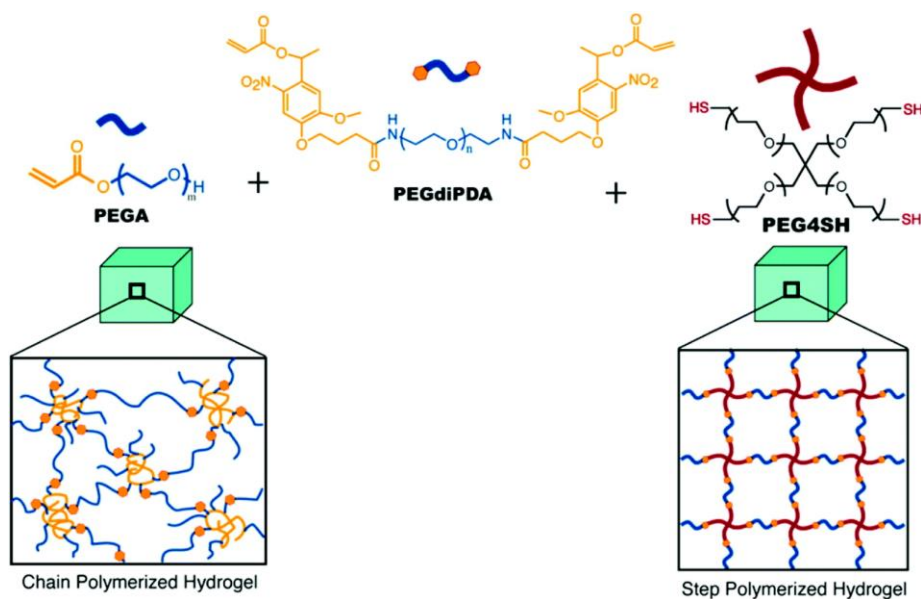


**Figure 1.13** Construction of photodegradable hydrogels by chain and step polymerization. CP gels, which are chain-polymerized hydrogels, were created by copolymerizing photolabile PEGA with PEGdiPDA by FRP. This process resulted in the creation of a unique network topology. [Recreated from ref. no. 63]

Tibbitt and his colleagues examined the mechanical and degrading characteristics of the hydrogel formed by step and chain polymerizations [63]. The same photodegradable crosslinking macromer based on diacrylated PEG was used to create chain- and step-polymerized hydrogels (PEGdiPDA). PEGdiPDA and a monoacrylated PEG macromer were copolymerized using FRP to create chain-polymerized hydrogels, which had a network topology that was homogeneous. Using Michael addition polymerization, step-polymerized hydrogels were synthesized by copolymerizing PEGdiDPA with PEG4SH, a thiol-terminated four-armed PEG (**Figure 1.13**). The integrity and homogeneity of the network in the step-polymerization gel improved its tensile toughness, shear strain to yield, and ductility.

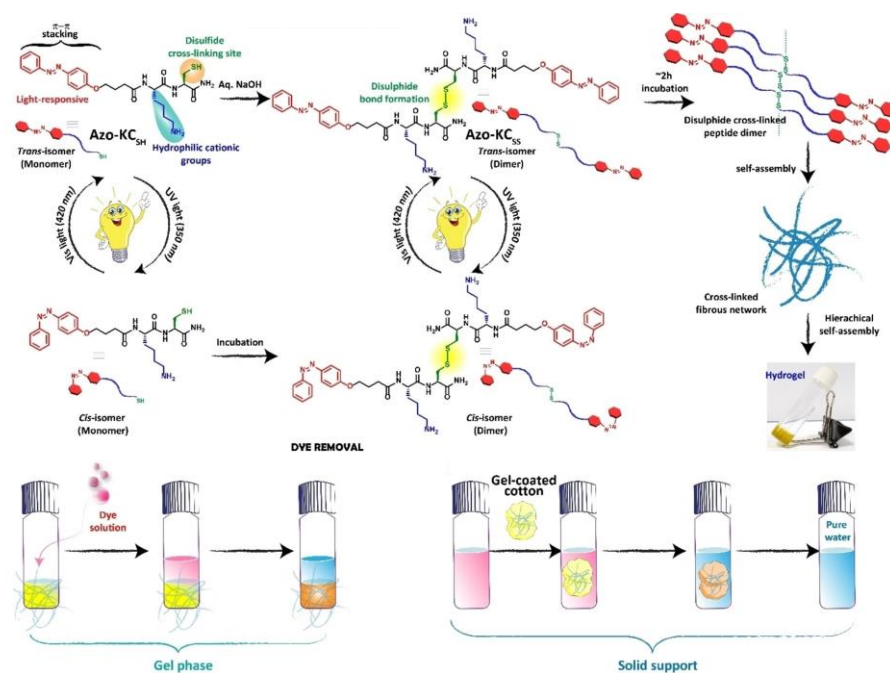


**Figure 1.14** The peptide hydrogelator's molecular structure, as well as its monomeric and their respective dimeric forms, Light driven trans to the cis transition of dimeric and monomeric form. [Recreated from ref. no. 64]

The formation of hydrogel is facilitated by both non-covalent and covalent interactions by the use of an ultrashort peptide hydrogelator that contains cysteine at its C-terminus [64]. The synthesized hydrogel was insoluble in an aqueous medium as well as buffers with different pH ranges from pH 1 to 13. Hydrogel showed injectable and thixotropic properties (**Figure 1.14**). The gel remained intact even after being exposed to UV light. Hydrogel was used to extract organic pigments from polluted water.

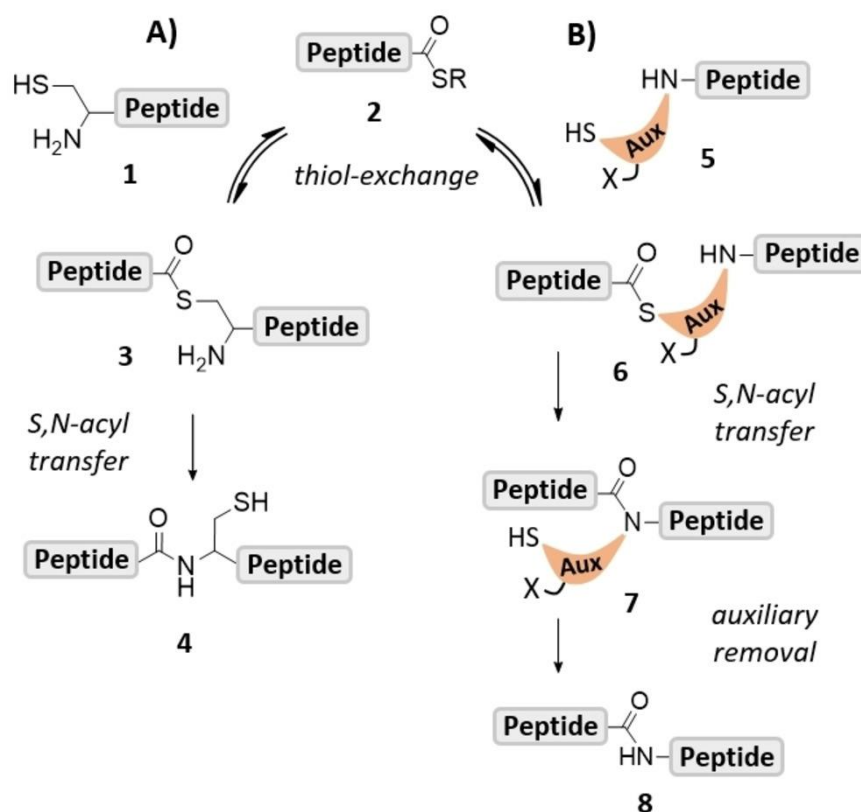


**Figure 1.15** The mechanistic steps of the (a) NCL (b) cysteine-free auxiliary mediated NCL. [Recreated from ref. no. 65]

Fuchs *et al.* used a thiol exchange reaction for the Native chemical ligation (NCL) [65]. The process involves a chemoselective reaction between a peptide segment without protection on its side chain, which has a thioester at its C-terminus, and another peptide segment lacking protection on its side chain, which has a cysteine residue at its N-terminus. An auxiliary called 2-mercapto-2-(pyridine-2-yl)ethyl (MPyE) was introduced to enhance the catalytic capabilities of native chemical ligation (**Figure 1.15**).

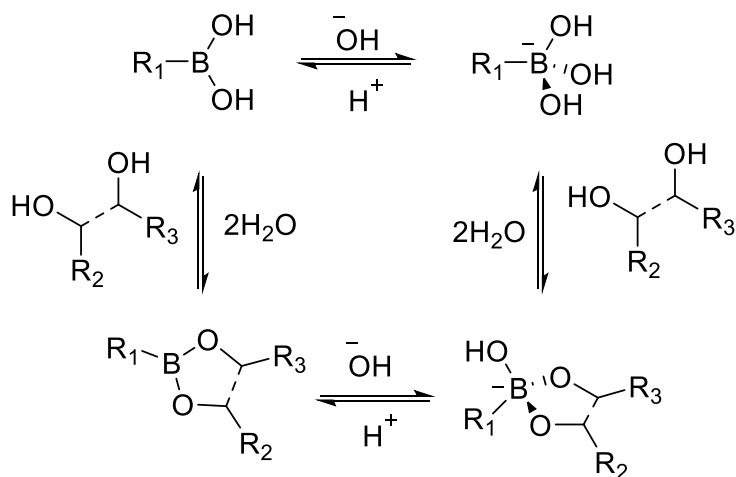


**Figure 1.16** Reaction of diol and boronic acid.

The most famous kind of dynamic covalent bond (DCB) that is involved in the self-assembly is the B-O, which involves dynamic boronate ester bonds. Boronic acid has a trigonal planar geometry with  $sp^2$  hybridization at its center boron atom [66,67]. When combined with cis-1,2 and 1,3-diols, boronic acids readily create boronate esters. An equilibrium exists in aqueous media between boronic acids and boronate ester (**Figure 1.16**). A change in this equilibrium towards hydroxyl boronate ester production is possible under certain ideal circumstances. The hybridization of the negatively charged B atom undergoes a shift to  $sp^3$  with a tetrahedral shape after the formation of the boronate ester [68]. Boronic acid reacts with 1,2- and 1,3-diols in water to produce a negatively charged boronate esters with a tetrahedral shape. However, when in an organic solvent, it generates neutral trigonal boronic esters with 1,2- or 1,3-diols [69]. Boronic acids have a fast and reversible interaction with cis-1,2 and 1,3-diols which results in the development of stable boronate esters. This process leads to the development of five-membered and six-membered cyclic rings, respectively [70]. The equilibrium strongly relies on the  $pK_a$  values of the boronic acids and the pH levels of the solutions as the boronate ester bond is dynamic. The equilibrium favors the production of boronate ester when the pH of the medium is equal to or greater than the  $pK_a$  of the boronic acid [71].

Under these circumstances, a tetrahedral boronate structure with a negative charge is created, which subsequently promotes its interaction with -OH groups of diols, leading to the formation of boronate esters. Conversely, the tetrahedral boronate esters with a negative charge have greater stability in large quantities of water at alkaline pH levels. At pH levels close to those of the body pH level, the reaction with diols is not preferred [72]. However, in acidic circumstances, the boronate esters are not stable, and the balance switches towards the formation of free boronic acids. The benefits of using boronic acid and boronate ester chemistry over other dynamic covalent bonds are (i) it works in an aqueous medium (ii) it mild reaction condition (iii) it works without any catalyst. Boronate esters are classified as "dynamic covalent" bonds due to their kinetically regulated exchange of bonds between free boronic acids and diols, as well as between boronate and boronic esters [73].

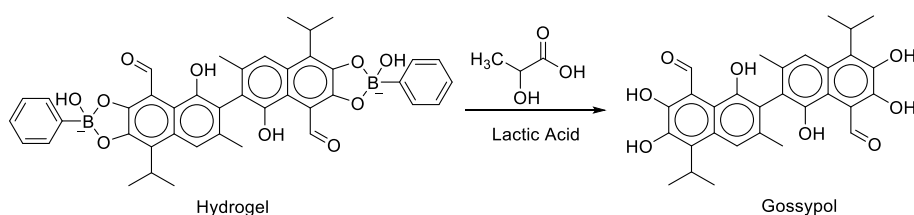


**Figure 1.17** The reaction scheme shows the breaking of cross-linking in the presence of the lactic acid which results in the release of the anticancer drug molecules.

Heleg-Shabtai *et al.* formed a hydrogel matrix by cross-linking of anticancerous drug gossypol and the chains of a phenylboronic acid functionalized with acrylamide copolymer [74]. The hydrogel was dissociated in an acidic environment with a pH of 4.5. The addition of lactic acid enhanced the dissociation of the hydrogel more than formic acid. The formation of a stable complex by the lactic acid and boronic acid bridging groups enhanced the breaking of the hydrogel in the presence of lactic acid. Lactic acid is present in cancer cells at high levels, and the environment around these cells is acidic (**Figure 1.17**).



The cross-linked hydrogel served as a responsive matrix for the regulated release of gossypol.

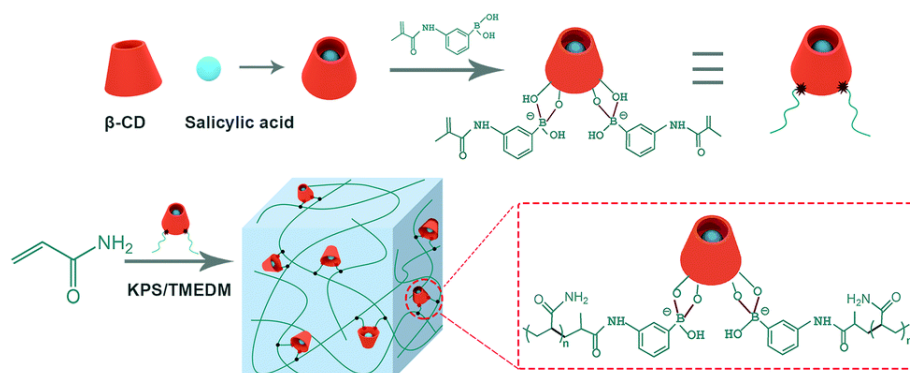


**Figure 1.18** The diagram illustrates the synthetic procedure for the formation of the  $\beta$ -CD/MPA hydrogel and the related intermolecular connections within the networks. [Recreated from ref. no. 75]

Chen *et al.* provided a straightforward technique for creating hydrogels that possess several properties such as pH responsiveness, drug encapsulation, and self-healing [75]. The hydrogel was used for the release of the encapsulated drug molecules. Salicylic acid was encapsulated inside  $\beta$ -CD via host-guest interactions. The hydrogel was formed by polymerizing acrylamide with cyclodextrin-phenylboronic acid, which acts as a reversible and pH-sensitive cross-linker (**Figure 1.18**).

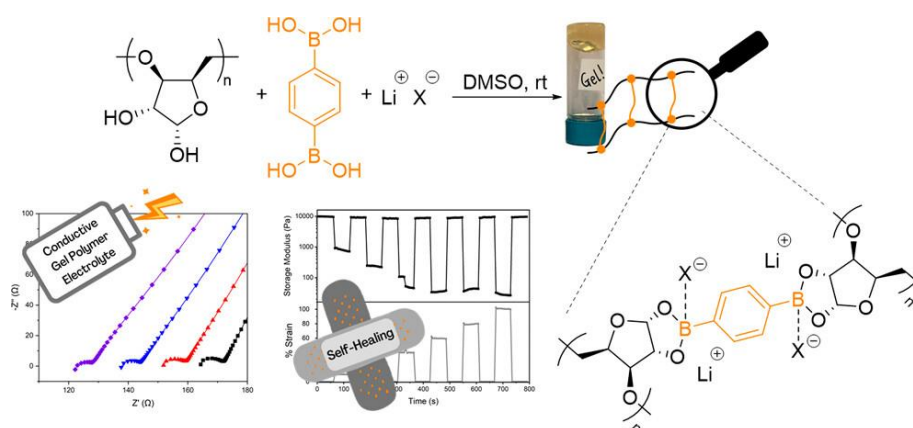


**Figure 1.19** Schematic diagram shows the formation of the boronic acid cross-link hydrogel and its application. [Recreated from ref. no. 76]

Daniel *et al.* synthesized an organogel by the formation of boronate ester between 1,4-phenylenediboronic acid and D-xylose derivative [76]. The organogel exhibited good self-healing properties. Lithium ions were incorporated by the inclusion of bis(trifluoromethanesulfonyl)imide (LiTFSI). The lithium-incorporated hydrogel showed good ionic conductivity and electrochemical stability (**Figure 1.19**).

### 1.1.5 Building blocks of DNA and RNA

DNA, also known as deoxyribonucleic acid, is a biomolecule that is made up of two biopolymer chains that are coiled with one other by H-bonding interactions. This results in the formation of a double helix structure [77-79]. DNA is responsible for carrying genetic information and plays a crucial role in cell reproduction, the creation of ribonucleic acid (RNA), and the synthesis of proteins. The DNA is stored within the nucleus of eukaryotic cells and is referred to as nuclear DNA [54]. In Eukaryotic organisms, DNA is also present in chloroplasts (chloroplast DNA) and mitochondria (mitochondrial DNA). On the other hand, DNA is located in the cytoplasm of prokaryotic biological cells. Ribonucleic acid, commonly known as RNA, is another kind of biomolecule that is constructed using a biomolecular chain. RNA is constructed by a single chain. The most important functions of RNA are the regulation of the expression of genes, the control of genes, the coding and decoding of genetic information, and the production of proteins [81]. On the other hand, the majority of cells have RNA in their cytoplasm, although the nucleus produces RNAs.

### 1.1.6 Nucleotides and Nucleosides

The nucleotides that makeup biopolymers of DNA and RNA are the essential building blocks and monomeric units themselves [82]. Phosphate linkage is responsible for the formation of a lengthy polymeric chain by nucleotides (**Figure 1.20**). The building blocks of nucleotides are nucleosides and a single phosphate group. A nucleoside is a molecule with five carbon atoms that contain pentose sugars and two heterocyclic nitrogenous base pairs (**Figure 1.20**). Nucleosides are

categorized as monophosphate, diphosphate, or triphosphate based on the number of phosphate groups they contain. Nucleosides that are monophosphate are known as nucleotides (**Figure 1.20**). There are two kinds of nitrogenous base pairs, distinguished by the heterocyclic rings (i) purine and (ii) pyrimidine (**Figure 1.20**).

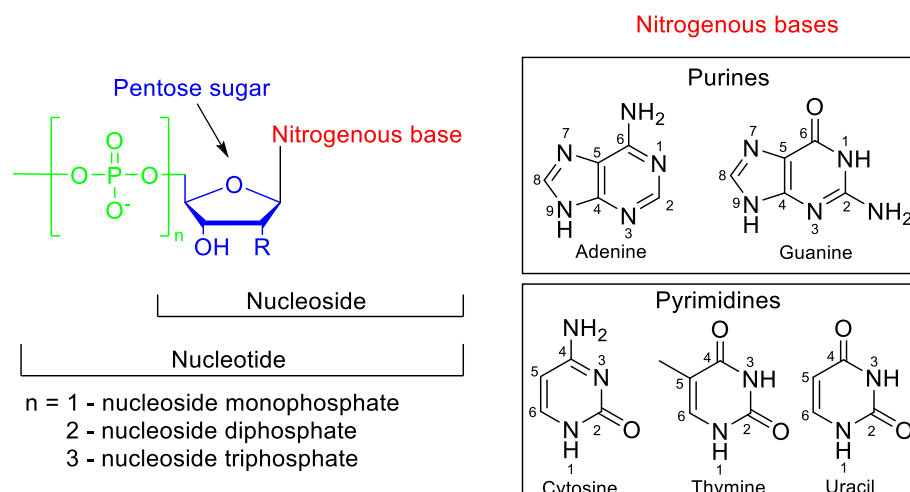


**Figure 1.20** Structures of nucleotide, nucleoside, purine, and pyrimidine nucleobases.

Two purine bases, adenine, and guanine, have heterocyclic aromatic rings which are fused. A pyrimidine base with a single heterocyclic aromatic ring is cytosine, thymine, or uracil. Four base pairs guanine, adenine, thymine, and cytosine are found in DNA. Glycosidic linkages are formed between the N9 nitrogen of purines and the N1 nitrogen of pyrimidine via the anomeric carbon C1 of the five-carbon pentose sugar. RNA consists of guanosine, adenosine, uridine, and cytidine nucleosides respectively (**Figure 1.21**). These nucleosides are formed from the bases adenine, guanine, cytosine, and uracil, respectively. The hydroxyl group linked to the C2' carbon in DNA nucleosides is substituted with a hydrogen atom. Therefore, the nucleosides found in DNA are referred to as deoxyribonucleosides (**Figure 1.21**). The nucleotides of DNA are referred to as deoxyguanosine, deoxyadenosine, thymidine, and

deoxycytidine, which are composed of guanine, adenine, thymine, and cytosine bases, respectively.

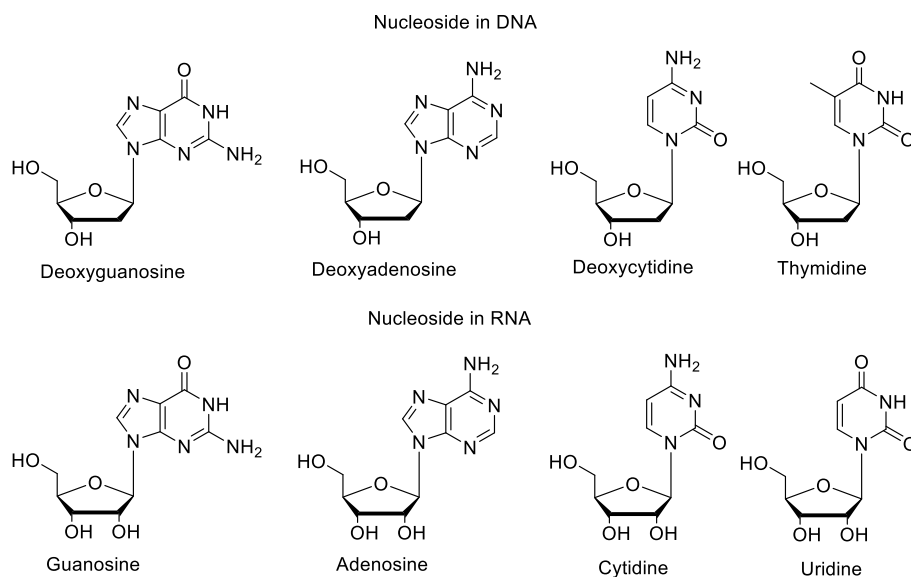


**Figure 1.21** Structures of nucleoside in DNA and RNA.

### 1.1.7 Supramolecular assemblies in DNA and RNA

The supramolecular double-helix coiled structure of DNA is formed by the interaction of two biopolymer chains by hydrogen bonding. James Watson and Francis Crick made the first discovery of the helical structure of DNA in 1953 [77]. The stability of the double helical structure of DNA is maintained by the interactions between complementary purine/pyrimidine base pairs. Both adenine and thymine possess two H-bonds, which allow them to interact with one another.

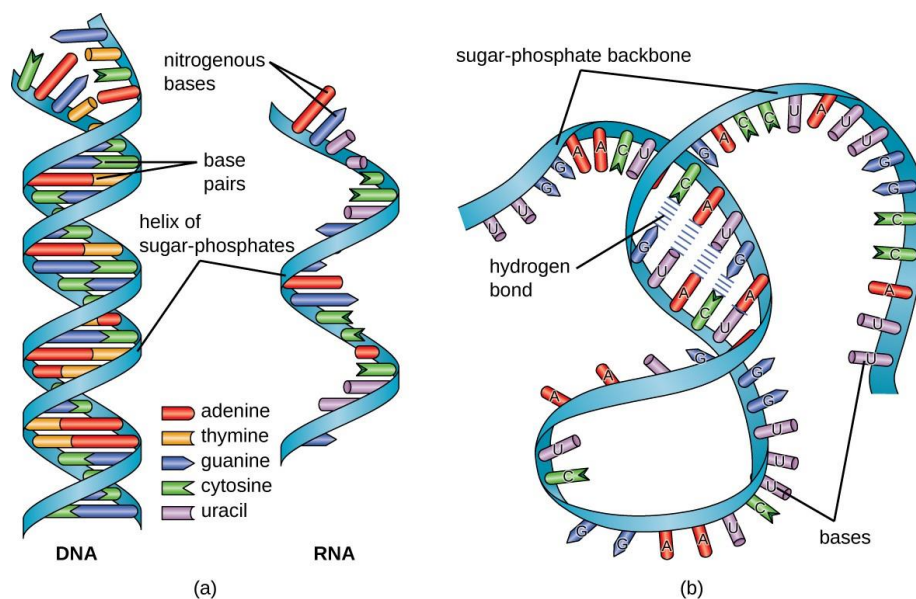


**Figure 1.22** (a) The double-stranded structure of DNA, whereas the typical single-stranded structure of RNA. (b) RNA can also form a secondary structure by the complementary base pairing. [Recreated from ref. no. 83]

The C6-NH<sub>2</sub> and N1 in adenine serve as a hydrogen bond donor and acceptor, respectively [83]. On the other hand, the C=O double bonds of C2 and N3 in thymine serve as the H-bond acceptor and donor, respectively. Three H-bonds allow guanine and cytosine to interact with one another. The C=O at the C6 carbon atom of guanine serves as an H-bond acceptor, whereas the -NH<sub>2</sub> at the C2 and N1-H serve as H-bond donors (**Figure 1.22**). In contrast, the C=O of C2 and N2 in cytosine serve as an H-bond acceptor, while the C3-NH<sub>2</sub> in cytosine serves as an H-bond donor. In contrast to one another, the two strands of DNA are oriented oppositely. When a strand in DNA is located in the direction of 3' to 5', the complementary opposite strand will be located in the direction of 5' to 3' (**Figure 1.22**). Both major and minor grooves are formed by the double helix structure of DNA. The term "major groove" refers to the groove that occurs inside the double helix when two phosphate-sugar backbones are located widely to one another, while the term "minor groove" refers to the groove that occurs when two backbones are located close to one another [84]. The grooves play a significant role in the process of binding with enzymes, biomolecules,

and proteins. However, in contrast to DNA, RNA is composed of a single biopolymeric chain. In the case of RNA, the double helix structure does not exist. On the other hand, a lengthy chain of RNA may self-assemble and fold over itself like that of a protein, provided that complementary base pairs are present. The H-bonding interactions that occur between the purine and pyrimidine base pairs are responsible for the self-assembly process. The H-bonding interactions that occur in RNA are comparable to those that occur in DNA; however, in RNA, uracil binds with guanine as a complementary base pair rather than cytosine. As a consequence of secondary folded structures of RNA, many tertiary structures are produced, including bulges, hairpin loops, and internal loops. Loops are very important because they safeguard the structural integrity of the structure, interact with enzymes, and bind with biomolecules. The three primary kinds of DNA are classified as A-DNA, B-DNA, and Z-DNA, depending on their supramolecular structural characteristics of the helix [85-87].

### 1.1.8 G-quartet and G-quadruplex

Among the nucleobases, guanine is capable of engaging in H-bonding interactions via the Hoogsteen face (**Figure 1.23**). The formation of G-quartet may be achieved by the interaction of four guanines through the Hoogsteen H-bonding mechanism [88-90].

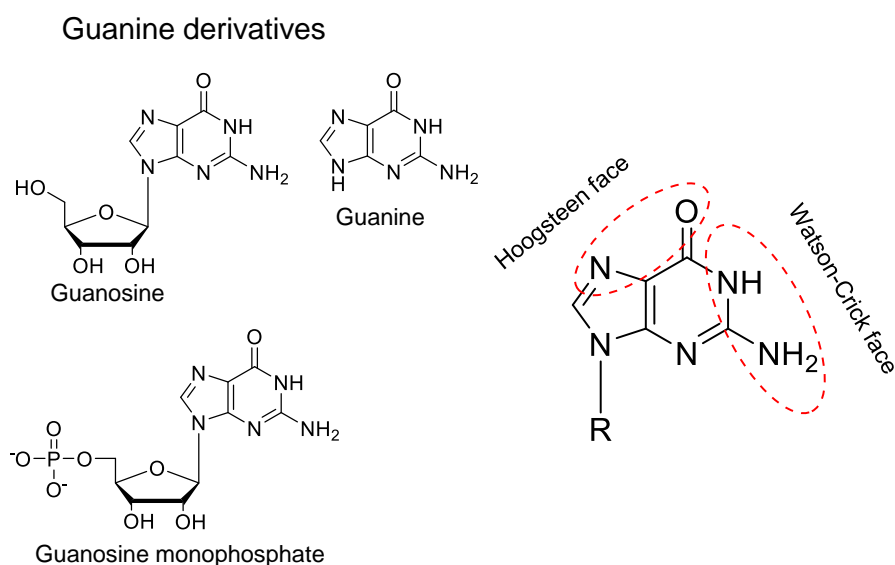


**Figure 1.23** A Few examples of guanine derivatives and Watson-crick and Hoogsteen faces in the guanine molecule.

Several G-quartets are stabilized by the process of binding with core metal ions, primarily with ions of the  $K^+$  and  $Na^+$ . Additionally, G-quadruplex structures are constructed by repeating G-quartet units of the same kind [88-90].

G4 units may be found in the guanine-rich moiety of DNA. In certain cases, it can be found in RNA. However, extended G-wires may be seen in situations where hundreds of G4 units are involved. In general, stacked G4 units comprising one to four units are the most prevalent. G-quadruplexes may be folded in a variety of different ways, depending on the direction in which the biopolymer chains are arranged (**Figure 1.24**). They can also take on a variety of folded forms, such as parallel G-quadruplexes, anti-parallel chains, anti-parallel baskets, and mixed structures [91,92].

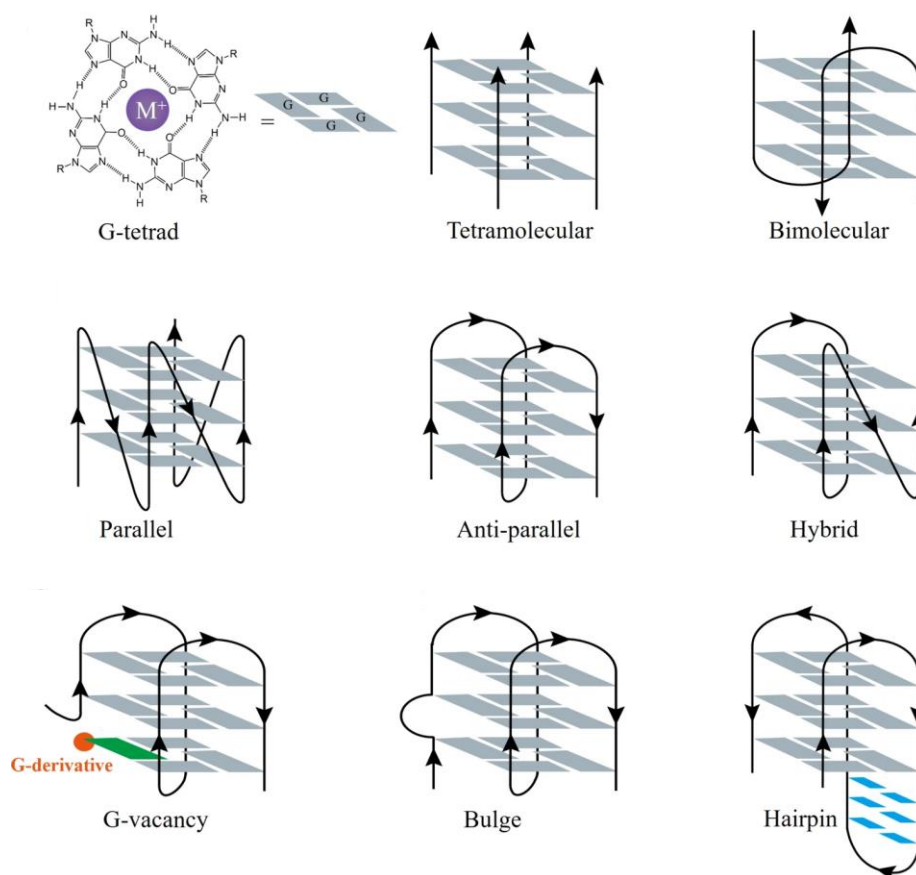


**Figure 1.24** The formation of the G-tetrad in the presence of the suitable monovalent cation. Different topologies of the G-quadruplex. [Recreated from ref. no. 92]

### 1.1.9 G-quadruplex in the Biological System

A significant portion of the DNA is found inside the chromosome, which is located within the nucleus of cells. The presence of G4s may be discovered in certain regions of the chromosome, genes, and the genomic region. When it comes to human cells, the immunoglobulin switch regions and telomeres are the most prevalent. As a result of the fact that G4 is responsible for several functions that are essential to the functioning of the biological system, it has become a very intriguing topic for researchers to investigate in the field of nanotechnology and drug targeting motifs [93].

### 1.1.10 G4 in the Replications of DNA

Researchers studied the origin of DNA replication. As per the literature, the bulk of human cell replications come from the G4 area (**Figure 1.25**). The research found that G4 units serve as the basis of the replication process in four kinds of human cells such as embryonic stem cells, induced pluripotent stem cells, HeLa cells, and fibroblasts [94-96]. The replication origin of DNA in viruses, such as SV40 virus and Epstein-Barr virus, initiates from G4-rich areas. However, the precise cause, complicated development method, and contributing aspects of the phenomena have not yet been fully disclosed [97,98].

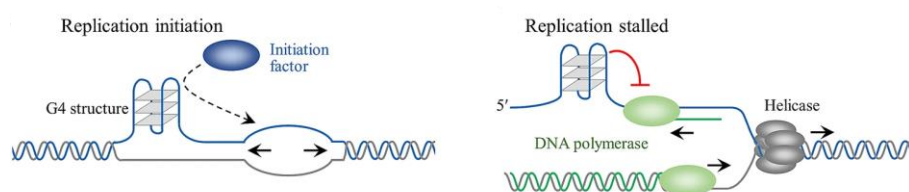
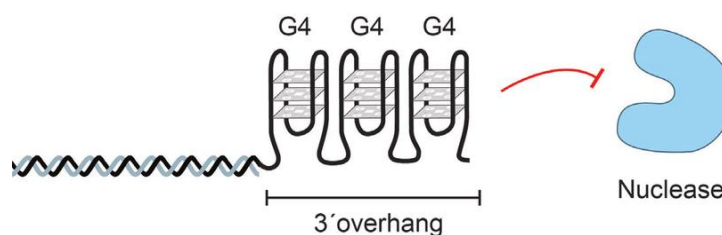


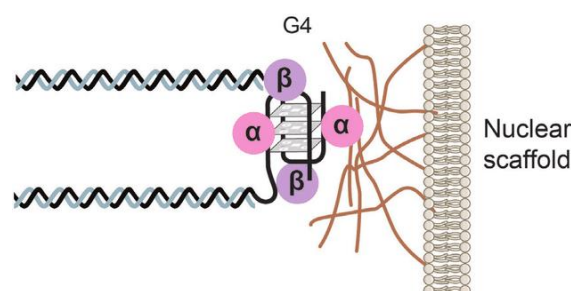
**Figure 1.25** G4 in the DNA replication. [Recreated from ref. no. 92]



(a) Protection of telomeres



(b) Organization of ciliate telomeres



(c) Binding of ligands to telomeric G4

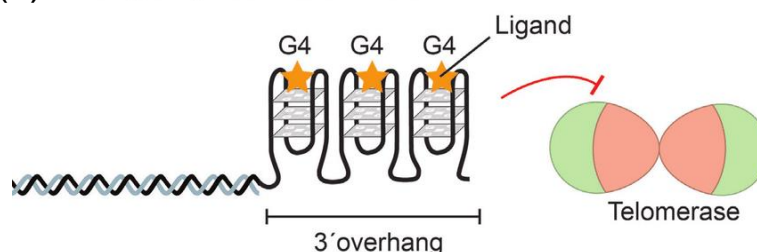


**Figure 1.26** (a) Proteins that are capped in G4 structures prevent the erroneous guiding of cellular repair mechanisms when DNA is damaged. (b) The G4 complexes present in the telomere protect nuclease enzymes. (c) Ligand or drug molecule binding assists in the stabilization of G4s. [Recreated from ref. no. 104]

### 1.1.11 DNA in the Telomere

The telomere, or end of the human chromosome, is linked to around 5–10 kb of TTAGGG repeating units [99,100]. The telomere region contains the majority of G4s due to the high concentrations of GGG units. Telomere lengthening occurs after each cell division, and when it reaches a certain length, it signals the beginning of cellular senescence

[101,102]. A telomere-specific reverse transcriptase enzyme known as telomerase is responsible for the telomere-shortening process. It has an RNA strand that can attach to telomeric DNA directly. Telomeres cause around 85% of tumors to be overexpressed [103]. Thus, telomeres play a crucial part in tumor control and cellular immortalization. The telomere is shielded by G4 complexes. The telomere consists of repeated G4 units that are protected by a protein complex, which differentiates them from damaged DNA. Since the process of repairing DNA causes the system to become unstable, it prevents cells from making erroneous attempts to repair the DNA and safeguard the telomere (**Figure 1.26a**). The G4 DNA region is very stable and not influenced by any nuclease enzyme from the outside (**Figure 1.26b**) [104]. It is believed that any measures to improve the stability of G4 DNA by attaching drugs or external ligands would be beneficial in the fight against cellular abnormalities (**Figure 1.26c**).

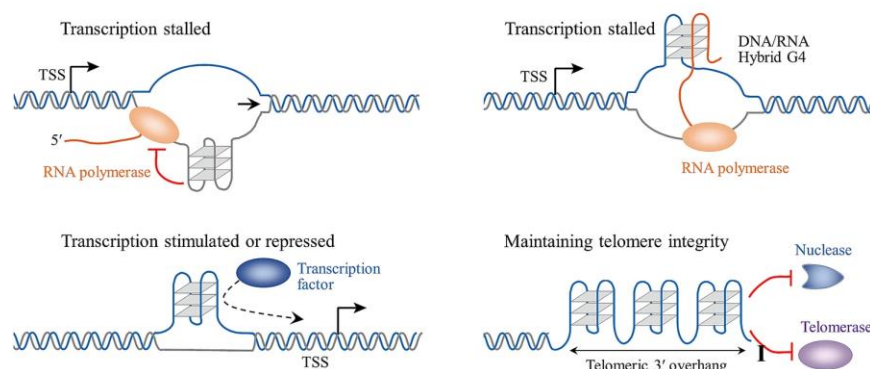


**Figure 1.27** The graphics demonstrate the role of G-quadruplex in DNA transcription. [Recreated from ref. no. 92]

### 1.1.12 Role of G-quadruplex in the DNA Transcription

G4 structures induce specific harm to the integrity of the genome during the process of transcription (**Figure 1.27**). Transcribing G-quadruplex regions produces R-loops, which are susceptible to transcription-induced genomic instability [92]. Just like G-loops, R-loops are quite similar. R-loops consist of a hybrid of RNA and DNA. However, it is important to note that not all R-loops have the non-template G4 DNA strand [105-107]. In these cases, G-loops are susceptible to being

targeted by various recombination factors. G4 structures shield the promoter regions of R-loop development from nucleotide methylation. The genomic instability resulting from transcription-induced G4 structures is determined by using gene analysis. The involvement of G-quadruplex has been proven by the use of G4 DNA as a ligand and pyridostatin [108,109].

### 1.1.13 Background of G-quadruplex Hydrogels

Bang was the first to report that gels could form with guanine derivatives in 1910 [110]. Subsequently, in 1962, Gellert *et al.* investigated the formation of a G-quadruplex structure by making a hydrogel using 5'-guanosine monophosphate (5'-GMP) [111]. In the 1970s, Guschlbauer and his colleagues explored more on G-quadruplex structures using guanosine derivatives [112]. In addition, Davis and his colleagues have made significant contributions to the G-quadruplex mechanism in both solid and gel phases [113-115]. Over the years, several hydrogels on G-quadruplex have been noted. These hydrogels have shown promise for diverse applications such as drug carriers, cell growth applications, sensing applications, and catalysis [116-118].

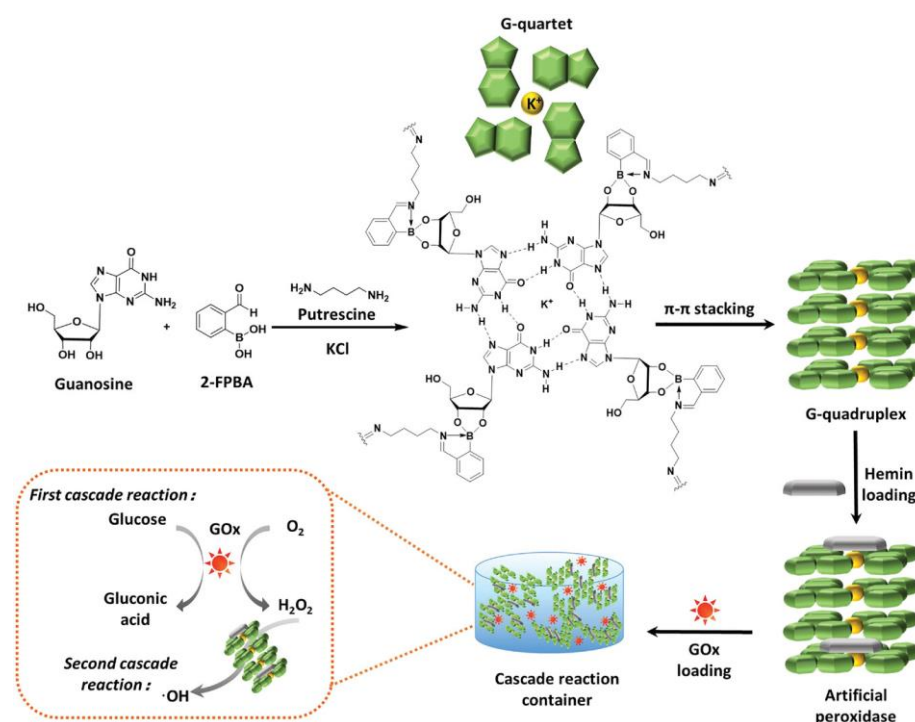


**Figure 1.28** The Scheme shows the formation of G-quadruplex hydrogel for the cascade reaction container. [Recreated from ref. no. 119]

Li *et al.* developed an antibacterial G-quadruplex hydrogel. The constituents of the hydrogel were 2-formylphenylboronic acid, putrescine, and guanosine [119]. The hydrogel matrices were used as a cascade reactor. The hemin and glucose-oxidase were loaded in the hydrogel. The  $O_2$  and glucose were transformed into  $H_2O_2$  and gluconic acid by enzymatic action of glucose-oxidase. The reactive oxygen species (ROS) were formed by the transformation of  $H_2O_2$ . The production of the ROS killed the bacteria. The G-quadruplex hydrogel was used for diabetic wound healing (**Figure 1.28**).

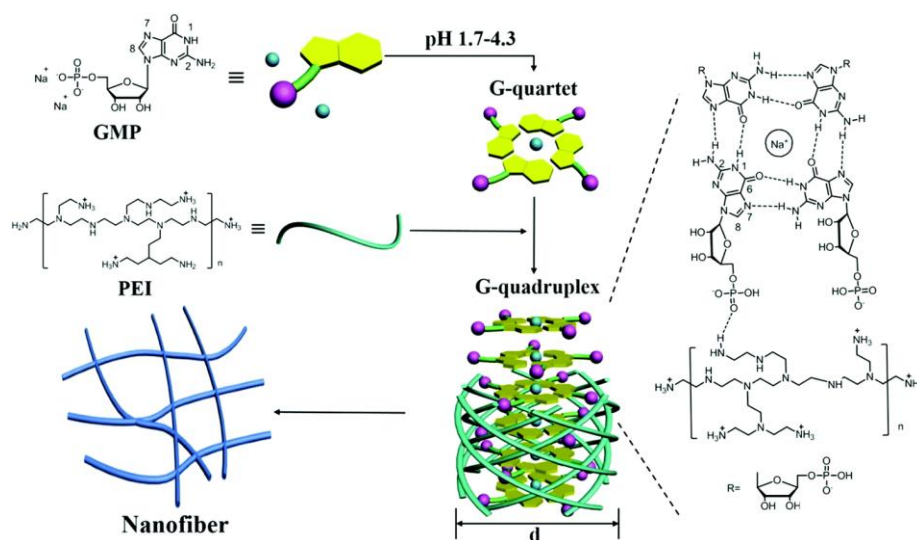


**Figure 1.29** The G-quadruplex hydrogels stabilized by PEI and their putative creation process. [Recreated from ref. no. 120]

Zhang *et al.* prepared a G-quadruplex hydrogel using guanosine monophosphate disodium salt (GMP) along with the hyperbranched poly(ethylenimine) [120]. They explored that the interaction between the cations ( $Na^+$ ) and GMP-quartet as well as the H-bonding interaction between poly(ethylenimine) and phosphate groups help to form the hydrogel at appropriate pH (**Figure 1.29**).

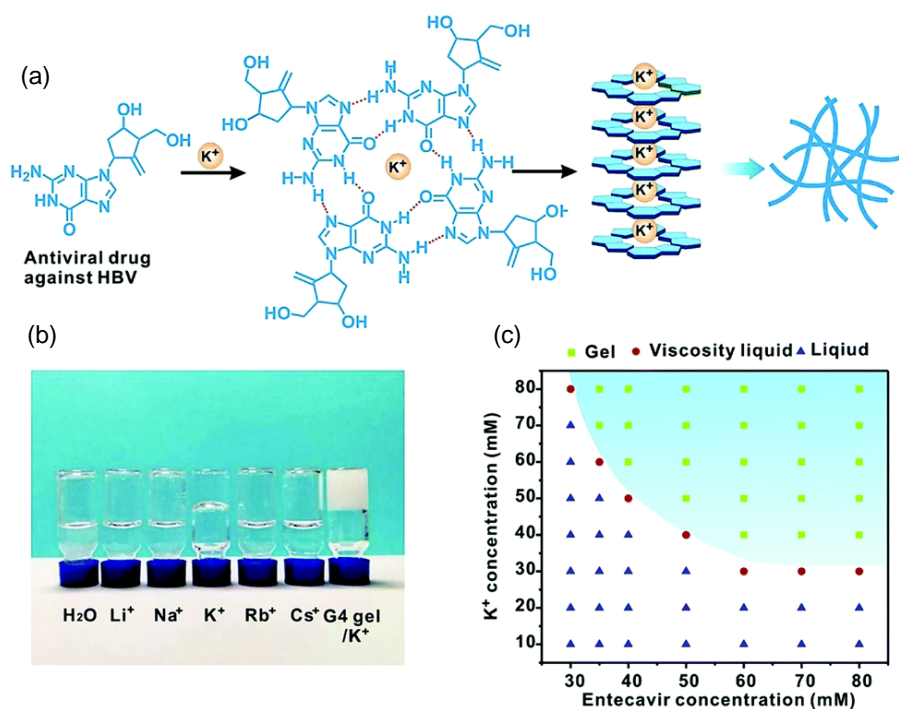


**Figure 1.30** (a) The formation of the G-quadruplex by the antiviral drug entecavir. (b) The cation selectivity of the hydrogel (c) The optimization diagram. [Recreated from ref. no. 121]

Hu *et al.* prepared a supramolecular G-quadruplex hydrogel (**Figure 1.30**) from the antiviral drugs entecavir, ganciclovir, and penciclovir in the presence of an appropriate monovalent cation [121]. The hydrogel showed excellent temperature responsiveness. The hydrogel was used for the release of drug molecules in a temperature-responsive manner. The hydrogels showed biocompatible and injectable properties.

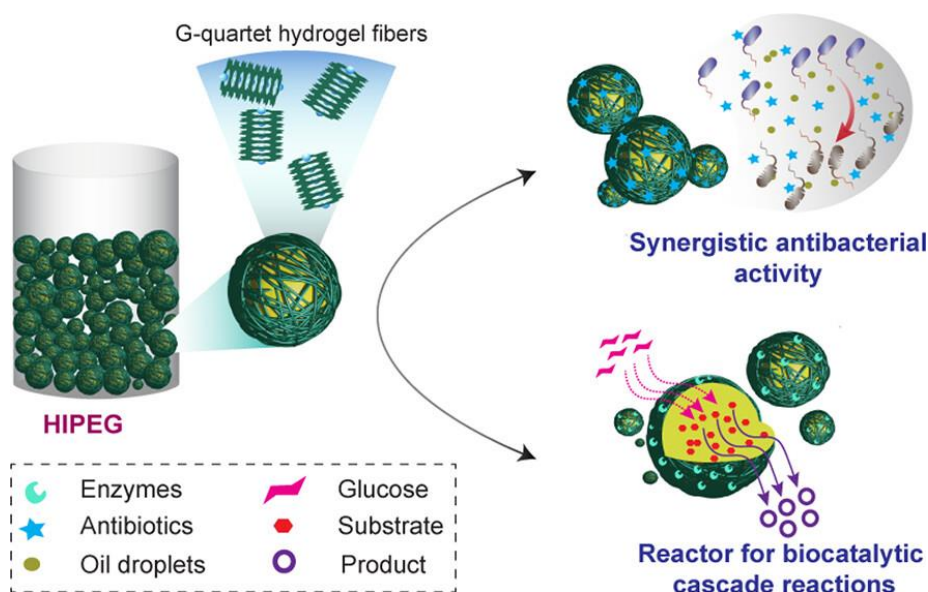


**Figure 1.31** The formation of the gel-immobilized high-internal-phase emulsions (HIPEG) using the G-quadruplex hydrogel. [Recreated from ref. no. 122]

Hydrogel scaffold based on G-quadruplex structures was developed by Das *et al.*, which exhibited stimuli-responsive behavior and a high internal phase emulsion [122]. This scaffold was used for biocatalytic cascades and demonstrated synergistic antimicrobial activity (**Figure 1.31**). The G-quadruplex hydrogel was prepared with guanosine and phenylboronic acid.

McGown *et al.* demonstrated a gel system consisting of binary G-quadruplexes containing Guanosine and 5'-GMP [123]. In this study, they varied the concentration of the Guanosine and GMP to make the hydrogel more stable. They also studied how the system's behavior changed depending on the temperature.

Mariani and his colleagues used Guanosine and 5'-GMP in varying proportions to enhance the stability of the gels. The gel medium was used to encapsulate certain compounds [124].

Kraatz *et al.* used a binary combination of 2'-deoxyguanosine (dG) and Guanosine (G) for gelation [125]. The mechanical strength, viscoelasticity, and thermal stability of this binary gel were adjusted by



using different metal ions as the stability of the G-quartet template depends on the size of the cations. An appropriate hydrogel was used for the transportation of vitamins.

Chen *et al.* developed a binary G4 hydrogel using guanosine (G) and isoguanosine (IsoG) as the main components [126]. The formation of hydrogel was assessed by screening with various monovalent alkali metal ions and the ratio of G and IsoG. The hydrogel was injectable and self-healable.

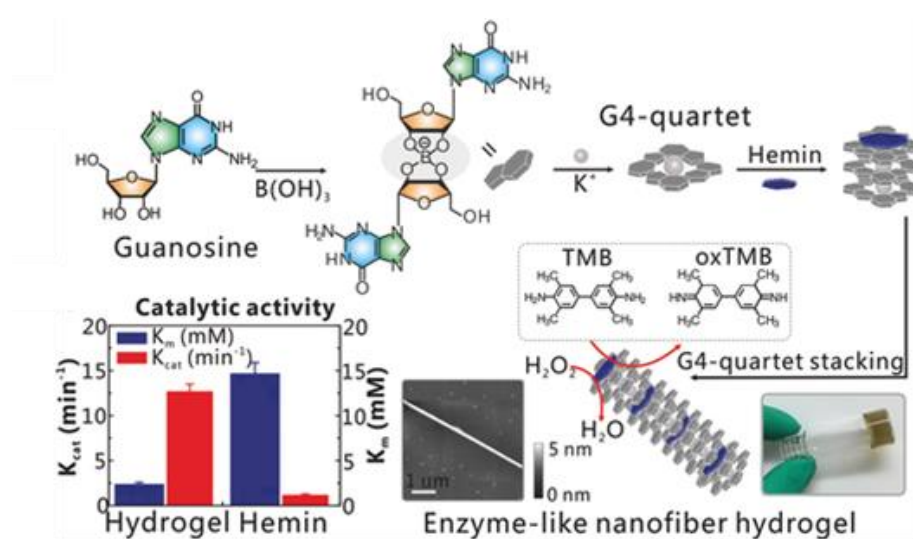


**Figure 1.32** The scheme illustrates the formation of the G-quadruplex hydrogel and shows the catalytic activity. [Recreated from ref. no. 127]

Pei *et al.* fabricated flexible electrochemical sensors using a G4 hydrogel, which was formed using guanosine and boric acid [127]. In addition, hemin was integrated into the G-quadruplex scaffold to provide enzyme-like functionality. The G-quadruplex hydrogel exhibited quick sol-gel transition and shear thinning behavior due to the presence of dynamic boronate linkages, which enables it to be printed as 'ink'. The hydrogel ink was effectively used to make a variety of designs. In addition, polyaniline was integrated into the G4 nanowires. It was used as a flexible electrochemical electrode. A flexible glucose biosensor was prepared by incorporating glucose oxidase into a hydrogel (**Figure 1.32**).

### 1.1.14 Hydrogel Formed by the Peptide-functionalized Molecules

Molecular self-assembly is a well-established method for creating organized structures with desired outcomes, requiring minimum human and machine involvement [128]. Self-assembled peptides can rival physiologically active proteins and provide valuable biological activities and structural diversity as flexible biomaterials [129,130]. Peptide amphiphiles, which have both hydrophobic and hydrophilic groups, are a kind of molecule that may be used as a component for molecular self-assembly [131]. The chemical structure of the aromatic amphiphiles which contain self-assembling peptides consists of three main components: aromatic protective group at the N-terminus, peptide molecule, and methoxycarbonyl group (**Figure 1.33**).

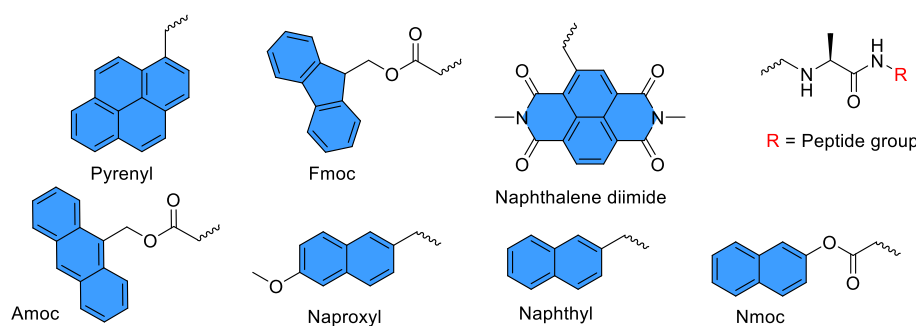


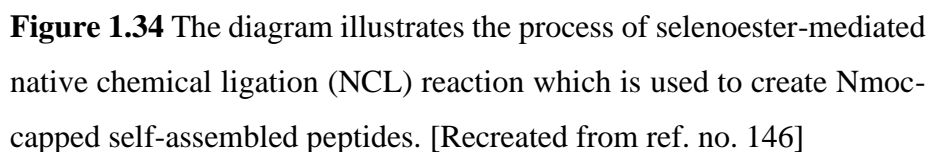
**Figure 1.33** Peptides based self-assembling building blocks with N-terminal protective groups.

Peptide amphiphiles can aggregate and construct a wide variety of supramolecular structures when they are in the presence of diverse stimuli under aqueous circumstances [132]. Typically, the short peptides are adorned to the synthetic hydrophobic moiety to aid in the formation of an organized pattern [133]. It is also possible to build self-assembling peptides utilizing the hydrophobic group that is covalently connected to hydrophilic moiety at both ends of the peptide. Bola-type peptides are characterized by the presence of two hydrophilic groups that are connected to a hydrophobic core [134-136]. These peptides are superior in terms of their ability to build nanostructures [137,138]. The supramolecular nano architectures that are shown by peptide-based bola



amphiphiles include the relevant functional groups that have broad-spectrum application possibilities [139,140]. The self-assembling Therapeutic peptides, which possess biological activity, are involved in the treatment of several diseases. The process of peptide assembly into stable structures based on thermodynamics is a typical occurrence among many bioactive peptides [141].

The peptide-based self-assembling materials are prepared by the use of several N-terminal aromatic-protecting groups [142]. These groups are capable of engaging in aromatic-aromatic interactions, possessing the necessary level of hydrophobicity needed for hydrogelation. Therefore, the peptides and amino acids are protected with a naphthalene group, which is an aromatic motif as well as biocompatible in nature. Thus, it is used in the construction of soft materials [143]. Das *et al.* developed an N-terminal protected peptide for the production of self-assembling materials based on peptides [144]. The protection was made by naphthalene-2-methoxycarbonyl (Nmoc). Nmoc-protected tripeptides were used to facilitate the development of enzyme-catalyzed Nmoc-protected peptides that are thermodynamically stable. This process is facilitated by  $\pi$ - $\pi$  stacking interactions [145]. The aforementioned group also documented the use of oxo-ester and seleno-ester as directing agents in the process of native chemical ligation (NCL) with the Nmoc protected peptide (**Figure 1.34**) [146].



This resulted in the formation of self-assembled materials at ambient temperature. In addition, the researchers used native chemical ligation and subsequent desulfurization procedures to regulate the process of peptide self-assembly [146]. The thiol groups in the cysteine and penicillamine were transformed into Val and Ala moieties using the desulfurization process [147].

In the field of nanomedicine and biomaterials, self-assembled peptide-based hydrogels are the prototypical examples of nanostructured materials. These hydrogels have a seemingly endless number of potential uses. N-terminal protected di- and tri-peptides exhibit significant hydrogelation properties and are considered efficient minimalist hydrogelators [148]. Exploring a broad range of chemical possibilities and adjusting hydrogel characteristics may be achieved by

the independent manipulation of the protecting group, side chain changes, and peptide sequence.

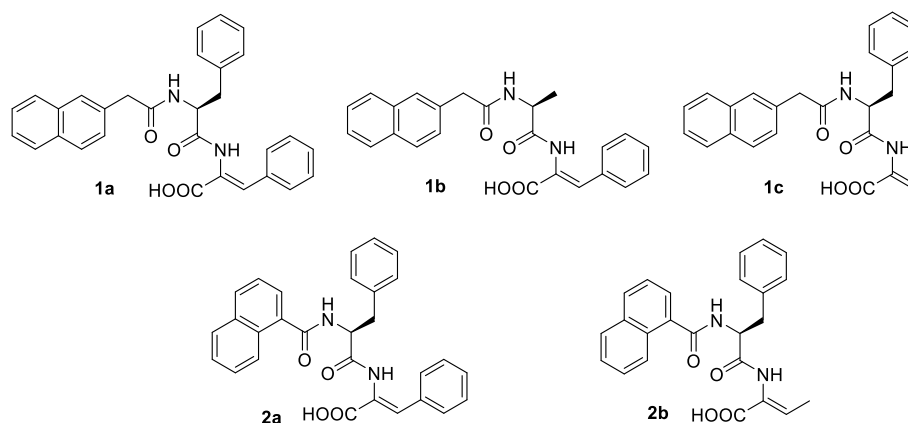


**Figure 1.35** The chemical structure of 2-naphthylacetyl (2-Naph; 1a–c) and 1-naphthaloyl (1-Nap; 2a, b).

Vilaca *et al.* synthesized a library of dehydropeptide with N-terminal protection by 2-naphthyl acetyl and 1-naphthoyl groups [148]. The use of the 2-naphthylacetyl group has been widely documented in the formation of peptide-based self-assembled hydrogels (**Figure 1.35**). In contrast, the 1-naphthaloyl group received less attention, perhaps due to the absence of a methylene linker connecting the aromatic ring of naphthalene with the peptide backbone. They explored that the dehydrodipeptides with an N-terminal protecting 1-naphthyl group form more robust gels at lower concentrations compared to dehydrodipeptides with an N-terminal protecting 2-naphthylacetyl group.

It is possible to generate self-supporting, thixotropic, and injectable soft biomaterials for a variety of biological purposes by functionalizing the N-terminal of amino acids and peptides with a much more robust, rigid, and aromatic anthracene ring [149]. The hydrophobicity of the peptides is increased by 9-Anthracenemethoxycarbonyl (Amoc) protected peptides to improve hydrogelation [150]. Furthermore, it was shown that Amoc aromatic peptides had a synergistic impact on three-dimensional stacking interactions which resulted in the formation of highly entangled fibrillar structures by self-assembly [151]. To produce a variety of Amoc-capped dipeptide-based hydrogelators, a powerful N-terminal

protecting group known as 9-anthracenemethoxycarbonyl (Amoc) was used. The same research team reported the formation of hydrogel using Amoc-capped dipeptides at ambient temperature [150]. The resulting hydrogels exhibited exceptional rheological characteristics which were suitable for many biological applications. The hydrogels exhibited many three-dimensional shapes and demonstrated the capacity to be injected using a syringe. The hydrogel was used for antimicrobial purposes. In a separate study, the same research team demonstrated the anti-inflammatory properties of Amoc capped peptide. This peptide could self-assemble in aqueous medium and formed an antibacterial, thixotropic, noncytotoxic, and injectable hydrogel. A recent study described the formation of a coassembled thixotropic hydrogel by combining  $\beta$ -cyclodextrin (CD) with the self-assembling AmocFF-OH hydrogelator [151]. The toughness of the hydrogels was adjusted by physically combining  $\beta$ -CD with Amoc-FF-OH, due to the optimal noncovalent interactions among peptides and  $\beta$ CD, which resulted in improved thixotropycity and syringe injectability.

Supramolecular soft biomaterials have been synthesized using Fmoc-protected peptides [152]. Peptides get their amphiphilicity via aromatic functionalities that are attached to their N-terminus [153]. In solid-phase peptide synthesis, the Fmoc-group is a popular and adaptable N-terminal protective group [154]. In recent times, self-supporting hydrogels have been made using Fmoc-protected peptides. Vegners and his colleagues prepared the dipeptide hydrogels using Fmoc-protected aliphatic amino acids. The thermoreversible properties of the peptide hydrogel were thoroughly investigated. The solution was formed at 100 °C. Then, the solution was gradually converted into hydrogel when the temperature of the solution was decreased. The drug molecules were also encapsulated into the hydrogel. In-vivo study was performed on rabbits to investigate how much antigenicity was caused by the drug-loaded hydrogel. The gel-to-sol transformation happened when the peptide reacted with vancomycin. The vancomycin disrupted the intermolecular H bonding and hydrophobic interactions amongst peptide hydrogelators, resulting

in a change from a gel to a liquid state [155]. Another study talked about an easy and reliable way to make a biomimetic peptide-based hydrogel that changed color based on the amount of potassium ions present [156]. The formation of peptide hydrogels was achieved by utilizing a technique that allowed the changes in pH in a controlled manner. Glucono- $\delta$ -lactone (GdL) was used as the acidifying agent in this process [157]. Using a different method, the introduction of a weak acid resulted in a quick alteration in pH which resulted in the formation of an inhomogeneous suspension within a clearer area. The authors explained that the kinetics involved in the formation of gluconic acid is slower due to the sustained hydrolysis of GdL. Consequently, the pH of the system decreased gradually which helped in the formation of a uniform hydrogel. The rheological characteristics of the hydrogels were greatly influenced when they were made using the NaOH / HCl technique. A modified aromatic dipeptide underwent self-assembly to develop a hydrogel [158]. The stiffness and three-dimensional structure of the hydrogel were the consequence of the aromatic interactions among the constituent units. The Fmoc-FF dipeptide has a fibrillar structure similar to amyloid-like morphology. Rheological results showed that mechanical strength was concentration-dependent. Hydrogels of peptide concentrations of 10 mg/mL were both strong and stiff. It was shown that several self-assembling dipeptides protected by Fmoc may be formed by combining four distinct amino acids such as G, A, F, and L [159]. The dipeptide hydrogels were prepared using the pH switch technique. The hydrogelation pH of the proposed peptides differed according to their  $pK_a$  values. For example, Fmoc-GG, Fmoc-AA, Fmoc-AG, Fmoc-FG, and FmocLG peptides had acidic pH ( $pH < 4$ ), whereas Fmoc-FF peptides had neutral pH ( $pH < 8$ ). Chemical functionalities of Fmoc hydrogels such as  $NH_2$ ,  $COOH$ , or  $OH$  were studied because of their potential impact on cellular survival [160]. Banerjee *et al.* documented the use of a Fmoc-protected hydrogelator (Fmoc-VD-OH) to produce a stable hydrogel at a concentration as low as 0.2% w/v [161]. The three-dimensional networks of the hydrogels were used to stabilize and prepare luminous silver nanoclusters. The

same group also unveiled a self-assembling proteolytic stable hydrogel composed of  $\beta$ -amino acid residue in peptides [162]. Viscoelastic hydrogels were generated by the peptides (Fmoc- $\beta$ A-F and Fmoc- $\beta$ A-V) containing  $\beta$ -amino acid residue, and they showed improved resistance to external forces. Optimal gelation conditions were achieved with a peptide concentration of 0.1% (w/v) in 50 mM PBS. Ikeda *et al.* recently published a set of self-assembling dipeptides based on  $\alpha$ -methyl L-phenylalanine that were protected with Fmoc [163]. They demonstrated that the hydrogelation ability and self-assembly were significantly affected by the location and quantity of methyl groups linked to the dipeptides. By combining the dipeptide (Fmoc-FF) with the novel ureidopeptide (FmocFuF), a new ureidopeptide with distinct characteristics was formed. The mechanical strength, shear thinning, and self-healing capabilities of the developed ureidopeptide gelator Fmoc-FuF were enhanced compared to Fmoc-FF hydrogel due to the increased hydrogen bonding interactions [164].

Researchers discovered several aromatic compounds that might engage in aromatic interactions and had the appropriate hydrophobicity for hydrogelation while working on several N-terminal protective groups [165]. Since the naphthene (Nap) group is a more biocompatible motif, it is used to protect peptides and amino acids in the production of soft biomaterials [166]. A self-assembling peptide conjugated with Nap, Nap-FF-NO, was described by Zhao and colleagues for use in myocardial infarction [167]. The researchers demonstrated that in reaction to  $\beta$ -galactosidase, the Nap-FF-NO peptide releases nitric oxide (NO) molecules, which enhance heart function via the promotion of angiogenesis. Researchers examined the self-assembly behavior of aromatic protecting groups linked to the N-terminal of peptides, such as Fmoc, benzyloxy-carbonyl (Cbz), and naphthalene (Nap) [168]. Several dipeptides, including Nap-FF, Nap-FY, Nap-FL, and Nap-FS, were prepared by the capping NAP group [168]. The author investigated the influence of N-terminal protection with aromatic and C-terminal protection with hydrophobic amino acids on the self-assembly of

various peptides. Peptide hydrophobicity (ClogP) and minimal gelation concentrations (MGC) were shown to have an inverse relationship. In contrast to Nap-FF and NapFL, Nap-FY and NapFS have a higher MGC value. A tetrapeptide called Naphthalene protected tetrapeptide (Nap-GFFpY-OMe) was synthesized as a very efficient gelator [169]. This tetrapeptide can self-assemble into a hydrogel by an enzymatic process at very low concentrations (0.01% w/v). Hydrogels were generated by other synthesized peptides such as NapGFFpY-OH and Nap-FFpY-OMe with MGC values of 0.08% and 0.4% (w/v) respectively. Furthermore, the presence of the N-terminal protecting group and G amino acid was essential for the formation of the excellent hydrogelator. Furthermore, the presence of the G amino acid and N-terminal protecting group was essential for the development of the hydrogelator. Peptides with a distinct N-terminal aromatic protecting group but a comparable peptide sequence (Fmoc-GFFpY-OMe) exhibited a greater MGC value (0.1% w/v) in comparison to the Nap-GFFpY-OMe peptide. A hydrogel was prepared by self-assembling Nap-GFFY peptide. The hydrogel was used to deliver ophthalmic drugs [170].

Additional aromatic protecting groups such as pyrene are located at the N-terminus of peptides which helps to strengthen aromatic stacking interactions [171]. The peptides and amino acids which were protected by the aromatic pyrene group, exhibit distinct monomer and excimer emissions at varying wavelengths depending on the specific circumstances [172]. Researchers were interested in creating self-assembled aggregates with specified functional structures due to the photoluminescence and intrinsic photophysical stability of the pyrene group. The pyrene group also has a higher fluorescence quantum yield than the anthracene group which means that the excimers formed by pyrene-protected peptides are much easier to detect. When pyrene-containing molecules self-assemble, their photophysical characteristics vary from those of their constituent parts. A change in the emission property of self-assembled materials containing pyrene may be observed visually. Specifically, pyrene-protected peptides exhibit excited-state

electron transfer from the fluorophore to various biological analytes and compounds. Biosensor systems and devices are made using hydrogels that contain pyrene and have ordered structural arrangements, these hydrogels are luminous. Several noncovalent interactions allow bioanalytics and molecules to be accommodated in the well-organized microenvironments provided by pyrene-containing peptides [173]. Bhattacharya *et al.* reported pyrene functionalized peptide which self-assembled to form the hydrogel [174]. Lee *et al.* prepared peptide amphiphiles with pyrene protection at the N-terminal [175]. These molecules were used to detect Ag<sup>+</sup> ions within HeLa cells. Xu *et al.* prepared two pyrene-functionalized pentapeptides such as Py-B (Py-IQEVNOH) and Py-A (Py-RMLRF-OH) [176].

The peptide-derived hydrogelators are synthesized by adding long-chain alkyl groups to the N-terminal end of peptides which promotes the aggregation of molecules via hydrophobic interactions in aqueous medium [177]. The hydrophilicity of the peptide amphiphiles is preserved by the incorporation of certain amino acids that engage in  $\pi$ - $\pi$  stacking interactions and hydrogen bonding [178]. Peptides with long alkyl chains exhibited exceptional aggregation characteristics and created soft biomaterials with integrated biological uses, including antibacterial and drug transport functions [179]. A simple alteration in the alkyl chain length may regulate the peptides' nano structural shape and aggregation concentrations [179]. Peptides have a wide range of self-assembling properties due to the varied sequences of amino acids that make them up [180]. Recent work by Hamley *et al.* used a variety of microscopic, spectroscopic, and small-angle X-ray scattering methods to investigate the biological activity and self-assembly of the amphiphilic lipopeptide PAEPKI-C16 [181]. The impact of a peptide sequence on the cytotoxicity against MCF-7 and human dermal fibroblast (HDFa) was intensively explored. Increased cytotoxicity was observed in the peptide containing free proline residue, suggesting that it may have used alternative self-assembly pathways. An  $\beta$ -sheet type nanotape structure was generated when a carnosine-derived lapidated



peptide (C16KTT $\beta$ AH) self-assembled into water [182]. The hydrogel slowly absorbed the bright Congo red dye and released it gradually over time. The MCF-7 cell line was used to check the anticancer activity of the hydrogel. Banerjee *et al.* used histidine amino acid to make a charged hydrogel that was mechanically and thermally stable. The imidazole ring of histidine is involved in the development of prolonged supramolecular structures via the use of noncovalent interactions between the self-assembling entities that have opposing charges [183]. Stupp *et al.* conceived and developed several soft biomaterials based on peptide amphiphiles for use in a variety of biological applications, including the regeneration of tissues and organs [184,185]. The appropriate mechanical strength of the hydrogel plays an important role in the three-dimensional growth and regeneration of the neuronal cells. Cell growth, proliferation, and adhesion are directly influenced by nanofibers, hence the hydrogels based on peptide amphiphiles demonstrated the healing of burn wounds [184]. Banerjee *et al.* explored a class of hydrogelators based on peptides that have a free amine group attached to their N-termini [186]. These hydrogelators include lengthy alkyl chains. The rheological results demonstrated that the hydrogels' stiffness increased as the alkyl chain length grew, likely owing to the enhanced hydrophobic contacts between the peptide amphiphiles. The FTIR and PXRD results revealed the presence of a hydrogen-bonded  $\beta$ -sheet structure with a  $\pi$ - $\pi$  stacking arrangement between peptide amphiphiles in their self-assembled form.

#### **1.1.15 Application of the Hydrogel**

Hydrogels, which consist of over 90% water and possess tissue-like strength and flexibility, find extensive usage in several biomedical fields including tissue engineering, wound healing, antibacterial therapy, and 3D bioprinting.

##### **1.1.15.1 Tissue Engineering**

Articular cartilage is a kind of tissue that does not have blood vessels and has a restricted ability to mend itself after experiencing trauma,

arthritis, or injuries connected to sports [187]. Cartilage lesions not only impose significant financial and psychological difficulties on patients, but they may also increase the likelihood of joint deterioration, deformity, or even disability [188]. In this situation, it is required to provide therapeutic intervention for abnormalities in the articular cartilage [189]. In recent times, supramolecular hydrogels have emerged as optimal materials for the regeneration of cartilage tissue.

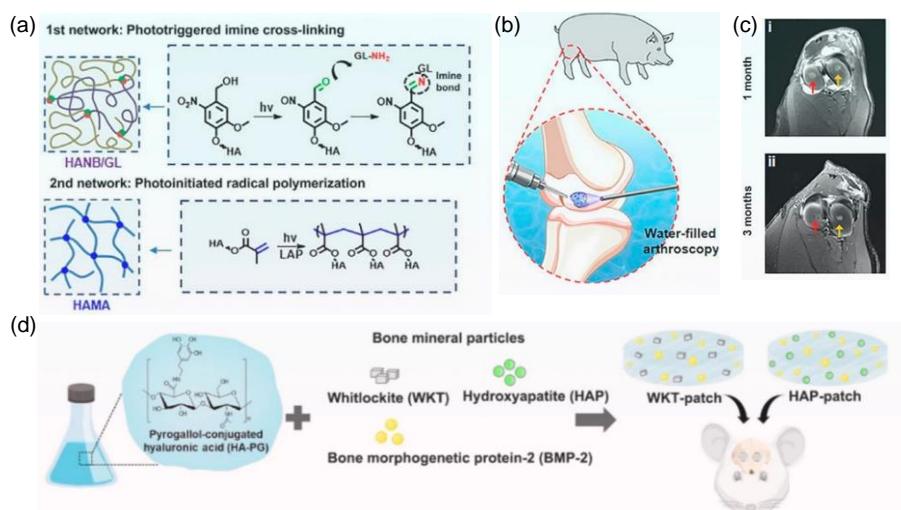


**Figure 1.36** (a) The scheme depicts the molecular composition of the sticky hydrogel. (b) Illustration depicting the use of sticky hydrogel for repairing articular cartilage. (c) Post-treatment magnetic resonance imaging. (d) The scheme shows the step-by-step procedure for making sticky HA-PG patches. [Recreated from ref. no. 192,193]

To improve the biological capabilities, scientists included tissue adhesiveness into the supramolecular hydrogel, resulting in a significant enhancement of tissue integration and cell adhesion [190]. Lu *et al.* developed a hydrogel called tissue-adhesive polydopamine–chondroitin sulfate–polyacrylamide (PDA-CS-PAM) to construct articular cartilage [191]. The PDA-CS-PAM hydrogel was able to simultaneously enable tissue integration and provide a biomimetic milieu for cartilage regeneration. This was accomplished without the incorporation of an external growth factor. Lin *et al.* described a hydrogel consisting of a double network. Hydrogel was prepared by radical polymerization as

well as photochemical imine cross-linking (**Figure 1.36a**) [192]. The ultrafast, robust, and adhesive properties of hydrogels made them acceptable for use in water-filled arthroscopy to repair cartilage for the articular cartilage (**Figure 1.36b**). The double-network hydrogel can cling to cartilage defect sites with uneven forms in an attractive manner (**Figure 1.36c**). Additionally, it enhances cell deposition and finally guarantees the regeneration of cartilage defects. The clinical testing provided further evidence that this pragmatic biomaterial approach has the potential to address articular cartilage abnormalities. Supramolecular adhesive hydrogels have notable benefits in repairing hard bones, in addition to their use in cartilage repair. Supramolecular adhesive hydrogels can mimic key characteristics of the extracellular matrix (ECM) and exhibit robust adherence to bone in complicated therapeutically significant scenarios, including bleeding, bodily fluid, and uneven surfaces. Supramolecular hydrogels with bone-adhesive capabilities may effectively secure hard tissues due to their exceptional cohesive mechanical characteristics, including strength, stiffness, and toughness [193,194]. Cho *et al.* developed a supramolecular sticky hydrogel patch that effectively promotes bone growth (**Figure 1.36d**). This hydrogel patch contained inorganic particles (HAP and WKT) and bone morphogenetic protein 2 (BMP-2), which are integrated into PG-conjugated HA (HA-PG) hydrogels [195].

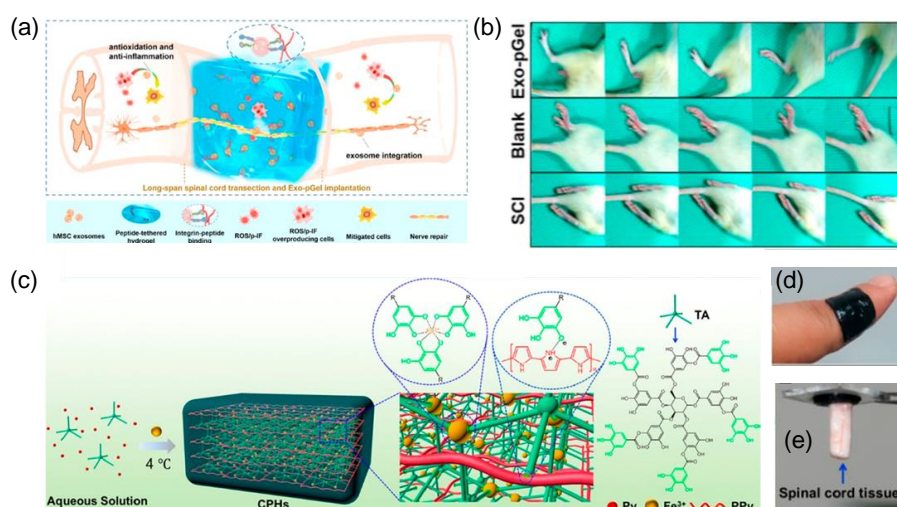


**Figure 1.37** (a) Schematic depicting the Exo-pGel treatment for spinal cord injury. (b) Images depicting the gaits of various animals. (c) Illustrative depiction of the process involved in creating hydrogels made of conducting polymers. Attachment of the hydrogel to (d) skin and (e) spinal cord tissue. [Recreated from ref. no. 199,200]

Neural tissue in the central and peripheral nervous system is vital for certain processes related to receiving, interpreting, and transmitting information [196]. Several neurodegenerative disorders such as Alzheimer's Disease, Parkinson's Disease, traumatic brain injury, spinal cord injury (SCI), and amyotrophic lateral sclerosis, are linked to the dysfunction of neural tissue. The restoration of brain tissue functions presents significant challenges in the clinical process due to the limited regenerating ability of neural tissues. Supramolecular adhesive hydrogel-based biomaterials have significant promise as an alternative treatment for treating brain tissues since they are capable of filling irregular defects in neural tissue. Another one of the most common causes of death throughout the world is spinal cord injuries (SCI), which may be defined as any damage that results in death to any component of the spinal cord or nerves. An innovative approach to spine regeneration has been made possible by the implantation of stem cells [197,198]. To treat spinal cord injuries (SCI), Gao and his colleagues developed a novel implantation technique that included the utilization of exosomes produced from human mesenchymal stem cells (HMSC) that were encapsulated in a peptide-modified supramolecular sticky hydrogel (**Figure 1.37a**) (Exo-p gel) [199]. Exosomes generated from hematopoietic stem cells (HMSC) were successfully implanted locally, resulting in good retention in the damaged tissue of the spinal cord. Exo-pGel was a successful technique to stimulate spinal cord regeneration and reconstruct hindlimb motor function in rat animal models, as revealed by in vivo research (**Figure 1.37b**). Other animal models also proved its effectiveness. Ning and his colleagues have successfully introduced a soft conductive polymer sticky hydrogel for repairing

spinal cord injuries (SCI) [200]. The supramolecular sticky hydrogel was created using tannic acid (TA) and a conductive polymer network based on polypyrrole (PPy) (**Figure 1.37c**). The presence of polyphenols on the TA molecule resulted in the hydrogel being able to adhere well to both the skin and spinal cord tissue (**Figure 1.37d, e**).

#### 1.1.15.2 Wound Healing

Gong *et al.* reported a new antibacterial hydrogel composed of phycocyanin (PC) and gallic acid (GA) with potential use in the treatment of bacterial infections in wounds [201]. The GP hydrogels facilitated adherence to the wound area and achieved a continuous release of GA and PC. Hence it effectively reduced inflammation and sped up wound healing in both bacteria-infected and normal mice by regulating the expression of the tight junction protein and alleviating oxidative stress (**Figure 1.38**).

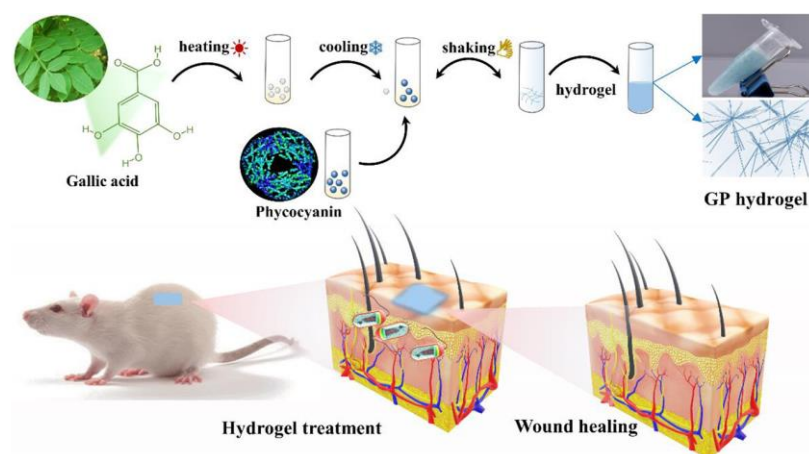


**Figure 1.38** The schematic illustration shows the formation of GP hydrogel and wound healing using mice model. [Recreated from ref. no. 201]

Liu *et al.* developed an injectable, self-healing, and multifunctional hydrogel for wound healing [202]. The modification was carried out on chitosan with tannic acid to implement anti-inflammatory and potential adhesion properties. The wound healing ability of the hydrogel was

studied *in vivo* (**Figure 1.39**). Hydrogel rapidly adapted to the wound area, halting bleeding, and facilitating cellular proliferation and wound healing. It had favorable anti-inflammatory characteristics during the early phase.

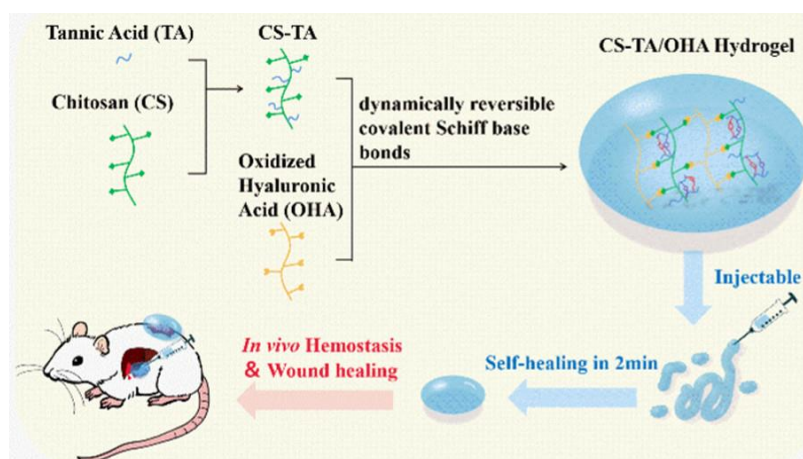


**Figure 1.39** The scheme depicts the formation of the hydrogel and its use in *in vivo* wound healing. [Recreated from ref. no. 202]

Gavel *et al.* developed a hydrogel by conjugating a dipeptide with an Amoc (9-anthracene methoxycarbonyl) using several noncovalent interactions.  $\beta$ -cyclodextrin (CD) was encapsulated to prepare a co-assembled thixotropic and injectable hydrogel, which was appropriate for use in wound healing [151]. The wound healing capacity of the co-assembled hydrogel was studied in mice using histopathology studies.

### 1.1.15.3 Drug Delivery

Hydrogel delivery methods may exploit the advantageous effects of drug administration and have been used in biomedicine. Hydrogels provide the ability to precisely regulate the release of different therapeutic agents, such as small-molecule medications, and macromolecular pharmaceuticals. Hydrogels are used as a platform to regulate the release of drugs due to their adjustable physical characteristics, ability to degrade in a controlled manner, and capacity to shield sensitive drugs from breaking down. These hydrogels facilitate

numerous chemical and physical interactions with the enclosed drugs, allowing for precise control over drug release [203].

Biswas *et al.* prepared a hydrogel by employing guanosine, 4-Arm PEG-NH<sub>2</sub>, and 2-formylphenylboronic acid. The biocompatible G-quadruplex hydrogel was used as a drug carrier [204]. The anticancer drug doxorubicin was loaded in the hydrogel. Using two distinct external pH solutions, the release study of the drug-loaded G-quadruplex-PEG hydrogel was examined (pH 7.4 and 4.8) (**Figure 1.40**).

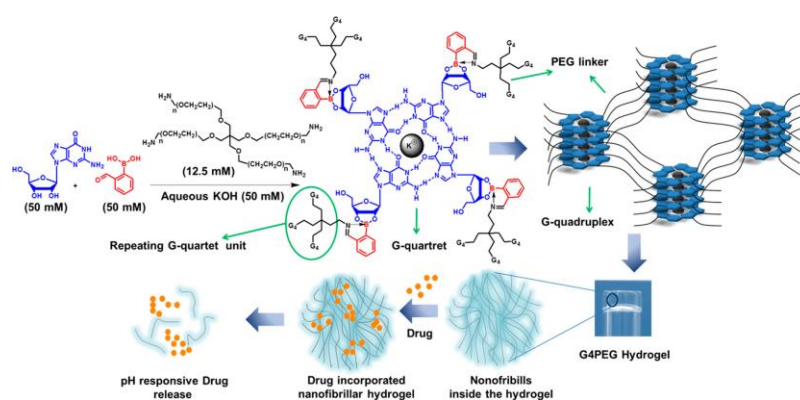


**Figure 1.40** The scheme demonstrates the formation of the G-quadruplex hydrogel and the use of the hydrogel for the delivery of the anticancer drug doxorubicin. [Recreated from ref. no. 204]

In another study, Ghosh *et al.* reported the formation of multi-component G-quadruplex hydrogel by 1-naphthaleneboronic acid and guanosine (G) [205]. A biocompatible G-quadruplex hydrogel that may be injected has been used to encapsulate and gradually release two crucial vitamins (B<sub>2</sub> and B<sub>12</sub>) over 40 hours at a pH level of 7.46, which is similar to the pH level seen in the human body (**Figure 1.41**).



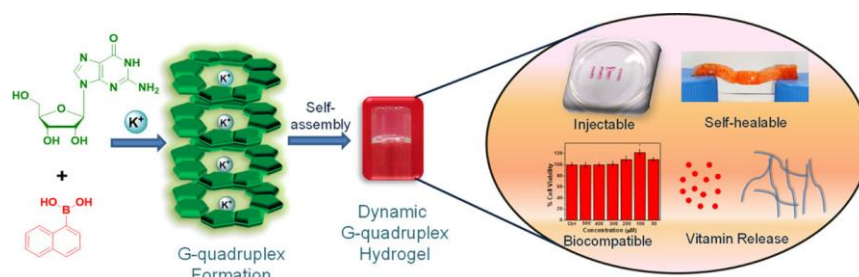


**Figure 1.41** The scheme demonstrates the formation of the hydrogel and the use of the hydrogel for the delivery of the vitamin molecules.  
[Recreated from ref. no. 205]

#### 1.1.15.4 3D Printing

3D printing is an expanding area that involves the creation of real items by depositing layers of material based on a pre-designed digital model. In the field of 3D bioprinting, it is possible to create intricate 3D structures of live human tissues or organs by combining them with hydrogels, known as bioinks. Bioinks are pliable hydrogel substances used in the process of 3D-bioprinting to encase live cells, bioactive elements, and growth factors. A bio-ink hydrogel should possess the following characteristics: (1) sufficient mechanical strength to support the cells (2) injectable (3) biocompatible (4) self-healing (5) thixotropic. There has been a significant rise in the number of people suffering from bone abnormalities resulting from trauma, osteoporosis, and bone tumors [206]. Clinicians have a significant problem when it comes to repairing irregular, recurrent, and massive bone abnormalities. Bone tissue engineering is becoming a suitable approach for replacing autologous bone grafting in the treatment of large bone deformities. Nevertheless, the adequacy of bone tissue engineering scaffolds in terms of their structure, degradation, microenvironment, and mechanics is insufficient. Three-dimensional (3D) printing is a sophisticated kind of additive manufacturing that is extensively used for bone restoration.



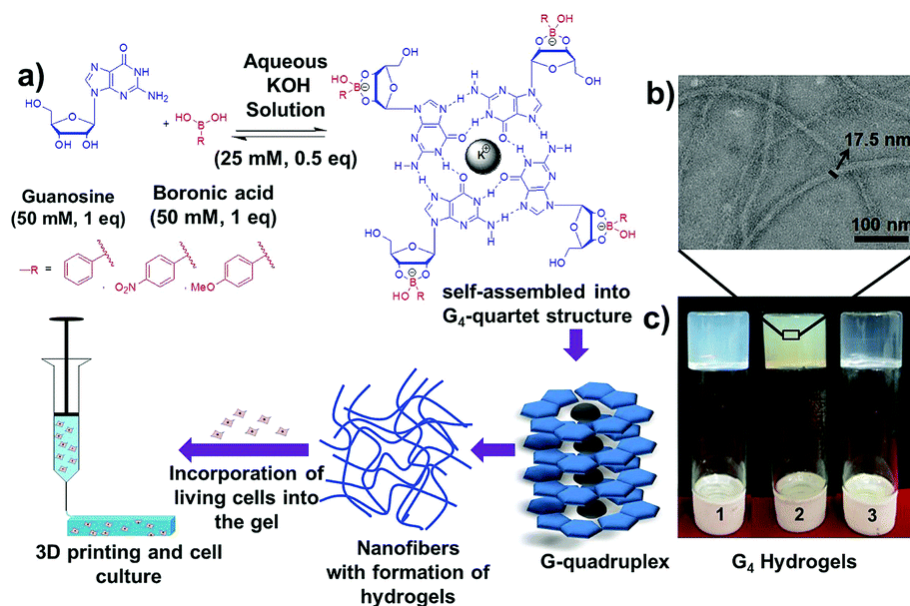


**Figure 1.42** The scheme illustrates the formation of the G-quadruplex hydrogel and the use of the hydrogel for 3D printing. [Recreated from ref. no. 207]

Biswas *et al.* reported a G-quadruplex extrudable hydrogel by using guanosine and phenylboronic acid. The inherent fluidity of the boronate ester-boronic acid equilibrium imparts crucial characteristics like as injectability, self-healing, and thixotropy, which are vital for 3D printing [207]. The gel was harmless and the printing technique did not harm the survival of the cells (**Figure 1.42**).

## 1.2 Summary

The Chapter 1 described molecular self-assembly and the formation of the hydrogel. The non-covalent interactions behind the hydrogel formation were discussed. The formation of a G-quadruplex structure via Hoogsteen H-bonding interaction was described. The importance of G-quadruplex structure in the replication, transcription, and translation of DNA was mentioned. The role of G-quadruplex in the formation of the hydrogel was outlined. This chapter mainly focused on the formation of the G-quadruplex hydrogel by guanine derivatives. Therefore, this chapter spoke about the recent progress of the guanine-functionalized

G-quadruplex hydrogels, peptide based hydrogels, and their applications.

### 1.3 Thesis Organization

This thesis consists of six chapters. **Chapter 1** provides an overview of the molecular self-assembly and the formation of the hydrogels using the self-assembly. The effects of physical and chemical stimuli in the formation of the hydrogel and their biomedical applications are discussed. In addition to the literature review in **Chapter 1**, the research works that had been carried out in the past five years are described in the following chapters. **Chapter 2** discusses the synthesis and development of guanine-functionalized phenylalanine derivatives. I varied the chain length of the long fatty acid to induce gelation properties in the synthesized nucleobase functionalized amino acid derivatives. Their self-aggregation was thoroughly studied in water by performing DOSY NMR. The synthesized biocompatible hydrogel was used for the pH-responsive release of the drug molecules. In **Chapter 3**, I synthesized and developed nucleobase-functionalized amino acid derivatives. The chemical reaction-driven formation of the supramolecular hydrogel is discussed here. The progress of the self-assembly over time is thoroughly studied using various spectroscopic techniques. In **Chapter 4**, I functionalized guanine with different amino acids. The self-assembly of the synthesized nucleopeptide is extensively studied using molecular dynamic simulations and DOSY NMR. The synthesized nucleopeptide hydrogel is biocompatible and possesses properties such as anti-bacterial, anti-inflammatory, non-hemolytic, and bio-stability. The hydrogel was used for *in vitro* wound healing. In **Chapter 5**, I designed and synthesized five different guanine functionalized amino acid derivatives. The lipase catalyze formation of the hydrogel is explored. This biocompatible hydrogel was used for studying cell migration and proliferation study. Finally, **Chapter 6** provides a comprehensive overview of the results obtained from the present Ph.D. research and outlines the future prospects of this study.

## 1.4 References

- [1] Pochan D, Scherman O (2021) Introduction: Molecular Self-Assembly. *Chem Rev* 121:13699–13700. <https://doi.org/10.1021/acs.chemrev.1c00884>.
- [2] Whitesides GM, Mathias JP, Seto CT (1991) Molecular Self-Assembly and Nanochemistry: a Chemical Strategy for the Synthesis of Nanostructures. *Science* 254:1312–1319. <https://doi.org/10.1126/science.1962191>.
- [3] Zhang S (2003) Fabrication of novel biomaterials through molecular self-assembly. *Nat Biotechnol* 21:1171–1178. <https://doi.org/10.1038/nbt874>.
- [4] Korbel J, Lindner SD, Hanel R, Thurner S (2021) Thermodynamics of structure-forming systems. *Nat Commun* 12:1127. <https://doi.org/10.1038/s41467-021-21272-7>.
- [5] Packwood DM, Han P, Hitosugi T (2017) Chemical and entropic control on the molecular self-assembly process. *Nat Commun* 8:14463. <https://doi.org/10.1038/ncomms14463>.
- [6] Johnson ER, Keinan S, Mori-Sánchez P, Contreras-García J, Cohen AJ, Yang W (2010) Revealing Noncovalent Interactions. *J Am Chem Soc* 132:6498–6506. <https://doi.org/10.1021/ja100936w>.
- [7] Adhav VA, Saikrishnan K (2023) The Realm of Unconventional Noncovalent Interactions in Proteins: Their Significance in Structure and Function. *ACS Omega* 8:22268–22284. <https://doi.org/10.1021/acsomega.3c00205>.
- [8] Jena S, Dutta J, Tulsiyan KD, Sahu AK, Choudhury SS, Biswal HS (2022) Noncovalent interactions in proteins and nucleic acids: beyond hydrogen bonding and  $\pi$ -stacking. *Chem Soc Rev* 51:4261–4286. <https://doi.org/10.1039/D2CS00133K>.

- [9] Cashion MP, Long TE (2009) Biomimetic Design and Performance of Polymerizable Lipids. *Acc Chem Res* 42:1016–1025. <https://doi.org/10.1021/ar800191s>.
- [10] Lee S, Saito K, Lee H-R, Lee MJ, Shibasaki Y, Oishi Y, Kim B-S (2012) Hyperbranched Double Hydrophilic Block Copolymer Micelles of Poly(ethylene oxide) and Polyglycerol for pH-Responsive Drug Delivery. *Biomacromole* 13:1190–1196. <https://doi.org/10.1021/bm300151m>.
- [11] Sun H, Jiang J, Xiao Y, Du J (2018) Efficient Removal of Polycyclic Aromatic Hydrocarbons, Dyes, and Heavy Metal Ions by a Homopolymer Vesicle. *ACS Appl Mater Inter* 10:713–722. <https://doi.org/10.1021/acsami.7b15242>.
- [12] Gao Y, Zhang X, Yang M, Zhang X, Wang W, Wegner G, Burger C (2007) Synthesis and Cylinder Microdomain Structures of Hybrid Block Copolymers of  $\pi$ -Conjugated and Dendritic Poly(phenylazomethine)s and Flexible and Linear PEO. *Macromole* 40:2606–2612. <https://doi.org/10.1021/ma062881l>.
- [13] Stojanovic A, Oliveira S, Fischer M, Seeger S (2013) Polysiloxane Nanotubes. *Chem Mater* 25:2787–2792. <https://doi.org/10.1021/cm400851k>.
- [14] Pir Cakmak F, Grigas AT, Keating CD (2019) Lipid Vesicle-Coated Complex Coacervates. *Langmuir* 35:7830–7840. <https://doi.org/10.1021/acs.langmuir.9b00213>.
- [15] Zhang H, Fang S, Wu Z, Islam SR, Qin X (2023) PAN/PAN-FPU Double-Layer Composite Nanofiber Air Filter Fabricated by Electrospinning for Filtering Oil and Salt Particles. *ACS Appl Nano Mater* 6:7619–7628. <https://doi.org/10.1021/acsanm.3c00781>.
- [16] Rispoli F, Spatola E, Del Giudice D, Cacciapaglia R, Casnati A, Baldini L, Di Stefano S (2022) Temporal Control of the Host–Guest

Properties of a Calix[6]arene Receptor by the Use of a Chemical Fuel. *J Org Chem* 87:3623–3629. <https://doi.org/10.1021/acs.joc.2c00050>.

[17] Rodgers P (2006) Top down, bottom up. *Nature Nanotech.* <https://doi.org/10.1038/nnano.2006.87>.

[18] Smith KH, Tejeda-Montes E, Poch M, Mata A (2011) Integrating top-down and self-assembly in the fabrication of peptide and protein-based biomedical materials. *Chem Soc Rev* 40:4563. <https://doi.org/10.1039/c1cs15064b>.

[19] Cook AB, Clemons TD (2022) Bottom-Up versus Top-Down Strategies for Morphology Control in Polymer-Based Biomedical Materials. *Advanced NanoBiomed Research* 2:2100087. <https://doi.org/10.1002/anbr.202100087>.

[20] Diaz Fernandez YA, Gschneidner TA, Wadell C, et al (2014) The conquest of middle-earth: combining top-down and bottom-up nanofabrication for constructing nanoparticle-based devices. *Nanoscale* 6:14605–14616. <https://doi.org/10.1039/C4NR03717K>.

[21] Feynman R.P. (1959), There's Plenty of Room at the Bottom, Caltech. *Eng. Sci.*, 23, 22-36 (ISSN 0013-7812).

[22] Iqbal P, Preece JA, Mendes PM (2012) Nanotechnology: The “Top-Down” and “Bottom-Up” Approaches. In: Gale PA, Steed JW (eds) *Supramolecular Chemistry*, 1st edn. Wiley. (ISBN: 9780470661345)

[23] Baig N, Kammakakam I, Falath W (2021) Nanomaterials: a review of synthesis methods, properties, recent progress, and challenges. *Mater Adv* 2:1821–1871. <https://doi.org/10.1039/D0MA00807A>.

[24] Kumar S, Bhushan P, Bhattacharya S (2018) Fabrication of Nanostructures with Bottom-up Approach and Their Utility in Diagnostics, Therapeutics, and Others. In: Bhattacharya S, Agarwal AK, Chanda N, Pandey A, Sen A. (eds) *Environmental, Chemical and Medical Sensors*. Springer Singapore, Singapore, pp 167–198. (ISBN: 978-981-10-7751-7)

- [25] Olafusi OS, Sadiku ER, Snyman J, Ndambuki JM, Kupolati WK (2019) Application of nanotechnology in concrete and supplementary cementitious materials: a review for sustainable construction. *SN Appl Sci* 1:580. <https://doi.org/10.1007/s42452-019-0600-7>.
- [26] Yang D (2022) Recent Advances in Hydrogels. *Chem Mater* 34:1987–1989. <https://doi.org/10.1021/acs.chemmater.2c00188>.
- [27] Ahmed EM (2015) Hydrogel: Preparation, characterization, and applications: A review. *Journal of Advanced Research* 6:105–121. <https://doi.org/10.1016/j.jare.2013.07.006>.
- [28] Kuzina MA, Kartsev DD, Stratonovich AV, Levkin PA (2023) Organogels versus Hydrogels: Advantages, Challenges, and Applications. *Adv Funct Materials* 33:2301421. <https://doi.org/10.1002/adfm.202301421>.
- [29] Xu X, Jerca VV, Hoogenboom R (2021) Bioinspired double network hydrogels: from covalent double network hydrogels via hybrid double network hydrogels to physical double network hydrogels. *Mater Horiz* 8:1173–1188. <https://doi.org/10.1039/D0MH01514H>.
- [30] Feng Z, Zuo H, Gao W, Ning N, Tian M, Zhang L (2018) A Robust, Self-Healable, and Shape Memory Supramolecular Hydrogel by Multiple Hydrogen Bonding Interactions. *Macromol Rapid Commun* 39:1800138. <https://doi.org/10.1002/marc.201800138>.
- [31] Song G, Zhang L, He C, Fang D-C, Whitten PG, Wang H (2013) Facile Fabrication of Tough Hydrogels Physically Cross-Linked by Strong Cooperative Hydrogen Bonding. *Macromole* 46:7423–7435. <https://doi.org/10.1021/ma401053c>.
- [32] Yu H, Xiao Q, Qi G, Chen F, Tu B, Zhang S, Li Y, Chen Y, Yu H, Duan P (2022) A Hydrogen Bonds-Crosslinked Hydrogels With Self-Healing and Adhesive Properties for Hemostatic. *Front Bioeng Biotechnol* 10:855013. <https://doi.org/10.3389/fbioe.2022.855013>.

- [33] Tuncaboylu DC, Sari M, Oppermann W, Okay O (2011) Tough and Self-Healing Hydrogels Formed via Hydrophobic Interactions. *Macromole* 44:4997–5005. <https://doi.org/10.1021/ma200579v>.
- [34] Jiang H, Duan L, Ren X, Gao G (2019) Hydrophobic association hydrogels with excellent mechanical and self-healing properties. *Eur Polym J* 112:660–669. <https://doi.org/10.1016/j.eurpolymj.2018.10.031>.
- [35] Kim H-J, Cho S, Oh SJ, Shin SG, Ryu HW, Jeong JH (2019) Tuning the Hydrophobicity of a Hydrogel Using Self-Assembled Domains of Polymer Cross-Linkers. *Materials* 12:1635. <https://doi.org/10.3390/ma12101635>.
- [36] PekaÅ™ M (2015) Hydrogels with Micellar Hydrophobic (Nano)Domains. *Front Mater* 1:.. <https://doi.org/10.3389/fmats.2014.00035>.
- [37] Ahn J, Park S, Lee JH, Jung SH, Moon S-J, Jung JH (2013) Fluorescent hydrogels formed by CH– $\pi$  and  $\pi$ – $\pi$  interactions as the main driving forces: an approach toward understanding the relationship between fluorescence and structure. *Chem Commun* 49:2109. <https://doi.org/10.1039/c2cc37249e>.
- [38] Xu D, Ma Y, Jing Z, Han L, Singh B, Feng J, Shen X, Cao F, Oleynikov P, Sun H, Terasaki O, Che S (2014)  $\pi$ – $\pi$  interaction of aromatic groups in amphiphilic molecules directing for single-crystalline mesostructured zeolite nanosheets. *Nat Commun* 5:4262. <https://doi.org/10.1038/ncomms5262>.
- [39] Birchall LS, Roy S, Jayawarna V, ughes M, Irvine E, Okorogheye GT, Saudi N, De Santis E, Tuttle T, Edwards AA, Ulijn RV (2011) Exploiting CH- $\pi$  interactions in supramolecular hydrogels of aromatic carbohydrate amphiphiles. *Chem Sci* 2:1349. <https://doi.org/10.1039/c0sc00621a>.

- [40] Ryan DM, Doran TM, Nilsson BL (2011) Complementary  $\pi$ - $\pi$  Interactions Induce Multicomponent Coassembly into Functional Fibrils. *Langmuir* 27:11145–11156. <https://doi.org/10.1021/la202070d>.
- [41] Han X, Kong H, Chen T, Gao J, Zhao Y, Sang Y, Hu G (2021) Effect of  $\pi$ - $\pi$  Stacking Interfacial Interaction on the Properties of Graphene/Poly(styrene-*b*-isoprene-*b*-styrene) Composites. *Nanomaterials* 11:2158. <https://doi.org/10.3390/nano11092158>.
- [42] Nakano T (2010) Synthesis, structure and function of  $\pi$ -stacked polymers. *Polym J* 42:103–123. <https://doi.org/10.1038/pj.2009.332>.
- [43] Pickering AL, Seeber G, Long D-L, Cronin L (2005) The importance of  $\pi$ - $\pi$ ,  $\pi$ -CH and N-CH interactions in the crystal packing of Schiff-base derivatives of *cis,cis*- and *cis,trans*-1,3,5-triaminocyclohexane. *CrystEngComm* 7:504. <https://doi.org/10.1039/b506718a>.
- [44] Perera MM, Ayres N (2020) Dynamic covalent bonds in self-healing, shape memory, and controllable stiffness hydrogels. *Polym Chem* 11:1410–1423. <https://doi.org/10.1039/C9PY01694E>.
- [45] Li L, Peng X, Zhu D, Zhang J, Xiao P (2023) Recent Progress in Polymers with Dynamic Covalent Bonds. *Macro Chemistry & Physics* 224:2300224. <https://doi.org/10.1002/macp.202300224>.
- [46] Wang S, Tavakoli S, Parvathaneni RP, Nawale GN, Oommen OP, Hilborn J, Varghese OP (2022) Dynamic covalent crosslinked hyaluronic acid hydrogels and nanomaterials for biomedical applications. *Biomater Sci* 10:6399–6412. <https://doi.org/10.1039/D2BM01154A>.
- [47] Yang H, Fustin C (2023) Design and Applications of Dynamic Hydrogels Based on Reversible C=N Bonds. *Macromol Chem Phys* 224:2300211. <https://doi.org/10.1002/macp.202300211>.



- [48] Černý J, Hobza P (2007) Non-covalent interactions in biomacromolecules. *Phys Chem Chem Phys* 9:5291. <https://doi.org/10.1039/b704781a>.
- [49] Saleh G, Gatti C, Lo Presti L, Contreras-García J (2012) Revealing Non-covalent Interactions in Molecular Crystals through Their Experimental Electron Densities. *Chemistry A European J* 18:15523–15536. <https://doi.org/10.1002/chem.201201290>.
- [50] Philips DS, Kartha KK, Politi AT, Krüger T, Albuquerque RQ, Fernández G (2019) Interplay between H-Bonding and Preorganization in the Evolution of Self-Assembled Systems. *Angew Chem Int Ed* 58:4732–4736. <https://doi.org/10.1002/anie.201813955>.
- [51] Cougnon FBL, Stefankiewicz AR, Ulrich S (2024) Dynamic covalent synthesis. *Chem Sci* 15:879–895. <https://doi.org/10.1039/D3SC05343A>.
- [52] Boehnke N, Cam C, Bat E, Segura T, Maynard HD (2015) Imine Hydrogels with Tunable Degradability for Tissue Engineering. *Biomacromole* 16:2101–2108. <https://doi.org/10.1021/acs.biomac.5b00519>.
- [53] Qu J, Zhao X, Ma PX, Guo B (2017) pH-responsive self-healing injectable hydrogel based on N-carboxyethyl chitosan for hepatocellular carcinoma therapy. *Acta Biomaterialia* 58:168–180. <https://doi.org/10.1016/j.actbio.2017.06.001>.
- [54] Zhang Z, He C, Chen X (2018) Hydrogels based on pH-responsive reversible carbon–nitrogen double-bond linkages for biomedical applications. *Mater Chem Front* 2:1765–1778. <https://doi.org/10.1039/C8QM00317C>.
- [55] Wang LL, Highley CB, Yeh Y, Galarraja JH, Uman S, Burdick JA (2018) Three-dimensional extrusion bioprinting of single- and double-network hydrogels containing dynamic covalent crosslinks. *J*

Biomedical Materials Res 106:865–875.  
<https://doi.org/10.1002/jbm.a.36323>.

[56] Domingues RMA, Silva M, Gershovich P, Betta S, Babo P, Caridade SG, Mano JF, Motta A, Reis RL, Gomes ME (2015) Development of Injectable Hyaluronic Acid/Cellulose Nanocrystals Bionanocomposite Hydrogels for Tissue Engineering Applications. *Bioconjugate Chem* 26:1571–1581.  
<https://doi.org/10.1021/acs.bioconjchem.5b00209>.

[57] Wiedemann C, Kumar A, Lang A, Ohlenschläger O (2020) Cysteines and Disulfide Bonds as Structure-Forming Units: Insights From Different Domains of Life and the Potential for Characterization by NMR. *Front Chem* 8:280.  
<https://doi.org/10.3389/fchem.2020.00280>.

[58] Sun M, Wang Y, Zhang Q, Xia Y, Ge W, Guo D (2017) Prediction of reversible disulfide based on features from local structural signatures. *BMC Genomics* 18:279. <https://doi.org/10.1186/s12864-017-3668-8>.

[59] Sevier CS, Kaiser CA (2002) Formation and transfer of disulphide bonds in living cells. *Nat Rev Mol Cell Biol* 3:836–847.  
<https://doi.org/10.1038/nrm954>.

[60] Dong H, Wang M, Fan S, Wu C, Zhang C, Wu X, Xue B, Cao Y, Deng J, Yuan D, Shi J (2022) Redox-Regulated Conformational Change of Disulfide-Rich Assembling Peptides. *Angew Chem Int Ed* 61:e202212829. <https://doi.org/10.1002/anie.202212829>.

[61] Guo R, Su Q, Zhang J, Dong A, Lin C, Zhang J (2017) Facile Access to Multisensitive and Self-Healing Hydrogels with Reversible and Dynamic Boronic Ester and Disulfide Linkages. *Biomacromole* 18:1356–1364. <https://doi.org/10.1021/acs.biomac.7b00089>.

[62] Tran VT, Mredha MdTI, Na JY, Seon J-K, Cui J, Jeon I (2020) Multifunctional poly(disulfide) hydrogels with extremely fast self-

healing ability and degradability. *J Chem Eng* 394:124941. <https://doi.org/10.1016/j.cej.2020.124941>.

[63] Tibbitt MW, Kloxin AM, Sawicki LA, Anseth KS (2013) Mechanical Properties and Degradation of Chain and Step-Polymerized Photodegradable Hydrogels. *Macromolecules* 46:2785–2792. <https://doi.org/10.1021/ma302522x>.

[64] Kanti Das B, Samanta R, Ahmed S, Pramanik B (2023) Disulphide Cross-Linked Ultrashort Peptide Hydrogelator for Water Remediation. *Chemistry A European J* 29:e202300312. <https://doi.org/10.1002/chem.202300312>.

[65] Fuchs O, Trunschke S, Hanebrink H, Reimann M, Seitz O (2021) Enabling Cysteine-Free Native Chemical Ligation at Challenging Junctions with a Ligation Auxiliary Capable of Base Catalysis. *Angew Chem Int Ed* 60:19483–19490. <https://doi.org/10.1002/anie.202107158>.

[66] Fyfe JWB, Watson AJB (2017) Recent Developments in Organoboron Chemistry: Old Dogs, New Tricks. *Chem* 3:31–55. <https://doi.org/10.1016/j.chempr.2017.05.008>.

[67] Nandy S, Paul S, Das KK, Kumar, P.; Ghorai, D.; Panda, S. (2021) Synthesis and reactivity of alkynyl boron compounds. *Org Biomol Chem* 19:7276–7297. <https://doi.org/10.1039/D1OB00465D>.

[68] Debiais M, Vasseur J, Smietana M (2022) Applications of the Reversible Boronic Acids/Boronate Switch to Nucleic Acids. *The Chem Rec* 22:e202200085. <https://doi.org/10.1002/tcr.202200085>.

[69] Bapat AP, Sumerlin BS, Sutti A (2020) Bulk network polymers with dynamic B–O bonds: healable and reprocessable materials. *Mater Horiz* 7:694–714. <https://doi.org/10.1039/C9MH01223K>.

[70] Pettignano A, Grijalvo S, Häring M, Eritja R, Tanchoux N, Quignard F, Díaz Díaz D (2017) Boronic acid-modified alginate enables direct formation of injectable, self-healing and multistimuli-responsive

hydrogels. Chem Commun 53:3350–3353.  
<https://doi.org/10.1039/C7CC00765E>.

[71] Van Duin M, Peters JA, Kieboom APG, Van Bakkum H (1984) Studies on borate esters 1. Tetrahedron 40:2901–2911.  
[https://doi.org/10.1016/S0040-4020\(01\)91300-6](https://doi.org/10.1016/S0040-4020(01)91300-6).

[72] Brooks WLA, Sumerlin BS (2016) Synthesis and Applications of Boronic Acid-Containing Polymers: From Materials to Medicine. Chem Rev 116:1375–1397. <https://doi.org/10.1021/acs.chemrev.5b00300>.

[73] Cash JJ, Kubo T, Bapat AP, Sumerlin BS (2015) Room-Temperature Self-Healing Polymers Based on Dynamic-Covalent Boronic Esters. Macromolecules 48:2098–2106.  
<https://doi.org/10.1021/acs.macromol.5b00210>.

[74] Heleg-Shabtai V, Aizen R, Orbach R, Aleman-Garcia MA, Willner I (2015) Gossypol-Cross-Linked Boronic Acid-Modified Hydrogels: A Functional Matrix for the Controlled Release of an Anticancer Drug. Langmuir 31:2237–2242. <https://doi.org/10.1021/la504959d>.

[75] Chen D, Ren G, Zhao X, Luo J, Wang H, Jia P (2021) A cyclodextrin-phenylboronic acid cross-linked hydrogel with drug hosting, self-healing, and pH-sensitive properties for sustained drug release. New J Chem 45:10711–10717.  
<https://doi.org/10.1039/D1NJ01228B>.

[76] Daniels EL, Runge JR, Oshinowo M, Leese HS, Buchard A (2023) Cross-Linking of Sugar-Derived Polyethers and Boronic Acids for Renewable, Self-Healing, and Single-Ion Conducting Organogel Polymer Electrolytes. ACS Appl Energy Mater 6:2924–2935.  
<https://doi.org/10.1021/acsaem.2c03937>.

[77] Watson JD, Crick FHC (1953) Molecular Structure of Nucleic Acids: A Structure for Deoxyribose Nucleic Acid. Nature 171:737–738.  
<https://doi.org/10.1038/171737a0>.

- [78] Wang JC (1979) Helical repeat of DNA in solution. *Proc Natl Acad Sci USA* 76:200–203. <https://doi.org/10.1073/pnas.76.1.200>.
- [79] Wilkins MHF, Stokes AR, Wilson HR (1953) Molecular Structure of Nucleic Acids: Molecular Structure of Deoxypentose Nucleic Acids. *Nature* 171:738–740. <https://doi.org/10.1038/171738a0>.
- [80] Holmes DS, Bonner J (1974) Sequence composition of rat nuclear deoxyribonucleic acid and high molecular weight nuclear ribonucleic acid. *Biochem* 13:841–848. <https://doi.org/10.1021/bi00702a001>.
- [81] Michelini F, Jaliha AP, Francia S, Meers C, Neeb ZT, Rossiello F, Gioia U, Aguado J, Jones-Weinert C, Luke B, Biamonti G, Nowacki M, Storici F, Carninci P, Walter NG, d’Adda Di Fagagna F (2018) From “Cellular” RNA to “Smart” RNA: Multiple Roles of RNA in Genome Stability and Beyond. *Chem Rev* 118:4365–4403. <https://doi.org/10.1021/acs.chemrev.7b00487>.
- [82] Ghosh A, Bansal M (2003) A glossary of DNA structures from A to Z. *Acta Crystallogr D Biol Crystallogr* 59:620–626. <https://doi.org/10.1107/S0907444903003251>.
- [83] Kanti Si M, Sen A, Ganguly B (2017) Exploiting Hydrogen Bonding Interactions to Probe Smaller Linear and Cyclic Diamines Binding to G-Quadruplexes: A DFT and Molecular Dynamics Study. *Phys. Chem. Chem. Phys.* 19:11474–11484. <https://doi.org/10.1039/C7CP00472A>.
- [84] Nguyen-Hackley DH, Ramm E, Taylor CM, Joung JK, Dervan PB, Pabo CO (2004) Allosteric Inhibition of Zinc-Finger Binding in the Major Groove of DNA by Minor-Groove Binding Ligands. *Biochem* 43:3880–3890. <https://doi.org/10.1021/bi030223c>.
- [85] Rich A, Nordheim A, Wang AH-J (1984) The Chemistry and Biology of Left-handed Z-DNA. *Annu Rev Biochem* 53:791–846. <https://doi.org/10.1146/annurev.bi.53.070184.004043>.

- [86] Ho PS (1994) The non-B-DNA structure of d(CA/TG)<sub>n</sub> does not differ from that of Z-DNA. *Proc Natl Acad Sci USA* 91:9549–9553. <https://doi.org/10.1073/pnas.91.20.9549>.
- [87] Wing R, Drew H, Takano T, Broka C, Tanaka S, Itakura K, Dickerson RE (1980) Crystal structure analysis of a complete turn of B-DNA. *Nature* 287:755–758. <https://doi.org/10.1038/287755a0>.
- [88] Miyoshi D, Nakao A, Sugimoto N (2002) Molecular Crowding Regulates the Structural Switch of the DNA G-Quadruplex. *Biochem* 41:15017–15024. <https://doi.org/10.1021/bi020412f>.
- [89] Dominick PK, Jarstfer MB (2004) A Conformationally Constrained Nucleotide Analogue Controls the Folding Topology of a DNA G-Quadruplex. *J Am Chem Soc* 126:5050–5051. <https://doi.org/10.1021/ja039192z>.
- [90] Fernando H, Rodriguez R, Balasubramanian S (2008) Selective Recognition of a DNA G-Quadruplex by an Engineered Antibody. *Biochem* 47:9365–9371. <https://doi.org/10.1021/bi800983u>.
- [91] Maizels N, Gray LT (2013) The G4 Genome. *PLoS Genet* 9:e1003468. <https://doi.org/10.1371/journal.pgen.1003468>.
- [92] Teng F-Y, Jiang Z-Z, Guo M, Tan X-Z, Chen F, Xi X-G, Xu Y (2021) G-quadruplex DNA: a novel target for drug design. *Cell Mol Life Sci* 78:6557–6583. <https://doi.org/10.1007/s00018-021-03921-8>.
- [93] Johnson FB (2020) Fundamentals of G-quadruplex biology. In: Neidle, S. (eds) *Quadruplex Nucleic Acids as Targets for Medicinal Chemistry. Annual Reports in Medicinal Chemistry*. Elsevier, pp 3–44. (ISBN: 978-0-12-821017-8)
- [94] Brosh RM (2013) DNA helicases involved in DNA repair and their roles in cancer. *Nat Rev Cancer* 13:542–558. <https://doi.org/10.1038/nrc3560>.

- [95] Cheung I, Schertzer M, Rose A, Lansdorp PM (2002) Disruption of dog-1 in *Caenorhabditis elegans* triggers deletions upstream of guanine-rich DNA. *Nat Genet* 31:405–409. <https://doi.org/10.1038/ng928>.
- [96] Besnard E, Babled A, Lapasset L, Milhavet O, Parrinello H, Dantec C, Marin J-M, Lemaitre J-M (2012) Unraveling cell type-specific and reprogrammable human replication origin signatures associated with G-quadruplex consensus motifs. *Nat Struct Mol Biol* 19:837–844. <https://doi.org/10.1038/nsmb.2339>.
- [97] Tuesuwan B, Kern JT, Thomas PW, Rodriguez M, Li J, David WM, Kerwin SM (2008) Simian Virus 40 Large T-Antigen G-Quadruplex DNA Helicase Inhibition by G-Quadruplex DNA-Interactive Agents. *Biochem* 47:1896–1909. <https://doi.org/10.1021/bi701747d>.
- [98] Norseen J, Johnson FB, Lieberman PM (2009) Role for G-Quadruplex RNA Binding by Epstein-Barr Virus Nuclear Antigen 1 in DNA Replication and Metaphase Chromosome Attachment. *J Virol* 83:10336–10346. <https://doi.org/10.1128/JVI.00747-09>.
- [99] De Lange T, Shiue L, Myers RM, Cox DR, Naylor SL, Killery AM, Varmus HE (1990) Structure and variability of human chromosome ends. *Mol Cell Biol* 10:518–527. <https://doi.org/10.1128/MCB.10.2.518>.
- [100] Moyzis RK, Buckingham JM, Cram LS, Dani M, Deaven LL, Jones MD, Meyne J, Ratliff RL, Wu JR (1988) A highly conserved repetitive DNA sequence, (TTAGGG)<sub>n</sub>, present at the telomeres of human chromosomes. *Proc Natl Acad Sci USA* 85:6622–6626. <https://doi.org/10.1073/pnas.85.18.6622>.
- [101] Harley CB, Futcher AB, Greider CW (1990) Telomeres shorten during ageing of human fibroblasts. *Nature* 345:458–460. <https://doi.org/10.1038/345458a0>.

- [102] Allsopp RC, Vaziri H, Patterson C, Goldstein S, Younglai EV, Futcher AB, Greider CW, Harley CB (1992) Telomere length predicts replicative capacity of human fibroblasts. *Proc Natl Acad Sci USA* 89:10114–10118. <https://doi.org/10.1073/pnas.89.21.10114>.
- [103] Shay JW, Bacchetti S (1997) A survey of telomerase activity in human cancer. *Eur J Cancer* 33:787–791. [https://doi.org/10.1016/S0959-8049\(97\)00062-2](https://doi.org/10.1016/S0959-8049(97)00062-2).
- [104] Lipps HJ, Rhodes D (2009) G-quadruplex structures: in vivo evidence and function. *Trends Cell Biol* 19:414–422. <https://doi.org/10.1016/j.tcb.2009.05.002>.
- [105] Aguilera A, García-Muse T (2012) R Loops: From Transcription Byproducts to Threats to Genome Stability. *Molecular Cell* 46:115–124. <https://doi.org/10.1016/j.molcel.2012.04.009>.
- [106] Kim N, Jinks-Robertson S (2012) Transcription as a source of genome instability. *Nat Rev Genet* 13:204–214. <https://doi.org/10.1038/nrg3152>.
- [107] Duquette ML, Handa P, Vincent JA, Taylor AF, Maizels N (2004) Intracellular transcription of G-rich DNAs induces formation of G-loops, novel structures containing G4 DNA. *Genes Dev* 18:1618–1629. <https://doi.org/10.1101/gad.1200804>.
- [108] Duquette ML, Huber MD, Maizels N (2007) G-Rich Proto-Oncogenes Are Targeted for Genomic Instability in B-Cell Lymphomas. *Cancer Research* 67:2586–2594. <https://doi.org/10.1158/0008-5472.CAN-06-2419>.
- [109] Ginno PA, Lott PL, Christensen HC, Korf I, Chédin F (2012) R-Loop Formation Is a Distinctive Characteristic of Unmethylated Human CpG Island Promoters. *Molecular Cell* 45:814–825. <https://doi.org/10.1016/j.molcel.2012.01.017>.
- [110] Bang I. (1910), *Biochem. Z., Untersuchungen über die Guanylsäure*. *Biochemische Zeitschrift*, 26, 293.



- [111] Gellert M, Lipsett MN, Davies DR (1962) Helix Formation by Guanylic Acid. *Proc Natl Acad Sci USA* 48:2013–2018. <https://doi.org/10.1073/pnas.48.12.2013>.
- [112] Chantot JF, Sarocchi M-T, Guschlbauer W (1971) Physico-chemical properties of nucleosides. *Biochimie* 53:347–354. [https://doi.org/10.1016/S0300-9084\(71\)80101-3](https://doi.org/10.1016/S0300-9084(71)80101-3).
- [113] Shi X, Mullaugh KM, Fettinger JC, Jiang Y, Hofstadler SA, Davis JT (2003) Lipophilic G-Quadruplexes Are Self-Assembled Ion Pair Receptors, and the Bound Anion Modulates the Kinetic Stability of These Complexes. *J Am Chem Soc* 125:10830–10841. <https://doi.org/10.1021/ja035267n>.
- [114] Davis JT, Spada GP (2007) Supramolecular architectures generated by self-assembly of guanosine derivatives. *Chem Soc Rev* 36:296–313. <https://doi.org/10.1039/B600282J>.
- [115] Peters GM, Skala LP, Plank TN, Hyman BJ, Manjunatha Reddy GN, Marsh A, Brown SP, Davis JT (2014) A  $G_4 \cdot K^+$  Hydrogel Stabilized by an Anion. *J Am Chem Soc* 136:12596–12599. <https://doi.org/10.1021/ja507506c>.
- [116] Peters GM, Skala LP, Davis JT (2016) A Molecular Chaperone for  $G_4$ -Quartet Hydrogels. *J Am Chem Soc* 138:134–139. <https://doi.org/10.1021/jacs.5b08769>.
- [117] Plank TN, Davis JT (2016) A  $G_4 \cdot K^+$  hydrogel that self-destructs. *Chem Commun* 52:5037–5040. <https://doi.org/10.1039/C6CC01494A>.
- [118] Davis JT (2004) G-Quartets 40 Years Later: From 5'-GMP to Molecular Biology and Supramolecular Chemistry. *Angew Chem Int Ed* 43:668–698. <https://doi.org/10.1002/anie.200300589>.
- [119] Li Y, Su L, Zhang Y, Liu Y, Huang F, Ren Y, An Y, Shi L, Van Der Mei HC, Busscher HJ (2022) A Guanosine-Quadruplex Hydrogel as Cascade Reaction Container Consuming Endogenous Glucose for

Infected Wound Treatment—A Study in Diabetic Mice. *Adv Sci* 9:2103485. <https://doi.org/10.1002/advs.202103485>.

[120] Zhang J, Li X, Sun X, Liu Y, Hao J, Tan Y, Song A (2019) G-Quadruplex based hydrogels stabilized by a cationic polymer as an efficient adsorbent of picric acid. *New J Chem* 43:18331–18338. <https://doi.org/10.1039/C9NJ03143J>.

[121] Hu J, Wang H, Hu Q, Cheng Y (2019) G-quadruplex-based antiviral hydrogels by direct gelation of clinical drugs. *Mater Chem Front* 3:1323–1327. <https://doi.org/10.1039/C9QM00209J>.

[122] Das S, Solra M, Sahoo J, Srivastava A, Fathima S, De M, Rana S (2024) G-Quadruplex Hydrogel-Based Stimuli-Responsive High-Internal-Phase Emulsion Scaffold for Biocatalytic Cascades and Synergistic Antimicrobial Activity. *Chem Mater* 36:759–771. <https://doi.org/10.1021/acs.chemmater.3c02173>.

[123] Yu Y, Nakamura D, DeBoyace K, Neisius AW, McGown LB (2008) Tunable Thermoassociation of Binary Guanosine Gels. *J Phys Chem B* 112:1130–1134. <https://doi.org/10.1021/jp709613p>.

[124] Carducci F, Yoneda JS, Itri R, Mariani P (2018) On the structural stability of guanosine-based supramolecular hydrogels. *Soft Matter* 14:2938–2948. <https://doi.org/10.1039/C8SM00299A>.

[125] Adhikari B, Shah A, Kraatz H-B (2014) Self-assembly of guanosine and deoxy-guanosine into hydrogels: monovalent cation guided modulation of gelation, morphology and self-healing properties. *J Mater Chem B* 2:4802–4810. <https://doi.org/10.1039/C4TB00702F>.

[126] Tang F, Feng H, Du Y, Xiao Y, Dan H, Zhao H, Chen Q (2018) Developing a Self-Healing Supramolecular Nucleoside Hydrogel Based on Guanosine and Isoguanosine. *Chem Asian J* 13:1962–1971. <https://doi.org/10.1002/asia.201800788>.

[127] Zhong R, Tang Q, Wang S, Zhang H, Zhang F, Xiao M, Man T, Qu X, Li L, Zhang W, Pei H (2018) Self-Assembly of Enzyme-Like

Nanofibrous G-Molecular Hydrogel for Printed Flexible Electrochemical Sensors. *Adv Mater* 30:1706887. <https://doi.org/10.1002/adma.201706887>.

[128] Mikhalevich V, Craciun I, Kyropoulou M, Palivan CG, Meier W (2017) Amphiphilic Peptide Self-Assembly: Expansion to Hybrid Materials. *Biomacromole* 18:3471–3480. <https://doi.org/10.1021/acs.biomac.7b00764>.

[129] Li J, Xing R, Bai S, Yan X (2019) Recent advances of self-assembling peptide-based hydrogels for biomedical applications. *Soft Matter* 15:1704–1715. <https://doi.org/10.1039/C8SM02573H>.

[130] Hendricks MP, Sato K, Palmer LC, Stupp SI (2017) Supramolecular Assembly of Peptide Amphiphiles. *Acc Chem Res* 50:2440–2448. <https://doi.org/10.1021/acs.accounts.7b00297>.

[131] Diaferia C, Balasco N, Altamura D, Sibillano T, Gallo E, Roviello V, Giannini C, Morelli G, Vitagliano L, Accardo A (2018) Assembly modes of hexaphenylalanine variants as function of the charge states of their terminal ends. *Soft Matter* 14:8219–8230. <https://doi.org/10.1039/C8SM01441H>.

[132] Wang C, Wang Z, Zhang X (2012) Amphiphilic Building Blocks for Self-Assembly: From Amphiphiles to Supra-amphiphiles. *Acc Chem Res* 45:608–618. <https://doi.org/10.1021/ar200226d>.

[133] Martin AD, Thordarson P (2020) Beyond Fmoc: a review of aromatic peptide capping groups. *J Mater Chem B* 8:863–877. <https://doi.org/10.1039/C9TB02539A>.

[134] Da Silva ER, Walter MNM, Reza M, Castelletto V, Ruokolainen J, Connon CJ, Alves WA, Hamley IW (2015) Self-Assembled Arginine-Capped Peptide Bolaamphiphile Nanosheets for Cell Culture and Controlled Wettability Surfaces. *Biomacromole* 16:3180–3190. <https://doi.org/10.1021/acs.biomac.5b00820>.

- [135] Edwards-Gayle CJC, Castelletto V, Hamley IW, Barrett G, Greco F, Hermida-Merino D, Rambo RP, Seitsonen J, Ruokolainen J (2019) Self-Assembly, Antimicrobial Activity, and Membrane Interactions of Arginine-Capped Peptide Bola-Amphiphiles. *ACS Appl Bio Mater* 2:2208–2218. <https://doi.org/10.1021/acsabm.9b00172>.
- [136] Nieto-Ortega B, Nebot VJ, Miravet JF, Escuder B, Navarrete JTL, Casado J, Ramírez FJ (2012) Vibrational Circular Dichroism Shows Reversible Helical Handedness Switching in Peptidomimetic 1 -Valine Fibrils. *J Phys Chem Lett* 3:2120–2124. <https://doi.org/10.1021/jz300725d>.
- [137] Biswas S, Das AK (2019) Tuning the Handedness: Role of Chiral Component in Peptide-Appended Bolaamphiphile-Based Coassembled Hydrogels. *Langmuir* 35:2383–2391. <https://doi.org/10.1021/acs.langmuir.8b03651>.
- [138] Fleming S, Ulijn RV (2014) Design of nanostructures based on aromatic peptide amphiphiles. *Chem Soc Rev* 43:8150–8177. <https://doi.org/10.1039/C4CS00247D>.
- [139] Kwak J, Park S-I, Lee S-Y (2013) Use of the self-assembly of tyrosine-containing bolaamphiphile molecules as a reactive template for metal deposition. *Colloids Surf B Biointerfaces* 102:70–75. <https://doi.org/10.1016/j.colsurfb.2012.07.038>.
- [140] Zheng C, Lin S, Chen Y, Li Y, Li B, Yang Y (2019) bola -Type Ala–Ala Dipeptides: Odd–Even Effect in Molecular Packing Structures. *Langmuir* 35:11406–11413. <https://doi.org/10.1021/acs.langmuir.9b01241>.
- [141] Chen L, Patrone N, Liang JF (2012) Peptide Self-Assembly on Cell Membranes to Induce Cell Lysis. *Biomacromole* 13:3327–3333. <https://doi.org/10.1021/bm301106p>.
- [142] Yang Z, Liang G, Ma M, Gao Y, Xu B (2007) Conjugates of naphthalene and dipeptides produce molecular hydrogelators with high

efficiency of hydrogelation and superhelical nanofibers. *J Mater Chem* 17:850–854. <https://doi.org/10.1039/B611255B>.

[143] Li M, Liu M, Shang Y, Ren C, Liu J, Jin H, Wang Z (2020) The substitution of a single amino acid with its enantiomer for control over the adjuvant activity of self-assembling peptides. *RSC Adv* 10:13900–13906. <https://doi.org/10.1039/C9RA10325B>.

[144] Rasale DB, Maity I, Konda M, Das AK (2013) Peptide self-assembly driven by oxo-ester mediated native chemical ligation. *Chem Commun* 49:4815. <https://doi.org/10.1039/c3cc41475b>.

[145] Rasale DB, Maity I, Das AK (2012) Emerging  $\pi$ -stacked dynamic nanostructured library. *RSC Adv* 2:9791. <https://doi.org/10.1039/c2ra21334f>.

[146] Rasale DB, Maity I, Das AK (2014) In situ generation of redox active peptides driven by selenoester mediated native chemical ligation. *Chem Commun* 50:11397–11400. <https://doi.org/10.1039/C4CC03835E>.

[147] Rasale DB, Konda M, Biswas S, Das AK (2016) Controlling Peptide Self-Assembly through a Native Chemical Ligation/Desulfurization Strategy. *Chem Asian J* 11:926–935. <https://doi.org/10.1002/asia.201501458>.

[148] Vilaça H, Carvalho A, Castro T, Castanheira EMS, Hilliou L, Hamley I, Melle-Franco M, Ferreira PMT, Martins JA (2023) Unveiling the Role of Capping Groups in Naphthalene N-Capped Dehydrodipeptide Hydrogels. *Gels* 9:464. <https://doi.org/10.3390/gels9060464v>.

[149] Awhida S, Draper ER, McDonald TO, Adams DJ (2015) Probing gelation ability for a library of dipeptide gelators. *J Colloid Interface Sci* 455:24–31. <https://doi.org/10.1016/j.jcis.2015.05.032>.

[150] Gavel PK, Dev D, Parmar HS, Bhasin S, Das AK (2018) Investigations of Peptide-Based Biocompatible Injectable Shape-

Memory Hydrogels: Differential Biological Effects on Bacterial and Human Blood Cells. *ACS Appl Mater Inter* 10:10729–10740. <https://doi.org/10.1021/acsami.8b00501>.

[151] Gavel PK, Kumar N, Parmar HS, Das AK (2020) Evaluation of a Peptide-Based Coassembled Nanofibrous and Thixotropic Hydrogel for Dermal Wound Healing. *ACS Appl Bio Mater* 3:3326–3336. <https://doi.org/10.1021/acsabm.0c00252>.

[152] Sharma P, Kaur H, Roy S (2019) Inducing Differential Self-Assembling Behavior in Ultrashort Peptide Hydrogelators Using Simple Metal Salts. *Biomacromole* 20:2610–2624. <https://doi.org/10.1021/acs.biomac.9b00416>.

[153] Debnath S, Roy S, Abul-Haija YM, Frederix PWJM, Ramalhet SM, Hirst AR, Javid N, Hunt NT, Kelly SM, Angulo J, Khimyak YZ, Ulijn RV (2019) Tunable Supramolecular Gel Properties by Varying Thermal History. *Chemistry A European J* 25:7881–7887. <https://doi.org/10.1002/chem.201806281>.

[154] Criado-Gonzalez M, Wagner D, Rodon Fores J, Blanck C, Schmutz M, Chaumont A, Rabineau M, Schlenoff JB, Fleith G, Combet J, Schaaf P, Jierry L, Boulmedais F (2020) Supramolecular Hydrogel Induced by Electrostatic Interactions between Polycation and Phosphorylated-Fmoc-Tripeptide. *Chem Mater* 32:1946–1956. <https://doi.org/10.1021/acs.chemmater.9b04823>.

[155] Vegners R, Shestakova I, Kalvinsh I, Ezzell RM, Janmey PA (1995) Use of a gel-forming dipeptide derivative as a carrier for antigen presentation. *J Pept Sci* 1:371–378. <https://doi.org/10.1002/psc.310010604>.

[156] Zhang Y, Gu H, Yang Z, Xu B (2003) Supramolecular Hydrogels Respond to Ligand–Receptor Interaction. *J Am Chem Soc* 125:13680–13681. <https://doi.org/10.1021/ja036817k>.

- [157] Adams DJ, Butler MF, Frith WJ, Kirkland M, Mullen L, Sanderson P (2009) A new method for maintaining homogeneity during liquid–hydrogel transitions using low molecular weight hydrogelators. *Soft Matter* 5:1856. <https://doi.org/10.1039/b901556f>.
- [158] Mahler A, Reches M, Rechter M, Cohen S, Gazit E (2006) Rigid, Self-Assembled Hydrogel Composed of a Modified Aromatic Dipeptide. *Adv Mater* 18:1365–1370. <https://doi.org/10.1002/adma.200501765>.
- [159] Jayawarna V, Ali M, Jowitt TA, Miller AF, Saiani A, Gough JE, Ulijn RV (2006) Nanostructured Hydrogels for Three-Dimensional Cell Culture Through Self-Assembly of Fluorenylmethoxycarbonyl–Dipeptides. *Advanced Materials* 18:611–614. <https://doi.org/10.1002/adma.200501522>.
- [160] Jayawarna V, Richardson SM, Hirst AR, Hodson NW, Saiani A, Gough JE, Ulijn RV (2009) Introducing chemical functionality in Fmoc-peptide gels for cell culture. *Acta Biomaterialia* 5:934–943. <https://doi.org/10.1016/j.actbio.2009.01.006>.
- [161] Adhikari B, Banerjee A (2010) Short-Peptide-Based Hydrogel: A Template for the In Situ Synthesis of Fluorescent Silver Nanoclusters by Using Sunlight. *Chemistry A European J* 16:13698–13705. <https://doi.org/10.1002/chem.201001240>.
- [162] Nanda J, Banerjee A (2012)  $\beta$ -Amino acid containing proteolitically stable dipeptide based hydrogels: encapsulation and sustained release of some important biomolecules at physiological pH and temperature. *Soft Matter* 8:3380. <https://doi.org/10.1039/c2sm07168a>.
- [163] Arakawa H, Takeda K, Higashi SL, Shibata A, Kitamura Y, Ikeda M (2020) Self-assembly and hydrogel formation ability of Fmoc-dipeptides comprising  $\alpha$ -methyl-L-phenylalanine. *Polym J* 52:923–930. <https://doi.org/10.1038/s41428-019-0301-5>.

- [164] Basavalingappa V, Guterman T, Tang Y, Nir S, Lei J, Chakraborty P, Schnaider L, Reches M, Wei G, Gazit E (2019) Expanding the Functional Scope of the Fmoc-Diphenylalanine Hydrogelator by Introducing a Rigidifying and Chemically Active Urea Backbone Modification. *Adv Sci* 6:1900218. <https://doi.org/10.1002/advs.201900218>.
- [165] Avinash MB, Govindaraju T (2018) Architectonics: Design of Molecular Architecture for Functional Applications. *Acc Chem Res* 51:414–426. <https://doi.org/10.1021/acs.accounts.7b00434>.
- [166] Ma M, Kuang Y, Gao Y, Zhang Y, Gao P, Xu B (2010) Aromatic–Aromatic Interactions Induce the Self-Assembly of Pentapeptidic Derivatives in Water To Form Nanofibers and Supramolecular Hydrogels. *J Am Chem Soc* 132:2719–2728. <https://doi.org/10.1021/ja9088764>.
- [167] Yao X, Liu Y, Gao J, Yang L, Mao D, Stefanitsch C, Li Y, Zhang J, Ou L, Kong D, Zhao Q, Li Z (2015) Nitric oxide releasing hydrogel enhances the therapeutic efficacy of mesenchymal stem cells for myocardial infarction. *Biomater* 60:130–140. <https://doi.org/10.1016/j.biomaterials.2015.04.046>.
- [168] Jain R, Khandelwal G, Roy S (2019) Unraveling the Design Rules in Ultrashort Amyloid-Based Peptide Assemblies toward Shape-Controlled Synthesis of Gold Nanoparticles. *Langmuir* 35:5878–5889. <https://doi.org/10.1021/acs.langmuir.8b04020>.
- [169] Wang H, Yang C, Tan M, Wang L, Kong D, Yang Z (2011) A structure–gelation ability study in a short peptide-based ‘Super Hydrogelator’ system. *Soft Matter* 7:3897. <https://doi.org/10.1039/c0sm01405b>.
- [170] Liang R, Luo Z, Pu G, Wu W, Shi S, Yu J, Zhang Z, Chen H, Li X (2016) Self-assembled peptide-based supramolecular hydrogel for ophthalmic drug delivery. *RSC Adv* 6:76093–76098. <https://doi.org/10.1039/C6RA11691D>.



- [171] Fleming S, Debnath S, Frederix PWJM, Hunt NT, Ulijn RV (2014) Insights into the Coassembly of Hydrogelators and Surfactants Based on Aromatic Peptide Amphiphiles. *Biomacromole* 15:1171–1184. <https://doi.org/10.1021/bm401720z>.
- [172] Reddy SMM, Dorishetty P, Augustine G, Deshpande AP, Ayyadurai N, Shanmugam G (2017) A Low-Molecular-Weight Gelator Composed of Pyrene and Fluorene Moieties for Effective Charge Transfer in Supramolecular Ambidextrous Gel. *Langmuir* 33:13504–13514. <https://doi.org/10.1021/acs.langmuir.7b03453>.
- [173] Madhu C, Roy B, Makam P, Govindaraju T (2018) Bicomponent  $\beta$ -sheet assembly of dipeptide fluorophores of opposite polarity and sensitive detection of nitro-explosives. *Chem Commun* 54:2280–2283. <https://doi.org/10.1039/C8CC00158H>.
- [174] Maiti B, Bhattacharjee S, Bhattacharya S (2019) Perfluoroarene induces a pentapeptidic hydrotrope into a pH-tolerant hydrogel allowing naked eye sensing of  $\text{Ca}^{2+}$  ions. *Nanoscale* 11:2223–2230. <https://doi.org/10.1039/C8NR08126C>.
- [175] Kim I, Jeong H-H, Kim Y-J, Lee N-E, Huh K, Lee C-S, Kim GH, Lee E (2014) A “Light-up” 1D supramolecular nanoprobe for silver ions based on assembly of pyrene-labeled peptide amphiphiles: cell-imaging and antimicrobial activity. *J Mater Chem B* 2:6478–6486. <https://doi.org/10.1039/C4TB00892H>.
- [176] Balachandra C, Govindaraju T (2020) Cyclic Dipeptide-Guided Aggregation-Induced Emission of Naphthalimide and Its Application for the Detection of Phenolic Drugs. *J Org Chem* 85:1525–1536. <https://doi.org/10.1021/acs.joc.9b02580>.
- [177] Fu Y, Li B, Huang Z, Li Y, Yang Y (2013) Terminal Is Important for the Helicity of the Self-Assemblies of Dipeptides Derived from Alanine. *Langmuir* 29:6013–6017. <https://doi.org/10.1021/la400910g>.

- [178] Restu WK, Nishida Y, Yamamoto S, Ishii J, Maruyama T (2018) Short Oligopeptides for Biocompatible and Biodegradable Supramolecular Hydrogels. *Langmuir* 34:8065–8074. <https://doi.org/10.1021/acs.langmuir.8b00362>.
- [179] Martí-Centelles R, Escuder B (2018) Morphology Diversity of L-Phenylalanine-Based Short Peptide Supramolecular Aggregates and Hydrogels. *ChemNanoMat* 4:796–800. <https://doi.org/10.1002/cnma.201800202>.
- [180] Hu T, Zhang Z, Hu H, Euston SR, Pan S (2020) A Comprehensive Study on Self-Assembly and Gelation of C 13 -Dipeptides—From Design Strategies to Functionalities. *Biomacromole* 21:670–679. <https://doi.org/10.1021/acs.biomac.9b01386>.
- [181] Pelin JNBD, Edwards-Gayle CJC, Castelletto V, Aguilar AM, Alves WA, Seitsonen J, Ruokolainen J, Hamley IW (2020) Self-Assembly, Nematic Phase Formation, and Organocatalytic Behavior of a Proline-Functionalized Lipopeptide. *ACS Appl Mater Inter* 12:13671–13679. <https://doi.org/10.1021/acsami.0c00686>.
- [182] Castelletto V, Edwards-Gayle CJC, Greco F, Hamley IW, Seitsonen J, Ruokolainen J (2019) Self-Assembly, Tunable Hydrogel Properties, and Selective Anti-Cancer Activity of a Carnosine-Derived Lipidated Peptide. *ACS Appl Mater Inter* 11:33573–33580. <https://doi.org/10.1021/acsami.9b09065>.
- [183] Bairagi D, Biswas P, Basu K, Hazra S, Hermida-Merino D, Sinha DK, Hamley IW, Banerjee A (2019) Self-Assembling Peptide-Based Hydrogel: Regulation of Mechanical Stiffness and Thermal Stability and 3D Cell Culture of Fibroblasts. *ACS Appl Bio Mater* 2:5235–5244. <https://doi.org/10.1021/acsabm.9b00424>.
- [184] Zhou S, Hokugo A, McClendon M, Zhang Z, Bakshi R, Wang L, Segovia LA, Rezzadeh K, Stupp SI, Jarrahy R (2019) Bioactive peptide amphiphile nanofiber gels enhance burn wound healing. *Burns* 45:1112–1121. <https://doi.org/10.1016/j.burns.2018.06.008>.

- [185] Godbe JM, Freeman R, Burbulla LF, Lewis J, Krainc D, Stupp SI (2020) Gelator Length Precisely Tunes Supramolecular Hydrogel Stiffness and Neuronal Phenotype in 3D Culture. *ACS Biomater Sci Eng* 6:1196–1207. <https://doi.org/10.1021/acsbiomaterials.9b01585>.
- [186] Nandi N, Gayen K, Ghosh S, Bhunia D, Kirkham S, Sen SK, Ghosh S, Hamley IW, Banerjee A (2017) Amphiphilic Peptide-Based Supramolecular, Noncytotoxic, Stimuli-Responsive Hydrogels with Antibacterial Activity. *Biomacromole* 18:3621–3629. <https://doi.org/10.1021/acs.biomac.7b01006>.
- [187] Kwon H, Brown WE, Lee CA, Wang D, Paschos N, Hu JC, Athanasiou KA (2019) Surgical and tissue engineering strategies for articular cartilage and meniscus repair. *Nat Rev Rheumatol* 15:550–570. <https://doi.org/10.1038/s41584-019-0255-1>.
- [188] Makris EA, Gomoll AH, Malizos KN, Hu JC, Athanasiou KA (2015) Repair and tissue engineering techniques for articular cartilage. *Nat Rev Rheumatol* 11:21–34. <https://doi.org/10.1038/nrrheum.2014.157>.
- [189] Kim IL, Mauck RL, Burdick JA (2011) Hydrogel design for cartilage tissue engineering: A case study with hyaluronic acid. *Biomater* 32:8771–8782. <https://doi.org/10.1016/j.biomaterials.2011.08.073>.
- [190] Shi Y, Hu X, Cheng J, Zhang X, Zhao F, Shi W, Ren B, Yu H, Yang P, Li Z, Liu Q, Liu Z, Duan X, Fu X, Zhang J, Wang J, Ao Y (2019) A small molecule promotes cartilage extracellular matrix generation and inhibits osteoarthritis development. *Nat Commun* 10:1914. <https://doi.org/10.1038/s41467-019-09839-x>.
- [191] Han L, Wang M, Li P, Gan D, Yan L, Xu J, Wang K, Fang L, Chan CW, Zhang H, Yuan H, Lu X (2018) Mussel-Inspired Tissue-Adhesive Hydrogel Based on the Polydopamine–Chondroitin Sulfate Complex for Growth-Factor-Free Cartilage Regeneration. *ACS Appl Mater Inter* 10:28015–28026. <https://doi.org/10.1021/acsami.8b05314>.

- [192] Hua Y, Xia H, Jia L, Zhao J, Zhao D, Yan X, Zhang Y, Tang S, Zhou G, Zhu L, Lin Q (2021) Ultrafast, tough, and adhesive hydrogel based on hybrid photocrosslinking for articular cartilage repair in water-filled arthroscopy. *Sci Adv* 7:eabg0628. <https://doi.org/10.1126/sciadv.abg0628>.
- [193] Bai S, Zhang X, Lv X, Zhang M, Huang X, Shi Y, Lu C, Song J, Yang H (2020) Bioinspired Mineral–Organic Bone Adhesives for Stable Fracture Fixation and Accelerated Bone Regeneration. *Adv Funct Materials* 30:1908381. <https://doi.org/10.1002/adfm.201908381>.
- [194] Huang W, Cheng S, Wang X, Zhang Y, Chen L, Zhang L (2021) Noncompressible Hemostasis and Bone Regeneration Induced by an Absorbable Bioadhesive Self-Healing Hydrogel. *Adv Funct Materials* 31:2009189. <https://doi.org/10.1002/adfm.202009189>.
- [195] Choi S, Lee JS, Shin J, et al (2020) Osteoconductive hybrid hyaluronic acid hydrogel patch for effective bone formation. *J Control Release* 327:571–583. <https://doi.org/10.1016/j.jconrel.2020.09.006>.
- [196] Peressotti S, Koehl GE, Goding JA, Green RA (2021) Self-Assembling Hydrogel Structures for Neural Tissue Repair. *ACS Biomater Sci Eng* 7:4136–4163. <https://doi.org/10.1021/acsbiomaterials.1c00030>.
- [197] Chen C, Tang J, Gu Y, Liu L, Liu X, Deng L, Martins C, Sarmento B, Cui W, Chen L (2019) Bioinspired Hydrogel Electrospun Fibers for Spinal Cord Regeneration. *Adv Funct Materials* 29:1806899. <https://doi.org/10.1002/adfm.201806899>.
- [198] Zhang Y, Li L, Mu J, Chen J, Feng S, Gao J (2020) Implantation of a functional TEMPO-hydrogel induces recovery from rat spinal cord transection through promoting nerve regeneration and protecting bladder tissue. *Biomater Sci* 8:1695–1701. <https://doi.org/10.1039/C9BM01530B>.

- [199] Li L, Zhang Y, Mu J, Chen J, Zhang C, Cao H, Gao J (2020) Transplantation of Human Mesenchymal Stem-Cell-Derived Exosomes Immobilized in an Adhesive Hydrogel for Effective Treatment of Spinal Cord Injury. *Nano Lett* 20:4298–4305. <https://doi.org/10.1021/acs.nanolett.0c00929>.
- [200] Zhou L, Fan L, Yi X, Zhou Z, Liu C, Fu R, Dai C, Wang Z, Chen X, Yu P, Chen D, Tan G, Wang Q, Ning C (2018) Soft Conducting Polymer Hydrogels Cross-Linked and Doped by Tannic Acid for Spinal Cord Injury Repair. *ACS Nano* 12:10957–10967. <https://doi.org/10.1021/acsnano.8b04609>.
- [201] Gong W, Huang H, Wang X, He W, Hu J (2023) Coassembly of Fiber Hydrogel with Antibacterial Activity for Wound Healing. *ACS Biomater Sci Eng* 9:375–387. <https://doi.org/10.1021/acsbiomaterials.2c00716>.
- [202] Liu S, Jiang N, Chi Y, Peng Q, Dai G, Qian L, Xu K, Zhong W, Yue W (2022) Injectable and Self-Healing Hydrogel Based on Chitosan-Tannic Acid and Oxidized Hyaluronic Acid for Wound Healing. *ACS Biomater Sci Eng* 8:3754–3764. <https://doi.org/10.1021/acsbiomaterials.2c00321>.
- [203] Li J, Mooney DJ (2016) Designing hydrogels for controlled drug delivery. *Nat Rev Mater* 1:16071. <https://doi.org/10.1038/natrevmats.2016.71>.
- [204] Biswas A, Ghosh T, Gavel PK, Das AK (2020) PEG Functionalized Stimuli Responsive Self-Healable Injectable Dynamic Imino-boronate G-quadruplex Hydrogel for the Delivery of Doxorubicin. *ACS Appl Bio Mater* 3:1052–1060. <https://doi.org/10.1021/acsabm.9b01034>.
- [205] Ghosh T, Biswas A, Gavel PK, Das AK (2020) Engineered Dynamic Boronate Ester-Mediated Self-Healable Biocompatible G-Quadruplex Hydrogels for Sustained Release of Vitamins. *Langmuir* 36:1574–1584. <https://doi.org/10.1021/acs.langmuir.9b03837>.

[206] Caprioli M, Roppolo I, Chiappone A, Larush L, Pirri CF, Magdassi S (2021) 3D-printed self-healing hydrogels via Digital Light Processing. *Nat Commun* 12:2462. <https://doi.org/10.1038/s41467-021-22802-z>.

[207] Biswas A, Malferrari S, Kalaskar DM, Das AK (2018) Arylboronate esters mediated self-healable and biocompatible dynamic G-quadruplex hydrogels as promising 3D-bioinks. *Chem Commun* 54:1778–1781. <https://doi.org/10.1039/C7CC09051J>.

## **Chapter 2**

### **Synthesis and Structural Studies of Nucleobase Functionalized Hydrogels for Controlled Release of Vitamins**





## 2.1 Introduction

The development of efficient drug delivery systems using biocompatible scaffolds is one of the important research areas in biomedical applications. The drug administration systems often use high doses to achieve therapeutic effectiveness leading to severe side effects in patients and high cost of treatment [1,2]. Therefore, sustain release of drug molecules is vital to maintaining a steady concentration in plasma. This minimizes the chance of drug fluctuation with respect to its maximum safe and minimum effective concentration. In this respect, hydrogels are the most popular choice as the drug carrier due to their favorable physicochemical and biological properties [3]. In literature, numerous polymeric hydrogel-based drug carriers have been reported. In most of these cases, it is observed that the release profile is biphasic in nature [4]. The synthesis and purification of these polymeric compound is a tedious process and batch to batch variation is also observed [5]. Therefore, low molecular weight hydrogels having biodegradable and biocompatible properties are often considered as the effective drug carrier [6]. Nucleobases and amino acids are the basic building-blocks of living organisms enabling self-assembly to create highly ordered and complex structures. The functionalization of the nucleobases with the amino acid generates a new class of nucleobase amino acid conjugate analogs with unique properties. The H-bonding capability of nucleobase makes them an attractive choice in the field of heterocyclic chemistry and biomedicine [7-9]. Bioinspired nucleoside guanosine derived hydrogels are well established in literature [10, 10]. Davis *et al.* reported guanosine boronic acid cross-linked ion selective G-quadruplex (G4) hydrogel where the role of metal ions on the stability was illustrated [12]. Additionally, they explained the stability of G4 in presence of anion and organic dye molecule [13]. A dynamic boronate ester bond between diol of sugar moieties and 1-naphthylboronic acid led to the development of stable G-quadruplex hydrogel [14]. The bioconjugation of a synthesized cytosine functionalized nucleopeptide with Guanine and 4-formylboronic acid resulted into the formation of

an injectable G-quadruplex hydrogel which displayed excellent inherent antibacterial activities [15]. A recent review described the biomedical applications of such dynamic boronate esters cross-linked guanosine-quadruplex hydrogels [16]. The supramolecular functional materials developed via the self-assembly of peptide biomolecules have been studied thoroughly over the past few years [17-19]. The self-assembly of the peptide-based molecules including peptide bolaamphiphiles, aromatic N-terminal capped peptides and short hybrid peptides led to the formation of different varieties of supramolecular nanostructures like vesicle, nanofiber, micelles, nanotubes and ribbons [20-22]. Therefore, these peptide-based supramolecular architectures find promising applications in various fields like drug delivery, cancer therapy and tissue engineering [23-29]. We envisioned the synthesis of an epitope assembled from a nucleobase and amino acid resulting in biomaterial with a unique self-assembling behaviour. Guanine, a purine nucleobase, potentially forms G-quadruplex skeleton in the presence of suitable monovalent alkali metal ions because of the presence of multiple hydrogen bonding donor and acceptor sites. Several reports demonstrate guanine based organo gels, however guanine linked amino acid hydrogels are rare [30,31]. Herein, we have explored the ability of guanine conjugated amino acid towards the formation of stable hydrogel via synergy of their self-assembly properties. We have synthesized nucleobase functionalized molecules using solution-phase synthetic procedure. Phenylalanine has been chosen over other amino acids as it shows greater tendency towards the formation of self-assembled hydrogel [32]. Further, we have introduced a long carbon chain spacer between guanine and L-phenylalanine to modulate the hydrophobicity of the newly designed nucleobase functionalized compounds. Vitamin B<sub>2</sub>, commonly known as riboflavin, is considered an essential vitamin for animals and humans because it constantly supplies energy to the cells and tissues. It also has an important role for the aerobic metabolism of fatty acids and amino acids. A very recent study recommends the daily uptake of vitamin B<sub>2</sub> for the male and female is 1.6 and 1.2 mg, respectively [33-35]. Similarly, vitamin B<sub>12</sub> is also an essential vitamin

of the human system. This vitamin has crucial roles in several biological functions including the synthesis of DNA, prevention of the accumulation of homocysteine, regeneration of methionine for methylation and protein synthesis. The deficiency of vitamin B<sub>12</sub> may cause some severe effects in the human body. The recommended daily uptake of vitamin B<sub>12</sub> is 2.4 µg. Sever deficiency of vitamin B<sub>12</sub> may lead to anemia, neurological disorder, bone loss and inflammation. Therefore, a steady and constant supply of vitamin B<sub>12</sub> are required for the normal functioning of the human body [36, 37]. We also explored the potential application of nucleobase functionalized hydrogel as a drug carrier. Two important vitamins B<sub>2</sub> and B<sub>12</sub> have been incorporated inside the hydrogel matrices. Their spontaneous and sustained release from the hydrogel matrices have been studied under three different pHs at a temperature of 37 °C. The main objectives of the current work include: (a) design and the synthesis of nucleobase functionalized hydrogel and investigate their self-assembling behaviour; (b) thixotropic and injectable nature of the nucleobase functionalized hydrogel; (c) use of the nucleobase functionalized hydrogel as effective drug delivery carrier; (d) evaluation of the proteolytic stability of the nucleobase functionalized hydrogel, and (e) biocompatibility nature of the hydrogel.

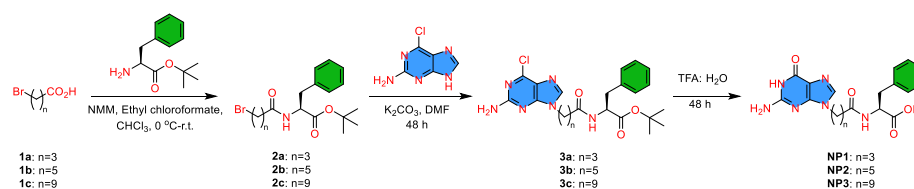
## **2.2 Experimental Section**

### **2.2.1 Materials and Methods**

The used solvents and reagents were purchased from commercially available sources like Alfa Aesar, Sigma Aldrich, Merck and Spectrochem Pvt. Ltd. 2-Amino-6-chloropurine and potassium carbonate (K<sub>2</sub>CO<sub>3</sub>) were obtained from Alfa Aesar. Ethyl chloroformate was purchased from Spectrochem whereas diethyl ether was purchased from Merck. *N*-methyl morpholine was obtained from SRL and 1-bromo decanoic acid, 1-bromo hexanoic acid and 1-bromo butanoic acid were obtained from TCI. L-Phenylalanine *tert*-butyl ester hydrochloride was purchased from Sigma Aldrich. For moisture sensitive reactions, dry solvent was used in the presence of N<sub>2</sub> or Ar gas. After completion of

the reaction, the crude products were purified by column chromatography method using silica as stationary phase and hexane, ethyl acetate or chloroform, methanol as a mobile phase. All  $^1\text{H}$  and  $^{13}\text{C}$  NMR spectra were set down on Bruker Avance (500 MHz) instrument at 25 °C. Mass spectra were set down on Bruker instrument by using ESI positive mode. The NMR spectra of all intermediates and final products were analyzed by using MestReNova software. Chemical shift was expressed in the form of ppm ( $\delta$ ) relative to surplus solvents protons as internal standards (DMSO- $d_6$ :  $\delta$  = 2.50 for  $^1\text{H}$  NMR; DMSO- $d_6$ :  $\delta$  39.50 for  $^{13}\text{C}$  NMR).

## 2.2.2 Synthesis of Compounds



**Scheme 2.1** Synthetic outline of nucleobase amino acid conjugates.

### 2.2.2.1 General Procedure for the Synthesis of 2a-c:

Under argon atmosphere, *N*-methyl morpholine was added in the solution of bromo acids (**1a-c**) in dry chloroform at 0 °C. The solution was left for stirring at this temperature. After 15 min, ethyl chloroformate was added into the solution and stirred vigorously at this temperature for additional 45 min before the addition of L-phenylalanine *tert*-butyl ester. Then the reaction mixture was allowed to stir for 1 h at 0 °C and then at room temperature for 16 h. The progress of the reaction was monitored by TLC. After the completion of the reaction, reaction mixture was diluted with water and washed with 1(N) NaOH (3×10) mL and then with brine, 0.5 (N) HCl (3×10) mL and finally with brine. The organic part was dried over  $\text{Na}_2\text{SO}_4$  and concentrate under vacuum. The product was used without further purification.

#### 2.2.2.2 Synthesis of 2a

The compound **2a** was synthesized as per the above-mentioned general procedure. Yield: 90%.  $^1\text{H}$  NMR (DMSO- $d_6$ , 500 MHz):  $\delta$  1.33 (s, 9H),

1.84-1.97 (m, 2H), 2.10-2.28 (m, 2H), 2.84-2.89 (m, 1H), 2.95-3.00 (m, 1H), 3.52-3.54 (t, 2H,  $J = 5, 5$  Hz), 4.33-4.38 (m, 1H), 7.19-7.29 (m, 5H), 8.28-8.30 (d, 1H,  $J = 10$  Hz).  $^{13}\text{C}$  NMR (DMSO- $d_6$ , 125 MHz):  $\delta$  24.74, 27.46, 28.01, 32.41, 35.22, 35.41, 37.43, 54.38, 80.94, 126.87, 128.58, 129.59, 137.87, 171.34, 172.42. (ESI-MS,  $m/z$ ):  $[\text{M}+\text{Na}]^+$  calculated for  $\text{C}_{17}\text{H}_{24}\text{BrNO}_3\text{Na}$ : 392.094; found 392.0776.

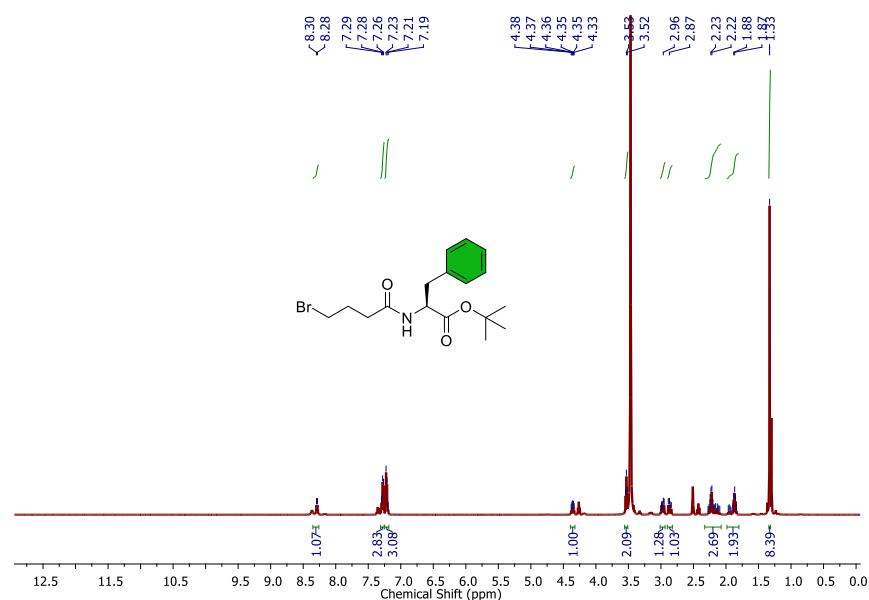


**Figure 2.1**  $^1\text{H}$  NMR (500 MHz, DMSO- $d_6$ ) spectrum of compound 2a.

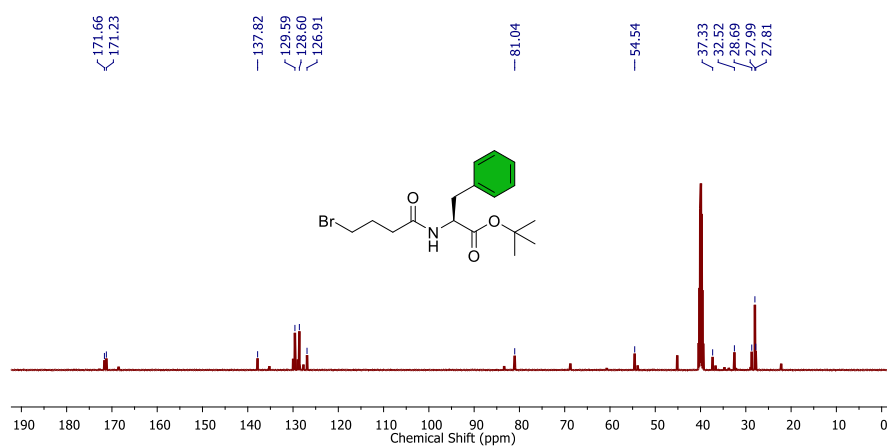


**Figure 2.2**  $^{13}\text{C}$  NMR (125 MHz, DMSO- $d_6$ ) spectrum of compound 2a.

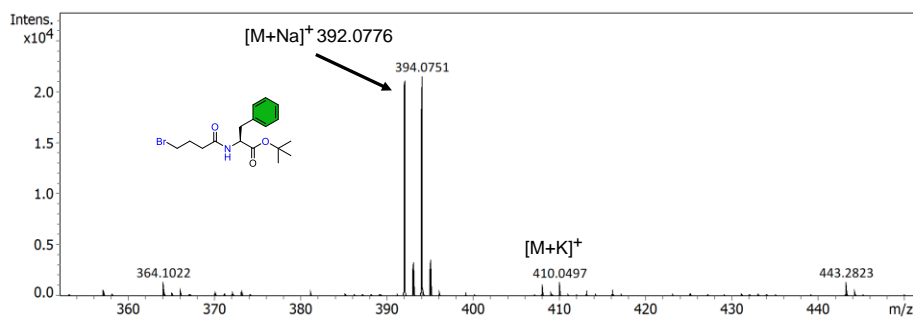


**Figure 2.3** ESI-MS spectrum of compound **2a**.

### 2.2.2.3 Synthesis of **2b**

The compound **2b** was synthesized as per the above-mentioned general procedure. Yield: 85%.  $^1\text{H}$  NMR (DMSO- $d_6$ , 500 MHz):  $\delta$  1.24-1.31 (m, 2H), 1.34 (s, 9H), 1.42-1.48 (m, 2H), 1.76-1.82 (m, 2H), 1.72-1.78 (m, 2H), 2.06-2.09 (m, 2H), 2.84-2.89 (m, 1H), 2.95-2.99 (m, 1H), 3.46-3.49 (t, 2H,  $J = 5, 10$  Hz), 4.35-4.40 (m, 1H), 7.20-7.30 (m, 5H), 8.16-8.17 (d, 1H,  $J = 5$  Hz).  $^{13}\text{C}$  NMR (DMSO- $d_6$ , 125 MHz):  $\delta$  24.74, 27.46, 28.01, 32.41, 35.22, 35.41, 37.43, 54.38, 80.94, 126.87, 128.58, 129.59, 137.87, 172.34, 172.42. (ESI-MS,  $m/z$ ):  $[\text{M}+\text{Na}]^+$  calculated for  $\text{C}_{19}\text{H}_{28}\text{BrNO}_3\text{Na}$  420.1253; found 420.1088.

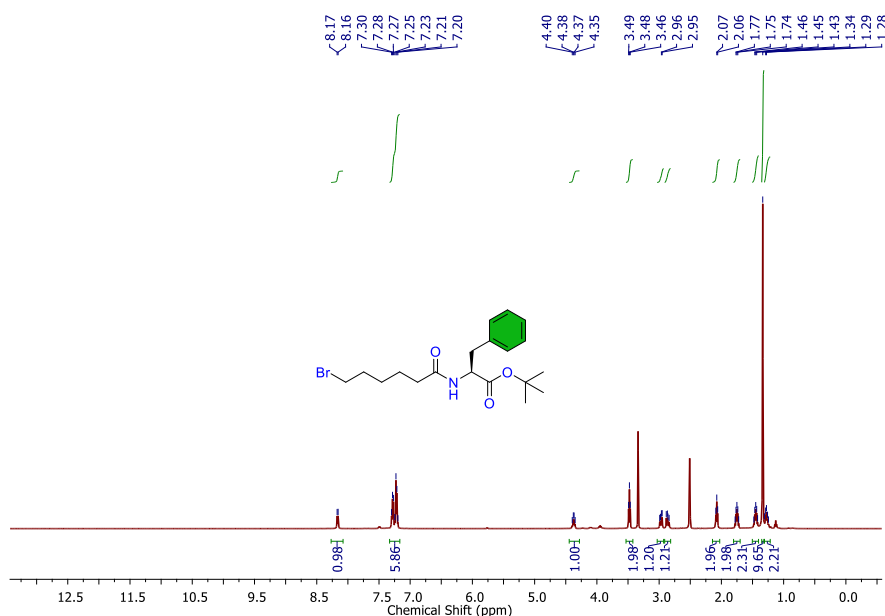


**Figure 2.4**  $^1\text{H}$  NMR (500 MHz, DMSO- $d_6$ ) spectrum of compound **2b**.

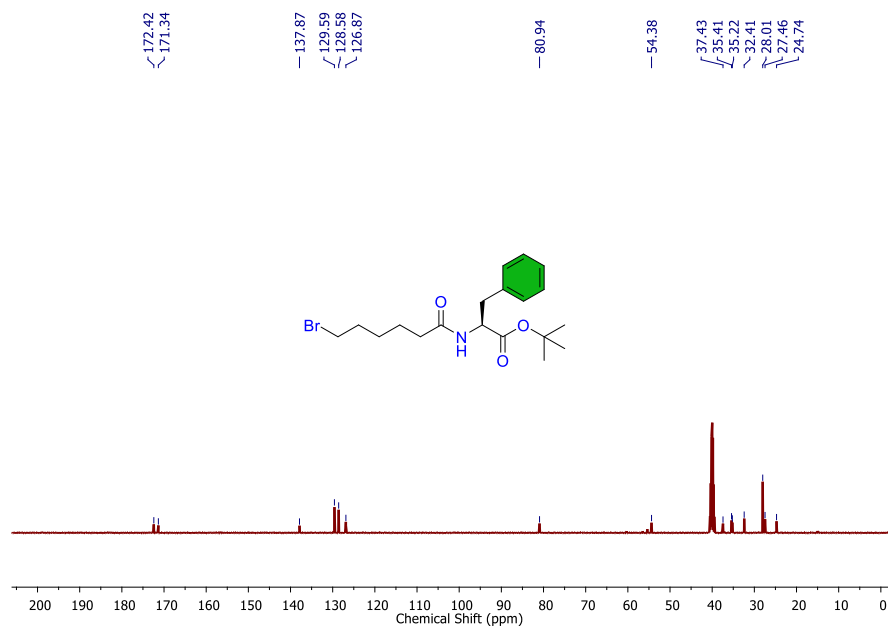


**Figure 2.5** <sup>13</sup>C NMR (125 MHz, DMSO-*d*<sub>6</sub>) spectrum of compound **2b**.

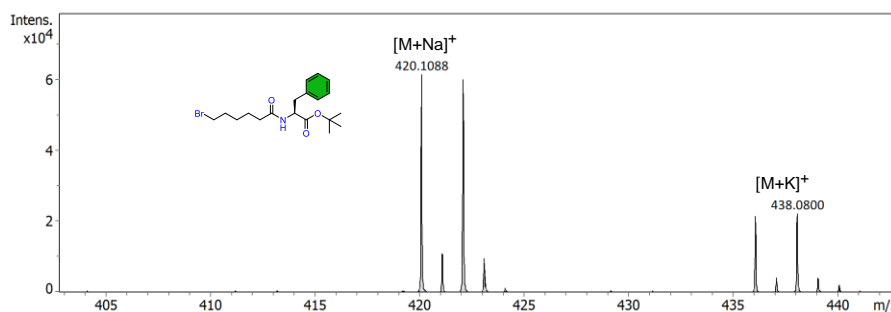


**Figure 2.6** ESI-MS spectrum of compound **2b**.

#### 2.2.2.4 Synthesis of **2c**

The compound **2c** was synthesized as per the above-mentioned general procedure. Yield: 88%. <sup>1</sup>H NMR (DMSO-*d*<sub>6</sub>, 500 MHz):  $\delta$  1.21-1.27 (m, 10H), 1.34 (s, 9H), 1.39-1.43 (m, 2H), 1.76-1.82 (m, 2H), 2.03-2.07 (m, 2H), 2.84-2.88 (m, 1H), 2.95-2.99 (m, 1H), 3.51-3.54 (t, 2H, *J* = 5, 10 Hz), 4.34-4.38 (m, 1H), 7.19-7.29 (m, 5H), 8.12-8.14 (d, 1H, *J* = 10 Hz). <sup>13</sup>C NMR (DMSO-*d*<sub>6</sub>, 125 MHz):  $\delta$  25.65, 28.00, 28.53, 28.87, 29.14, 29.22, 32.72, 35.46, 35.61, 37.39, 54.40, 55.37, 80.88, 126.84, 128.55, 129.57, 137.91, 171.36, 172.61. (ESI-MS, *m/z*): calculated for C<sub>19</sub>H<sub>28</sub>BrNO<sub>3</sub>Na 476.1879 [M+Na]<sup>+</sup>; found 476.1771.

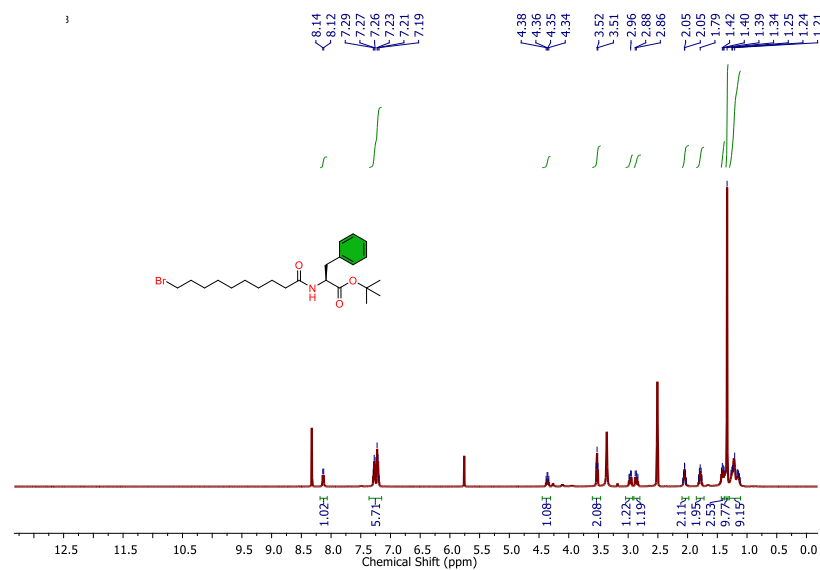


**Figure 2.7** <sup>1</sup>H NMR (500 MHz, DMSO-*d*<sub>6</sub>) spectrum of compound 2c.

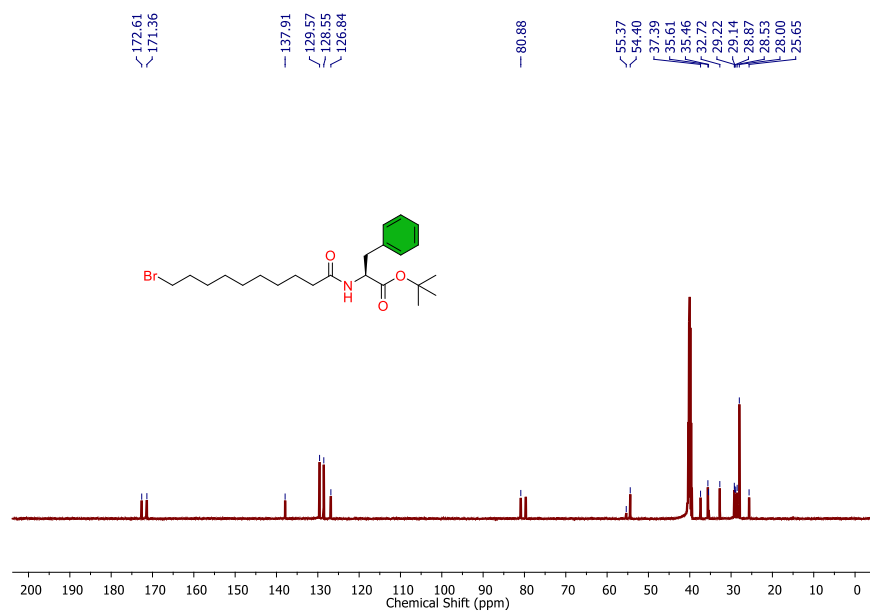


**Figure 2.8** <sup>13</sup>C NMR (125 MHz, DMSO-*d*<sub>6</sub>) spectrum of 2c.

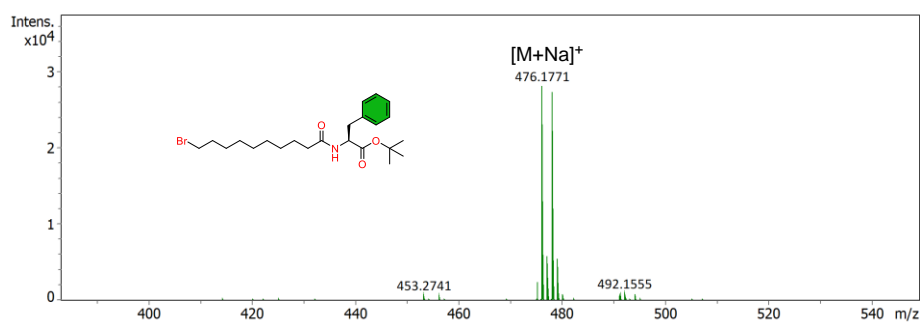


**Figure 2.9** ESI-MS spectrum of compound 2c.



#### 2.2.2.5 General Procedure for the Synthesis of 3a-c:

2-Amino-6-chloropurine was added in the solution of dry DMF (10 mL) under argon atmosphere. Then  $K_2CO_3$  was added in the solution. Finally, bromo acid was added dropwise into the solution and the reaction was left for stirring for 24 h. The progress of the reaction was monitored by TLC. After the completion of the reaction, the reaction mixture was diluted with ethyl acetate and washed with water several times, finally with brine and dried over  $Na_2SO_4$ . After the evaporation of the solvent under rotary evaporator, the reaction mixture was purified by silica gel column chromatography. The major product was N9 alkylated purine product (eluent:  $CHCl_3$ : MeOH = 99:1) and the minor product was N7 alkylated purine product (eluent:  $CHCl_3$ : MeOH = 94:6).

#### 2.2.2.6 Compound 3a:

The compound **3a** was synthesized as per the above-mentioned general procedure. Yield: 65%.  $^1H$  NMR ( $DMSO-d_6$ , 500 MHz):  $\delta$  1.32 (s, 9H), 1.91-1.96 (m, 2H), 2.06-2.09 (m, 2H), 2.83-2.88 (m, 1H), 2.93-2.97 (m, 1H), 3.96-3.99 (t, 2H,  $J = 5, 10$  Hz), 4.34-4.39 (m, 1H), 6.91 (s, 2H) 7.18-7.29 (m, 5H), 8.05 (s, 1H) 8.24-8.26 (d, 1H,  $J = 10$  Hz).  $^{13}C$  NMR ( $DMSO-d_6$ , 125 MHz):  $\delta$  25.45, 27.99, 32.28, 37.41, 43.01, 54.44, 81.07, 123.86, 126.91, 128.61, 129.59, 137.75, 143.72, 149.78, 154.53, 160.22, 171.29, 171.58. (ESI-MS,  $m/z$ ): (ESI-MS,  $m/z$ ):  $[M+Na]^+$  calculated for  $C_{22}H_{27}ClN_6O_3Na$  481.1833; found 481.1728.

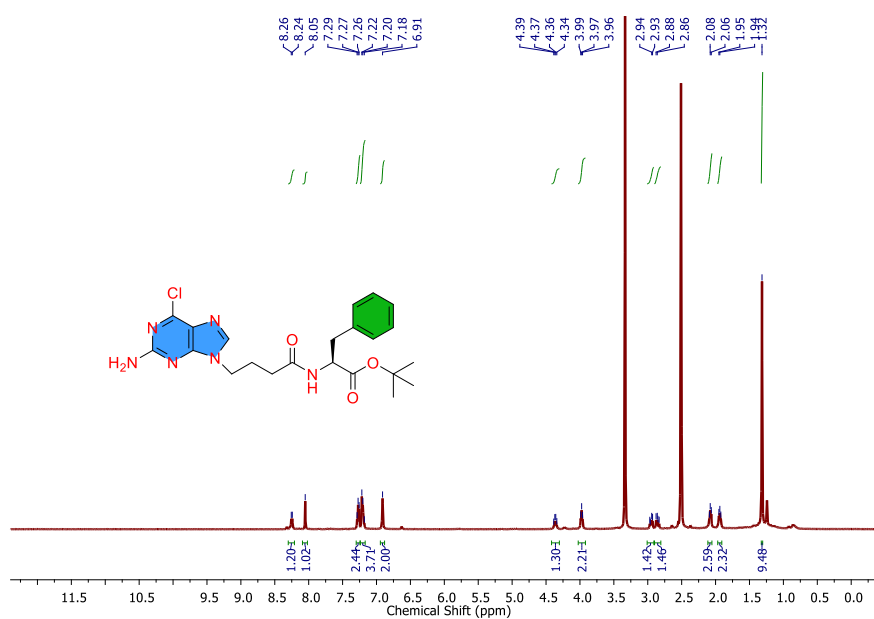


**Figure 2.10** <sup>1</sup>H NMR (500 MHz, DMSO-*d*<sub>6</sub>) spectrum of compound 3a.

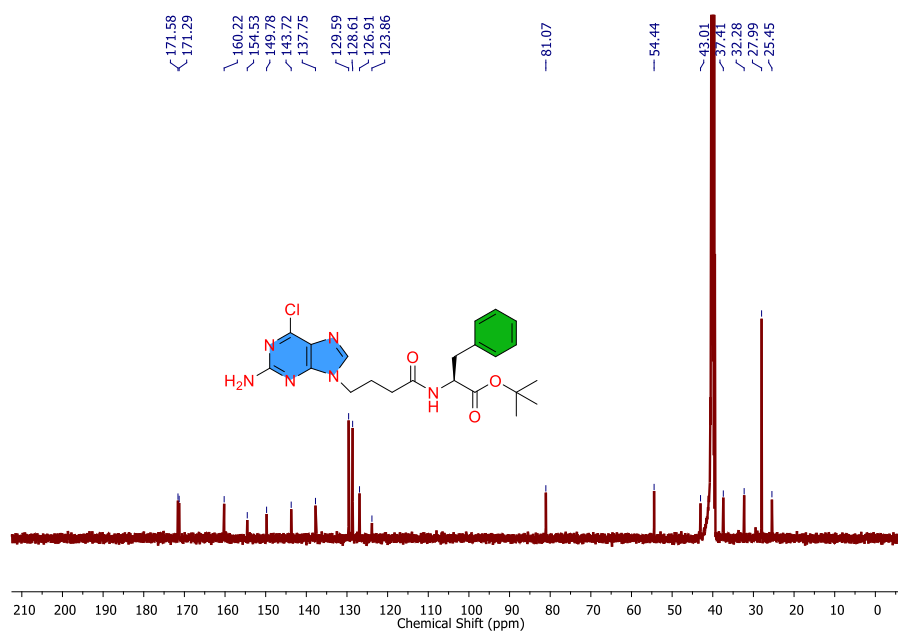


**Figure 2.11** <sup>13</sup>C NMR (125 MHz, DMSO-*d*<sub>6</sub>) spectrum of compound 3a.

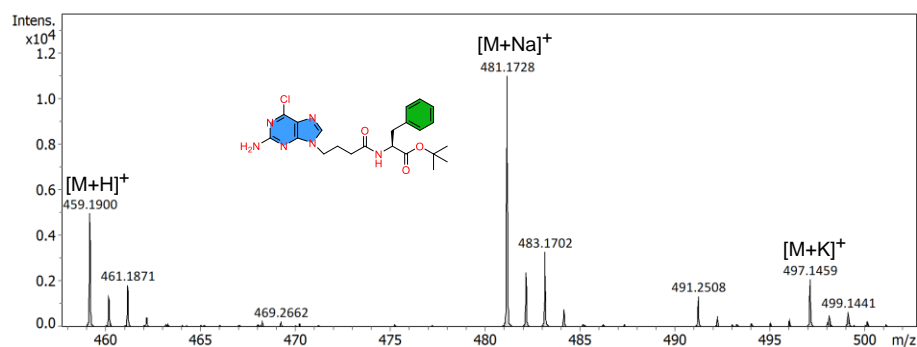


**Figure 2.12** ESI-MS spectrum of compound **3a**.

### 2.2.2.7 Compound **3b**:

The compound **3b** was synthesized as per the above-mentioned general procedure. Yield: 62%.  $^1\text{H}$  NMR (DMSO- $d_6$ , 500 MHz):  $\delta$  1.13-1.18 (m, 2H), 1.31 (s, 9H), 1.43-1.49 (m, 2H), 1.70-1.76 (m, 2H), 2.05-2.08 (m, 2H), 2.82-2.87 (m, 1H), 2.93-2.97 (m, 1H), 3.98-4.01 (dd, 2H,  $J = 5, 10$  Hz), 4.33-4.38 (m, 1H), 6.90 (s, 2H), 7.18-7.28 (m, 5H), 8.12 (s, 1H), 8.13-8.14 (d, 1H,  $J = 5$  Hz),  $^{13}\text{C}$  NMR (DMSO- $d_6$ , 125 MHz):  $\delta$  25.03, 25.89, 27.99, 29.12, 35.19, 37.42, 43.31, 54.37, 80.95, 123.82, 126.88, 128.57, 129.58, 137.83, 143.68, 149.76, 154.52, 160.21, 171.33, 172.45. (ESI-MS,  $m/z$ ):  $[\text{M}+\text{Na}]^+$  calculated for  $\text{C}_{24}\text{H}_{31}\text{ClN}_6\text{O}_3\text{Na}$  509.2146; found 509.2049.

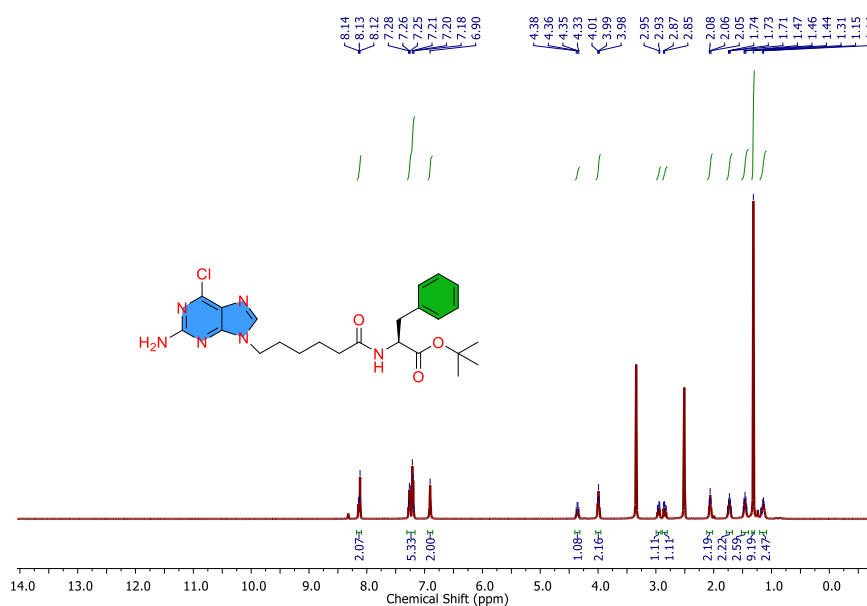


**Figure 2.13**  $^1\text{H}$  NMR (500 MHz, DMSO- $d_6$ ) spectrum of compound **3b**.

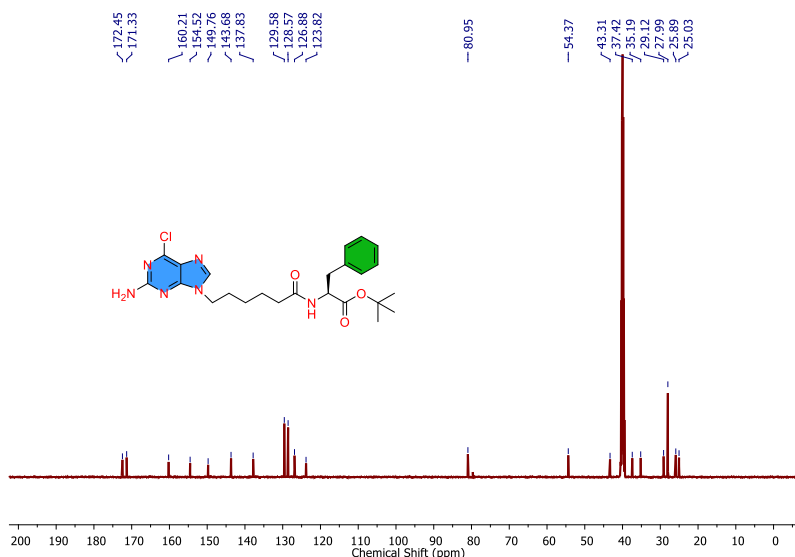


**Figure 2.14**  $^{13}\text{C}$  NMR (125 MHz,  $\text{DMSO}-d_6$ ) spectrum of compound **3b**.

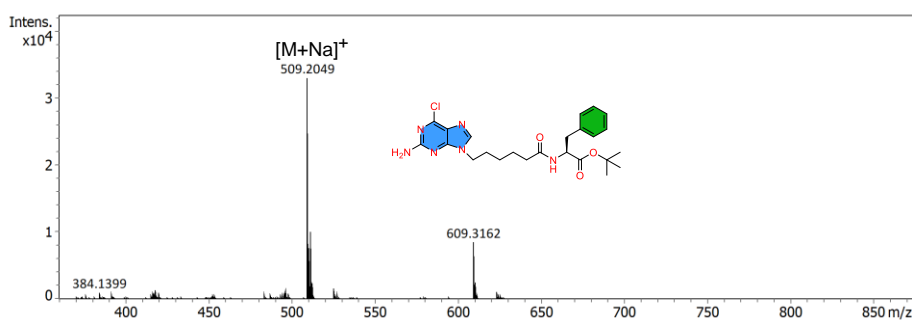


**Figure 2.15** ESI-MS spectrum of compound **3b**.

#### 2.2.2.8 Compound **3c**:

The compound **3c** was synthesized as per the above-mentioned general procedure. Yield: 67%.  $^1\text{H}$  NMR ( $\text{DMSO}-d_6$ , 500 MHz):  $\delta$  1.13-1.24 (m, 10H), 1.32 (s, 9H), 1.38-1.42 (m, 2H), 1.73-1.79 (m, 2H), 2.02-2.05 (m, 2H), 2.83-2.87 (m, 2H), 2.94-2.98 (m, 1H), 4.02-4.05 (t,  $J = 5$ , 10 Hz), 4.33-4.37 (m, 1H), 6.90 (s, 1H), 7.17-7.28 (m, 5H), 8.11-8.13 (d, 1H,  $J = 10$  Hz), 8.14 (s, 1H).  $^{13}\text{C}$  NMR ( $\text{DMSO}-d_6$ , 125 MHz):  $\delta$  25.62, 26.47, 27.99, 28.85, 28.90, 29.12, 29.21, 29.40, 35.45, 37.37, 43.47, 54.39, 80.89, 123.82, 126.83, 128.55, 129.57, 137.90, 143.74, 149.76, 154.54, 160.21, 171.36, 172.61. (ESI-MS,  $m/z$ ):  $[\text{M}+\text{H}]^+$  calculated for  $\text{C}_{28}\text{H}_{40}\text{ClN}_6\text{O}_3$  543.2772; found 543.2615.

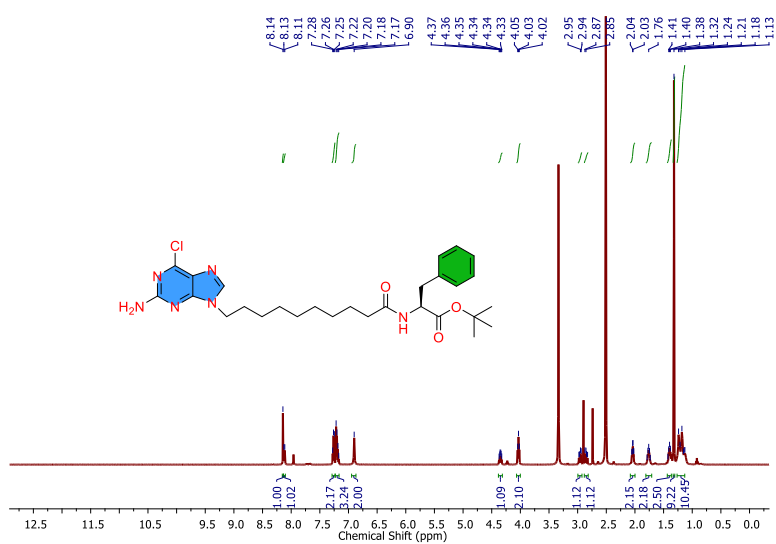


**Figure 2.16**  $^1\text{H}$  NMR (500 MHz,  $\text{DMSO}-d_6$ ) spectrum of compound 3c.

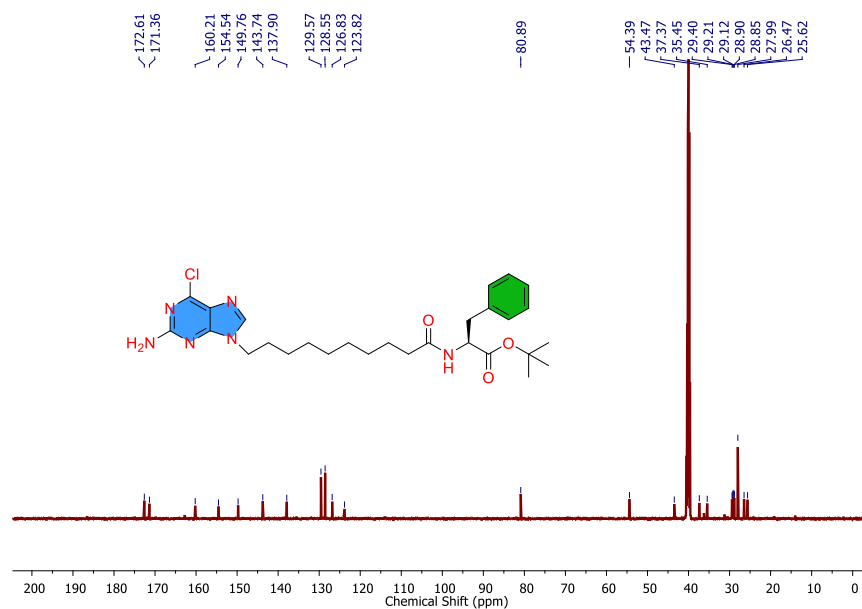


**Figure 2.17**  $^{13}\text{C}$  NMR (125 MHz,  $\text{DMSO}-d_6$ ) spectrum of compound 3c.

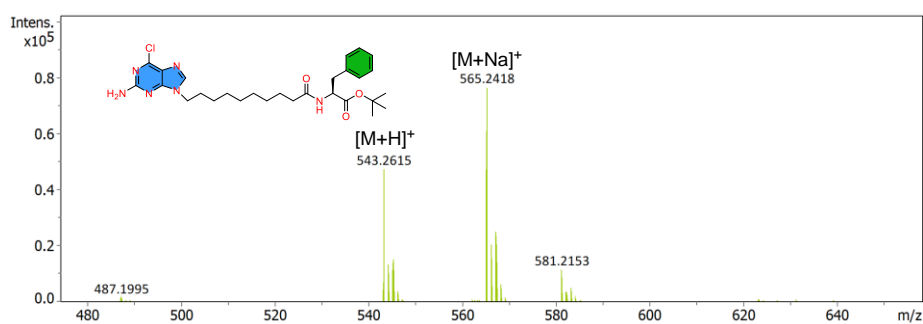


**Figure 2.18** ESI-MS spectrum of compound 3c.

### 2.2.2.9 General Procedure for the Synthesis of Compound NP1-3:

Compounds **3a-c** were dissolved in 5 mL TFA: H<sub>2</sub>O (3:1) solution. Then, the reaction was left for stirring for 48 h at room temperature. The progress of the reaction was monitored by thin layer chromatography (TLC). After the completion of the reaction, TFA was evaporated under vacuum. The reaction was washed with diethyl ether to obtain the white solid.

### 2.2.2.10 Compound NP1:

The compound **NP1** was synthesized as per the above-mentioned general procedure. Yield: 82%. <sup>1</sup>H NMR (DMSO-*d*<sub>6</sub>, 500 MHz):  $\delta$  1.84-1.90 (m, 2H), 2.03-2.09 (m, 2H), 2.81-2.86 (m, 1H), 3.04-3.08 (m, 1H), 3.85-3.87 (t, 2H, *J* = 5, 5 Hz), 4.42-4.46 (m, 1H), 6.57 (s, 2H), 7.17-7.28 (m, 5H), 7.87 (s, 1H), 8.23-8.24 (d, 1H, *J* = 5 Hz), 10.72-10.73 (d, 1H, *J* = 5 Hz), 12.70 (s, 1H). <sup>13</sup>C NMR (DMSO-*d*<sub>6</sub>, 125 MHz):  $\delta$  25.72, 32.26, 37.16, 43.02, 53.79, 115.27, 126.86, 128.62, 129.51, 137.84, 138.14, 151.23, 154.36, 156.59, 171.62, 173.62. (ESI-MS, *m/z*): calculated for [M+H]<sup>+</sup> C<sub>18</sub>H<sub>21</sub>N<sub>6</sub>O<sub>4</sub> 385.1546; found 385.1719.

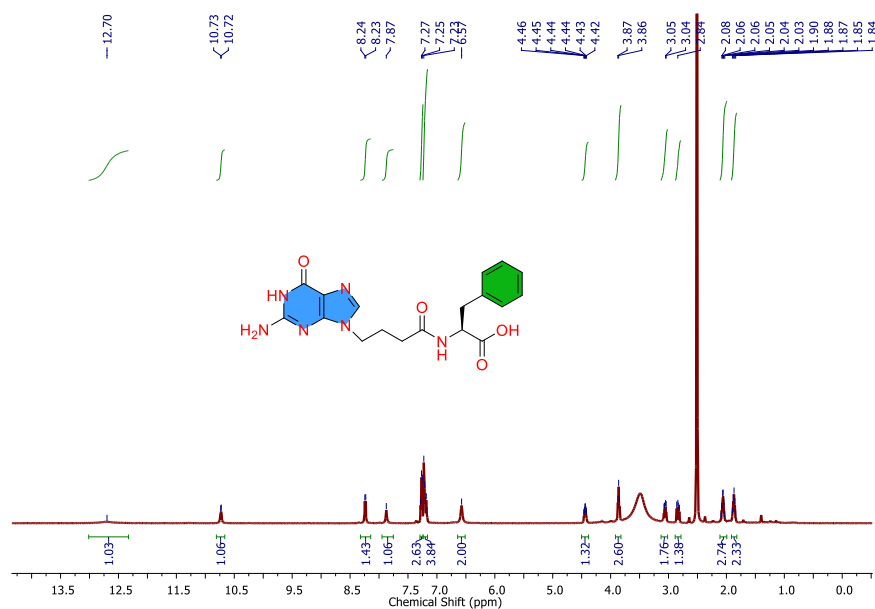


**Figure 2.19** <sup>1</sup>H NMR (500 MHz, DMSO-*d*<sub>6</sub>) spectrum of compound NP1.

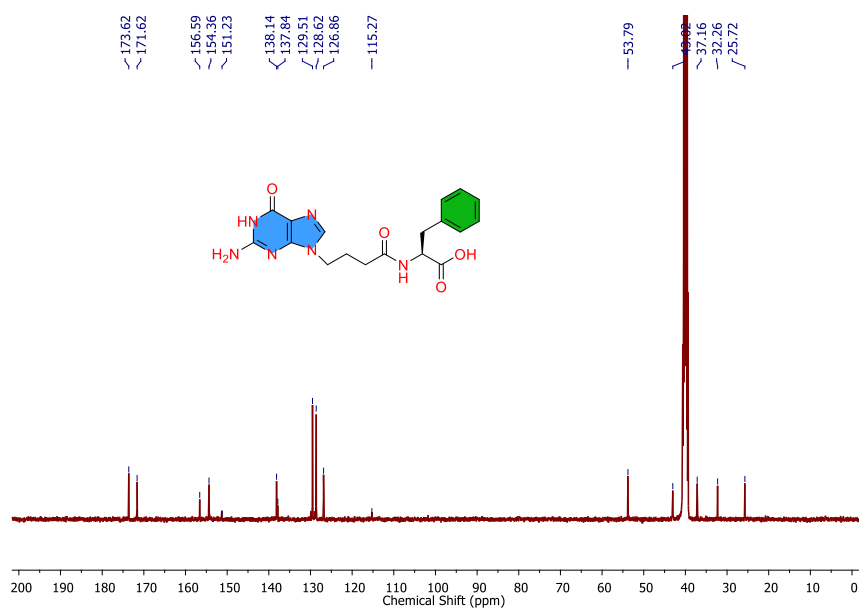


**Figure 2.20** <sup>13</sup>C NMR (125 MHz, DMSO-*d*<sub>6</sub>) spectrum of compound **NP1**.

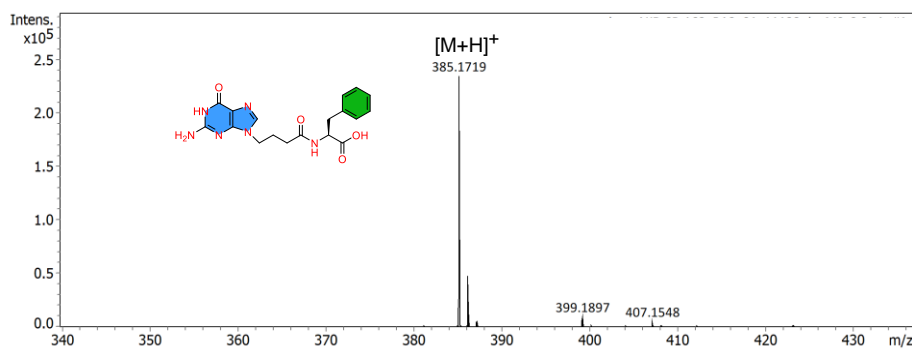


**Figure 2.21** ESI-MS spectrum of compound **NP1**.

### 2.2.2.11 Compound NP2:

The compound **NP2** was synthesized as per the above-mentioned general procedure. Yield: 85%. <sup>1</sup>H NMR (DMSO-*d*<sub>6</sub>, 500 MHz): δ 1.07-1.17 (m, 2H), 1.40-1.46 (m, 2H), 1.68-1.74 (m, 2H), 2.01-2.09 (m, 2H), 2.80-2.85 (m, 1H), 3.04-3.07 (m, 1H), 3.94-3.97 (t, 2H, *J* = 5, 10 Hz), 4.41-4.45 (m, 1H), 6.86 (s, 2H), 7.18-7.28 (m, 5H), 8.12-8.13 (d, 1H, *J* = 5 Hz), 8.50 (s, 1H), 11.15 (s, 1H), 12.67 (s, 1H). <sup>13</sup>C NMR (DMSO-*d*<sub>6</sub>, 125 MHz): 24.95, 25.66, 28.99, 35.19, 37.22, 44.16, 53.72, 111.40, 126.81, 128.57, 129.52, 137.58, 138.20, 150.68, 155.23, 159.08, 172.46,

173.67. (ESI-MS,  $m/z$ ):  $[M+H]^+$  calculated for  $C_{20}H_{23}N_6O_4$  413.1859; found 413.2173.

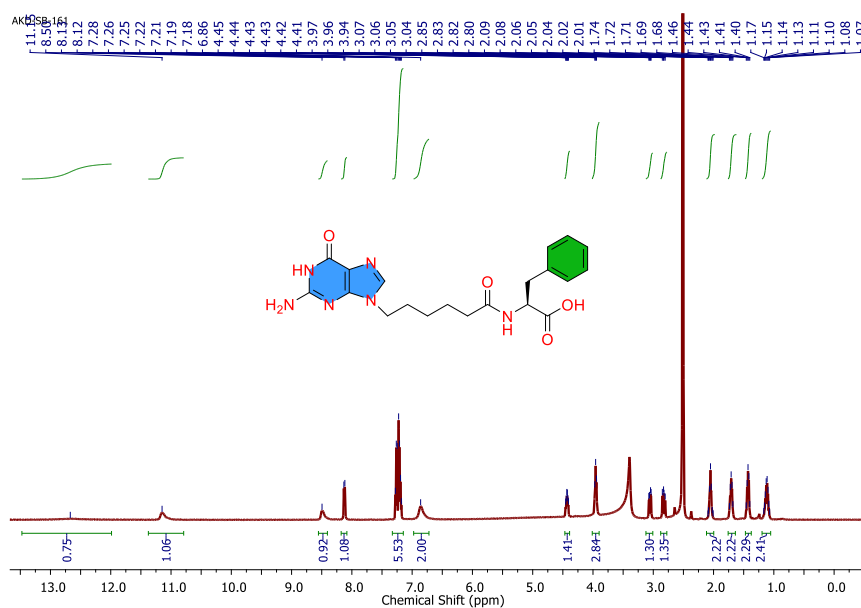


**Figure 2.22** <sup>1</sup>H NMR (500 MHz, DMSO-*d*<sub>6</sub>) spectrum of compound NP2.

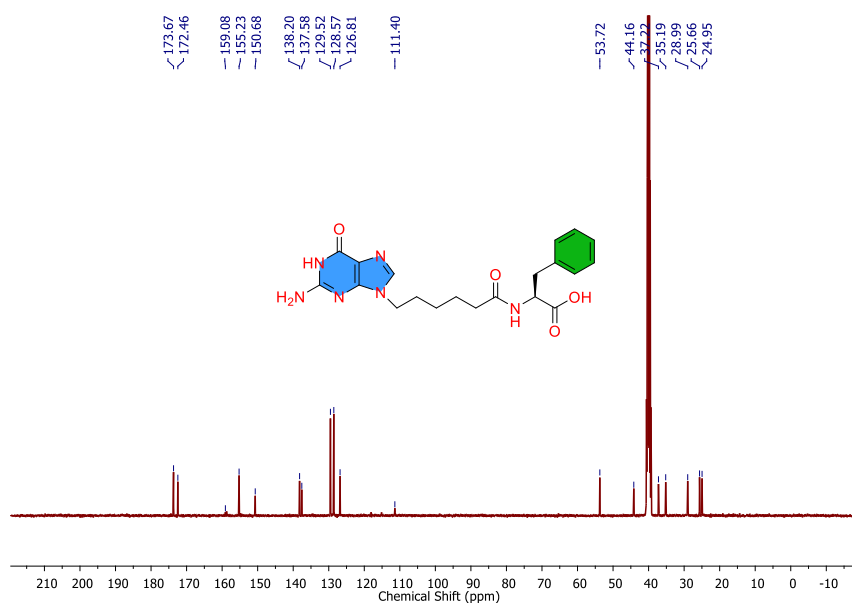


**Figure 2.23** <sup>13</sup>C NMR (125 MHz, DMSO-*d*<sub>6</sub>) spectrum of compound NP2.



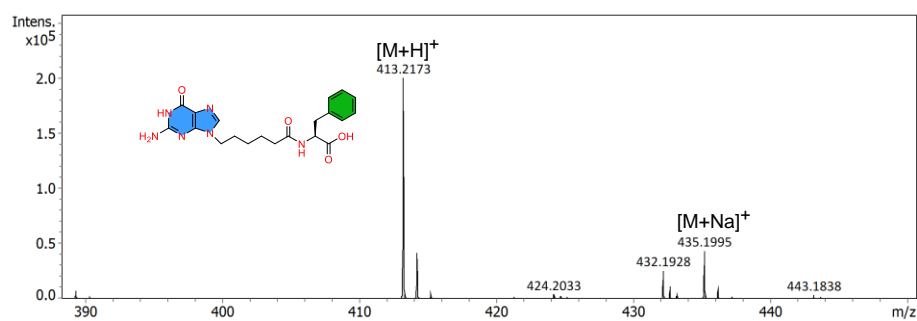


**Figure 2.24** ESI-MS spectrum of compound **NP2**.

### 2.2.2.12 Compound NP3:

The compound **NP3** was synthesized as per the above-mentioned general procedure. Yield: 81%.  $^1\text{H}$  NMR (DMSO- $d_6$ , 500 MHz):  $\delta$  1.08-1.23 (m, 10H), 1.34-1.40 (m, 2H), 1.73-1.78 (m, 2H), 2.01-2.04 (m, 2H), 2.81-2.85 (m, 2H), 3.03-3.07 (m, 1H), 3.96-3.99 (t, 2H,  $J = 5, 10$  Hz), 4.40-4.44 (m, 1H), 6.65 (s, 1H), 7.16-7.27 (m, 5H), 8.08-8.10 (d, 1H,  $J = 10$  Hz), 8.17 (s, 1H) 10.85 (s, 1H) 12.64 (s, 1H).  $^{13}\text{C}$  NMR (DMSO- $d_6$ , 125 MHz): 25.60, 26.33, 28.84, 28.90, 29.14, 29.19, 29.43, 35.51, 37.20, 44.00, 53.70, 113.02, 126.78, 128.55, 129.51, 137.72, 138.25, 150.96, 154.81, 155.80, 172.63, 173.71. (ESI-MS,  $m/z$ ):  $[\text{M}+\text{H}]^+$  calculated for  $\text{C}_{24}\text{H}_{33}\text{N}_6\text{O}_4$  469.2485; found 469.2615.

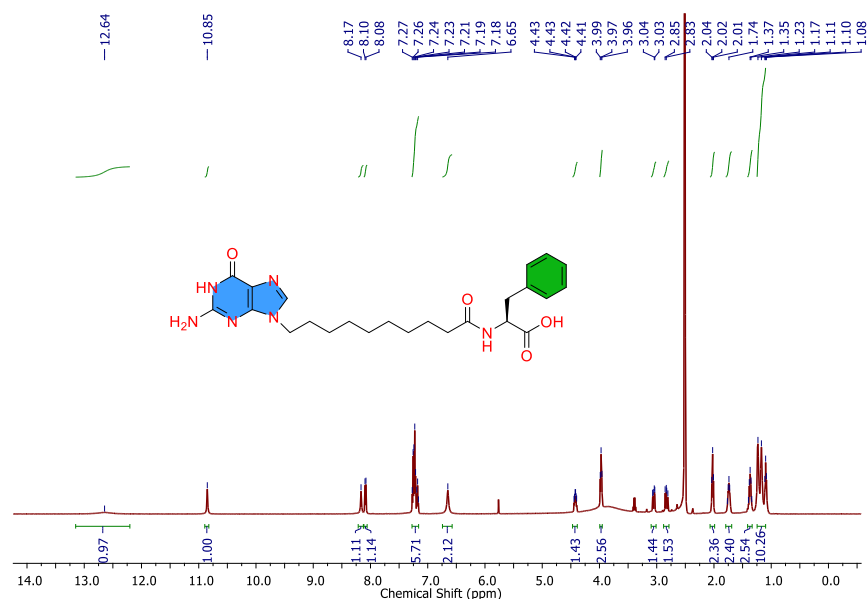


**Figure 2.25**  $^1\text{H}$  NMR (500 MHz, DMSO- $d_6$ ) spectrum of compound **NP3**.

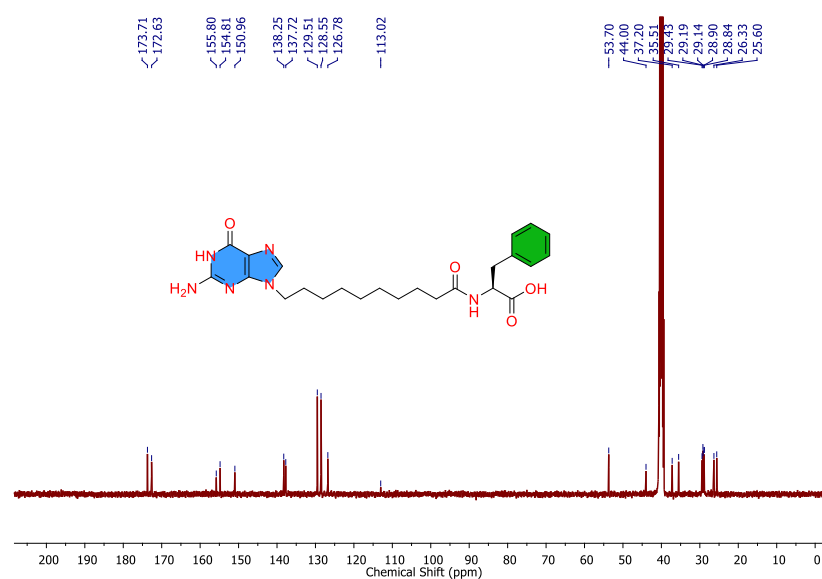


**Figure 2.26**  $^{13}\text{C}$  NMR (125 MHz,  $\text{DMSO}-d_6$ ) spectrum of compound **NP3**.

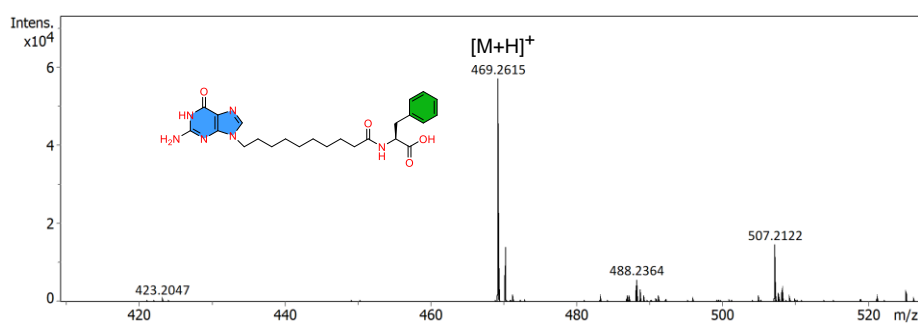


**Figure 2.27** ESI-MS spectrum of compound **NP3**.

### 2.2.3 Preparation of Hydrogel

The synthesized nucleobase functionalized compounds (**NP1**, **NP2** and **NP3**) (30 mM) (see SI for experimental procedure) powders were placed inside a glass vial and solubilized by the addition of 50  $\mu\text{L}$  of KOH (0.5 N) solution, respectively. The complete dissolution of the compounds was achieved by 5 min ultrasonication followed by vortex to mix the compounds appropriately, and the pH of the medium was 10. Dropwise addition of 0.1 N HCl to the solution results in lowering of the pH. Therefore, the clear solution became viscous gradually in 15 min and turned into the hydrogel. The final pH of the hydrogel was 6.8. Among

the synthesized nucleobase amino acid conjugates, only compound **NP3** formed the hydrogel which was confirmed by inverting the vial.

#### **2.2.4 Proteolytic Stability**

The proteolytic stability of the synthesized nucleobase functionalized hydrogel was carried out in the phosphate buffer at the physiological pH 7.4 and temperature 37 °C. The proteolytic stability was checked in the presence of proteinase K and chymotrypsin. The synthesized gel was incubated with enzymes to check the proteolytic stability.

#### **2.2.5 Circular Dichroism Spectroscopy**

The presence of the G-quadruplex structure inside the hydrogel was analysed by circular dichroism (CD) spectrometer (Jasco J-815). The **NP3** hydrogel (30 mmol L<sup>-1</sup>) was diluted to 0.2 mM using double distilled water and the spectra were recorded within the range from 190 to 320 nm. The bandwidth value was set at 1 nm with 0.1 data pitch and scanning speed was set at 20 nm min<sup>-1</sup> and 4 s.

#### **2.2.6 Fluorescence Spectroscopy**

The presence of G-quadruplex structure inside the hydrogel was analyzed by the fluorescence spectroscopy. For this experiment, hydrogel was prepared in a quartz cuvette, and freshly prepared 100 µL of 1 mM ThT solution was added in the hydrogel and kept it under incubation for 4 h. The fluorescence spectra of the ThT incorporated hydrogel were collected on Horiba Scientific spectrophotometer (model no: FluoroMax-4) using a quartz cuvette at 25 °C. The width of the slit was set at 2 nm for the emission spectra and the data pitch value was 1 nm. Emission spectra of the ThT containing hydrogel was recorded at an excitation wavelength of 450 nm and the data range was 460-800 nm.

#### **2.2.7 FT-IR Spectroscopy**

The FT-IR spectrum was recorded for the synthesized nucleobase functionalized amino acid conjugate (**NP3**) and the xerogel of the **NP3**. FT-IR spectrum was recorded through a Bruker (Tensor 27)

spectrophotometer using the KBr pellet. Scan range was between 400 and 4000  $\text{cm}^{-1}$  over 64 scans at a resolution of 4  $\text{cm}^{-1}$  and an interval of 1  $\text{cm}^{-1}$ .

### **2.2.8 X-ray Diffraction (XRD) Measurement**

X-ray diffraction (XRD) pattern of the synthesized nucleobase functionalized amino acid (NP3) and its xerogel were measured using Rigaku Smartlab automated multipurpose X-ray diffractometer with a wavelength of 0.154 nm ( $\text{Cu K}_\alpha$ ) at 25 °C. PXRD analysis of the xerogel was performed by placing the sample on a glass plate.

### **2.2.9 Rheological Behaviour of the Hydrogel**

Viscoelastic characterization of the hydrogel was carried out by rheology. Anton Paar Physica rheometer (model no MCR 301) was used for all rheological experiments. The linear viscoelastic region (LVR) of the synthesized hydrogel was determined by the amplitude sweep experiment at a constant frequency of 10 rad/s. Hydrogel was placed on the rheometer disc by using a micropipette. A parallel plate of diameter 25 mm was used for this experiment. The TruGap was set at 0.5 mm. The mechanical strengths of the hydrogels were determined by frequency sweep experiment. In the frequency sweep experiment, the storage modulus ( $G'$ ) and loss modulus ( $G''$ ) were plotted as a function of frequency. The range of frequency was of 0.1–100  $\text{rad s}^{-1}$ . The thixotropic properties of the synthesized hydrogel were determined by step-strain experiments. Throughout the experiment a constant frequency of 10 rad/s was maintained.

### **2.2.10 Diffusion Ordered NMR Spectroscopy (DOSY)**

Nucleobase amino acid conjugate solutions were prepared in  $\text{D}_2\text{O}$  at 10 mM concentration of the synthesized NPs as a compromise between solubility and NMR signal intensity. DOSY spectra were acquired at 500 MHz using a Bruker Avance 600 spectrometer using the Bruker pulse program ledbpgp2s at 298 K.

### **2.2.11 Morphological Study of the Hydrogel**

Morphological characterization of the hydrogel was carried out using various microscopic techniques such as SEM, AFM and TEM. SEM images of the hydrogel were captured using Zeiss field emission scanning electron microscope (model no Supra55 Zeiss). For the FE-SEM experiment, 50  $\mu\text{L}$  of the hydrogels was taken in an Eppendorf, and diluted with 100  $\mu\text{L}$  of water. Then it was crushed finely with a gel crusher and finally, 10  $\mu\text{L}$  of diluted hydrogel (10 mM) was placed on a glass slide. The samples were dried under air and finally in a vacuum. The samples were coated with gold for imaging. TEM images were snapped with a JEOL microscope (model: JEM-2100). The operating voltage was set at 200 kV and a field-emission gun transmission electron microscope (model: Tecnai G2, F30) was operated at a voltage of 300 kV. Hydrogel (50  $\mu\text{L}$ ) was dissolved in 450  $\mu\text{L}$  of water, and the dilute solution of the hydrogels (3 mM) was dried on carbon-coated copper grids (300 mesh) by slow evaporation in air and then allowed to dry separately under reduced pressure at room temperature. The nanostructural morphology of hydrogels was analyzed by TEM experiments using 3% phosphotungstic acid as a negative stain. AFM study was performed by drop casting of 20  $\mu\text{L}$  of the hydrogel solution over a mica and allowed it to dry in air at room temperature. The hydrogel solution was prepared by dissolving 50  $\mu\text{L}$  of the hydrogel (1.5 mM) in 950  $\mu\text{L}$  of the water. AFM images were recorded in tapping mode on a Park systems (NX 10) AFM instrument.

### **2.2.12 HPLC Analysis**

HPLC grade acetonitrile and water were used without further purification. The dynamic reaction mixture was characterized by reverse phase symmetry C18 column (250 x 4.6 cm, 5  $\mu\text{m}$  particle size). UV-Vis absorbance was monitored at 254 nm. Separations were achieved by running the column with acetonitrile-water as eluent at a flow rate of 1  $\text{ml min}^{-1}$  at 25  $^{\circ}\text{C}$ . The sample preparation involved mixing of 20  $\mu\text{L}$  of hydrogelator solution with acetonitrile. The samples were then filtered

through a 0.45  $\mu\text{m}$  syringe filter (Whatman, 150 units, 13 mm diameter, 2.7 mm pore size) prior to injection. A 20  $\mu\text{L}$  of sample was injected into a Dionex Acclaim ® 120 C 18 column of 250 mm length with an internal diameter of 4.6 mm and 5  $\mu\text{m}$  fused silica particles at a flow rate of 1  $\text{mL min}^{-1}$ .

### 2.2.13 Drug Release Study

To study the diffusion mediated vitamin release from the G-quadruplex hydrogels, the vitamin containing hydrogel was prepared in a 5 mL clean vial. Phosphate buffer solution (1 mL, 50 mM, pH = 7.4) was added to the above hydrogel as a diffusion media. An aliquot (200  $\mu\text{L}$ ) of the diffusion media were pulled out from the externally added upper solution, initially at 15 min interval then 30 min and finally at 5 h interval. The absorption of the collected aliquot was taken on a Jasco V750 UV-vis spectrophotometer. An equal volume of fresh phosphate buffer solution (200  $\mu\text{L}$ , 50 mM, pH 7.4) was added to maintain the total volume constant. The cumulative amount ( $M_t$ ) of the entrapped vitamin, releases from the hydrogel network at a specific time  $t$ , was estimated according to the following equation,

$$M_t = C_t V + \sum C_{t-1} V_s$$

where  $C_t$  denotes the release amount of vitamin molecules at a particular time  $t$ , while  $V$  denotes the total volume including hydrogel as well as diffusion media and  $V_s$  is the volume that pulled out at different time intervals.

The cumulative percentages of the released vitamins were estimated according to the following equation.

$$M_{t\%} = \frac{M_t}{M_{total}}$$

where  $M_{t\%}$  denotes the percentage of vitamin release from the gel matrix,  $M_t$  denotes the amount of released vitamins at time  $t$ ,  $M_{total}$  is the total amount of the loaded vitamin in the hydrogel matrix.

#### **2.2.14 Preparation of Vitamin Loaded Hydrogel**

Vitamins B<sub>2</sub> and B<sub>12</sub> were encapsulated into the hydrogel matrix (30 mM, 1 mL), respectively. To formulate vitamin loaded hydrogel, first the respective vitamins were dissolved in D.I. water (2 mg/mL) to prepare the vitamin solutions. Then, small aliquots (150 µL) of the above-mentioned vitamin solutions were mixed with the gelator solution during the preparation of the hydrogel to formulate the vitamin loaded hydrogel. During gelation, the final concentrations of the vitamins B<sub>2</sub> and B<sub>12</sub> were 0.3 mg/mL and 0.2 mg/mL, respectively.

#### **2.2.15 Cell Viability**

The *in vitro* cytotoxicity of the nucleobase amino acid conjugated hydrogel was evaluated by MTT assay. The human embryonic kidney 293 (HEK 293) and breast cancer cell lines (MCF-7) were used for the MTT assay.

**2.2.16 Live and Dead Cell Imaging** Biocompatibility of the NP3 hydrogel toward MCF-7 cell line was determined by the Live/Dead assay. In the 24-well plate, ~250 cells/well were seeded. This plate was incubated for 24 h. After that, the gel was placed within cells and incubated at 37 °C for 24 h in the presence of 5% CO<sub>2</sub>. On the next day, the hydrogel and the DMEM media were removed. Then, the cells were stained with hoechst (5 µg/mL) and propidium iodide (PI, 3 µg/mL) at 37 °C for 30 min, respectively. Post incubation, the cells were washed with phosphate-buffered saline (PBS) and Live/Dead images were captured with Fluoview FV100 (OLYMPUS, Tokyo, Japan) confocal microscope. For imaging, the 405 nm laser was used for hoechst, and 559 nm laser was used for PI.

#### **2.2.17 Statistical Analyses**

The biological data are shown as mean ± standard error of the mean. <sup>#</sup>p < 0.05; as compared to the control group. The data were analyzed by one-way ANOVA (nonparametric), using a Graph Pad Prism (GraphPad, San Diego, CA).

## 2.3 Results and Discussion

We have prepared three guanine functionalized molecules (**NP1**, **NP2** and **NP3**) using a conventional solution-phase synthetic procedure (see SI **Scheme S1**). The newly synthesized nucleobase amino acid conjugates were found to be insoluble in water. Therefore, the synthesized **NP**'s were dissolved in ultrapure water by basification of the medium with the gradual addition of 0.5 M KOH to reach pH 10. Next, the pH of the medium was reduced to 7 by the slow addition of 0.1 M HCl solution over a period of 15 min. During this process, it is noteworthy that only **NP3** formed self-supported hydrogel and was assigned as **NP3** hydrogel. The prepared **NP3** hydrogel was stable upto 4 weeks. The minimum gelation concentration (MGC) of the hydrogel is 30 mM. The final pH of the hydrogel was 6.8. In case of **NP1** and **NP2**, precipitation was observed instead of hydrogelation (**Figure 22.8a**) at a concentration of 35 mM which was above the MGC. The overall gelation studies clearly reveal that the size of long aliphatic carbon chain had a direct impact in the formation of the hydrogel. The ClogP values of **NP1**, **NP2** and **NP3** are calculated as -0.159, 0.324 and 2.44, respectively [38,39]. Therefore, the introduction of the long fatty acid chain increases the hydrophobicity of the synthesized nucleobase amino acid conjugates.



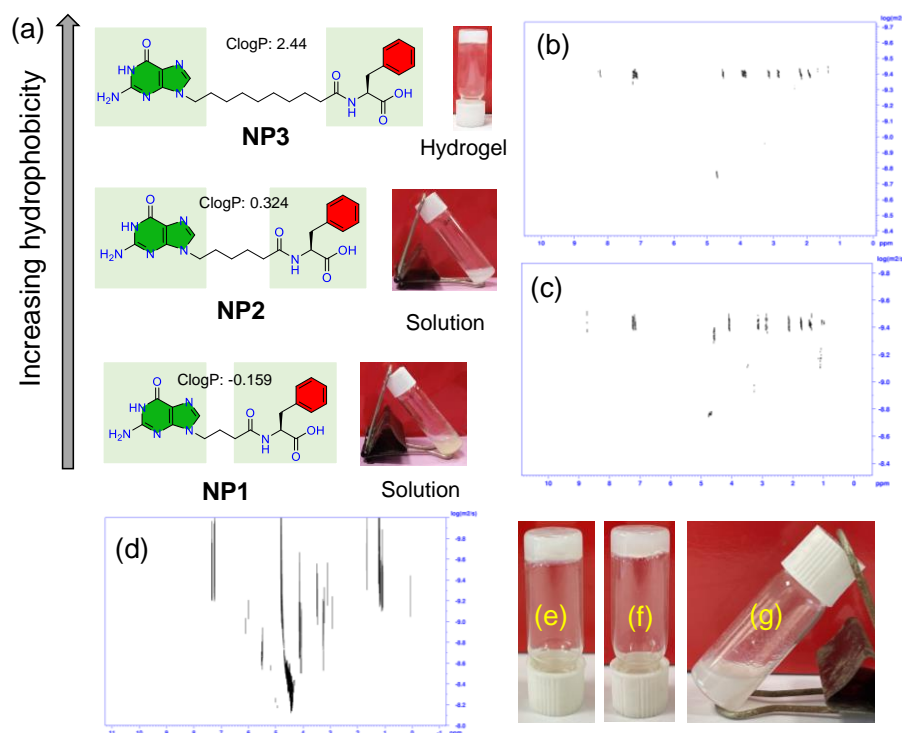
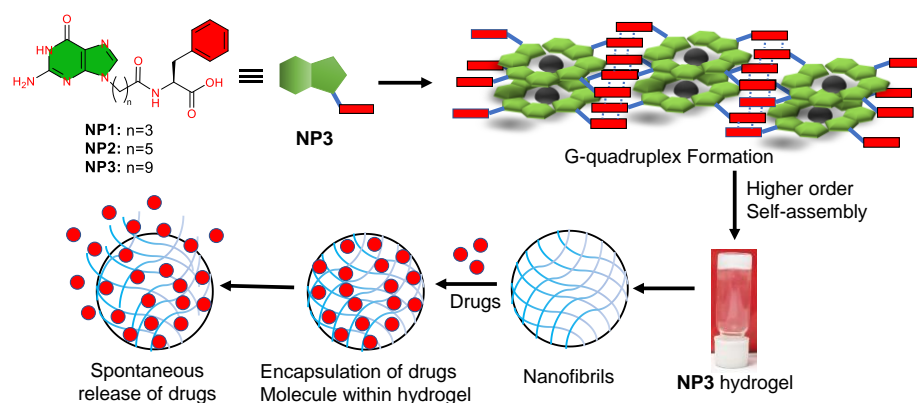


**Figure 2.28** (a) The increasing hydrophobicity in the synthesized nucleobase peptide conjugated molecule induces proper hydrophilic and hydrophobic which in turn leads to the formation of the hydrogel. DOSY NMR spectrum of 10 mM (b) **NP1**, (c) **NP2** and, (d) **NP3** in  $D_2O$  at 298K. Optical images of **NP3** hydrogel formed in (e) LiOH and (f) NaOH. (g) Precipitation was observed when prepared with KCl (100 mM) solution.

Therefore, **NP1** and **NP2** are more hydrophilic in comparison with **NP3**. In **NP3**, the hydrophobicity and hydrophilicity are properly balanced which resulted in the formation of the stable **NP3** hydrogel. Clearly, the C9 lipid chain positioned between nucleobase and amino acid appears to be a crucial factor in driving the gelation of **NP3**. The diffusion ordered NMR spectra (DOSY) were recorded for the synthesized **NP**'s to get further insight into the supramolecular aggregation propensity [40]. DOSY is used to estimate the diffusion coefficient of the aggregates by the Stokes-Einstein equation. Diffusion coefficient ( $D$ ,  $10^{-10} \text{ m}^2 \text{ s}^{-1}$ ) for the aromatic protons of the phenyl moieties of the **NP1**, **NP2** and **NP3** are 4.035, 3.635 and 0.01178, respectively. Thus, showing

greater affinity of the **NP3** towards aggregation (**Figure 2.28b-d**). It is noteworthy to mention that guanine moiety often forms a self-assembled G-quadruplex structure through the H-bonding and  $\pi$ - $\pi$  stacking interaction in the presence of suitable monovalent metal cations [41,42]. Therefore, the role of alkali metal cations in stabilizing the G-quadruplex was also evaluated by preparing the hydrogel in presence of NaOH or LiOH. It was observed that weak hydrogels were formed in both solutions (**Figure 2.28e-g**) [44-46]. Perhaps the ionic radii of  $\text{Li}^+$  and  $\text{Na}^+$  ions are too small to fit appropriately within the pocket of G-quadruplex to furnish a strong gel. The formation of strong and stable hydrogel with alkali metal cation  $\text{K}^+$  supports the presence of the Hoogsteen-like H-bonding interactions among the guanine base to stabilize the G-quartet framework [47,48]. The  $\pi$ - $\pi$  stacking interaction among the monovalent alkali metal cation-based G-quartet motif and the phenyl moieties results in columnar structure which in turn forms the supramolecular nanofibrous stiffer G-quadruplex hydrogel (**Scheme 2.2**).



**Scheme 2.2** Graphical illustration demonstrating the development of **NP3** hydrogel with the support of suitable monovalent alkali metal ion and the utilization of hydrogel to study the release of vitamins from the hydrogel matrices.

The formation of stronger hydrogel in the presence of monovalent alkali metal ion  $\text{K}^+$  indicates the cation selective behavior of the **NP3** hydrogel. Additionally, the length of the hydrophobic carbon chain has a

significant contribution in stabilizing the **NP3** hydrogel [49,50]. These factors jointly have an important role in the formation of stable nanofibrous hydrogel.

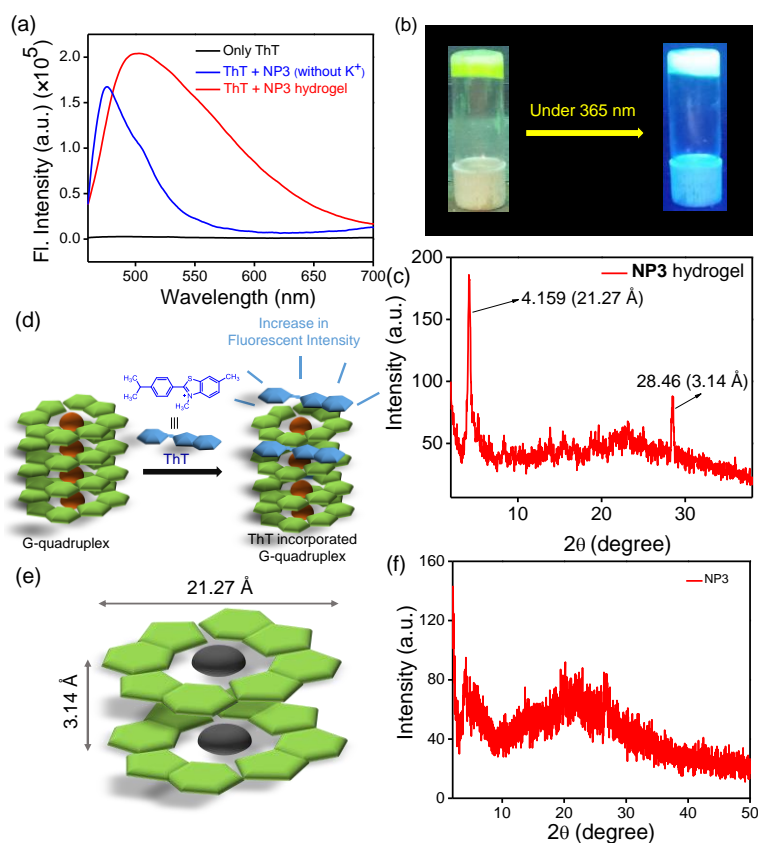


**Figure 2.29** (a) Fluorescence spectra of ThT solution (black line), ThT loaded **NP3** without K<sup>+</sup> (blue line) and ThT loaded **NP3** hydrogel (in presence of K<sup>+</sup>) (red line). (b) Optical photographs of ThT loaded **NP3** hydrogel under daylight (left) and under 365 nm UV light (right). (c) Plausible mechanism of enhancement of fluorescence intensity in presence of ThT. (d) Wide angle powder X-ray diffraction pattern of the **NP3** xerogel. (e) Graphical presentation of the G-quadruplex showing the distance between two consecutive stacked G-quartet and the width of the quartet. (f) Wide angle PXRD spectrum of **NP3**.

The presence of the G-quadruplex structure within the hydrogel was studied by using Thioflavin T binding assay. Thioflavin T, a cationic dye is generally used to recognize the presence of the most important secondary structure of DNA. The cationic fluorogenic dye, thioflavin T

(ThT) intercalates in between the G-quartet planes, which subsequently increases the fluorescence intensity [51,52]. Therefore, in our hydrogel system, we incorporated ThT solution (0.1 mM) during the hydrogel preparation and studied the corresponding emissive behavior of the ThT-incorporated G-quadruplex **NP3** hydrogel. The fluorescence spectrum of ThT-loaded **NP3** hydrogel exhibited an intense emission maximum at 498 nm upon excitation at 450 nm. However, the bare ThT solution displays a very weak fluorescence at 483 nm upon excitation at 450 nm (**Figure 2.29a**). We also recorded the fluorescence of ThT incorporated **NP3** solution (no metal ions). The fluorescence spectrum of ThT incorporated **NP3** solution (no metal ions) shows an emission peak at 476 nm. The significant change of intensity and shift in emission maxima in comparison to the bare ThT and ThT incorporated **NP3** (no metal ions) in fluorescence spectrum is attributed to the intercalation of the ThT molecules within the stacked G-quartet layer formed by the guanine moiety in the **NP3** in the presence of  $K^+$  ions (**Figure 2.29b**). Therefore, Thioflavin T binding experiment shows the significance of  $K^+$  ions in the formation of the G-quadruplex. The optical images of the ThT incorporated hydrogel were captured under day light and under UV light. This observation also demonstrated the enhancement of fluorescence intensity under UV light after the addition of ThT (**Figure 2.29c**). Therefore, the ThT binding fluorescence assay revealed the presence of G-quartet-like stacked assembly inside the **NP3** hydrogel. The wide-angle powder X-ray diffraction (PXRD) experiment also favored the presence of G-quadruplex like assembly inside the hydrogel. In this assay, the lyophilized **NP3** hydrogel powder was used. The PXRD of the **NP3** hydrogel also supported G-quadruplex structure. The PXRD spectra showed a sharp peak at  $2\theta = 4.159^\circ$  corresponding to the distance ( $d = 21.27 \text{ \AA}$ ) of width of a G-quartet unit. Further, the Bragg diffraction peak at  $2\theta = 28.46^\circ$  corresponds to the  $d$  value  $3.14 \text{ \AA}$ , which refers to the  $\pi$ - $\pi$  stacking distance among two consecutive stacked G-quartets moieties (**Figure 2.29d, e**) [53,54]. We also performed wide angle PXRD of the **NP3** powder. However, no prominent peaks were found in the above-mentioned region (**Figure 2.29f**). Therefore, the

wide angle PXRD experiments confirmed the existence of the G-quadruplex like structure inside the **NP3** hydrogel state.

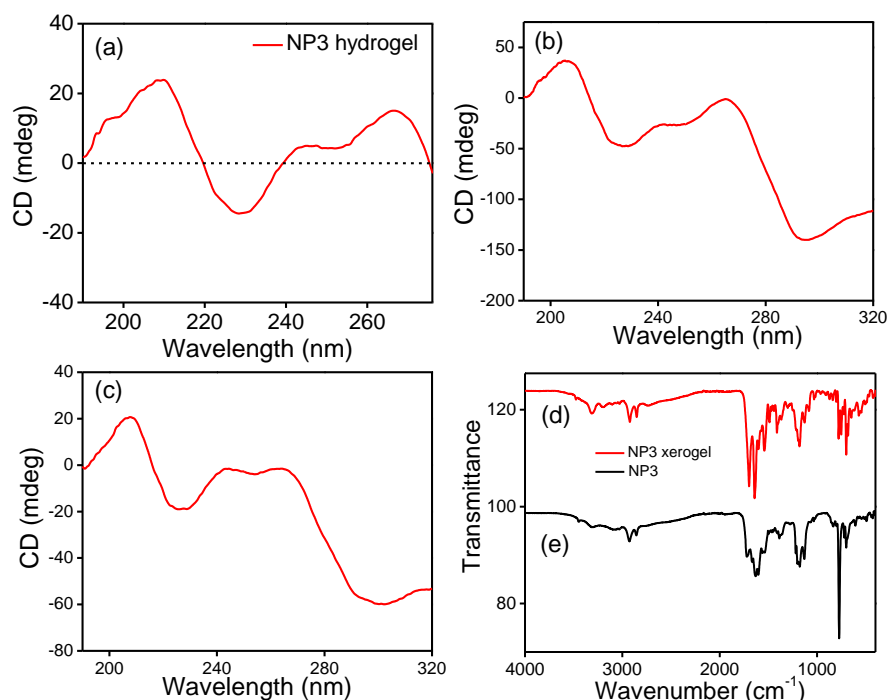


**Figure 2.30** (a) CD spectrum of the **NP3** hydrogel (0.2 mM). Circular dichroism spectra of the **NP3** hydrogel prepared with (b) NaOH and (c) LiOH. FT-IR spectra of (d) **NP3** compound and (e) xerogel of **NP3**.

The CD spectrum for the **NP3** hydrogel was taken in the range between 190-290 nm [55]. The spectrum for the **NP3** hydrogel showed a positive absorption peak at 260 nm in addition with a negative absorption peak at 230 nm, indicating the parallel G-quartet topology inside the **NP3** hydrogel (**Figure 2.30a**) [56]. The sequential positive and negative peaks appeared because of  $\pi$ - $\pi$  stacking interaction among the G-quartet moiety. In addition, there was another peak at 208 nm indicating the  $n$ - $\pi^*$  transition in the phenyl moiety [57,58]. Further, the role of monovalent alkali metal cations in the formation of G-quartet hydrogel were also confirmed by using the CD spectroscopy. The hydrogel was prepared using NaOH and LiOH solutions and the CD spectra were recorded in both the cases. The peak at 260 nm becomes flattened for both ions (**Figure 2.30b, c**) [59]. Hence,  $\text{Li}^+$  and  $\text{Na}^+$  ions could not stabilize the G-quartet framework which resulted in a weak hydrogel.

Hence, the CD spectra confirmed the presence of  $K^+$  ion stabilized G-quartet type framework inside the **NP3** hydrogel. Fourier-transform infrared spectroscopy (FTIR) experiment was carried out to characterize nucleobase functionalized amino acid conjugated G-quadruplex hydrogel. The  $-C=O$  stretching frequency for the amide bond in guanine moiety of the **NP3** is observed at  $1722\text{ cm}^{-1}$ . The amide N-H bending and stretching peaks appear at  $1561\text{ cm}^{-1}$ ,  $1537\text{ cm}^{-1}$  and  $3318\text{ cm}^{-1}$ ,  $3450\text{ cm}^{-1}$ , respectively (**Figure 2.30d**) [23,25]. However, in **NP3** xerogel, the  $-C=O$  stretching frequency of the amide bond of the guanine moiety appeared at  $1699\text{ cm}^{-1}$  indicating the presence of H-bonding interaction with the metal ion in the quadruplex structure (**Figure 2.30e**).

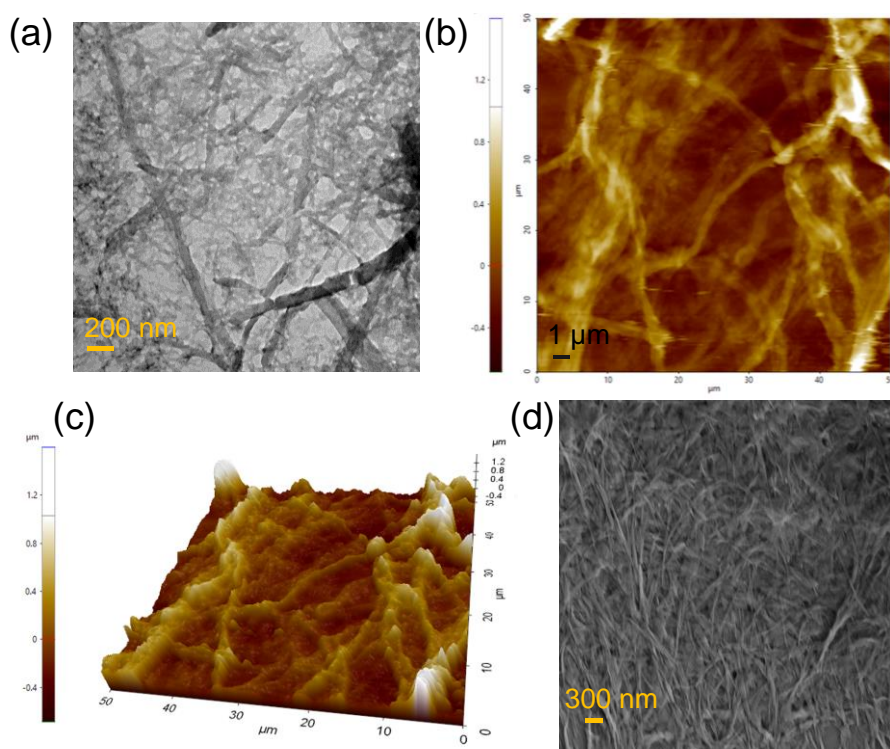


**Figure 2.31** (a) TEM image shows the presence of nanofibrillar morphology inside the **NP3** hydrogel. (b) AFM image also reveals nanofibrillar morphology in the hydrogel state. (c) AFM 3D height profile image of **NP3** hydrogel. (d) SEM image of **NP3** hydrogel.

The self-assembled morphology inside the nucleobase functionalized amino acid conjugated **NP3** hydrogel was investigated by several microscopic techniques such as high-resolution transmission electron

microscopy (HR-TEM), atomic force microscopy (AFM) and field emission scanning electron microscopy (FESEM) [60]. The HR-TEM images of the **NP3** hydrogel confirm the existence of several thicker fibers with an average width of 44 nm fibers along with the thinner fibers of an average width of 18.57 nm (**Figure 2.31a**). Therefore, the HR-TEM images demonstrated the co-existence of dense nanofibrillar morphology inside the hydrogel matrices. The AFM images of the **NP3** hydrogel also suggested the presence of nanofibrillar morphology inside the **NP3** hydrogel (**Figure 2.31b and c**). Further, the FE-SEM images of the **NP3** hydrogel support both the observation obtained from TEM and AFM analysis. The SEM image also revealed the presence of nanofibrillar morphology inside the hydrogel (**Figure 2.31d**). The SEM image showed the average width of thick and thin nanofibers was 48 and 20 nm, respectively. Therefore, all the microscopic techniques SEM, TEM and AFM display the presence of nanofibrillar networks inside the gel which lead to the formation of **NP3** hydrogel. Therefore, the presence of dense twisted chains of nanofiber entrapped water molecules to form a cage-like structure assisting in the formation of self-assembled hydrogel. The rheological experiments were conducted to analyze the viscoelastic nature of the **NP3** hydrogel [61-63]. At first, amplitude sweep test was executed to know the zone where deformation occurs. In this experiment, the magnitude of the applied shear strain was changed at a fixed frequency ( $10 \text{ rad s}^{-1}$ ). The variation of storage modulus ( $G'$ ) and loss modulus ( $G''$ ) values are constant at a lower strain ( $<5\%$ ). Therefore, amplitude sweep experiment shows the unperturbed nature of the hydrogel state at lower strain where hydrogel state was retained. However, the storage modulus ( $G'$ ) gradually decreased with increase in shear strain ( $>10\%$ ) indicating transformation of hydrogel state to the sol state (**Figure 2.32a**). The frequency sweep test was performed at a fixed strain of 1% over the frequency range of 100 to  $0.1 \text{ rad s}^{-1}$ . During the entire analysis, the  $G'$  values were consistently greater than the values of  $G''$  suggesting the formation of solid-like viscoelastic nature of the **NP3** hydrogel (**Figure 2.32b**).

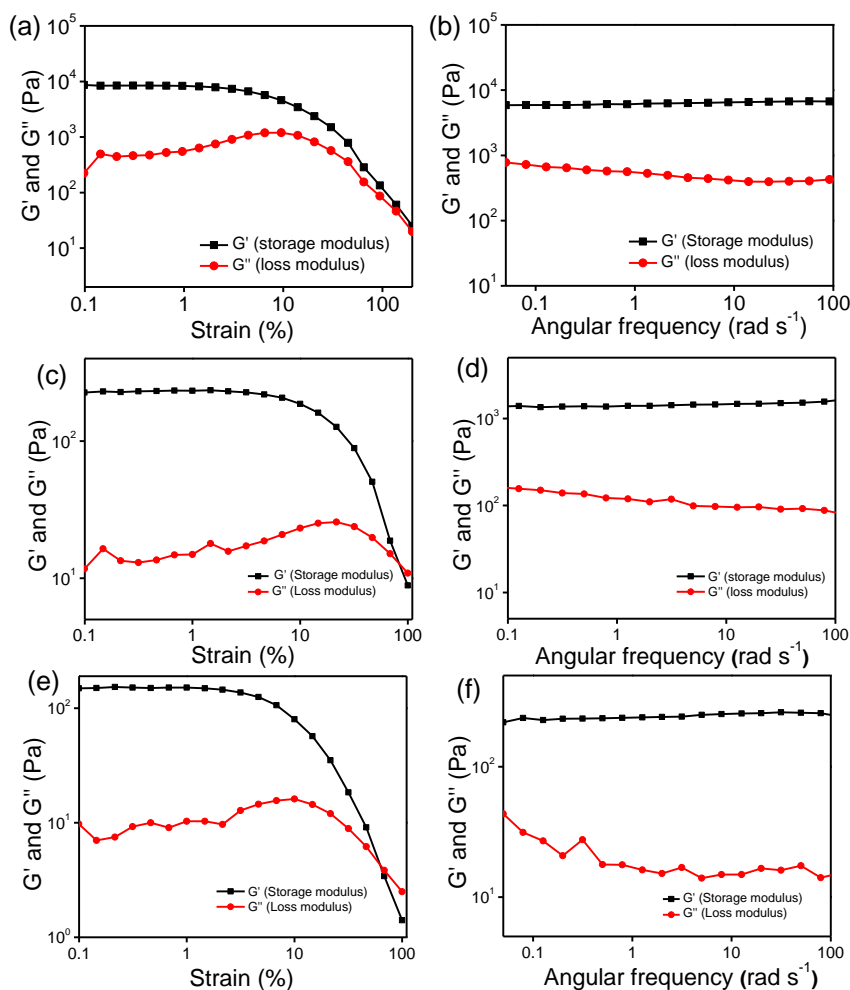


**Figure 2.32** Rheological experiments of **NP3** hydrogel: (a) amplitude strain-sweep experiment where frequency was fixed at 10 rad. s<sup>-1</sup> and (b) the frequency sweep test at fixed strain of 1%. Rheological experiments of **NP3** hydrogel prepared in NaOH (c) Amplitude sweep experiment. (d) Frequency sweep experiment at a constant strain of 0.5%. Rheological experiments of **NP3** hydrogel prepared in LiOH. (e) Amplitude sweep experiment. (f) Frequency sweep experiment at a constant strain of 0.5%.

The amplitude sweeps and the frequency sweep experiments were also conducted for the other hydrogels prepared with LiOH and NaOH. The  $G'$  and  $G''$  values obtained from both experiments were lower when compared to the hydrogel formed in presence of  $K^+$  ions (**Figure 2.32c, d, e, f**). Weaker hydrogels are formed when  $K^+$  ions are replaced with  $Li^+$  and  $Na^+$  ions. Therefore, the ion selectivity character of the  $G'$



quadruplex nanofibrous hydrogel was also favoured from rheological study.

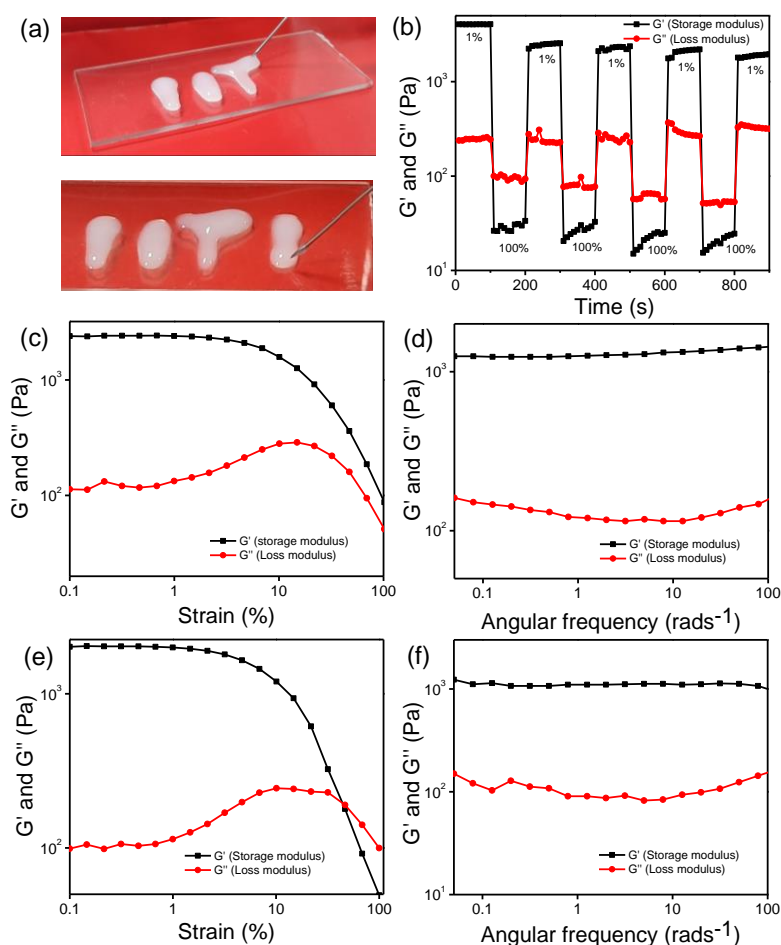


**Figure 2.33** (a) Optical photographs demonstrate the Injectability nature of the **NP3** hydrogel. (b) Dynamic step-strain sweep profile of the **NP3** hydrogel at a constant angular frequency of  $10 \text{ rad.s}^{-1}$ . Rheological experiment of vitamin  $B_2$  loaded hydrogel: (c) Amplitude sweep experiment. (d) Frequency sweep experiment. Rheological experiment of vitamin  $B_{12}$  loaded hydrogel: (e) Amplitude sweep experiment. (f) Frequency sweep experiment.

The injectability nature of the **NP3** hydrogel was also checked (**Figure 2.33a**). For this study, **NP3** hydrogel (2 mL) was kept within the empty glass syringe and was pulled out through a 24G needle. Hydrogel was easily passed through the needle without blockage and the gel state was quickly restored after extrusion. Now-a-days, biocompatible hydrogels are widely used as injectable matrices for tissue engineering purposes

because of their minimal invasiveness and stimuli responsive properties. Besides, injectability also adds an extra advantage for the use of hydrogel as a cargo in localized drug delivery application. Therefore, the synthesis and formulation of the new class of injectable **NP3** hydrogels may provide many applications in the biomedical field such as drug delivery. The thixotropic property of the **NP3** hydrogel was also estimated by performing dynamic step-strain sweep experiment. Thixotropy is an important property of hydrogel which extends the possibility of its use in the area such as drug release and stem cell proliferation [64,65]. In this experiment, applied strain was varied periodically (low-high-low). High strain was applied for a period of 100s to break the hydrogel and followed by its restoration at lower strain which was also applied for 100s. This cycle was repeated 4 times to validate the thixotropic character of the **NP3** nanofibrous hydrogel (**Figure 2.33b**). At the fixed lower applied strain, the higher  $G'$  value than  $G''$  attributed to the presence of the nanofibrous hydrogel. However,  $G'$  decreases and becomes lower than the  $G''$  with the sudden increase of strain (100%) suggesting the deformation of the hydrogel state and its transformation into sol condition. Interestingly, after lowering the strain from 100 to 1%, the  $G'$  value became higher again indicating the restoration of the hydrogel state. Therefore, this experiment revealed the thixotropic property of the **NP3** hydrogel. Further, the mechanical strength of the vitamins B<sub>2</sub> and B<sub>12</sub> loaded hydrogels was also checked. The amplitude sweep experiment was executed for both vitamins loaded hydrogels at a fixed frequency of 10 rad/s (**Figure 2.33 c, d**). Then, the frequency sweep experiment was also performed for both hydrogels at a fixed strain of 1%. For the vitamin loaded hydrogels, the  $G'$  values remained higher than  $G''$  indicating the existence of solid-like viscoelastic nature of the hydrogel throughout the experiment. Therefore, from both the rheological experiments, it is evident that the solid-like viscoelastic nature of the hydrogel was properly maintained even after the encapsulation of the vitamins (**Figure 2.33 e, f**).

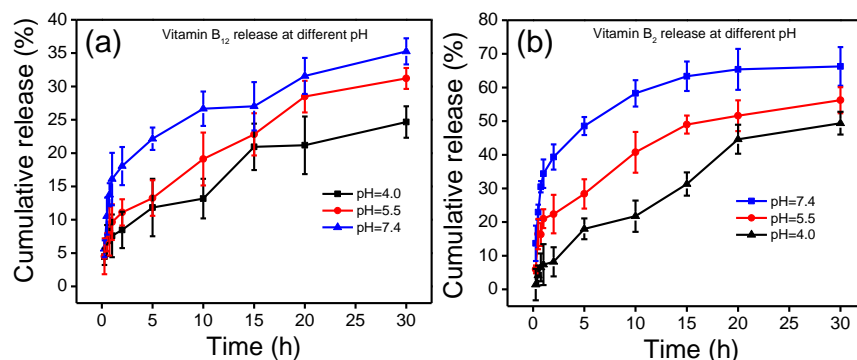


**Figure 2.34** Cumulative release (%) of vitamins: (a) release profiles of vitamin B<sub>12</sub> and (b) release profiles of vitamin B<sub>2</sub> from the gel matrices at pH = 4.0, 5.5, 7.4. Error bars represent SD, n = 3.

Biomolecules derived hydrogels are often used for slow release of different drug molecules from the gel matrix due to their biocompatibility and low cytotoxicity [66,67]. Hence, owing to the importance of these vitamins, both the vitamins were encapsulated into the dense and entangled nanofibrillar networks of the **NP3** hydrogel. Vitamins B<sub>2</sub> and B<sub>12</sub> were loaded *in-situ* separately at the time of formation of the hydrogel and remain in a stable condition for 12 h. The release study of the entrapped vitamins from the **NP3** hydrogel was examined at three different pHs (4.0, 5.5, 7.4). To observe the release of vitamins from the hydrogel, phosphate buffer (1 mL; pH 7.4; 50 mM) was added over the hydrogel (1 mL) and the whole system was kept under incubation at 37 °C. For the release study, a small portion of aliquots (200 µL) was withdrawn at different time interval from the vitamin loaded hydrogel and its corresponding UV-Vis absorbance was measured. The absorption maxima of vitamin B<sub>2</sub> and vitamin B<sub>12</sub> were 446 and 550 nm, respectively. The release of vitamins was observed up to 30 h. After 30 h, 66% of entrapped vitamin B<sub>2</sub> and 35% of vitamin B<sub>12</sub> were released from the hydrogel at pH 7.4 (**Figure 2.34a** and **2.34b**). However, the release rate gradually decreases with lowering the pH from 7.4 to 5.5 and 4.0. The dispersion of the hydrogel in the buffer is slower at lower pH. The nanofibers disperse more rapidly in a higher pH environment, allowing the encapsulated vitamin molecules to diffuse at a faster rate at pH 7.4. The release of the vitamins B<sub>2</sub> and B<sub>12</sub> after 30 h

at pH 5.5 were 56% and 31% whereas at pH 4.0, the release was 49% and 35%, respectively. The faster release of vitamin B<sub>2</sub> in contrast with vitamin B<sub>12</sub> is directly attributed to the lower molecular weight of vitamin B<sub>2</sub> as compared to vitamin B<sub>12</sub>. These vitamins loaded hydrogels were stable in the buffer solution up to 30 h after that the slow degradation of the hydrogel matrix was observed. The complete dissolution of the hydrogel was observed after 36 h.

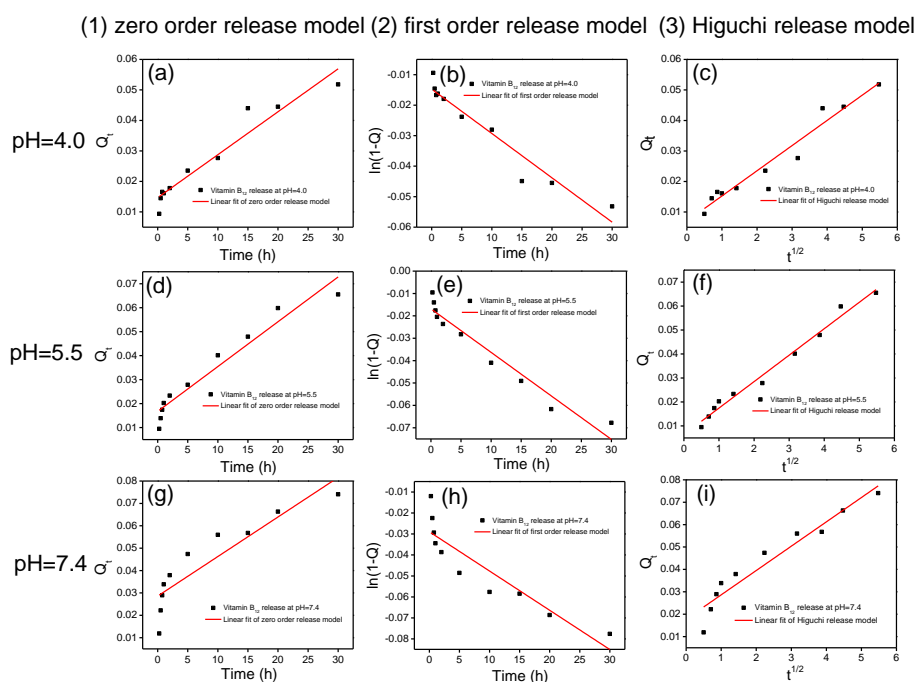


**Figure 2.35** Model fittings of vitamin B<sub>12</sub> release profile with different equations: (1) Zero-order release model at pH (a) 4.0, (b) 5.5 (c) 7.4, (2) first-order release model at pH (d) 4.0, (e) 5.5, (f) 7.4, (3) Higuchi release model at pH (g) 4.0, (h) 5.5 (i) 7.4.

We have further studied the pH responsive release behavior of the vitamins B<sub>2</sub> and B<sub>12</sub> from the hydrogel matrices at temperature (37 °C) from the linear fitting of the three commonly used drug release model (a) Zero-order release model, (b) second order release model and (c) Higuchi release model.

**Table 2.1** Kinetic parameters of vitamin release obtained by fitting in three different release models

Vitamin Release (pH)	Zero-order model		First order model		Higuchi model	
	$K_0$	$R^2$	$K_1$	$R^2$	$K_H$	$R^2$
B <sub>2</sub> (7.4)	0.00489	0.68165	0.00573	0.7011	0.03127	0.86365
B <sub>12</sub> (7.4)	0.00177	0.79554	0.00187	0.80821	0.01086	0.92026
B <sub>2</sub> (5.5)	0.00498	0.84878	0.0056	0.86328	0.03028	0.95732
B <sub>12</sub> (5.5)	0.00187	0.93379	0.00194	0.93704	0.01103	0.98413
B <sub>2</sub> (4.0)	0.00518	0.95405	0.00565	0.95893	0.03014	0.97155
B <sub>12</sub> (4.0)	0.00141	0.92461	0.00145	0.92697	0.00826	0.95933

The rate constant value in different release models indicated the stimuli responsive behavior of the hydrogel. The larger value of the rate constant indicated the faster release of the vitamins from the hydrogel as well as greater stimuli responsiveness character of the matrices. The  $R^2$  value indicated the fitting of the equation with release model equation. From the above data, the best fitting value was obtained with the Higuchi model (**Table 2.1**).

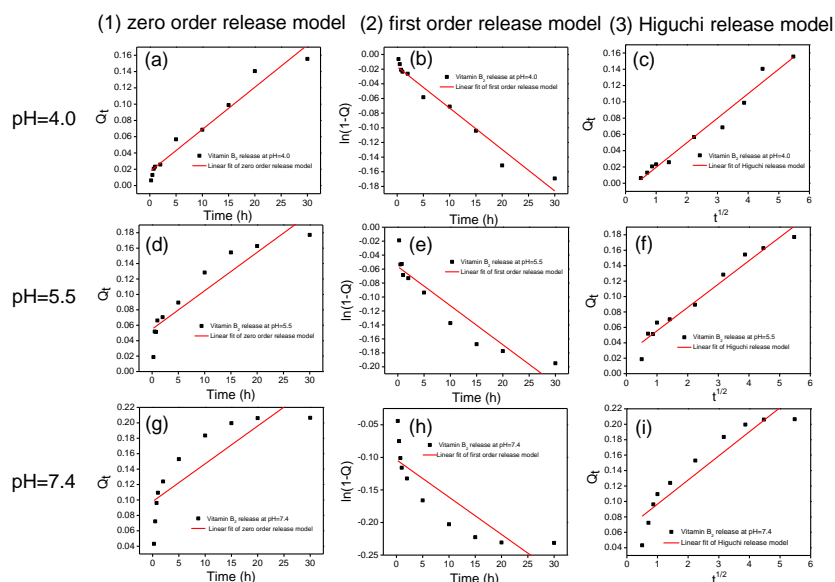


**Figure 2.36** Model fittings of vitamin B<sub>2</sub> release profile with different equations: lease (1) Zero-order release model at pH (a) 4.0, (b) 5.5 (c)

7.4, (2) first-order release model at pH (d) 4.0, (e) 5.5, (f) 7.4, (3) Higuchi release model at pH (g) 4.0, (h) 5.5 (i) 7.4.

The rest of the models such as zero-order model, first order model did not fit well to their corresponding equations (**Figure 2.35 and 2.36**). Therefore, the release of the vitamins from the **NP3** hydrogel networks follows the Higuchi model [68,69].

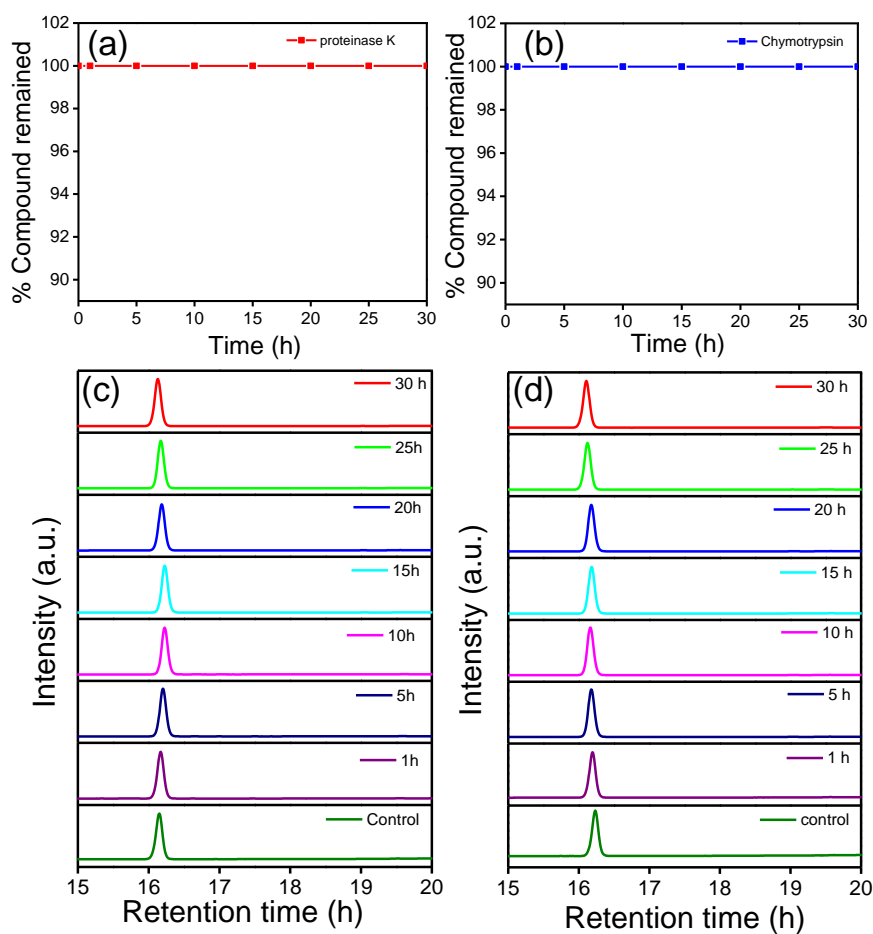


**Figure 2.37** Time-dependent progress of digestion of hydrogelator **NP3** by (a) proteinase K and (b) chymotrypsin. Time-dependent HPLC Chromatograms of **NP3** hydrogelator with (c) proteinase K and (d) chymotrypsin.

Biostability is an important requirement for biomaterials. Thus, we tested the stability of hydrogelator with potential protease enzymes including proteinase K and chymotrypsin, which hydrolyse a wide range of peptides by cleaving the amide bonds. The hydrogelator **NP3** was

incubated with proteolytic enzymes in phosphate buffer solution at pH = 7.4 (50 mM, buffer concentration) under 37 °C for a period of 30 h. The digestion course of the hydrogelator was monitored by performing HPLC (high performance liquid chromatography) at the different time intervals (**Figure 2.37a and 2.37b**). In the HPLC chromatogram, no new peak was observed upon incubation with enzymes (**Figure 2.37c and 2.37d**). The **NP3** hydrogelator show great resistance to enzymatic digestion suggesting the excellent biostability of these nucleobases amino acid conjugate [70]. Overall, the newly synthesized **NP3** hydrogel shows excellent biostability, which makes it a promising biomaterial for different biomedical applications.

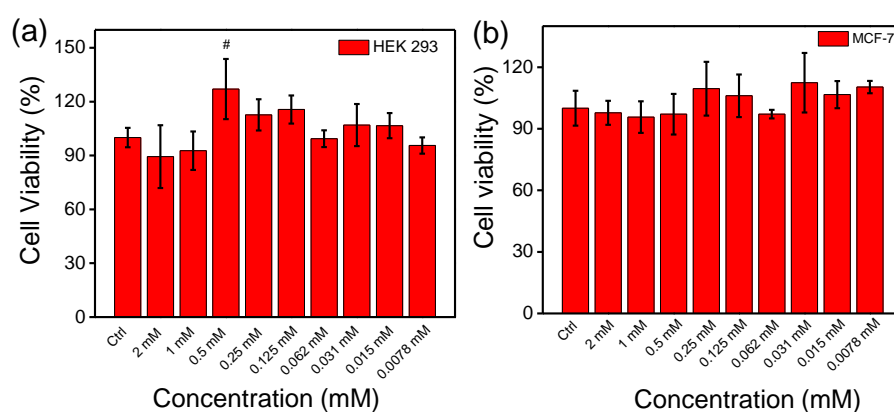


**Figure 2.38** Concentration dependent (2-0.0078 mM) MTT cell viability experiment of **NP3** hydrogel against (a) HEK 293 and (b) MCF-7 cells. Statistical analysis of data was carried out by one-way ANOVA test. A collection of biological triplicates served as the basis for all the findings. *P* values were calculated using GraphPad Prism software version 9.0. *P* values < 0.05 were considered statistically significant and represented by # increased, the remaining data points show non-significant changes (*N* = 3).

Investigating the cytotoxicity of the hydrogel is important to determine its suitability for future applications in biology. The *in-vitro* biocompatibility of the synthesized **NP3** hydrogel was evaluated using two cell lines: epithelial human embryonic kidney cells (HEK 293) and breast cancer cells (MCF-7). Different concentrations of the hydrogel

(2-0.00778 mM) were tested in the cytotoxicity experiments. The results of the MTT assay showed that the **NP3** hydrogel had a cell viability of over 96% in the concentration range of 0.5-0.00778 mM after 24 h of incubation for HEK 293 cells (**Figure 2.38a**). However, at higher concentrations (1 and 2 mM), the hydrogel showed some cytotoxicity. Similarly, the **NP3** hydrogel displayed nontoxic behaviour towards MCF-7 cell lines, with over 94% cell viability (**Figure 2.38b**).

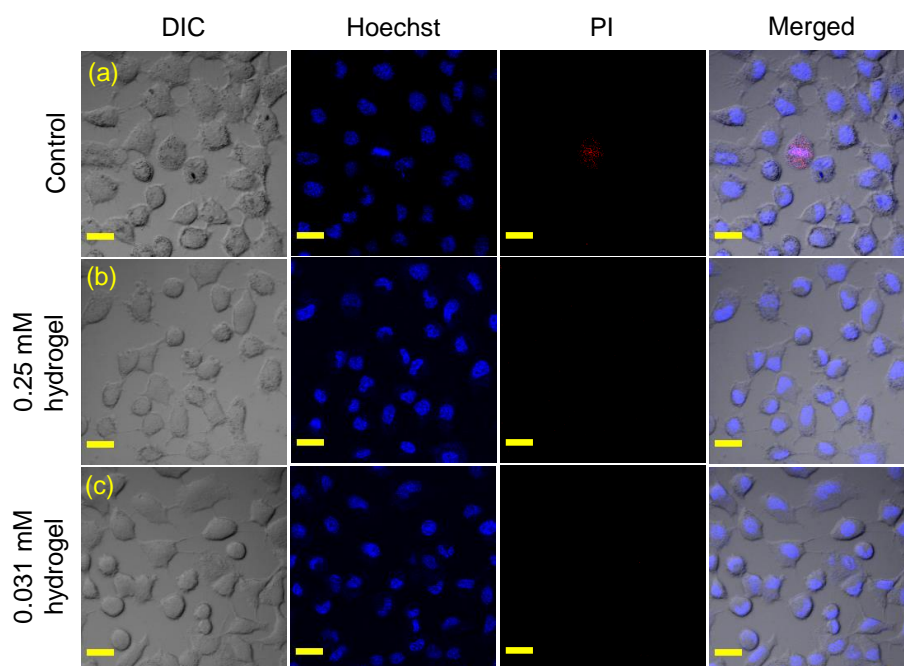


**Figure 2.39** Biocompatibility assessment of **NP3** hydrogels using the MCF-7 cell line. (a) Control, (b) 0.25 mM **NP3** hydrogel, (c) 0.031 mM **NP3** hydrogel (Scale bar 20  $\mu$ m).

Therefore, the MTT assay was conducted on both HEK 293 and MCF-7 cells to confirm that the hydrogel is biocompatible. The biocompatibility of the synthesized **NP3** hydrogel was further supported by the live/dead cell imaging assay. Hoechst blue fluorescent dye was used to stain live cells and propidium iodide was used to stain the dead cells. The CLSM images clearly demonstrate that the **NP3** hydrogel is non-toxic to the MCF-7 cell line after a 24 h incubation period (**Figure 2.39**). In conclusion, both cytotoxicity experiments have confirmed that the synthesized guanine functionalized hydrogel is nontoxic, making it a potential candidate for further biological experiments.



## 2.4 Conclusion

We have successfully synthesized guanine functionalized molecules with variable carbon chain length. The **NP3** formed stable G-quadruplex nanofibrous hydrogel with the support of suitable monovalent alkali metal ions. The Hoogsteen type H-bonding interaction among the guanine moieties and  $\pi$ - $\pi$  stacking were the driving force in the formation G-quadruplex hydrogel. The presence of G-quadruplex inside the hydrogel was demonstrated by circular dichroism spectroscopy, wide angle powder X-ray diffraction study and cationic ThT dye binding study. The effect of monovalent alkali metal ions on the stability of G-quadruplex was also checked. The viscoelastic behaviors of the hydrogel were also determined by the rheological experiments. Hydrogel was thixotropic and found injectable in nature. The existence of thick and thin nanofibrous morphology inside the hydrogel matrix was characterized with the help of microscopic techniques such as SEM, TEM and AFM. Hydrogel was further utilized for pH responsive sustained delivery of the vitamins like vitamin B<sub>2</sub> and B<sub>12</sub>. The synthesized **NP3** showed excellent biostability towards hydrolytic enzymes proteinase K and chymotrypsin suggesting the improved biostability of this nucleobase amino acid conjugates. The MTT assay clearly revealed that the hydrogel was non-cytotoxic in nature. Therefore, bioinspired newly synthesized **NP3** hydrogel may be useful in the biomedicine field because of its inherent biocompatible and injectable nature.

## 2.5 Reference

- [1] Li J, Mooney DJ (2016) Designing hydrogels for controlled drug delivery. *Nat Rev Mater* 1:16071. <https://doi.org/10.1038/natrevmats.2016.71>.
- [2] Raza F, Zafar H, You X, Khan A, Wu J, Ge L (2019) Cancer nanomedicine: focus on recent developments and self-assembled peptide nanocarriers. *J Mater Chem B* 7:7639–7655. <https://doi.org/10.1039/C9TB01842E>.

- [3] Das D, Roy A, Pal S (2023) A Polysaccharide-Based pH-Sensitive Hybrid Hydrogel as a Sustained Release Matrix for Antimicrobial Drugs. *ACS Appl Polym Mater* 5:3348–3358. <https://doi.org/10.1021/acsapm.2c02256>.
- [4] Han Z, Wang P, Mao G, Yin T, Zhong D, Yiming B, Hu X, Jia Z, Nian G, Qu S, Yang W (2020) Dual pH-Responsive Hydrogel Actuator for Lipophilic Drug Delivery. *ACS Appl Mater Inter* 12:12010–12017. <https://doi.org/10.1021/acsami.9b21713>.
- [5] Baral A, Roy S, Dehsorkhi A, Hamley IW, Mohapatra S, Ghosh S, Banerjee A (2014) Assembly of an Injectable Noncytotoxic Peptide-Based Hydrogelator for Sustained Release of Drugs. *Langmuir* 30:929–936. <https://doi.org/10.1021/la4043638>.
- [6] Baek K, Noblett AD, Ren P, Suggs LJ (2020) Self-assembled nucleotriptide hydrogels provide local and sustained doxorubicin release. *Biomater Sci* 8:3130–3137. <https://doi.org/10.1039/D0BM00134A>.
- [7] Morbioli I, Casnati A, Esko JD, Tor Y, Sansone F (2021) Calixarene-decorated liposomes for intracellular cargo delivery. *Org Biomol Chem* 19:6598–6602. <https://doi.org/10.1039/D1OB01055G>.
- [8] Lupu A, Gradinaru LM, Gradinaru VR, Bercea M (2023) Diversity of Bioinspired Hydrogels: From Structure to Applications. *Gels* 9:376. <https://doi.org/10.3390/gels9050376>.
- [9] Baek K, Noblett AD, Ren P, Suggs LJ (2019) Design and Characterization of Nucleopeptides for Hydrogel Self-Assembly. *ACS Appl Bio Mater* 2:2812–2821. <https://doi.org/10.1021/acsabm.9b00229>.
- [10] Way AE, Korpusik AB, Dorsey TB, Buerkle LE, Von Recum HA, Rowan SJ (2014) Enhancing the Mechanical Properties of Guanosine-Based Supramolecular Hydrogels with Guanosine-Containing Polymers. *Macromolecules* 47:1810–1818. <https://doi.org/10.1021/ma402618z>.

- [11] Chen Z, Zhou P, Guo Y, Anna Bai J, Qiao R, Li C (2022) Guanosine Borate Hydrogel and Self-Assembled Nanostructures Capable of Enantioselective Aldol Reaction in Water. *J Org Chem* 87:2624–2631. <https://doi.org/10.1021/acs.joc.1c02573>.
- [12] Peters GM, Skala LP, Plank TN, Oh H, Manjunatha Reddy GN, Marsh A, Brown SP, Raghavan SR, Davis JT (2015) G4-Quartet- $M^+$  Borate Hydrogels. *J Am Chem Soc* 137:5819–5827. <https://doi.org/10.1021/jacs.5b02753>.
- [13] Peters GM, Skala LP, Plank TN, Hyman BJ, Manjunatha Reddy GN, Marsh A, Brown SP, Davis JT (2014) A G4  $\cdot K^+$  Hydrogel Stabilized by an Anion. *J Am Chem Soc* 136:12596–12599. <https://doi.org/10.1021/ja507506c>.
- [14] Ghosh T, Biswas A, Gavel PK, Das AK (2020) Engineered Dynamic Boronate Ester-Mediated Self-Healable Biocompatible G-Quadruplex Hydrogels for Sustained Release of Vitamins. *Langmuir* 36:1574–1584. <https://doi.org/10.1021/acs.langmuir.9b03837>.
- [15] Ghosh S, Ghosh T, Bhowmik S, Patidar MK, Das AK (2023) Nucleopeptide-Coupled Injectable Bioconjugated Guanosine-Quadruplex Hydrogel with Inherent Antibacterial Activity. *ACS Appl Bio Mater* 6:640–651. <https://doi.org/10.1021/acsabm.2c00912>.
- [16] Ghosh T, Das AK (2023) Dynamic boronate esters cross-linked guanosine hydrogels: A promising biomaterial for emergent applications. *Coord Chem Rev* 488:215170. <https://doi.org/10.1016/j.ccr.2023.215170>.
- [17] Oyen E, Martin C, Caveliers V, Maddar A, Van Mele B, Hoogenboom R, Hernot S, Ballet S (2017) In Vivo Imaging of the Stability and Sustained Cargo Release of an Injectable Amphipathic Peptide-Based Hydrogel. *Biomacromole* 18:994–1001. <https://doi.org/10.1021/acs.biomac.6b01840>.

- [18] Nam J, Lim H-K, Kim NH, Park JK, Kang ES, Kim Y-T, Heo C, Lee O-S, Kim S-G, Yun WS, Suh M, Kim YH (2020) Supramolecular Peptide Hydrogel-Based Soft Neural Interface Augments Brain Signals through a Three-Dimensional Electrical Network. *ACS Nano* 14:664–675. <https://doi.org/10.1021/acsnano.9b07396>.
- [19] Panja S, Fuentes-Caparrós AM, Cross ER, Cavalcanti L, Adams DJ (2020) Annealing Supramolecular Gels by a Reaction Relay. *Chem Mater* 32:5264–5271. <https://doi.org/10.1021/acs.chemmater.0c01483>.
- [20] Loh XJ, Del Barrio J, Lee T-C, Scherman OA (2014) Supramolecular polymeric peptide amphiphile vesicles for the encapsulation of basic fibroblast growth factor. *Chem Commun* 50:3033–3035. <https://doi.org/10.1039/C3CC49074B>.
- [21] Burgess NC, Sharp TH, Thomas F, Wood CW, Thomson AR, Zaccai NR, Brady RL, Serpell LC, Woolfson DN (2015) Modular Design of Self-Assembling Peptide-Based Nanotubes. *J Am Chem Soc* 137:10554–10562. <https://doi.org/10.1021/jacs.5b03973>.
- [22] Rüter A, Kuczera S, Pochan DJ, Olsson U (2019) Twisted Ribbon Aggregates in a Model Peptide System. *Langmuir* 35:5802–5808. <https://doi.org/10.1021/acs.langmuir.8b03886>.
- [23] Biswas A, Ghosh T, Gavel PK, Das AK (2020) PEG Functionalized Stimuli Responsive Self-Healable Injectable Dynamic Imino-boronate G-quadruplex Hydrogel for the Delivery of Doxorubicin. *ACS Appl Bio Mater* 3:1052–1060. <https://doi.org/10.1021/acsabm.9b01034>.
- [24] Biswas A, Malferrari S, Kalaskar DM, Das AK (2018) Arylboronate esters mediated self-healable and biocompatible dynamic G-quadruplex hydrogels as promising 3D-bioinks. *Chem Commun* 54:1778–1781. <https://doi.org/10.1039/C7CC09051J>.
- [25] Ghosh T, Biswas A, Bhowmik S, Das AK (2021) Pt Nanoparticles Supported on a Dynamic Boronate Ester-Based G-quadruplex Hydrogel

as a Nanoreactor. *Chem Asian J* 16:215–223.  
<https://doi.org/10.1002/asia.202001284>.

[26] Mandal B, Maiti S, Aaryashree, Siddharth G, Das M, Agarwal A, Das AK (2020) Organo-di-benzoic-acidified ZnO Nanohybrids for Highly Selective Detection of CO at Low Temperature. *J Phys Chem C* 124:7307–7316. <https://doi.org/10.1021/acs.jpcc.0c01044>.

[27] Singh D, Jadhav RG, Das AK (2021) Electrodeposition of Binder-Free Peptide/Co(OH)<sub>2</sub> Nanohybrid Electrodes for Solid-State Symmetric Supercapacitors. *Energy Fuels* 35:16152–16161. <https://doi.org/10.1021/acs.energyfuels.1c01850>.

[28] He H, Liu S, Wu D, Xu B (2020) Enzymatically Formed Peptide Assemblies Sequester Proteins and Relocate Inhibitors to Selectively Kill Cancer Cells. *Angew Chem Int Ed* 59:16445–16450. <https://doi.org/10.1002/anie.202006290>.

[29] Gavel PK, Kumar N, Parmar HS, Das AK (2020) Evaluation of a Peptide-Based Coassembled Nanofibrous and Thixotropic Hydrogel for Dermal Wound Healing. *ACS Appl Bio Mater* 3:3326–3336. <https://doi.org/10.1021/acsabm.0c00252>.

[30] Cooper CB, Kang J, Yin Y, Yu Z, Wu H-C, Nikzad S, Ochiai Y, Yan H, Cai W, Bao Z (2020) Multivalent Assembly of Flexible Polymer Chains into Supramolecular Nanofibers. *J Am Chem Soc* 142:16814–16824. <https://doi.org/10.1021/jacs.0c07651>.

[31] Deng Y, Zhang Q, Qu D-H (2023) Emerging Hydrogen-Bond Design for High-Performance Dynamic Polymeric Materials. *ACS Materials Lett* 5:480–490. <https://doi.org/10.1021/acsmaterialslett.2c00865>.

[32] Das T, Häring M, Haldar D, Díaz Díaz D (2018) Phenylalanine and derivatives as versatile low-molecular-weight gelators: design, structure and tailored function. *Biomater Sci* 6:38–59. <https://doi.org/10.1039/C7BM00882A>.

- [33] Mokhtari P, Ghaedi M (2019) Water compatible molecularly imprinted polymer for controlled release of riboflavin as drug delivery system. *Eur Polym J* 118:614–618. <https://doi.org/10.1016/j.eurpolymj.2019.06.038>.
- [34] Arabi M, Ghaedi M, Ostovan A (2017) Development of a Lower Toxic Approach Based on Green Synthesis of Water-Compatible Molecularly Imprinted Nanoparticles for the Extraction of Hydrochlorothiazide from Human Urine. *ACS Sustainable Chem Eng* 5:3775–3785. <https://doi.org/10.1021/acssuschemeng.6b02615>.
- [35] Boughriba S, Souissi N, Nasri R, Nasri M, Li S (2021) pH sensitive composite hydrogels based on gelatin and reinforced with cellulose microcrystals: In depth physicochemical and microstructural analyses for controlled release of vitamin B<sub>2</sub>. *Mater Today Commun* 27:102334. <https://doi.org/10.1016/j.mtcomm.2021.102334>.
- [36] Obeid R, Heil SG, Verhoeven MMA, Van Den Heuvel EGHM, De Groot LCPGM, Eussen SJPM (2019) Vitamin B<sub>12</sub> Intake From Animal Foods, Biomarkers, and Health Aspects. *Front Nutr* 6:93. <https://doi.org/10.3389/fnut.2019.00093>.
- [37] Gruber K, Puffer B, Kräutler B (2011) Vitamin B<sub>12</sub>-derivatives—enzyme cofactors and ligands of proteins and nucleic acids. *Chem Soc Rev* 40:4346. <https://doi.org/10.1039/c1cs15118e>.
- [38] Kaur H, Roy S (2021) Designing aromatic N-cadherin mimetic short-peptide-based bioactive scaffolds for controlling cellular behaviour. *J Mater Chem B* 9:5898–5913. <https://doi.org/10.1039/D1TB00598G>.
- [39] Jain R, Roy S (2020) Tuning the gelation behavior of short laminin derived peptides via solvent mediated self-assembly. *Mater Sci Eng C* 108:110483. <https://doi.org/10.1016/j.msec.2019.110483>.
- [40] Frederix PWJM, Scott GG, Abul-Haija YM, Kalafatovic D, Pappas CG, Javid N, Hunt NT, Ulijn RV, Tuttle T (2015) Exploring the

sequence space for (tri-)peptide self-assembly to design and discover new hydrogels. *Nature Chem* 7:30–37. <https://doi.org/10.1038/nchem.2122>.

[41] Tong X, Ga L, Eerdun C, Zhao R, Ai J (2022) Simple Monovalent Metal Ion Logical Order to Regulate the Secondary Conformation of G-Quadruplex. *ACS Omega* 7:39224–39233. <https://doi.org/10.1021/acsomega.2c05243>.

[42] Toro PM, Saldias M, Valenzuela-Barra G (2023) Metal-Organic Compounds as Anticancer Agents: Versatile Building Blocks for Selective Action on G-quadruplexes. *CMC* 30:573–600. <https://doi.org/10.2174/0929867329666220606160209>.

[43] Zhou J, Tateishi-Karimata H, Mergny J-L, Cheng M, Feng Z, Miyoshi D, Sugimoto N, Li C (2016) Reevaluation of the stability of G-quadruplex structures under crowding conditions. *Biochimie* 121:204–208. <https://doi.org/10.1016/j.biochi.2015.12.012>.

[44] Bhattacharyya D, Mirihana Arachchilage G, Basu S (2016) Metal Cations in G-Quadruplex Folding and Stability. *Front Chem* 4: <https://doi.org/10.3389/fchem.2016.00038>.

[45] Nishio M, Tsukakoshi K, Ikebukuro K (2021) G-quadruplex: Flexible conformational changes by cations, pH, crowding and its applications to biosensing. *Biosens Bioelectron* 178:113030. <https://doi.org/10.1016/j.bios.2021.113030>.

[46] Li X, Sánchez-Ferrer A, Bagnani M, Adamcik J, Azzari P, Hao J, Song A, Liu H, Mezzenga R (2020) Metal ions confinement defines the architecture of G-quartet, G-quadruplex fibrils and their assembly into nematic tactoids. *Proc Natl Acad Sci USA* 117:9832–9839. <https://doi.org/10.1073/pnas.1919777117>.

[47] Soyfer, V. N., & Potaman, V. N. (1996). Triple-helical nucleic acids. Springer Science & Business Media. (ISBN: 978-0-387-94495-1) (<https://doi.org/10.1007/978-1-4612-3972-7>)

- [48] Saenger, W. (1984). Principles of Nucleic Acid Structure. Springer. New York, Berlin, Heidelberg. (ISBN: 978-1-4612-5190-3) (<https://doi.org/10.1007/978-1-4612-5190-3>)
- [49] Laraman FJ, Fisk H, Whittaker DTE, Cherryman JH, Diorazio LJ (2022) Investigating the Activation Kinetics of Phosphoramidites for Oligonucleotide Synthesis. *Org Process Res Dev* 26:764–772. <https://doi.org/10.1021/acs.oprd.1c00195>.
- [50] Langford GJ, Raeburn J, Ferrier DC, Hands PJW, Shaver MP (2019) Morpholino Oligonucleotide Cross-Linked Hydrogels as Portable Optical Oligonucleotide Biosensors. *ACS Sens* 4:185–191. <https://doi.org/10.1021/acssensors.8b01208>.
- [51] Mohanty J, Barooah N, Dhamodharan V, Harikrishna S, Pradeepkumar PI, Bhasikuttan AC (2013) Thioflavin T as an Efficient Inducer and Selective Fluorescent Sensor for the Human Telomeric G-Quadruplex DNA. *J Am Chem Soc* 135:367–376. <https://doi.org/10.1021/ja309588h>.
- [52] Xu S, Li Q, Xiang J, Yang Q, Sun H, Guan A, Wang L, Liu Y, Yu L, Shi Y, Chen H, Tang Y (2016) Thioflavin T as an efficient fluorescence sensor for selective recognition of RNA G-quadruplexes. *Sci Rep* 6:24793. <https://doi.org/10.1038/srep24793>.
- [53] Peters GM, Skala LP, Davis JT (2016) A Molecular Chaperone for G4-Quartet Hydrogels. *J Am Chem Soc* 138:134–139. <https://doi.org/10.1021/jacs.5b08769>.
- [54] Li Y, Su L, Zhang Y, Liu Y, Huang F, Ren Y, An Y, Shi L, Van Der Mei HC, Busscher HJ (2022) A Guanosine-Quadruplex Hydrogel as Cascade Reaction Container Consuming Endogenous Glucose for Infected Wound Treatment—A Study in Diabetic Mice. *Adv Sci* 9:2103485. <https://doi.org/10.1002/advs.202103485>.



- [55] Hudson JS, Ding L, Le V, Lewis E, Graves D (2014) Recognition and Binding of Human Telomeric G-Quadruplex DNA by Unfolding Protein 1. *Biochem* 53:3347–3356. <https://doi.org/10.1021/bi500351u>.
- [56] Zhou B, Geng Y, Liu C, Miao H, Ren Y, Xu N, Shi X, You Y, Lee T, Zhu G (2018) Characterizations of distinct parallel and antiparallel G-quadruplexes formed by two-repeat ALS and FTD related GGGGCC sequence. *Sci Rep* 8:2366. <https://doi.org/10.1038/s41598-018-20852-w>.
- [57] Babu SS, Praveen VK, Ajayaghosh A (2014) Functional  $\pi$ -Gelators and Their Applications. *Chem Rev* 114:1973–2129. <https://doi.org/10.1021/cr400195e>.
- [58] del Villar-Guerra R, Trent JO, Chaires JB (2018) G-Quadruplex Secondary Structure Obtained from Circular Dichroism Spectroscopy. *Angew Chem Int Ed* 57:7171–7175. <https://doi.org/10.1002/anie.201709184>.
- [59] Carvalho J, Queiroz JA, Cruz C (2017) Circular Dichroism of G-Quadruplex: a Laboratory Experiment for the Study of Topology and Ligand Binding. *J Chem Educ* 94:1547–1551. <https://doi.org/10.1021/acs.jchemed.7b00160>.
- [60] Kubota R, Tanaka W, Hamachi I (2021) Microscopic Imaging Techniques for Molecular Assemblies: Electron, Atomic Force, and Confocal Microscopies. *Chem Rev* 121:14281–14347. <https://doi.org/10.1021/acs.chemrev.0c01334>.
- [61] Grindy SC, Lenz M, Holten-Andersen N (2016) Engineering Elasticity and Relaxation Time in Metal-Coordinate Cross-Linked Hydrogels. *Macromolecules* 49:8306–8312. <https://doi.org/10.1021/acs.macromol.6b01523>.
- [62] Speetjens FW, Mahanthappa MK (2015) Synthesis and Rheological Characterization of Poly(vinyl acetate- *b* -vinyl alcohol- *b* -vinyl

acetate) Triblock Copolymer Hydrogels. *Macromole* 48:5412–5422.  
<https://doi.org/10.1021/acs.macromol.5b00410>.

[63] Unterman S, Charles LF, Strecker SE, Kramarenko D, Pivovarchik D, Edelman ER, Artzi N (2017) Hydrogel Nanocomposites with Independently Tunable Rheology and Mechanics. *ACS Nano* 11:2598–2610. <https://doi.org/10.1021/acsnano.6b06730>.

[64] Ma Y, Shi L, Liu F, Zhang Y, Pang Y, Shen X (2019) Self-assembled thixotropic silver cluster hydrogel for anticancer drug release. *J Chem Eng* 362:650–657.  
<https://doi.org/10.1016/j.ccej.2019.01.096>.

[65] Zanna N, Focaroli S, Merlettini A, Gentilucci L, Teti G, Falconi M, Tomasini C (2017) Thixotropic Peptide-Based Physical Hydrogels Applied to Three-Dimensional Cell Culture. *ACS Omega* 2:2374–2381.  
<https://doi.org/10.1021/acsomega.7b00322>.

[66] Wei D, Xiao W, Sun J, et al (2015) A biocompatible hydrogel with improved stiffness and hydrophilicity for modular tissue engineering assembly. *J Mater Chem B* 3:2753–2763.  
<https://doi.org/10.1039/C5TB00129C>.

[67] Zhong Y, Seidi F, Li C, Zhong M, Guo L, Fan H, Zhang X (2021) Antimicrobial/Biocompatible Hydrogels Dual-Reinforced by Cellulose as Ultrastretchable and Rapid Self-Healing Wound Dressing. *Biomacromole* 22:1654–1663.  
<https://doi.org/10.1021/acs.biomac.1c00086>.

[68] Li Y, Liu Y, Ma R, Xu Y, Zhang Y, Li B, An Y, Shi L (2017) A G-Quadruplex Hydrogel via Multicomponent Self-Assembly: Formation and Zero-Order Controlled Release. *ACS Appl Mater Inter* 9:13056–13067. <https://doi.org/10.1021/acsami.7b00957>.

[69] Lian Q, Liu H, Zheng X, Jia D, Liu C, Wang D (2020) Synthesis of polyacrylonitrile nanoflowers and their controlled pH-sensitive drug

release behavior. RSC Adv 10:15715–15725.  
<https://doi.org/10.1039/D0RA01427C>.

[70] Li X, Kuang Y, Lin H, Gao Y, Shi J, Xu B (2011) Supramolecular Nanofibers and Hydrogels of Nucleopeptides. *Angew Chem Int Ed* 50:9365–9369. <https://doi.org/10.1002/anie.201103641>.

## **Chapter 3**

### **Chemical Reaction Driven Self-assembly of a Nucleobase Functionalized Molecule**



### 3.1 Introduction

Molecular self-assembly is the process of creating desirable nanostructures by organizing designed molecular building blocks with proper intra- and intermolecular interactions [1,2]. In the living system, molecular assemblies are exploited to create necessary structures in living organisms, including the cytoskeleton, chromatin, organelles, and cell membrane. Moreover, molecular assembly processes are involved in important biological functions such as protein folding, RNA transcription, and DNA replication [3-6]. Inspired from the naturally occurring self-assembly, scientists are trying to mimicking such assemblies in the laboratory conditions. Different stimuli have been employed to create molecular self-assemblies, including pH, enzyme, light, ultrasound, temperature, electric field, magnetic field, and chemical reactions [7-12]. Molecular self-assembly is facilitated by a variety of noncovalent interactions, including coordination interactions, hydrophobic effects, hydrogen bonding, ionic interactions and van der Waals forces [13-16]. Materials built from molecular self-assemblies are easily impacted by outside stimuli since noncovalent interactions are often much weaker than the covalent ones. This is why, in addition to synthetic chemistry, molecular self-assembly has gained importance as a method for producing novel materials. These interactions help to create a range of self-assembling functional materials, such as gels, liquids, elastomers, and hard materials. Supramolecular hydrogels generated by the self-assembly of small molecules have gained attention because to their unique characteristics such as biocompatibility, synthetic feasibility, low toxicity, and intrinsic biodegradability [17]. Therefore, peptides based functional materials are used in various fields like tissue engineering, drug delivery, wound healing, biosensing, 3D bioprinting [18-20]. Recently Gaharwar *et al.* developed a novel type of light-responsive in situ gelation system that is based on the dynamic interactions between thermoresponsive polymers functionalized with thiols and MoS<sub>2</sub> nanoparticles. They have shown that the formation of the mechanically cross-linked hydrogel via physical absorption and

chemical conjugation upon exposing the precursors solution to the NIR light [21]. In another report, a peptide system's pH may be lowered in a regulated way by the hydrolysis of glucono- $\delta$ -lactone (GDL), facilitating the subsequent creation of a self-supporting hydrogel [22]. Chemical reactions such as amide bond formation, ester hydrolysis have been used to add covalent bonds and functionalities which enable the molecules to form the order structures by the non-covalent interactions. Roy *et al.* revealed that the hydrolysis of the ester by using subtilisin leads to the formation of the hydrogel. They further studied the reaction kinetics by varying the concentration of the enzyme [23]. Rasale *et al.* reported a new strategy to regulate the molecular self-assembly under thermodynamic control using the protease thermolysin [24]. Ulijn group utilized a protease enzyme, which is generally used to hydrolyze the peptide bonds in the aqueous medium. They reported a fundamentally innovative technique by employing thermolysin to achieve the reverse reaction, which synthesizes the peptide hydrogelators and undergo self-assembly to form the nanofibrous structures [25]. Das *et al.* reported the esterification of peptide bolaamphiphiles using lipase catalysis which resulted in the formation of a hydrogel that self-assembled into nanofibrous supramolecular structures [26].

Herein, the self-assembly of a nucleobase functionalized gelator (**NP**) driven by chemical reaction has been reported. In general, methylation of nucleobases of DNA is a significant metabolic process [27-31]. Nucleobases are methylated, when a methyl group is transferred to a nucleobase by an internal or external methylating agent, modifying a DNA segment's function without altering its sequence [32,33]. The methylation of DNA by these agents can result in the change of its heterocyclic bases or backbone in a number of ways. DNA methylation is essential for the regular development of mammals and is involved in a number of important biological processes, including ageing, carcinogenesis, X-chromosome inactivation, genomic imprinting, and the repression of transposable elements [34,35]. DNA methylation is an epigenetic process which regulates the tissue differentiation and gene expression. It has the ability to suppress transcription, thereby affecting

gene expression. Additionally, the loss of methylation is linked with gene activation [36,37]. In some circumstances, DNA methylation may directly obstruct the binding of transcription factors. Therefore, methylation is an important biological process [38,39]. Given the importance of the methylation, guanine is methylated to introduce the supramolecular order in the synthesized guanine functionalized molecules. Here in this report, the use of the dimethyl sulphate as methylating agent is addressed to drive the self-assembly. The chemical reactions directed self-assembly are rarely reported in the literature. Therefore, the objectives of this study are (a) to achieve the chemical reaction driven self-assembly of a nucleobase-functionalized (**NP**) hydrogelator, (b) to use the dimethyl sulphate in the formation of methylated products, (c) to study the change in morphology over time after the addition of the dimethyl sulphate.

## **3.2 Experimental Section**

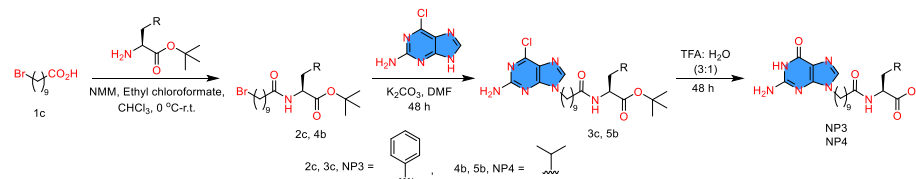
### **3.2.1 Materials and Methods**

The used solvents and reagents were purchased from commercially available sources like Alfa Aesar, Sigma Aldrich, Merck, and Spectrochem Pvt. Ltd. 2-Amino-6-chloropurine and potassium carbonate ( $K_2CO_3$ ) were obtained from Alfa Aesar. Ethyl chloroformate was purchased from Spectrochem whereas diethyl ether was purchased from Merck. N-Methylmorpholine was obtained from SRL and 10-Bromodecanoic acid was obtained from TCI. L-phenylalanine *tert*-butyl ester hydrochloride and L-leucine *tert*-butyl ester hydrochloride were purchased from Sigma Aldrich. Dimethyl sulfoxide- $d_6$ , chloroform- $d$ , deuterium oxide was purchased from Sigma Aldrich. Dimethyl sulphate was purchased from Spectrochem. For moisture sensitive reactions, dry solvent was used in the presence of  $N_2$  or Ar gas. After completion of the reaction, the crude products were purified by column chromatography method using silica as stationary phase and hexane, ethyl acetate or chloroform, methanol as a mobile phase. Thin-layer chromatography (TLC) was performed on aluminium backed silica plates (silica gel 60, 20×20 cm, UV 254) and visualized under UV light



( $\lambda = 254$  nm or 365 nm). All  $^1\text{H}$  and  $^{13}\text{C}$  NMR spectra were set down on Bruker Avance (500 MHz) instrument at 25 °C. Mass spectra were set down on Bruker instrument by using ESI positive mode. The NMR spectra of all intermediates and final products were analysed by using Mestrenova software. Chemical shift was expressed in the form of ppm ( $\delta$ ) relative to surplus solvents protons as internal standards (DMSO- $d_6$ :  $\delta = 2.50$ ,  $\text{CDCl}_3$  at 7.26 ppm for  $^1\text{H}$  NMR; DMSO- $d_6$ :  $\delta = 39.50$ ,  $\text{CDCl}_3$  at 77.16 ppm for  $^{13}\text{C}$  NMR).

### 3.2.2 Synthesis of NP3 and NP4



**Scheme 3.1.** Synthesis of NP3 and NP4.

### 3.2.3 General procedure for the synthesis of 2c, 4b:

Under argon atmosphere, 4-methylmorpholine was added in the solution of 10-bromodecanoic acid in dry chloroform at 0 °C. The solution was left for stirring at this temperature. After 15 min, ethyl chloroformate was added into the solution and stirred vigorously at this temperature for additional 45 min before the addition of *tert*-butyl ester was added. Then the reaction mixture was allowed to stir for 1 h at 0 °C and then at room temperature for 16 h. The progress of the reaction was monitored by TLC.  $R_f = 0.32$  for 2c and 0.37 for 4b (hexane/EtOAc 70:30). After the completion of the reaction, reaction mixture was diluted with water and washed with 1(N) NaOH (3×10) mL and then with brine, 0.5 (N) HCl (3×10) mL and finally with brine. The organic part was dried over  $\text{Na}_2\text{SO}_4$  and concentrate under vacuum. The product was used without further purification.

### 3.2.4 Synthesis of 2c:

The compound **2c** was synthesized as per the above-mentioned general procedure. Yield: 85%.  $^1\text{H}$  NMR ( $\text{CDCl}_3$ , 400 MHz):  $\delta$  1.29 (m, 10H), 1.43 (s, 10H), 1.62 (m, 2H), 1.86 (m, 2H), 2.18 (t, 3H,  $J = 8, 8$  Hz), 2.30

(t, 1H,  $J = 8, 8$  Hz), 2.46 (m, 1H), 3.42 (t, 2H,  $J = 8, 8$  Hz), 4.78 (m, 1H), 5.93 (d, 1H,  $J = 4$  Hz), 7.23 (m, 5H). (ESI-MS,  $m/z$ ):  $[M+Na]^+$   $C_{23}H_{36}BrNO_3Na$  478.1753; found 478.1753.

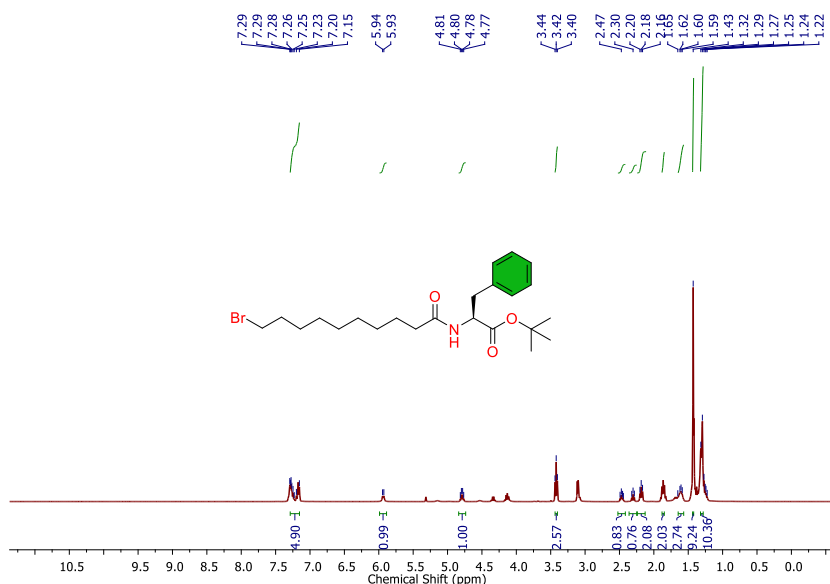


**Figure 3.1**  $^1H$  NMR (500 MHz,  $DMSO-d_6$ ) spectrum of compound **2c**.

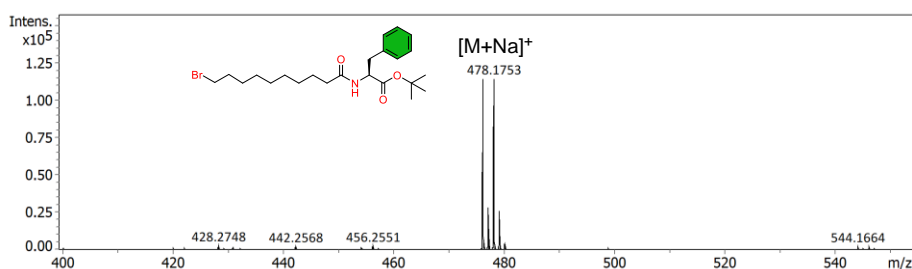


**Figure 3.2** ESI-MS spectrum of compound **2c**.

### 3.2.5 Synthesis of **4b**:

The compound **4b** was synthesized as per the above-mentioned general procedure. Yield: 82%.  $^1H$  NMR ( $DMSO-d_6$ , 500 MHz):  $\delta$  0.82 (d, 3H,  $J = 5$  Hz), 0.88 (d, 3H,  $J = 10$  Hz), 1.25 (s, 10H), 1.38 (s, 9H), 1.47 (m, 4H), 1.63 (m, 1H), 1.78 (m, 2H), 2.09 (t, 2H,  $J = 5, 10$  Hz), 3.51 (t, 2H,  $J = 5, 10$  Hz), 4.14 (m, 1H), 8.02 (d, 1H,  $J = 10$  Hz). (ESI-MS,  $m/z$ ):  $[M+Na]^+$  calculated for  $C_{20}H_{38}BrNO_3$ : 442.2035; found 442.1919.

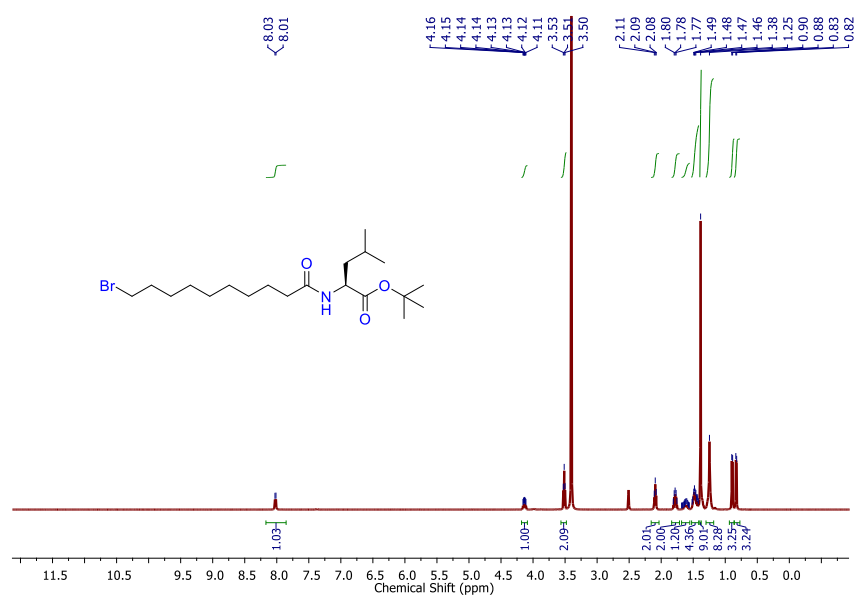


**Figure 3.3**  $^1\text{H}$  NMR (500 MHz,  $\text{DMSO}-d_6$ ) spectrum of compound **4b**.

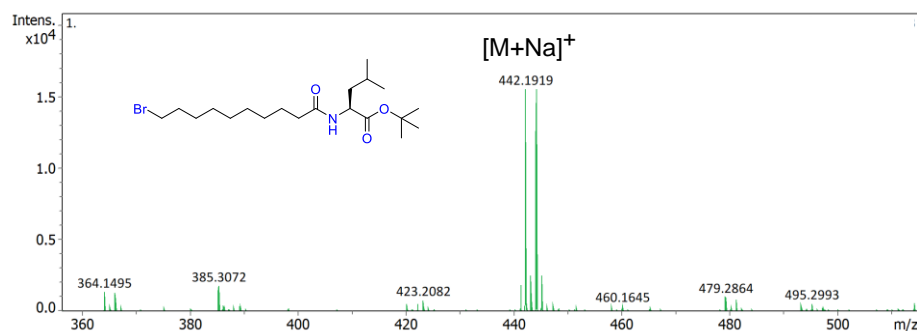


**Figure 3.4** ESI-MS spectrum of compound **4b**.

### 3.2.6 General procedure for the synthesis of **3c**, **5b**:

2-Amino-6-chloropurine was added in the solution of dry DMF (10 mL) under argon atmosphere. Then  $\text{K}_2\text{CO}_3$  was added in the solution. Finally, bromo acid coupled ester protected amino acid was added dropwise into the solution and the reaction was left for stirring for 24 h. The progress of the reaction was monitored by TLC.  $R_f = 0.35$  for **3c** and 0.41 for **5b** ( $\text{CHCl}_3/\text{MeOH}$  95:5) After the completion of the reaction, the reaction mixture was diluted with ethyl acetate and washed with water several times, finally with brine and dried over  $\text{Na}_2\text{SO}_4$ . After the evaporation of the solvent under rotary evaporator, the reaction mixture was purified by silica gel (mesh 100-200) column chromatography. The major product was N9 alkylated purine product

(eluent: CHCl<sub>3</sub>: MeOH = 99:1) and the minor product was N7 alkylated purine product (eluent: CHCl<sub>3</sub>: MeOH = 94:6).

### 3.2.7 Compound 3c:

The compound **3c** was synthesized as per the above-mentioned general procedure. Yield: 62%. <sup>1</sup>H NMR (DMSO-*d*<sub>6</sub>, 400 MHz): δ 1.23 (m, 10H), 1.32 (s, 9H), 1.40 (m, 3H), 1.76 (m, 2H), 2.04 (t, 2H, *J* = 4, 8 Hz), 2.85 (m, 1H), 2.97 (m, 1H), 4.03 (t, 3H, *J* = 4, 8 Hz), 4.36 (m, 1H), 6.91 (s, 2H), 7.22 (m, 5H), 8.15 (s, 1H). <sup>13</sup>C NMR (DMSO-*d*<sub>6</sub>, 100 MHz): δ 25.63, 26.47, 27.99, 28.84, 28.90, 29.12, 29.21, 29.40, 35.45, 37.37, 43.47, 54.40, 80.89, 123.82, 126.84, 128.56, 129.57, 137.90, 143.75, 149.76, 154.54, 160.21, 171.36, 172.61. (ESI-MS, *m/z*): calculated for [M+Na]<sup>+</sup> C<sub>28</sub>H<sub>39</sub>ClN<sub>6</sub>O<sub>3</sub>Na 565.2664; found 565.2672.

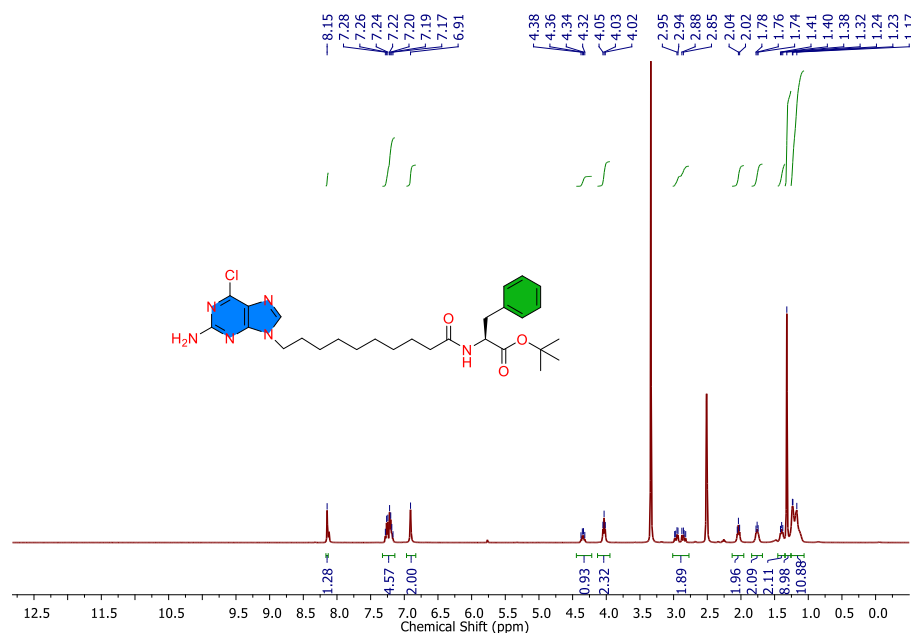


**Figure 3.5** <sup>1</sup>H NMR (500 MHz, DMSO-*d*<sub>6</sub>) spectrum of compound **3c**.

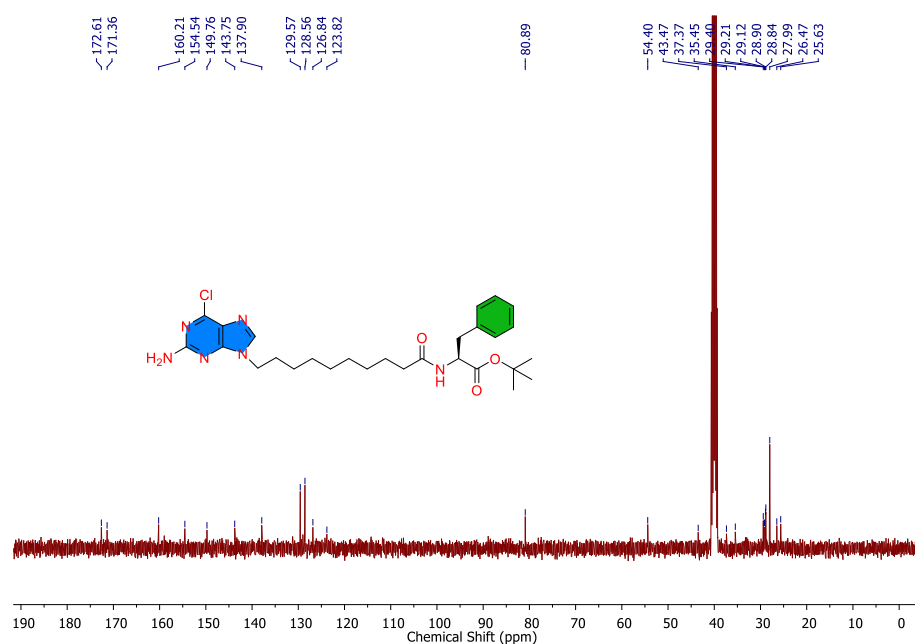


**Figure 3.6**  $^{13}\text{C}$  NMR (125 MHz,  $\text{DMSO-}d_6$ ) spectrum of compound **3c**.

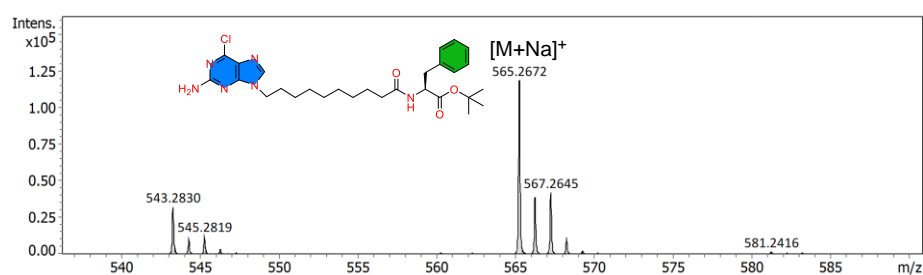


**Figure 3.7** ESI-MS spectrum of compound **3c**.

### 3.2.8 Compound **5b**:

The compound **5b** was synthesized as per the above-mentioned general procedure. Yield: 65%.  $^1\text{H}$  NMR ( $\text{DMSO-}d_6$ , 500 MHz):  $\delta$  0.74 (d, 3H,  $J = 5$  Hz), 0.80 (d, 3H,  $J = 5$  Hz), 1.14 (s, 10H), 1.30 (s, 9H), 1.39 (m, 4H), 1.53 (m, 1H), 1.69 (m, 2H), 2.01 (t, 2H,  $J = 5$ , 10 Hz), 3.96 (t, 2H,  $J = 5$ , 5 Hz), 4.05 (m, 1H), 6.81 (s, 1H), 7.94 (d, 1H,  $J = 5$  Hz), 8.06 (s, 1H).  $^{13}\text{C}$  NMR ( $\text{DMSO-}d_6$ , 125 MHz):  $\delta$  21.7, 23.1, 24.7, 25.7, 26.4, 28.0, 28.8, 29.0, 29.2, 29.3, 35.4, 40.5, 43.4, 51.3, 80.6, 123.8, 143.7, 149.7, 154.5, 160.1, 172.4, 172.8. (ESI-MS,  $m/z$ ):  $[\text{M}+\text{H}]^+$  calculated for  $\text{C}_{25}\text{H}_{41}\text{ClN}_6\text{O}_3$  509.2929; found 509.2953.

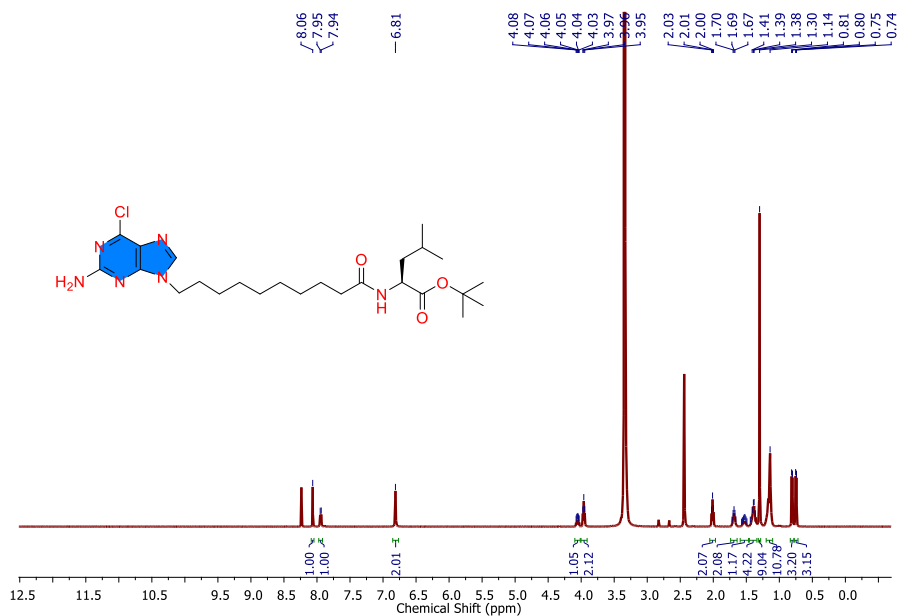


**Figure 3.8** <sup>1</sup>H NMR (500 MHz, DMSO-*d*<sub>6</sub>) spectrum of compound **5b**.

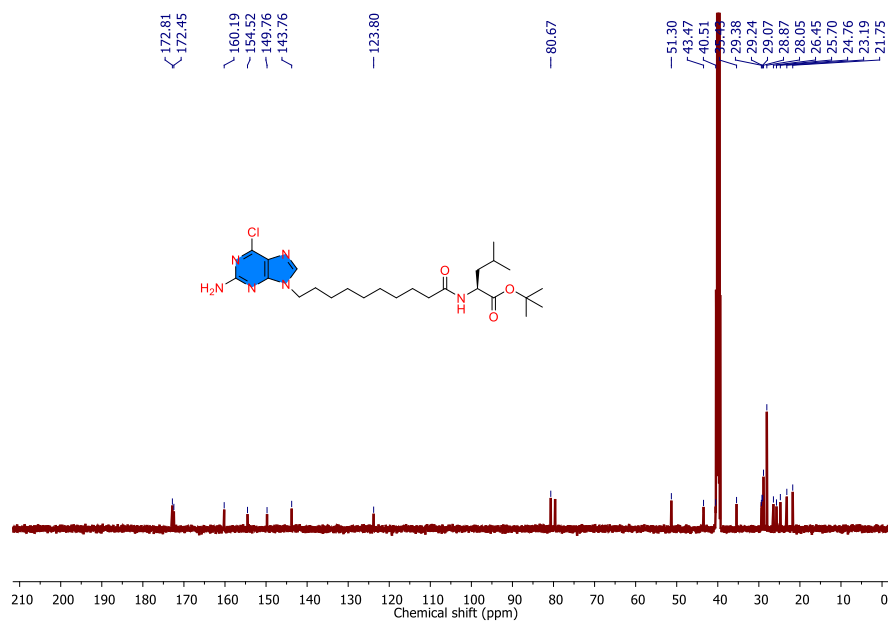


**Figure 3.9** <sup>13</sup>C NMR (125 MHz, DMSO-*d*<sub>6</sub>) spectrum of compound **5b**.

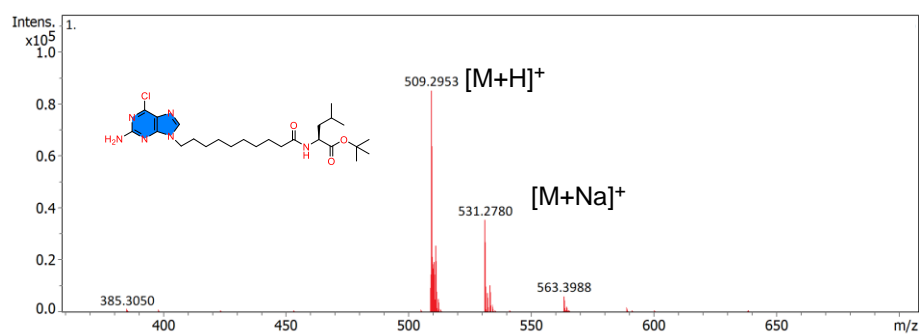


**Figure 3.10** ESI-MS spectrum of compound **5b**.

### 3.2.9 General procedure for the synthesis of compound NP3, NP4:

Compounds **NP3** and **NP4** were dissolved in 5 mL TFA: H<sub>2</sub>O (3:1) solution. Then, the reaction was left for stirring for 48 h at room temperature. The progress of the reaction was monitored by High performance liquid chromatography (HPLC). After the completion of the reaction, TFA was evaporated under vacuum. The reaction was washed with diethyl ether to obtain the white solid.

### 3.2.10 Compound NP3:

The compound **NP3** was synthesized as per the above-mentioned general procedure. Yield: 87%. <sup>1</sup>H NMR (DMSO-*d*<sub>6</sub>, 400 MHz):  $\delta$  1.17 (m, 10H), 1.39 (m, 2H), 1.74 (m, 2H), 2.02 (t, 2H, *J* = 4, 8 Hz), 2.83 (m, 1H), 3.06 (m, 1H), 3.98 (t, 2H, *J* = 8, 8 Hz), 4.42 (m, 1H), 6.70 (s, 1H), 7.21 (m, 5H), 8.09 (d, 1H, *J* = 8 Hz), 8.24 (s, 1H), 10.93 (s, 1H), 12.66 (s, 1H). <sup>13</sup>C NMR (DMSO-*d*<sub>6</sub>, 100 MHz):  $\delta$  25.60, 26.36, 28.84, 28.91, 29.14, 29.21, 29.51, 35.51, 37.19, 43.84, 53.70, 119.94, 126.78, 128.55, 129.51, 137.77, 138.24, 151.08, 154.64, 156.07, 172.62, 173.71. (ESI-MS, *m/z*): calculated for [M+H]<sup>+</sup> C<sub>24</sub>H<sub>33</sub>N<sub>6</sub>O<sub>4</sub> 469.2558; found 469.2555.

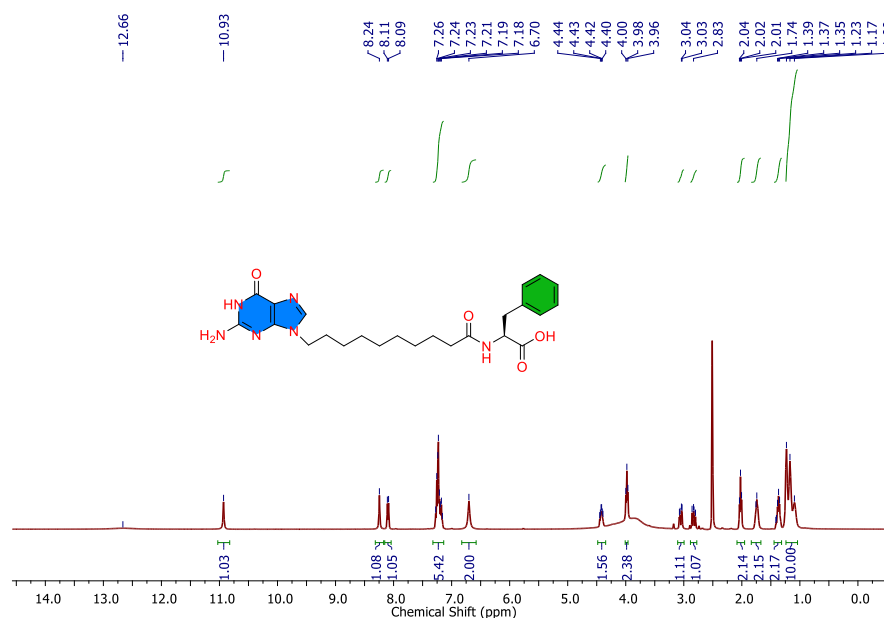


**Figure 3.11** <sup>1</sup>H NMR (500 MHz, DMSO-*d*<sub>6</sub>) spectrum of compound **NP3**.

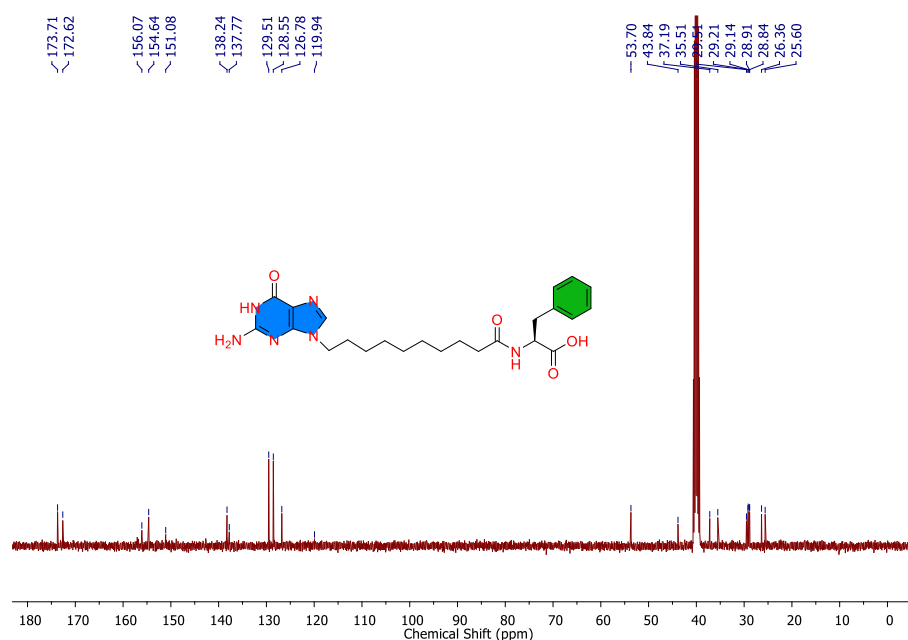


**Figure 3.12**  $^{13}\text{C}$  NMR (125 MHz,  $\text{DMSO-}d_6$ ) spectrum of compound NP3.

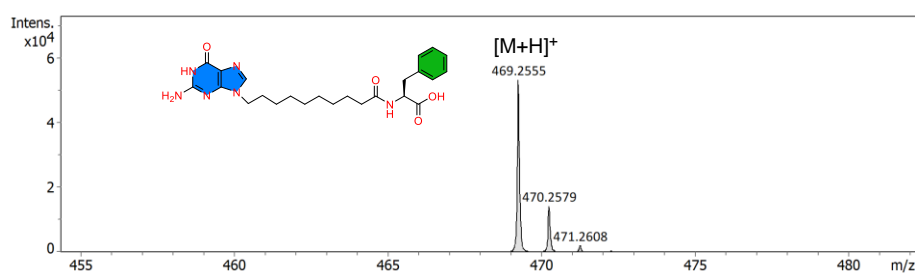


**Figure 3.13** ESI-MS spectrum of compound NP3.

### 3.2.11 Compound NP4:

The compound **NP4** was synthesized as per the above-mentioned general procedure. Yield: 82%.  $^1\text{H}$  NMR ( $\text{DMSO-}d_6$ , 500 MHz):  $\delta$  0.76 (d, 3H,  $J = 5$  Hz), 0.80 (d, 3H,  $J = 5$  Hz), 1.16 (s, 10H), 1.42 (m, 4H), 1.54 (m, 1H), 1.69 (m, 2H), 2.03 (m, 2H), 3.92 (t, 2H,  $J = 5$ , 10 Hz), 4.14 (m, 1H), 6.90 (s, 2H), 7.93 (d, 1H,  $J = 5$  Hz), 8.25 (s, 1H), 10.95 (d, 1H,  $J = 5$  Hz), 12.34 (s, 1H).  $^{13}\text{C}$  NMR ( $\text{DMSO-}d_6$ , 125 MHz):  $\delta$  21.6, 23.3, 24.7, 25.6, 26.2, 28.8, 28.9, 29.1, 29.2, 29.2, 35.4, 44.2, 50.4, 111.7, 137.6, 150.7, 155.1, 155.3, 172.7, 174.7. (ESI-MS,  $m/z$ ): calculated for  $[\text{M}+\text{H}]^+$   $\text{C}_{21}\text{H}_{34}\text{N}_6\text{O}_4$  435.2642; found 435.2800.



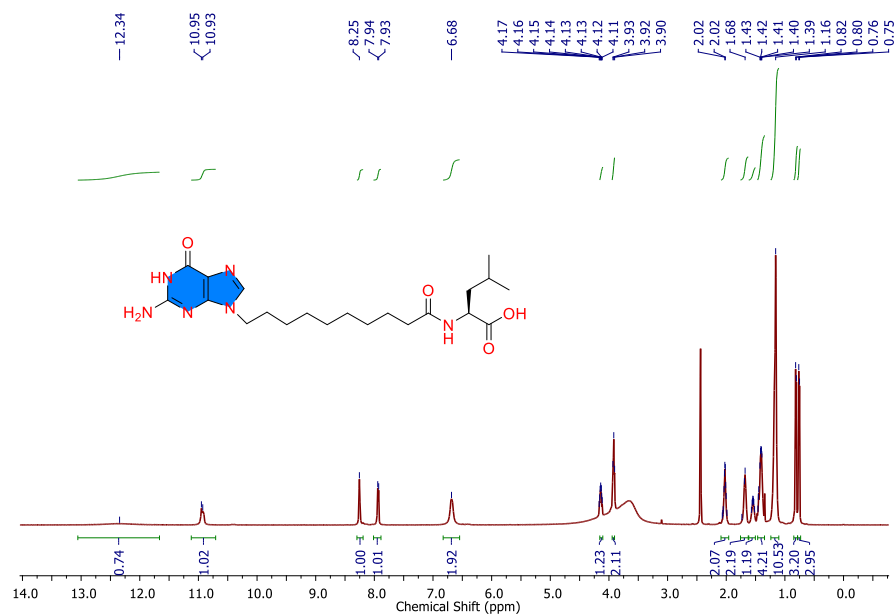


**Figure 3.14** <sup>1</sup>H NMR (500 MHz, DMSO-*d*<sub>6</sub>) spectrum of compound NP4.

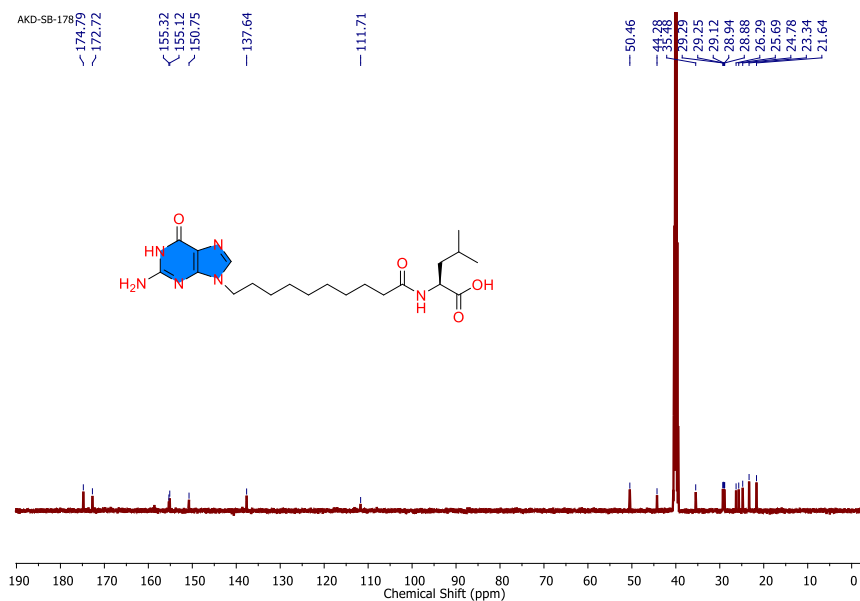


**Figure 3.15** <sup>13</sup>C NMR (125 MHz, DMSO-*d*<sub>6</sub>) spectrum of compound NP4.

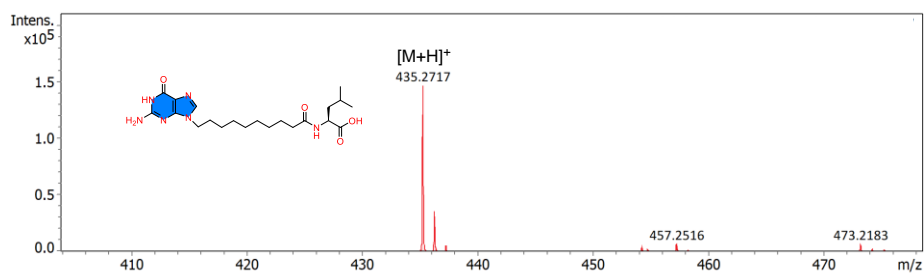


**Figure 3.16** ESI-MS spectrum of compound NP4.

### **3.2.12 HPLC Analysis**

The progress of the reaction was monitored by HPLC (model no Dionex ultimate 3000). It was consisted with pump, autosampler and detector. The sample was passed through C18 column (model no- Dionex Acclaim ® 120 C18, length of the column was 250 mm and internal diameter was 4.6 mm, particle size was 5 µm). A 42 min programme was set with a flow rate of 1 ml/min. The mobile phase was consisting of 0.1% TFA/Water (A) and 0.1% TFA/ACN (B). The programme was set as follow: 0-4 min 20% of B and 80% of A, 4-35 min 80% of B and 20% of A, 35-40 min 80% of B and 20% of A, 40-42 min 20% of B and 80% of A. The sample for the HPLC was prepared by dissolving 10 µl of reaction mixture in 1:1 mixture of ACN and water. The sample was filtered through a syringe filter (diameter 0.45 µm). The chromatograms were recorded at 254 nm.

### **3.2.13 pH**

The pH of the medium was recorded by using METTLER TOLEDO benchtop pH meter. HANNA Glass electrode (model no: HI1330) was used to record the pH of the medium. The 4.6 mg of the compound was taken in a clean and oven dry vial. Then, 50 µL of the 0.5 (N) KOH solution was added to completely dissolve the compound and 450 µL of the DI water was added. Finally, 5 µL of DMS was added. Then the pH of the medium was recorded at different time interval.

### **3.2.14 Circular Dichroism Spectroscopy**

The formation of the secondary structures of DNA inside the hydrogel was assessed by performing circular dichroism (CD) spectroscopy. Jasco J-815 Spectrometer was used to record data. CD spectra were recorded at different time interval after the addition of the DMS. The bandwidth value was set at 1 nm, with 0.1 data pitch and scanning speed was set at 20 nm min<sup>-1</sup> and 4 s. The hydrogel was diluted to at different time interval to prepare 250 µM solution.

### **3.2.15 FT-IR**

FT-IR spectra of the hydrogel and the compounds were recorded through Bruker spectrometer by using KBr pallet. The spectra were

recorded within the range between 400-4000  $\text{cm}^{-1}$  with 64 scans at a resolution of 4  $\text{cm}^{-1}$  and interval of 1  $\text{cm}^{-1}$ .

### **3.2.16 UV-Vis Spectroscopy**

The UV-Vis spectra of the DMS induce hydrogel were recorded by Jasco V 750 in a quartz cell (path length 1 mm) within the range 700–200 nm with a data pitch of 0.1 nm. The bandwidth was set at 1 nm, the scanning speed was 20  $\text{nm min}^{-1}$ , and the response time was 1 s.

### **3.2.17 Fluorescence Spectroscopy**

The fluorescence spectra were collected on Horiba Scientific spectrophotometer (model no- FluoroMax-4) using a quartz cuvette at 25 °C to account the progress of the self-assembly after the addition of the dimethyl sulphate. The width of the slit was set at 2 nm for the emission spectra and the data pitch value was 1 nm. Emission spectra of the was recorded at  $\lambda_{\text{ex}}$  of 280 nm and the data range was 262-490 nm.

### **3.2.18 Rheological Behavior of the Hydrogel**

Rheological studies were conducted to assess the mechanical strength of the hydrogel. Rheological studies were conducted at a temperature of 25 °C using an Anton Paar rheometer (model no: Physica MCR 301). The time dependent change in the viscosity was measured. To perform this experiment, 20 mM of the compound was dissolved in the 50  $\mu\text{L}$  of the 0.5 (N) KOH solution and then 450  $\mu\text{L}$  of water was added into the solution. The DMS was added prior to the experiment. The viscoelastic characteristics of the hydrogel were assessed by the quantification of the storage modulus ( $G'$ ) and loss modulus ( $G''$ ). Small aliquot (1 mL) of the hydrogel was placed onto a rheometer plate using a micro spatula and maintained in a hydrated state with the aid of a solvent trap. In this study, a parallel plate made of stainless steel with a diameter of 25 mm was used to enclose a hydrogel sample using TruGap, which had a thickness of 0.5 mm. The purpose of doing the amplitude sweep experiment was to ascertain the specific range of deformation inside the hydrogel where linear viscoelastic behaviour may be reliably observed. The specific strain (0.5%) for the hydrogel was established by analysis of its linear viscoelastic (LVE) behaviour at a constant frequency of 10

rad s<sup>-1</sup>. The mechanical properties of the hydrogel were assessed by a frequency sweep experiment, employing the strain percentage previously measured in an amplitude sweep experiment. The frequency range included in this study was 0.05–100 rad s<sup>-1</sup>. The purpose of the study was to assess the thixotropic and self-healing properties of the hydrogel using a step strain experiment. The experiment included applying a sequence of low-high-low strains every 100 seconds, while maintaining a constant frequency of 10 rad/s.

### **3.2.19 Morphological Study of the Hydrogel**

Morphological characterization of the hydrogel was carried out by various microscopic techniques such as confocal laser scanning microscope (CLSM), Scanning electron microscope (SEM), Transmission electron microscope (TEM). CLSM images were acquired using OLYMPUS microscope (model no- FV1200MPE, IX-83) by 100x objective. The video was captured using Zeiss Axio Imager.A2. An excitation beam of 405 nm was used. For the CLSM experiment 50 µL of the **NP3** hydrogel was taken in an Eppendorf, then 450 µL of milliQ water was added into it. Then, hydrogel was mixed with water by vortex. Finally, 5 µL of the solution was taken out from the mixture and placed on confocal glass slide for imaging. Zeiss made scanning electron microscope (model no: Zeiss supra-55) was used for SEM experiment. The accelerating voltage for SEM images was set at 5 kv. The SEM images were captured in SE2 mode. The sample for SEM imaging was prepared in a similar manner. TEM images were captured by a JEOL made microscope (model no Tecnai G2, F30) with an accelerating voltage of 300 kV. For the TEM experiment the **NP3** hydrogel 50 µL was taken in an eppendorf, then 950 µL of milliQ water was added into it. Vortex was performed to mix the hydrogel properly with the water. Then a small portion of it was kept on the carbon coated copper grid and dried. The drop casted solution was dried by slow evaporation and finally at reduced pressure before taking the images. Phosphotungstic acid (2%, w/v) was utilized as a negative staining. The hydrogel solution (20 mM) was diluted to 1 mM to record the video. 10 µL from the diluted solution was placed on the glass slide. The video was captured through 100x

153

Dimethyl sulphate (DMS), which is a methylating agent, is commonly used for methylation purposes [41,42]. DMS hydrolyzes in water to produce methanol and sulphuric acid. Therefore, the production of sulphuric acid in the solution decreases the pH, which may aid in the formation of a self-supporting hydrogel. In this study, DMS is utilized as the methylating agent. The synthesized guanine-functionalized molecules contain multiple sites that can be methylated. The product that may results from methylating N7 of purine ring has been named as PDT1, the product that may results from methylating the carboxylate (methyl ester derivative) has been named PDT2, and the product that may results from the N7 and the carboxylate group has been named PDT3, the product that may results from  $\text{-NH}_2$  methylation has been named PDT4 and the product that may results from methylation of O6 of the purine ring has been named PDT5. It was observed that the major product obtained after adding DMS was PDT1, while the minor products were PDT2 and PDT3, respectively (**Scheme 3.2**). The NPs were dissolved in a small amount of 0.5 (N) KOH. The addition of KOH resulted in the formation of carboxylate anion in the solution due to the strong electrostatic repulsion. The addition of 5 equivalent DMS was to the solution resulted in the formation of the activated building block for self-assembly. In case of **NP3** system, a self-supporting hydrogel was formed within 30 min with a 40% conversion.

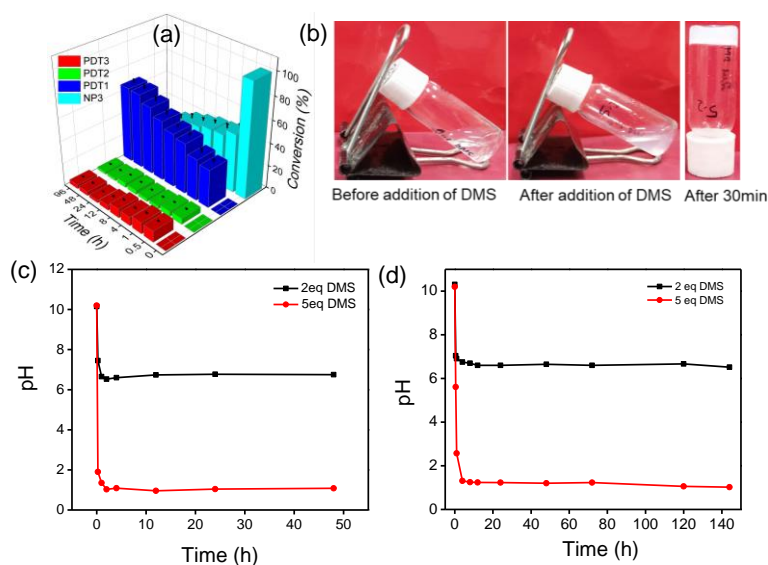


**Figure 3.17.** Conversion plot of (a) **NP3** after the addition of DMS, show the formation methylated products. Formation of the hydrogel after the addition of dimethyl sulphate. (b) Formation of the hydrogel after the addition of dimethyl sulphate. The change of the pH of the medium of (c) **NP3** and (d) **NP3** after the addition of 2 and 5 equivalent of DMS.

The maximum conversion of 70% was achieved after 48 h from the addition of the DMS (**Figure 3.17a**). The optical photographs also indicate the formation of the hydrogel from **NP3** after 30 min of adding the DMS (**Figure 3.17b**). The progress of the reaction was monitored using HPLC. The change in pH after addition of DMS was also recorded. The abrupt changes in pH were noticed, but after 2 h of the reaction, the pH value became constant (**Figure 3.17c and 3.17d**). The HPLC study demonstrates the production of a library of methylating compounds.

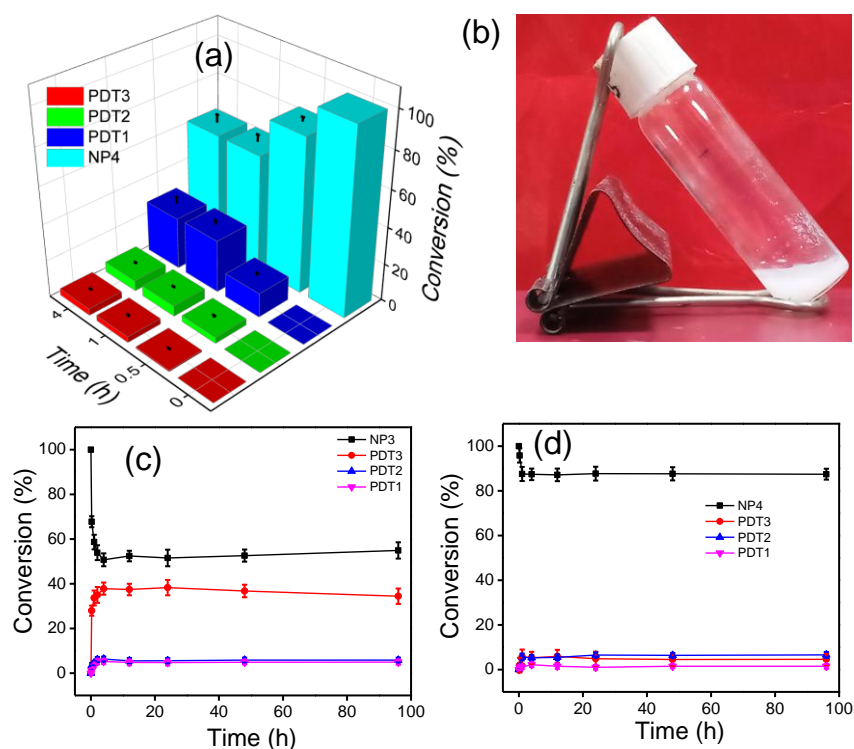


**Figure 3.18.** Conversion plot of (a) **NP4**. No significant change is observed for **NP4** after 4 h. (b) Precipitate formed after the addition of the DMS in

**NP4.** (c) The conversion of **NP3** after the addition of 2 equiv DMS (d) The conversion of **NP4** after the addition of 2 equiv DMS.

The minor products were achieved with negligible conversion. For **NP4**, a maximum 40% conversion was observed for the major product (**Figure 3.18a**). However, no hydrogel formation is observed for **NP4**, precipitate is formed after the addition of DMS (**Figure 3.18b**). The lower conversion of the desired product may be the main factors for this precipitation formation. The conversion was also checked varying amounts of DMS for both of the systems. Two different concentrations (2 and 5 equiv.) of DMS were added to the precursor solution to activate them for self-assembly. In the case of the **NP3** system, the conversion was higher when 5 equivalents of the DMS were added compared to 2 equivalents (**Figure 3.18c and 3.18d**). The hydrogelation was observed when 5 equivalents of the DMS was added to the reaction medium. The conversion was also studied for the **NP4** system. In all cases, the conversion was negligible compared to the **NP3** system, and no hydrogelation was observed at any concentration of DMS.

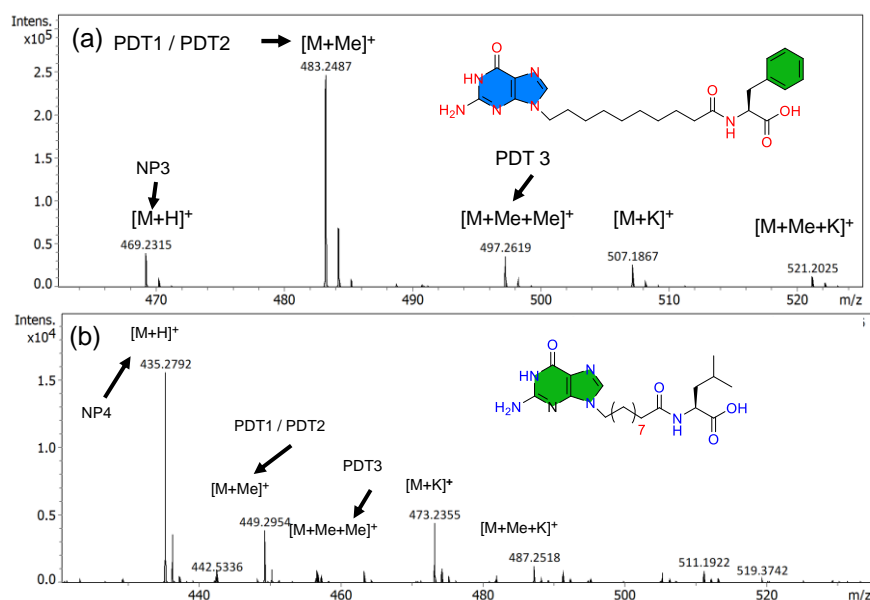


**Figure 3.19.** (a) ESI-MS spectrum after the formation of the **NP3** hydrogel. (b) ESI-MS spectrum of the precipitate of **NP4**.



The formation of the activated assembling building block was confirmed using electrospray ionization mass spectrometry (ESI-MS) (**Figure 3.19a and 3.19b**).

An FT-IR experiment was carried out to assess the presence of H-bonding and the secondary structure in the **NP3** hydrogel and **NP3**. The FT-IR spectra of the compound **NP3** and its corresponding hydrogel indicate that the presence of hydrogen bonding is significant in the formation of the hydrogel.

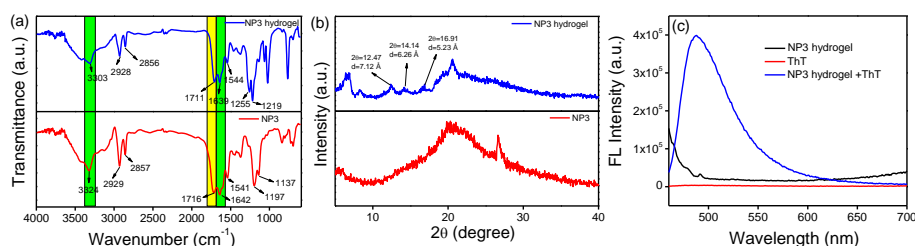


**Figure 3.20.** FT-IR spectra of (a) the **NP3** hydrogel and the gelator precursor **NP3**. (b) Wide angle powder XRD spectrum of **NP3** hydrogel and **NP3**. (c) Fluorescence spectra of **NP3**, ThT and ThT incorporated in **NP3** hydrogel.

There is a change in the -OH stretching frequency in the hydrogel state in comparison with the compound. The -OH stretching frequency of the carboxylic acid of **NP3** hydrogel is 3303 cm<sup>-1</sup>, whereas in the compound (**NP3**), the frequency is 3324 cm<sup>-1</sup>. This shift is believed to be caused by the involvement of the hydroxyl moiety in the hydrogen bonding interaction [43]. The change was also observed in the amide I and amide II regions [43]. In the **NP3** hydrogel, the carbonyl stretching frequency is 1711 cm<sup>-1</sup> and 1639 cm<sup>-1</sup>, respectively whereas the stretching frequency of the carbonyl in **NP3** is 1716 cm<sup>-1</sup> and 1642 cm<sup>-1</sup>. The N-H bending peaks at 1544 cm<sup>-1</sup> and 1541 cm<sup>-1</sup> in the amide II region appeared for **NP3** hydrogel and **NP3** respectively (**Figure 3.20a**) [43,44]. The shift in the stretching frequencies to lower wavenumber suggests the presence of order structures which lead to the formation of the hydrogel [45,46]. Further, wide-angle powder X-ray diffraction experiments were performed on both **NP3** and **NP3** hydrogels to

investigate the formation of stacked structures in the self-assembled state. In the **NP3** hydrogel spectrum, the peaks at  $2\theta = 12.7, 14.1, 16.9$  correspond to the  $d$  value of  $7.1 \text{ \AA}, 6.2 \text{ \AA}, 5.2 \text{ \AA}$ . These peaks are appeared due the presence of the secondary structures in the hydrogel [47,48]. The appearance of the new peaks was observed in **NP3** hydrogel spectrum in comparison to **NP3**. This experiment confirms the presence of the secondary structure of the nucleic acid inside the hydrogel matrices, which contribute to the formation of a self-supported hydrogel (**Figure 3.20b**). The presence of the secondary structure of the nucleic acid inside the hydrogel was studied using a thioflavin T (ThT) binding assay [49]. ThT is a cationic dye commonly used to detect the secondary structure of DNA. In an aqueous medium, ThT shows a very weak emission at  $483 \text{ nm}$  when excited at  $450 \text{ nm}$ . However, an increase in fluorescence intensity is observed when ThT binds with the **NP3** hydrogel. Therefore, this experiment shows an increased fluorescence intensity at  $488 \text{ nm}$  when excited at  $450 \text{ nm}$ . Consequently, the enhancement of ThT fluorescence indicates the presence of secondary structure of the nucleic acid within the hydrogel (**Figure 3.20c**) [50].

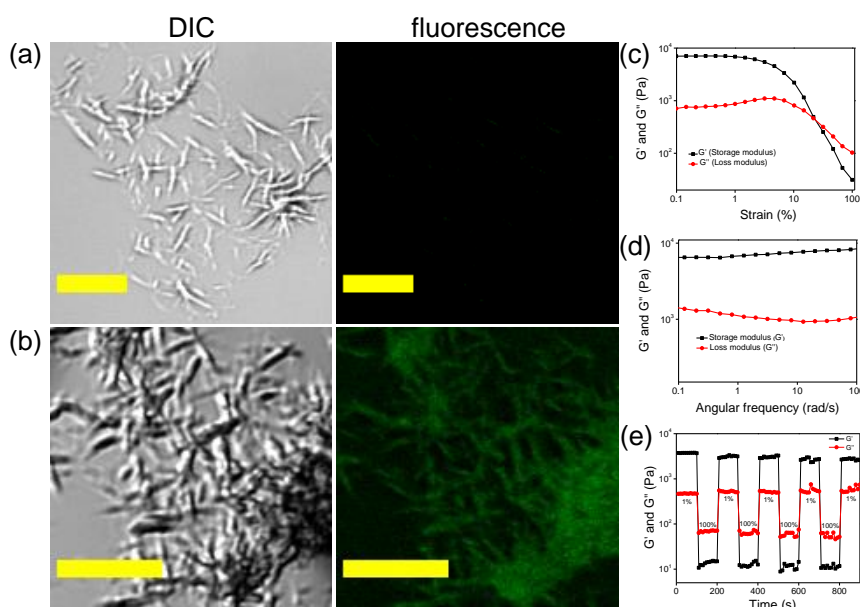


**Figure 3.21.** Confocal laser scanning microscopy images (DIC, Fluorescence) of (a) **NP3** hydrogel and (b) ThT loaded **NP3** hydrogel (scale bar =  $5 \mu\text{m}$ ). The images were taken after the formation of the

**NP3** hydrogel at day 1. Rheological experiments (c) amplitude sweeps experiment (d) frequency sweep experiment. Dynamic step-strain sweep profile of **NP3** hydrogel at a constant angular frequency of  $10 \text{ rad s}^{-1}$ .

The existence of secondary structures drives the formation of the hydrogel. The confocal laser scanning microscopy images also demonstrate that the fluorescence intensity of the hydrogel increases after the incorporation of ThT (**Figure 3.21a and 3.21b**) [51]. Further, these images clearly demonstrate the presence of fibers inside the hydrogel which contribute to its formation. The mechanical properties of the **NP3** hydrogel were studied by performing rheological experiments. The rheological experiments were carried out to understand the viscoelastic nature of the hydrogel formed by self-assembly of **NP3** with the addition of DMS [52]. The amplitude sweep experiment was carried out to determine the linear viscoelastic region at a constant frequency of  $10 \text{ rad/s}$ . The difference between storage modulus ( $G'$ ) and loss modulus ( $G''$ ) remains constant at lower strain. This indicates that the microstructure inside the hydrogel remains undisturbed. Although, the **NP3** hydrogel gradually converts into a sol as the strain increases. This occurs when the storage modulus intersects with the loss modulus, resulting to the disruption of the hydrogel networks [53]. The frequency sweep experiment was carried in the range of  $0.1$  to  $100 \text{ rad/s}$ , with a constant strain of  $1\%$ . During the experiment, the  $G'$  and  $G''$  values remained parallel to each other, suggesting the viscoelastic nature of the **NP3** hydrogel (**Figure 3.21c and 3.21d**). The thixotropic nature of the hydrogel was investigated through a cyclic dynamic strain sweep experiment. In this experiment, the applied strain was gradually increased from  $1\%$  to  $100\%$  over a period of  $100 \text{ s}$ , and then decreased back to  $1\%$  at the end of each cycle. This cycle was repeated 8 times to check the thixotropic nature of the **NP3** hydrogel. At lower strain levels, the storage modulus ( $G'$ ) values are higher than the loss modulus ( $G''$ ) values which indicates the presence of a stable hydrogel network. However, the storage modulus values decrease when the strain suddenly increases to  $100\%$ , and they become lower than the

loss modulus values. This indicates a transformation from the gel state to the sol state [54]. Once again, when the strain decreases suddenly to 1%, the storage modulus values gradually increase, suggesting the restoration of the gel state. The self-recovery of the hydrogel was 80% compared to the first cycle. This experiment reveals that the hydrogel has thixotropic properties (**Figure 3.21e**). Further, the progress of the self-assembly was investigated by performing time dependent changes in viscosity, fluorescence, turbidity of the reaction medium, and change in CD spectra over time [55-57]. These experiments were performed after the addition of DMS to **NP3**.

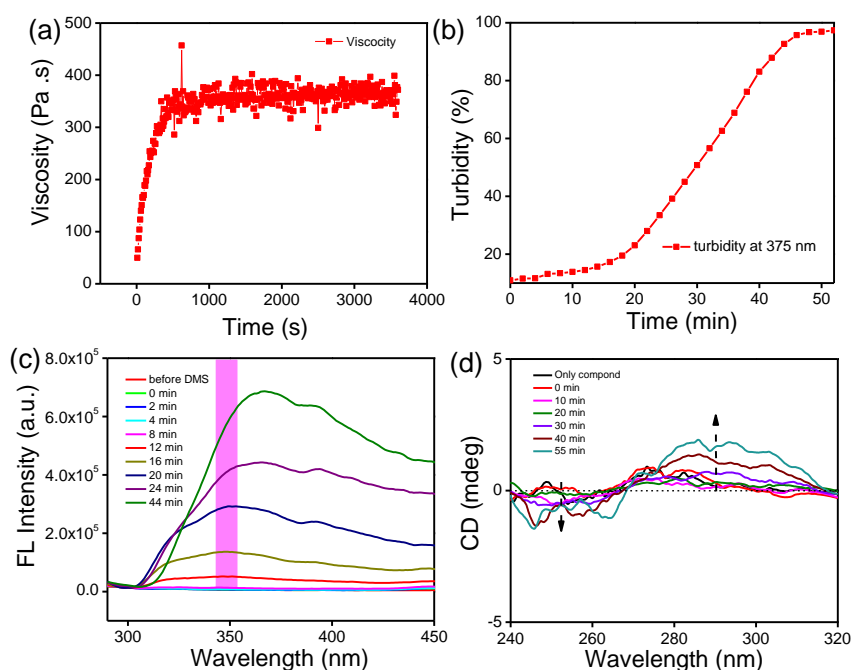


**Figure 3.22.** (a) The increase of viscosity with the time demonstrates the formation of the hydrogel after the addition of the DMS. (b) UV turbidity experiment. (c) Time dependent fluorescence spectra (d) time dependent CD spectra of the **NP3** hydrogel after the addition of the DMS.

The time dependent change in the viscosity of the system was evaluated by performing rheological experiment after the addition of DMS. As shown in **Figure 3.22a**, the addition of DMS causes an increase in viscosity of the reaction medium over time, as the energy is gradually stored in the system. The increase in viscosity suggests that the self-

assembly in the **NP3**/DMS system progresses over time [58,59]. The UV-vis turbidity experiment was carried out to observe the influence of DMS on the conversion of **NP3** to its corresponding methylated products. The results of this experiment show that the solution turns into turbid rapidly after adding DMS. The turbidity (%) reaches a constant value after 42 min. Therefore, this experiment provides evidence for the formation of higher order self-assembly through the addition of DMS (**Figure 3.22b**). Fluorescence has the potential to investigate the process of self-assembly due to its high sensitivity and selectivity. Luminogens, which have aggregation-induced characteristics, exhibit weak emission in solution but exhibit strong emission when they aggregate [60,61]. The self-assembly of **NP3** after adding DMS was further monitored using fluorescence and CD spectroscopy. The fluorescence spectra of **NP3** were recorded after adding DMS, upon excitation at 280 nm. Initially, there was no fluorescence before the addition of DMS. However, upon addition of DMS, the fluorescence intensity gradually increased due to aggregation induced emission phenomena. Therefore, the fluorescence experiment suggests that the self-assembly of **NP3** started after adding the methylating agent DMS (**Figure 3.22c**). The formation of the supramolecular order structure after the addition of DMS was studied. Circular dichroism (CD), an important spectroscopic technique, was used to study the secondary structure of the nucleic acid and biomolecules [62]. Therefore, CD spectroscopy was used to determine the progress of the self-assembly and presence of secondary structure of the nucleobase-functionalized molecule after adding DMS. In this study, a 200  $\mu$ m solution of **NP3** was prepared from an aliquot and the corresponding spectra were recorded at different time intervals. The CD spectrum of the DMS driven self-assembled hydrogel shows a positive peak at 280 nm and a negative peak at 248 nm (**Figure 3.22d**). The appearance of bisignate peaks indicates that the presence of nucleic acid secondary structures which helped to form the stable **NP3** hydrogel [63]. It is also important to note that no prominent peaks were observed before the addition of the DMS. The peaks only appear after the addition of the DMS. Additionally, the intensity of the peaks increases over time.

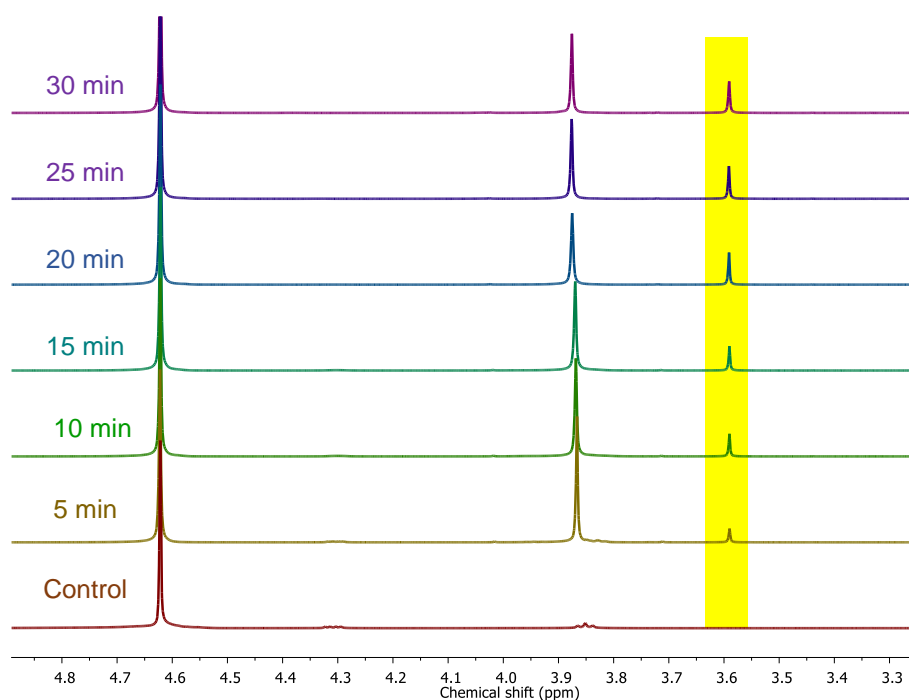


**Figure 3.23.** Time dependent NMR spectra depicting the formation of active molecules after the addition of dimethyl sulphate. From, the NMR spectrum, it is evident that the addition of DMS activate the precursor molecule which undergo higher order self-assembly to form the hydrogel. The control spectra are taken without DMS.

The formation of the activated building blocks after the addition of the DMS is studied by recording the  $^1\text{H}$  spectra at different time interval [64]. The time dependent  $^1\text{H}$ -NMR spectra also reveal the formation of active building blocks after the addition of dimethyl sulphate. The NMR spectrum was recorded in  $\text{D}_2\text{O}$  solvent. First, 5 mg of **NP3** was taken in a 2 mL eppendorf and 50  $\mu\text{L}$  of 0.5 N KOH was added (prepared in  $\text{D}_2\text{O}$ ) to dissolve the compound. Finally, 450  $\mu\text{L}$   $\text{D}_2\text{O}$  was added and then, the whole solution was then transferred into the NMR tube, and 5 equivalents of dimethyl sulphate were added into the same NMR tube. The spectra of **NP3** were recorded at 5 min intervals after the addition of the DMS. The NMR spectra clearly reveal the gradual formation of methylated product over time after the addition of the DMS. The peak at  $\delta = 3.67$  ppm represents the protons of the methyl group formed at N7 of the purine ring of **NP3**. However, the peak at  $\delta = 3.96$  ppm represents the proton in the dimethyl sulphate (**Figure 3.23**). Therefore, the DMS

activates **NP3**, which undergo higher order self-assembly to formed self-supporting hydrogel.

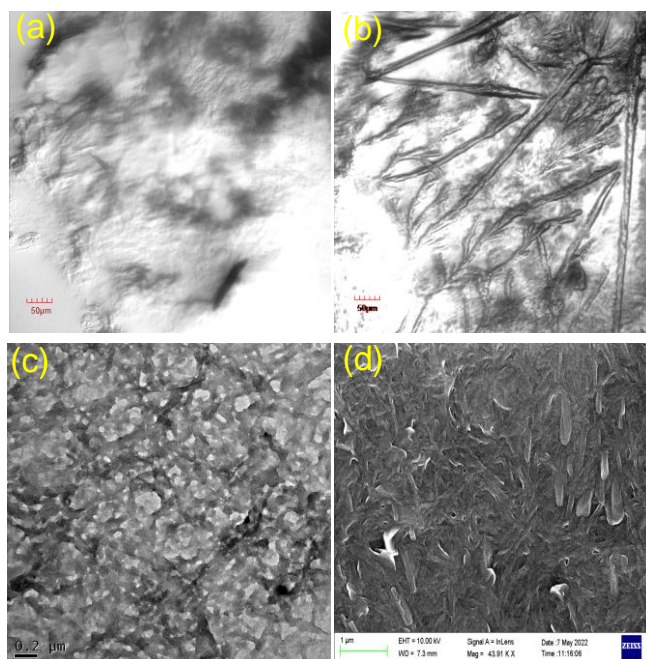


**Figure 3.24.** (a) CLSM image captured after the addition of the DMS (0 min) (b) CLSM images taken after 15 min from the addition of the DMS at the same region. Morphological assessment: (c) TEM (d) SEM images of the DMS-driven **NP3** hydrogel demonstrate the presence of fiber. The images were taken after the formation of the **NP3** hydrogel at day 1.

The presence of fibrous morphology was further characterized by electron microscopic techniques such as confocal laser scanning microscope (CLSM), FESEM and TEM [65]. The formation of the dense fiber after the addition of the DMS was observed by CLSM. (**Figure 3.24a and 3.24b**). SEM images suggest the presence of the nanofiber morphology inside the hydrogel (**Figure 3.24c and 3.24d**). The nanofiber inside helped to form the hydrogel [66]. The average width of the nanofiber is 45 nm. This observation, supported by a TEM image, was initially obtained from an SEM experiment. The average width of the nanofiber is 41 nm. It is conclusively shown by CLSM, FESEM and TEM that the fiber forms after the addition of DMS.

### 3.4 Conclusion

In conclusion, the formation of hydrogel by methylation of the synthesized nucleobase amino acid conjugates using the dimethyl sulphate was demonstrated. The dimethyl sulphate activated the gelator precursor to form the hydrogel by higher order self-organization. The formation of the activated gelator molecule was monitored by HPLC. Time dependent  $^1\text{H}$  NMR spectroscopy indicated the formation of activated self-assemble building block of **NP3**. Time dependent fluorescence, UV-turbidity experiment, time dependent CD and time dependent rheology depicted the progress of the self-assembly with time. ThT dye binding assay, wide angle powder XRD experiment and CD experiment revealed the nucleic acid secondary structure inside the hydrogel. This study is anticipated to pave a new way to mimic the biological processes using methylation with the guanine-based nucleic acids.

### 3.5 Reference

- [1] Pochan D, Scherman O (2021) Introduction: Molecular Self-Assembly. Chem Rev 121:13699–13700. <https://doi.org/10.1021/acs.chemrev.1c00884>.
- [2] Zhao X, Pan F, Xu H, Yaseen M, Shan H, Hauser, CAE, Zhang S, Lu, JR (2010) Molecular self-assembly and applications of designer peptide amphiphiles. Chem Soc Rev 39:3480. <https://doi.org/10.1039/b915923c>.
- [3] Fyfe MCT, Stoddart JF (1997) Synthetic Supramolecular Chemistry. Acc Chem Res 30:393–401. <https://doi.org/10.1021/ar950199y>.
- [4] Lehn J-M (2002) Toward Self-Organization and Complex Matter. Science 295:2400–2403. <https://doi.org/10.1126/science.1071063>.
- [5] Lei Z-C, Wang X, Yang L, Qu H, Sun Y, Yang Y, Li W, Zhang, W-B, Cao X-Y, Fan C, Li G, Wu J, Tian Z-Q (2024) What can molecular



assembly learn from catalysed assembly in living organisms? *Chem Soc Rev* 53:1892–1914. <https://doi.org/10.1039/D3CS00634D>.

[6] Van Den Ent F, Amos LA, Löwe J (2001) Prokaryotic origin of the actin cytoskeleton. *Nature* 413:39–44. <https://doi.org/10.1038/35092500>.

[7] Ghosh G, Barman R, Sarkar J, Ghosh S (2019) pH-Responsive Biocompatible Supramolecular Peptide Hydrogel. *J Phys Chem B* 123:5909–5915. <https://doi.org/10.1021/acs.jpcc.9b02999>.

[8] Sun S, Liang H-W, Wang H, Zou Q (2022) Light-Triggered Self-Assembly of Peptide Nanoparticles into Nanofibers in Living Cells through Molecular Conformation Changes and H-Bond Interactions. *ACS Nano* 16:18978–18989. <https://doi.org/10.1021/acsnano.2c07895>.

[9] Guo J, Yu X, Zhang Z, Li Y (2019) Self-healing gels triggered by ultrasound with color-tunable emission based on ion recognition. *J Colloid Interface Sci* 540:134–141. <https://doi.org/10.1016/j.jcis.2019.01.012>.

[10] Guo J, Li Y, Zhang Y, Ren J, Yu X, Cao X (2021) Switchable Supramolecular Configurations of  $\text{Al}^{3+}$ /LysTPY Coordination Polymers in a Hydrogel Network Controlled by Ultrasound and Heat. *ACS Appl Mater Inter* 13:40079–40087. <https://doi.org/10.1021/acsami.1c10150>.

[11] Wang H, Li H, Gu P, Huang C, Chen S, Hu C, Lee E, Xu J, Zhu J (2023) Electric, magnetic, and shear field-directed assembly of inorganic nanoparticles. *Nanoscale* 15:2018–2035. <https://doi.org/10.1039/D2NR05821A>.

[12] Gao Y, Shi J, Yuan D, Xu B (2012) Imaging enzyme-triggered self-assembly of small molecules inside live cells. *Nat Commun* 3:1033. <https://doi.org/10.1038/ncomms2040>.

[13] Zheng S, Chen X, Shen K, Cheng Y, Ma L, Ming X (2024) Hydrogen Bonds Reinforced Ionogels with High Sensitivity and Stable

Autonomous Adhesion as Versatile Ionic Skins. *ACS Appl Mater Inter* 16:4035–4044. <https://doi.org/10.1021/acsami.3c16195>.

[14] Zheng S, Chen X, Shen K, Cheng Y, Ma L, Ming X (2024) Hydrogen Bonds Reinforced Ionogels with High Sensitivity and Stable Autonomous Adhesion as Versatile Ionic Skins. *ACS Appl Mater Inter* 16:4035–4044. <https://doi.org/10.1021/acsami.3c16195>.

[15] Gabrielli V, Baretta R, Pilot R, Ferrarini A, Frasconi M (2022) Insights into the Gelation Mechanism of Metal-Coordinated Hydrogels by Paramagnetic NMR Spectroscopy and Molecular Dynamics. *Macromole* 55:450–461. <https://doi.org/10.1021/acs.macromol.1c01756>.

[16] Hu W, Wang Z, Xiao Y, Zhang S, Wang J (2019) Advances in crosslinking strategies of biomedical hydrogels. *Biomater Sci* 7:843–855. <https://doi.org/10.1039/C8BM01246F>.

[17] Li J, Xing R, Bai S, Yan X (2019) Recent advances of self-assembling peptide-based hydrogels for biomedical applications. *Soft Matter* 15:1704–1715. <https://doi.org/10.1039/C8SM02573H>.

[18] Xu F, Dawson C, Lamb M, Mueller E, Stefanek E, Akbari M, Hoare T (2022) Hydrogels for Tissue Engineering: Addressing Key Design Needs Toward Clinical Translation. *Front Bioeng Biotechnol* 10:849831. <https://doi.org/10.3389/fbioe.2022.849831>.

[19] Li J, Mooney DJ (2016) Designing hydrogels for controlled drug delivery. *Nat Rev Mater* 1:16071. <https://doi.org/10.1038/natrevmats.2016.71>.

[20] Gavel PK, Kumar N, Parmar HS, Das AK (2020) Evaluation of a Peptide-Based Coassembled Nanofibrous and Thixotropic Hydrogel for Dermal Wound Healing. *ACS Appl Bio Mater* 3:3326–3336. <https://doi.org/10.1021/acsabm.0c00252>.

[21] Lee HP, Lokhande G, Singh KA, Jaiswal MK, Rajput S, Gaharwar AK (2021) Light-Triggered In Situ Gelation of Hydrogels using 2D

Molybdenum Disulfide (MoS<sub>2</sub>) Nanoassemblies as Crosslink Epicenter. *Adv Mater* 33:2101238. <https://doi.org/10.1002/adma.202101238>.

[22] Chen L, Revel S, Morris K, Adams DJ (2010) Energy transfer in self-assembled dipeptide hydrogels. *Chem Commun* 46:4267. <https://doi.org/10.1039/c003052j>.

[23] Kaur H, Roy S (2021) Enzyme-Induced Supramolecular Order in Pyrene Dipeptide Hydrogels for the Development of an Efficient Energy-Transfer Template. *Biomacromole* 22:2393–2407. <https://doi.org/10.1021/acs.biomac.1c00187>.

[24] Rasale DB, Maity I, Das AK (2012) Emerging  $\pi$ -stacked dynamic nanostructured library. *RSC Adv* 2:9791. <https://doi.org/10.1039/c2ra21334f>.

[25] Toledano S, Williams RJ, Jayawarna V, Ulijn RV (2006) Enzyme-Triggered Self-Assembly of Peptide Hydrogels via Reversed Hydrolysis. *J Am Chem Soc* 128:1070–1071. <https://doi.org/10.1021/ja056549l>.

[26] Das AK, Maity I, Parmar HS, McDonald TO, Konda M (2015) Lipase-Catalyzed Dissipative Self-Assembly of a Thixotropic Peptide Bolaamphiphile Hydrogel for Human Umbilical Cord Stem-Cell Proliferation. *Biomacromole* 16:1157–1168. <https://doi.org/10.1021/bm501835v>.

[27] Cha JN, Stucky GD, Morse DE, Deming TJ (2000) Biomimetic synthesis of ordered silica structures mediated by block copolypeptides. *Nature* 403:289–292. <https://doi.org/10.1038/35002038>.

[28] Choy JS, Wei S, Lee JY, Tan S, Chu S, Lee T-H (2010) DNA Methylation Increases Nucleosome Compaction and Rigidity. *J Am Chem Soc* 132:1782–1783. <https://doi.org/10.1021/ja910264z>.

[29] Luo H-Y, Shen H-Y, Perkins RS, Wang Y-X (2022) Adenosine Kinase on Deoxyribonucleic Acid Methylation: Adenosine Receptor-

Independent Pathway in Cancer Therapy. *Front Pharmacol* 13:908882.  
<https://doi.org/10.3389/fphar.2022.908882>.

[30] Ban DK, Liu Y, Wang Z, Ramachandran S, Sarkar N, Shi Z, Liu W, Karkisaval AG, Martinez-Loran E, Zhang F, Glinsky G, Bandaru PR, Fan C, Lal R (2020) Direct DNA Methylation Profiling with an Electric Biosensor. *ACS Nano* 14:6743–6751.  
<https://doi.org/10.1021/acsnano.9b10085>.

[31] Wang J, Chen L, Gui C, Zhu J, Zhu B, Zhu Z, Li Y, Chen D (2023) A nanopore counter for highly sensitive evaluation of DNA methylation and its application in in vitro diagnostics. *Analyst* 148:1492–1499.  
<https://doi.org/10.1039/D3AN00035D>.

[32] Drabløs F, Feyzi E, Aas PA, Vaagbø CB, Kavli B, Bratlie MS, Peña-Díaz J, Otterlei M, Slupphaug G, Krokan HE (2004) Alkylation damage in DNA and RNA—repair mechanisms and medical significance. *DNA Repair* 3:1389–1407.  
<https://doi.org/10.1016/j.dnarep.2004.05.004>.

[33] Mishina Y, Duguid EM, He C (2006) Direct Reversal of DNA Alkylation Damage. *Chem Rev* 106:215–232.  
<https://doi.org/10.1021/cr0404702>.

[34] Oldrini B, Vaquero-Siguero N, Mu Q, Kroon P, Zhang Y, Galán-Ganga M, Bao Z, Wang Z, Liu H, Sa JK, Zhao J, Kim H, Rodriguez-Perales S, Nam D-H, Verhaak RGW, Rabadan R, Jiang T, Wang J, Squatrito M (2020) MGMT genomic rearrangements contribute to chemotherapy resistance in gliomas. *Nat Commun* 11:3883.  
<https://doi.org/10.1038/s41467-020-17717-0>.

[35] Soll JM, Sobol RW, Mosammamaparast N (2017) Regulation of DNA Alkylation Damage Repair: Lessons and Therapeutic Opportunities. *Trends Biochem Sci* 42:206–218.  
<https://doi.org/10.1016/j.tibs.2016.10.001>.

- [36] Jena NR, Shukla PK, Jena HS, Mishra PC, Suhai S (2009) O6-Methylguanine Repair by O6-Alkylguanine-DNA Alkyltransferase. *J Phys Chem B* 113:16285–16290. <https://doi.org/10.1021/jp907836w>.
- [37] Lee H-T, Sanford S, Paul T, Choe J, Bose A, Opresko PL, Myong S (2020) Position-Dependent Effect of Guanine Base Damage and Mutations on Telomeric G-Quadruplex and Telomerase Extension. *Biochem* 59:2627–2639. <https://doi.org/10.1021/acs.biochem.0c00434>.
- [38] Zhang P, Qiu T, Liu L, Lv F, Li Z, Ying J, Wang S (2020) Conjoint Analysis of DNA Methylation for Tumor Differentiation Using Cationic Conjugated Polymers. *ACS Appl Bio Mater* 3:2867–2872. <https://doi.org/10.1021/acsabm.0c00047>.
- [39] Yu W, Zhang L, Wei Q, Shao A (2020) O6-Methylguanine-DNA Methyltransferase (MGMT): Challenges and New Opportunities in Glioma Chemotherapy. *Front Oncol* 9:1547. <https://doi.org/10.3389/fonc.2019.01547>.
- [40] Bhowmik S, Ghosh T, Sanghvi YS, Das AK (2023) Synthesis and Structural Studies of Nucleobase Functionalized Hydrogels for Controlled Release of Vitamins. *ACS Appl Bio Mater* 6:5301–5309. <https://doi.org/10.1021/acsabm.3c00582>.
- [41] Wolfenden R, Yuan Y (2007) Monoalkyl sulfates as alkylating agents in water, alkylsulfatase rate enhancements, and the “energy-rich” nature of sulfate half-esters. *Proc Natl Acad Sci USA* 104:83–86. <https://doi.org/10.1073/pnas.0609644104>.
- [42] Skow CAR, Bicking MKL (1986) Direct alkylation of carboxylic in aqueous samples. *Chromatographia* 21:157–160. <https://doi.org/10.1007/BF02311745>.
- [43] Pal VK, Jain R, Roy S (2020) Tuning the Supramolecular Structure and Function of Collagen Mimetic Ionic Complementary Peptides via Electrostatic Interactions. *Langmuir* 36:1003–1013. <https://doi.org/10.1021/acs.langmuir.9b02941>.

- [44] Peters GM, Skala LP, Plank TN, Oh H, Manjunatha Reddy GN, Marsh A, Brown SP, Raghavan SR, Davis JT (2015) G4-Quartet·M<sup>+</sup> Borate Hydrogels. *J Am Chem Soc* 137:5819–5827. <https://doi.org/10.1021/jacs.5b02753>.
- [45] Arnal-Hérault C, Pasc A, Michau M, Cot D, Petit E, Barboiu M (2007) Functional G-Quartet Macroscopic Membrane Films. *Angew Chem Int Ed* 46:8409–8413. <https://doi.org/10.1002/anie.200702605>.
- [46] Ghosh S, Ghosh T, Bhowmik S, Patidar MK, Das AK (2023) Nucleopeptide-Coupled Injectable Bioconjugated Guanosine-Quadruplex Hydrogel with Inherent Antibacterial Activity. *ACS Appl Bio Mater* 6:640–651. <https://doi.org/10.1021/acsabm.2c00912>.
- [47] Ghosh T, Biswas A, Bhowmik S, Das AK (2021) Pt Nanoparticles Supported on a Dynamic Boronate Ester-Based G-quadruplex Hydrogel as a Nanoreactor. *Chem Asian J* 16:215–223. <https://doi.org/10.1002/asia.202001284>.
- [48] Arnal-Hérault C, Banu A, Barboiu M, Michau M, van der Lee A (2007) Amplification and Transcription of the Dynamic Supramolecular Chirality of the Guanine Quadruplex. *Angew Chem Int Ed* 119:4346–4350. <https://doi.org/10.1002/anie.200700787>.
- [49] Zhang S, Ding Y, Wei H (2014) Ruthenium Polypyridine Complexes Combined with Oligonucleotides for Bioanalysis: A Review. *Molecules* 19:11933–11987. <https://doi.org/10.3390/molecules190811933>.
- [50] Mohanty J, Barooah N, Dhamodharan V, Harikrishna S, Pradeepkumar PI, Bhasikuttan AC (2013) Thioflavin T as an Efficient Inducer and Selective Fluorescent Sensor for the Human Telomeric G-Quadruplex DNA. *J Am Chem Soc* 135:367–376. <https://doi.org/10.1021/ja309588h>.
- [51] Xu S, Li Q, Xiang J, Yang Q, Sun H, Guan A, Wang L, Liu Y, Yu L, Shi Y, Chen H, Tang Y (2016) Thioflavin T as an efficient

fluorescence sensor for selective recognition of RNA G-quadruplexes. *Sci Rep* 6:24793. <https://doi.org/10.1038/srep24793>.

[52] Townsend JM, Beck EC, Gehrke SH, Berkland CJ, Detamore MS (2019) Flow behavior prior to crosslinking: The need for precursor rheology for placement of hydrogels in medical applications and for 3D bioprinting. *Prog Polym Sci* 91:126–140. <https://doi.org/10.1016/j.progpolymsci.2019.01.003>.

[53] Barbucci R, Pasqui D, Favaloro R, Panariello G (2008) A thixotropic hydrogel from chemically cross-linked guar gum: synthesis, characterization and rheological behaviour. *Carbohydr Res* 343:3058–3065. <https://doi.org/10.1016/j.carres.2008.08.029>.

[54] Zhang H, Guo H, Liu Y, Shi C, Pan L, Zhang X, Zou J-J (2023) Thixotropic composite hydrogels based on agarose and inorganic hybrid gellants. *Chin J Chem Eng* 54:240–247. <https://doi.org/10.1016/j.cjche.2022.03.005>.

[55] Maiti S, Fortunati I, Ferrante C, Scrimin P, Prins LJ (2016) Dissipative self-assembly of vesicular nanoreactors. *Nature Chem* 8:725–731. <https://doi.org/10.1038/nchem.2511>.

[56] Gottarelli G, Lena S, Masiero S, Pieraccini S, Spada GP (2008) The use of circular dichroism spectroscopy for studying the chiral molecular self-assembly: An overview. *Chirality* 20:471–485. <https://doi.org/10.1002/chir.20459>.

[57] Pignataro MF, Herrera MG, Dodero VI (2020) Evaluation of Peptide/Protein Self-Assembly and Aggregation by Spectroscopic Methods. *Molecules* 25:4854. <https://doi.org/10.3390/molecules25204854>.

[58] Zhong R, Tang Q, Wang S, Zhang H, Zhang F, Xiao M, Man T, Qu X, Li L, Zhang W, Pei H (2018) Self-Assembly of Enzyme-Like Nanofibrous G-Molecular Hydrogel for Printed Flexible

Electrochemical Sensors. *Adv Mater* 30:1706887.  
<https://doi.org/10.1002/adma.201706887>.

[59] Lorenzo MM, Decker CG, Kahveci MU, Paluck SJ, Maynard HD (2016) Homodimeric Protein–Polymer Conjugates via the Tetrazine–trans -Cyclooctene Ligation. *Macromole* 49:30–37.  
<https://doi.org/10.1021/acs.macromol.5b02323>.

[60] Peng H-Q, Liu B, Wei P, Zhang P, Zhang H, Zhang J, Li K, Li Y, Cheng Y, Lam JWY, Zhang W, Lee C-S, Tang BZ (2019) Visualizing the Initial Step of Self-Assembly and the Phase Transition by Stereogenic Amphiphiles with Aggregation-Induced Emission. *ACS Nano* 13:839–846. <https://doi.org/10.1021/acsnano.8b08358>.

[61] Zhao Z, Chen S, Shen X, Mahtab F, Yu Y, Lu P, Lam JWY, Kwok HS, Tang BZ (2010) Aggregation-induced emission, self-assembly, and electroluminescence of 4,4'-bis(1,2,2-triphenylvinyl)biphenyl. *Chem Commun* 46:686–688. <https://doi.org/10.1039/B915271G>.

[62] Greenfield NJ (2006) Using circular dichroism spectra to estimate protein secondary structure. *Nat Protoc* 1:2876–2890.  
<https://doi.org/10.1038/nprot.2006.202>.

[63] Baek K, Noblett AD, Ren P, Suggs LJ (2019) Design and Characterization of Nucleopeptides for Hydrogel Self-Assembly. *ACS Appl Bio Mater* 2:2812–2821. <https://doi.org/10.1021/acsabm.9b00229>.

[64] Martin JC (1961) NMR spectroscopy as an analytical tool in organic chemistry. *J Chem Educ* 38:286.  
<https://doi.org/10.1021/ed038p286>.

[65] Kubota R, Tanaka W, Hamachi I (2021) Microscopic Imaging Techniques for Molecular Assemblies: Electron, Atomic Force, and Confocal Microscopies. *Chem Rev* 121:14281–14347.  
<https://doi.org/10.1021/acs.chemrev.0c01334>.



[66] Srikamut P, Theerasilp M, Crespy D (2023) Nanofibers as precursors for the rapid formation of hydrogels. *Chem Commun* 59:9952–9955. <https://doi.org/10.1039/D3CC01654D>.

## **Chapter 4**

# **Design and Synthesis of a Nucleobase Functionalized Peptide Hydrogel: *in vitro* Assessment of Anti-inflammatory and Wound Healing Effects**



## 4.1 Introduction

The skin, being the largest organ and the body's first line of defense, is crucial for shielding the body from germs and environmental damage. However, the skin is easily damaged, and once it has significant flaws, it takes a long time to heal [1]. Millions of people experience agony, suffering, and in extreme instances, disability due to wounds from burns, trauma, surgery, and chronic diseases. The global demand for wound dressing material is on the rise. Consequently, the financial burden of medical treatment is also increasing [2]. As a result, basic and efficient wound care remains a challenging issue that presents significant obstacles for the healthcare system. Wound healing is a crucial aspect of healthcare, aiming to restore normal cells and tissues function to protect against external threats, chemical and mechanical damage, and regulate body temperature [3-5]. However, wound repair encounters numerous obstacles, including bacterial infections and the immune and inflammatory processes involved in the restoration of healthy cells and tissues [6-10]. The skin is recognized as the biggest and most rapidly developing organ in an animal's body, functioning as a regenerative and self-restoring barrier between the body and extrinsic surroundings. Therefore, a potential hydrogel for wound healing should possess antimicrobial properties, facilitate gas exchange, and maintain a moist environment to support cell proliferation and cell migration. Wound healing is a complex process that involves several stages, including (a) inflammation, (b) coagulation, (c) mesenchymal cell proliferation, differentiation and migration, (d) re-epithelization and (e) angiogenesis [11,12]. The initial and preliminary stages of the wound healing process involve coagulation or hemostasis, which is achieved through fibrin formation, platelet aggregation, and vascular constriction to staunch the haemorrhage. The wound tissues and hemostatic clot secrete pro adhesive molecules, proinflammatory cytokines as well as several growth factors like platelet-based growth factor, epidermal, and fibroblast [13]. The proinflammatory cytokines initiate inflammation by sequentially attracting inflammatory cells, such as neutrophils,

macrophages and lymphocytes at the injury site. Inflammatory cells are liable for removing invading microorganisms, cellular debris and apoptotic cells from the wound site [13,14]. However, if inflammation is excessive and prolonged, it can trigger a cycle of pro-inflammatory signals that delay wound healing [15]. Therefore, controlling these proinflammatory signals is also important for the wound healing process. It is widely recognized that moist environments play a key role in accelerating wound healing, while dry surroundings can cause cell death, resulting in delayed healing [16]. However, excessive moisture near the wound can lead to microbial infection, resulting the wound to become a non-healing inflammatory condition [17]. Intrinsic antibacterial hydrogels, which eliminate bio-contaminants and maintain a moist environment, are an alternate kind of biomaterial for the wound healing process [18]. Furthermore, it is crucial that the optimal biomaterials for wound healing do not elicit any unwanted inflammatory or allergic reactions [19]. Recently, peptide-based soft materials have become significant [20,21]. As peptides have a unique biological role, activity, and specificity and are broadly distributed in the human body, both naturally occurring and chemically synthesized peptide molecules display a wide spectrum of biological effects [22-26]. Interestingly, peptides can form supramolecular architectures through various non-covalent weak interactions such as H-bonding and  $\pi$ - $\pi$  stacking [27-30]. Numerous reports in the literature report self-assembling peptide-based biomaterials that are efficient in repairing wound tissue [31-34]. These well-organized peptides possess a wide range of properties, including stimulating cellular and humoral immunity, mimicking extracellular matrix, and delivering drug molecules. The presence of nanofiber in the self-assembled peptide nanostructure resembles with the composition and structure of fibrin in the extracellular matrix, which aids in the healing of injured tissues and facilitates in the recovery of their cellular activities [35-37]. Moreover, low-molecular-weight peptide functionalized hydrogelators have better biocompatibility and biodegradability. Therefore, these peptide functionalized hydrogelators

are suitable for most tissue engineering applications [38]. Additionally, self-assembling peptide functionalized molecules can adapt to changes in complex wound healing processes and have shown significant promise for multimodal therapy [39]. Consequently, Hydrogels based on self-assembling peptides have several uses in biomedicine and nanotechnology, such as topical medications, immunological adjuvant therapy, tumor treatment, 3D tissue cell culture, tissue healing, and tissue regeneration [40-42]. Despite the progress in peptide based self-assembling materials, they still lack certain properties such as anti-inflammation. Nucleoside analogs are known to have anti-inflammatory effects [43,44]. In this study, we functionalized self-assembling peptide with the nucleobase guanine to form a nucleopeptide hydrogel. Guanine, having a number of H-bonding donor acceptor sides, can form self-assembled structures. Hence, this study focuses on the development and production of nucleopeptide based bioactive biomaterials, which have the ability to heal wounds. The key objectives of this project include: (a) designing and synthesizing guanine functionalized peptide molecules, (b) formation of self-assembling biomaterials from the newly synthesized nucleopeptides, (c) testing the self-assembly propensity through molecular dynamic simulation, (d) conducting in vitro cytotoxicity assays, (e) performing in vitro wound healing assays, (f) assessing the hemolytic activity of the synthesized hydrogel, (g) evaluating anti-inflammatory activity of the **NP5** hydrogel and (h) testing the antibacterial activity of the **NP5** hydrogel.

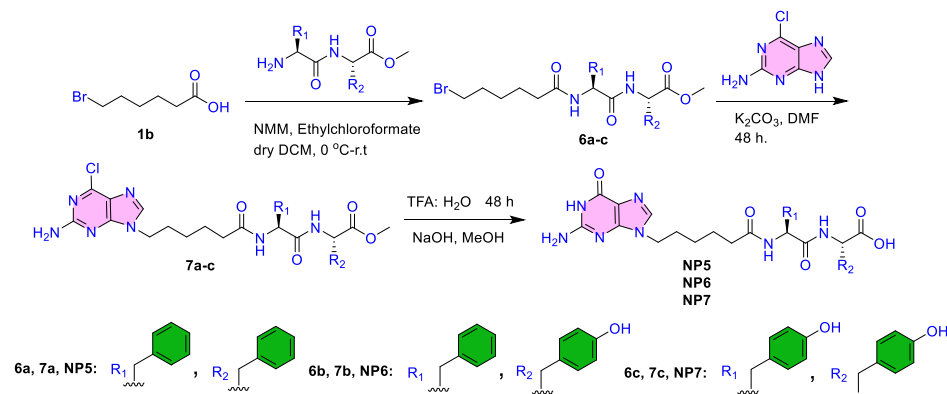
## **4.2 Experimental Section**

### **4.2.1 Materials and Methods**

The used solvents and reagents were purchased from commercially available sources like Alfa Aesar, Sigma Aldrich, Merck and Spectrochem Pvt. Ltd. India. 2-Amino-6-chloropurine and potassium carbonate ( $K_2CO_3$ ) were obtained from Alfa Aesar. Ethyl chloroformate was purchased from Spectrochem whereas diethyl ether was purchased from Merck. 4-Methylmorpholine was obtained from SRL and 6-Bromohexanoic acid were obtained from TCI. L-Phenylalanine, L-

tyrosine were purchased from SRL. Fetal bovine serum, MTT (3-(4,5-dimethyl-2-thiazolyl)-2,5-diphenyl-2H-tetrazolium bromide, Dulbecco's Modified Eagle Medium (DMEM) and Streptomycin were obtained from Himedia. FDA, DCFDA and propidium iodide were obtained from Invitrogen. For moisture sensitive reactions, dry solvent was used in the presence of N<sub>2</sub> or Ar gas. After completion of the reaction, the crude products were purified by column chromatography method using silica as stationary phase and hexane, ethyl acetate or chloroform, methanol as a mobile phase. All <sup>1</sup>H and <sup>13</sup>C NMR spectra were set down on Bruker Avance (500 MHz) instrument at 25 °C. Mass spectra were set down on Bruker instrument by using ESI positive mode. The NMR spectra of all intermediates and final products were analyzed by using MestReNova software. Chemical shift was expressed in the form of ppm ( $\delta$ ) relative to surplus solvents protons as internal standards (DMSO-*d*<sub>6</sub>:  $\delta$  = 2.50 for <sup>1</sup>H NMR; DMSO-*d*<sub>6</sub>:  $\delta$  39.50 for <sup>13</sup>C NMR).

#### 4.2.2 Synthesis of NPs



**Scheme 4.1** Synthesis of Nucleobase functionalized peptide derivatives (NPs)

#### 4.2.3 General procedure for the synthesis of 6a-c:

Under argon atmosphere 4-methylmorpholine was added in the solution of 6-bromohexanoic acid in dry chloroform at 0 °C. The solution was left for stirring at this temperature. After 15 min, ethyl chloroformate was added into the solution and stirred vigorously at this temperature for additional 45 min before the addition of acid protected dipeptide and 4-

methylmorpholine. Then the reaction mixture was allowed to stir for 1 h at 0 °C and then at room temperature for 16 h. The progress of the reaction was monitored by TLC. After the completion of the reaction, reaction mixture was diluted with chloroform and washed with 1(N) NaOH (3×10 mL) and then with brine, 1 (N) HCl (3×10 mL) and finally with brine. The organic part was dried over Na<sub>2</sub>SO<sub>4</sub> and concentrate under vacuum.

#### 4.2.4 Synthesis of 6a:

<sup>1</sup>H NMR (DMSO-*d*<sub>6</sub>, 400 MHz): 1.19-1.28 (m, 2H), 1.35-1.46 (m, 2H), 1.72-1.79 (m, 2H), 2.04-2.07 (t, 2H, *J* = 4, 8 Hz), 2.71-2.77 (m, 1H), 2.99-3.04 (m, 1H), 3.08-3.13 (m, 1H), 3.48-3.51 (t, 2H, *J* = 4, 8 Hz), 3.65 (s, 1H), 4.53-4.58 (m, 1H), 4.60-4.65 (m, 1H), 7.24-7.36 (m, 10H), 8.02-8.04 (d, 1H, *J* = 4 Hz), 8.47-8.49 (d, 1H, *J* = 4 Hz). (ESI-MS, *m/z*): [M+Na]<sup>+</sup> calculated for C<sub>25</sub>H<sub>31</sub>BrN<sub>2</sub>O<sub>4</sub>Na 525.1359; found 525.1152

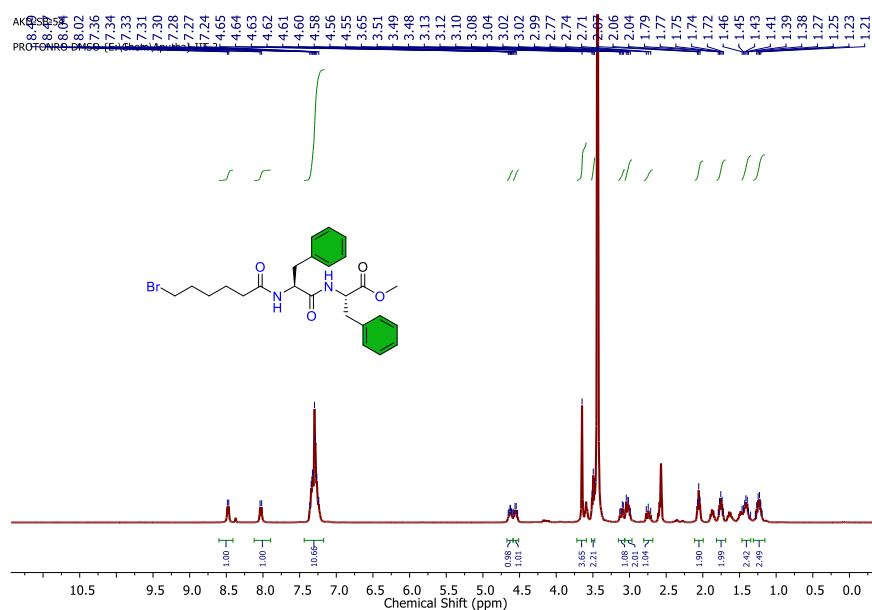


**Figure 4.1.** <sup>1</sup>H NMR (500 MHz, DMSO-*d*<sub>6</sub>) spectrum of **6a**.

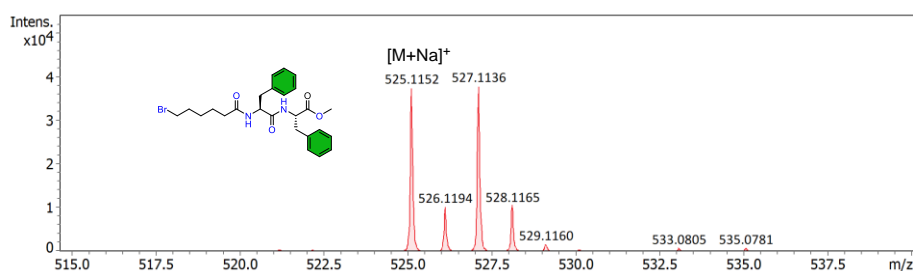




**Figure 4.2** ESI-MS spectrum of **6a**.

#### 4.2.5 Synthesis of **6b**:

$^1\text{H}$  NMR ( $\text{DMSO-}d_6$ , 500 MHz): 1.14-1.20 (m, 2H), 1.31-1.40 (m, 2H), 1.58-1.73 (m, 2H), 2.66-2.71 (m, 1H), 2.82-2.99 (m, 4H), 3.43-3.45 (t, 1H,  $J = 5$ , 5 Hz), 3.53-3.55 (t, 1H,  $J = 5$ , 5 Hz), 3.58 (s, 3H), 4.38-4.43 (m, 1H), 4.55-4.60 (m, 1H), 6.65-6.67 (d, 2H,  $J = 10$  Hz), 6.99-7.00 (d, 2H,  $J = 5$  Hz), 7.16-7.27 (m, 5H), 7.97-7.99 (d, 1H,  $J = 10$  Hz), 8.33-8.34 (d, 1H,  $J = 5$  Hz), 9.23 (s, 1H). (ESI-MS,  $m/z$ ):  $[\text{M}+\text{Na}]^+$  calculated for  $\text{C}_{25}\text{H}_{31}\text{BrN}_2\text{O}_5\text{Na}$  541.1416; found 541.1010.

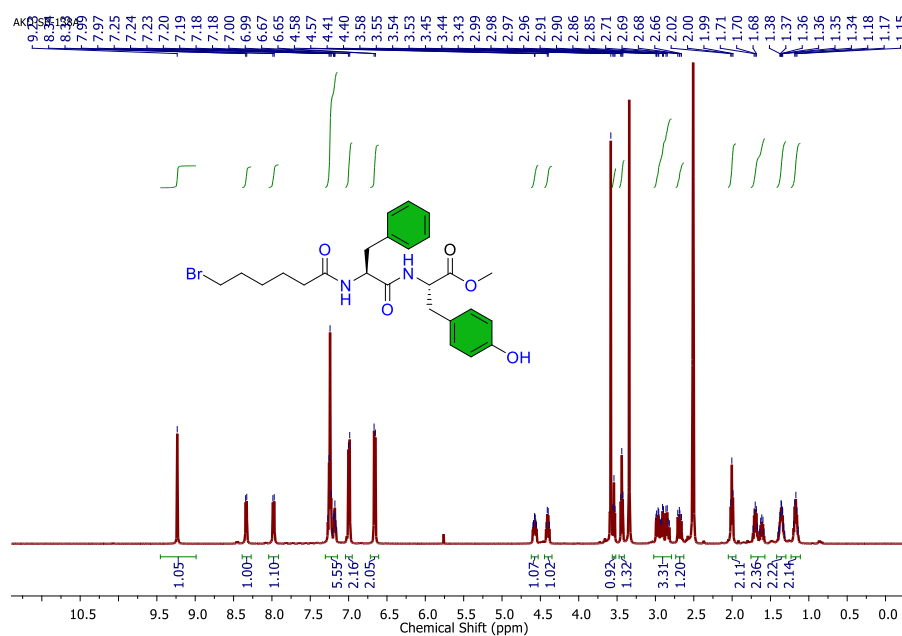


**Figure 4.3.**  $^1\text{H}$  NMR (500 MHz,  $\text{DMSO-}d_6$ ) spectrum of **6b**.

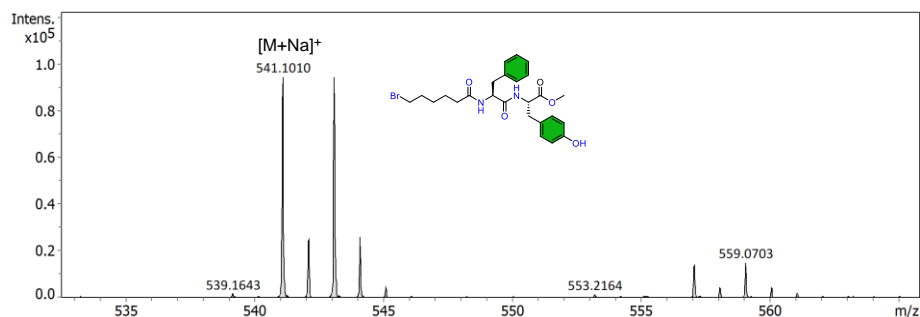


**Figure 4.4** ESI-MS spectrum of **6b**.

#### 4.2.6 Synthesis of 6c:

$^1\text{H}$  NMR (DMSO- $d_6$ , 400 MHz): 1.19-1.24 (m, 2H), 1.36-1.39 (m, 2H), 1.61-1.75 (m, 2H), 1.99-2.03 (t, H,  $J = 8$ , 8 Hz), 2.80-2.93 (m, 4H), 3.44-3.47 (t, 2H,  $J = 4$ , 8 Hz), 3.57 (s, 1H), 4.36-4.41 (m, 1H), 4.44-4.47 (m, 1H), 6.62-6.66 (t, 4H,  $J = 8$ , 8 Hz), 6.97-7.02 (t, 4H,  $J = 8$ , 12 Hz), 7.88-7.90 (d, 1H,  $J = 8$  Hz) 8.26-8.28 (d, 1H,  $J = 8$  Hz), 9.13 (s, 1H), 9.22 (s, 1H). (ESI-MS,  $m/z$ ):  $[\text{M}+\text{Na}]^+$  calculated for  $\text{C}_{25}\text{H}_{31}\text{BrN}_2\text{O}_6\text{Na}$  557.1365; found 557.1105.

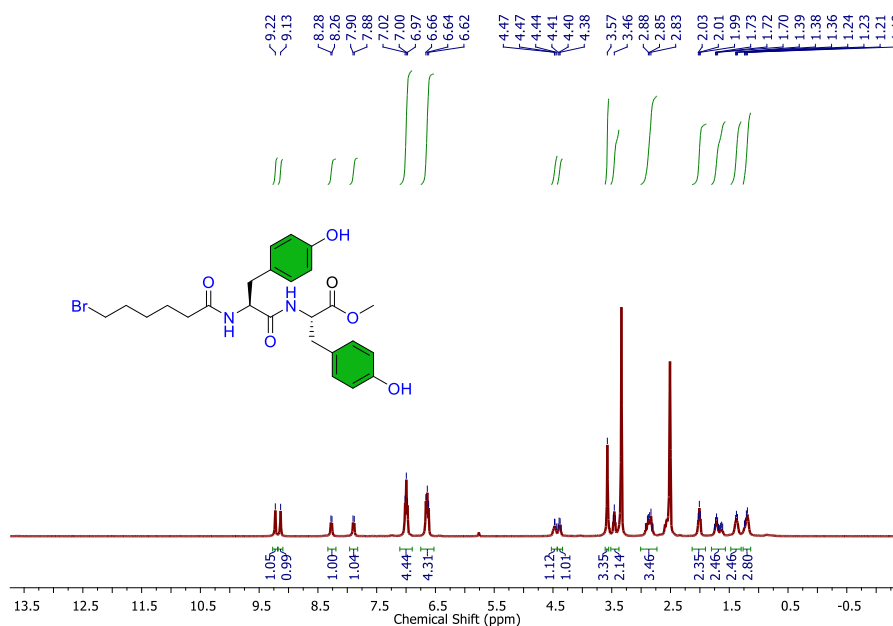


**Figure 4.5.**  $^1\text{H}$  NMR (500 MHz, DMSO- $d_6$ ) spectrum of **6c**.

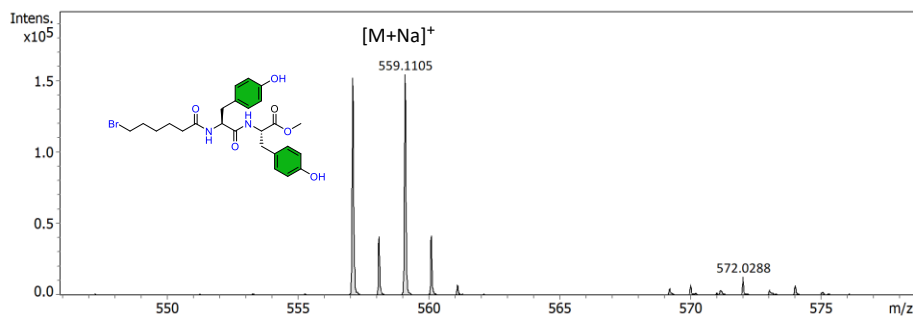


**Figure 4.6** ESI-MS spectrum of **6c**.

#### 4.2.7 General procedure for the synthesis of 7a-c:

Here the compounds were synthesized following previously reported synthetic procedure. 2-Amino-6-chloropurine was added in the solution of dry DMF (10 mL) under argon atmosphere. Then  $K_2CO_3$  was added in the solution. Finally, 6-bromohexanoic acid was added dropwise into the solution and the reaction was left for stirring for 24 h. The progress of the reaction was monitored by TLC. After the completion of the reaction, the reaction mixture was diluted with ethyl acetate and washed with water several times, finally with brine and dried over  $Na_2SO_4$ . After the evaporation of the solvent under rotary evaporator, the reaction mixture was purified by silica gel column chromatography. The major product was N9 alkylated product (eluent:  $CHCl_3$ : MeOH = 99:1) and the minor product was N7 alkylated product (eluent:  $CHCl_3$ : MeOH = 94:6).

#### 4.2.8 Synthesis of 7a:

$^1H$  NMR ( $DMSO-d_6$ , 500 MHz): 1.01-1.07 (m, 2H), 1.36-1.40 (m, 2H), 1.62-1.70 (m, 2H), 1.97-2.00 (t, 2H,  $J = 5, 10$  Hz), 2.64-2.69 (m, 2H), 2.93-2.98 (m, 2H), 3.02-3.06 (m, 1H), 3.58 (s, 3H), 3.93-3.96 (t, 2H,  $J = 5, 10$  Hz), 4.47-4.51 (m, 1H), 4.53-4.58 (m, 1H), 6.90 (s, 2H), 7.14-7.29 (m, 5H) 7.94-7.96 (d, 1H,  $J = 10$  Hz), 8.10 (s, 1H), 8.42-8.44 (d, 1H,  $J = 10$  Hz), 9.23 (s, 1H). (ESI-MS,  $m/z$ ):  $[M+Na]^+$  calculated for  $C_{30}H_{34}ClN_7O_4Na$  614.2361; found 614.2266.

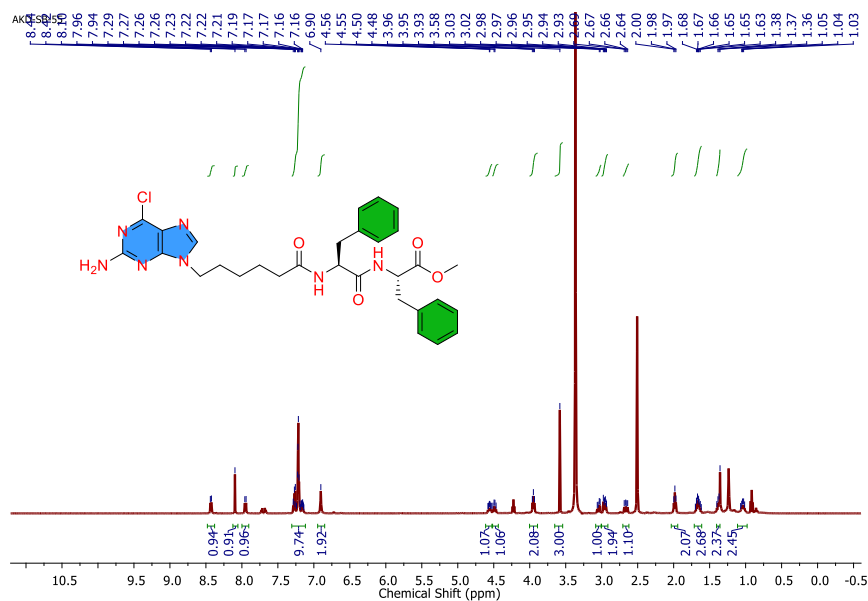


**Figure 4.7.**  $^1\text{H}$  NMR (500 MHz,  $\text{DMSO}-d_6$ ) spectrum of **7a**.

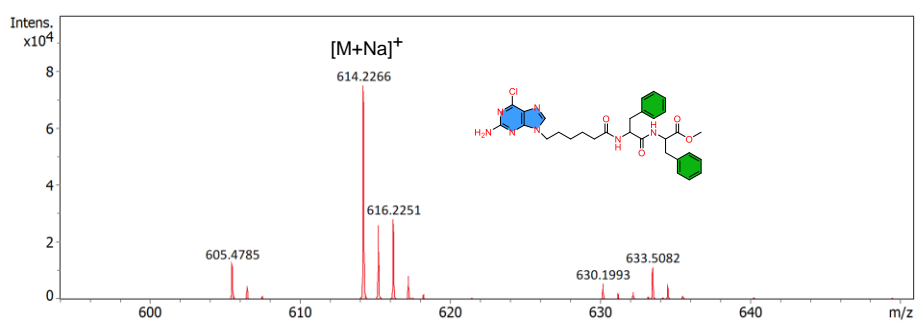


**Figure 4.8** ESI-MS spectrum of **7a**.

#### 4.2.9 Synthesis of 7b:

$^1\text{H}$  NMR ( $\text{DMSO}-d_6$ , 500 MHz): 0.99-1.05 (m, 2H), 1.32-1.40 (m, 2H), 1.62-1.68 (m, 2H), 1.96-1.99 (d, 2H,  $J = 5, 10$  Hz), 2.62-2.67 (m, 1H), 2.79-2.84 (m, 1H), 2.87-2.96 (m, 2H), 3.56 (s, 1H), 3.92-3.94 (t, 1H,  $J = 5, 10$  Hz), 4.36-4.40 (m, 1H), 4.51-4.56 (m, 1H), 6.63-6.64 (d, 2H,  $J = 5$  Hz), 6.87 (s, 2H), 6.97-6.98 (d, 2H,  $J = 5$  Hz), 7.12-7.21 (m, 5H), 7.93-7.95 (d, 2H,  $J = 10$  Hz) 8.07 (s, 1H), 8.32-8.33 (d, 1H,  $J = 5$  Hz), 9.27 (s, 1H). (ESI-MS,  $m/z$ ):  $[\text{M}+\text{H}]^+$  calculated for  $\text{C}_{30}\text{H}_{35}\text{ClN}_7\text{O}_5$  608.2310; found 608.2286.

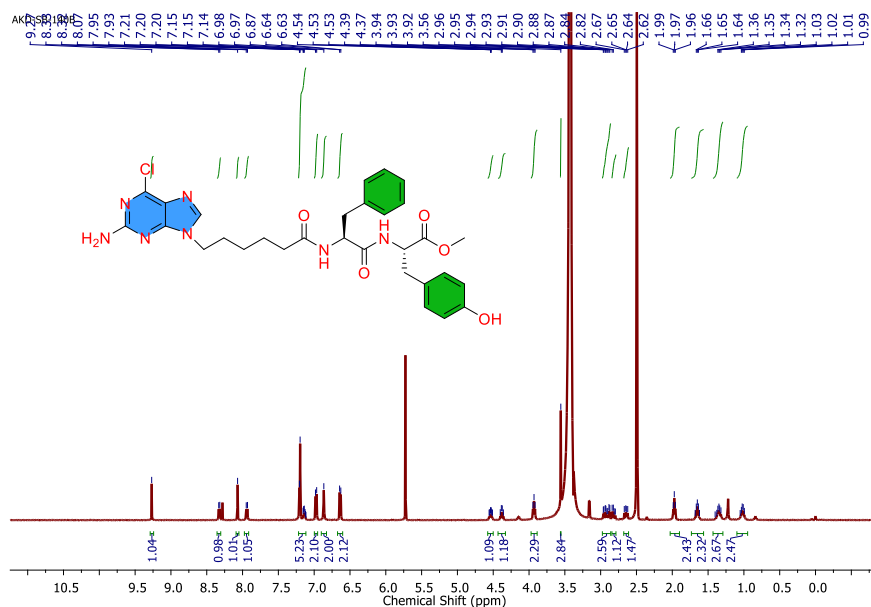


**Figure 4.9.**  $^1\text{H}$  NMR (500 MHz,  $\text{DMSO}-d_6$ ) spectrum of **7b**.

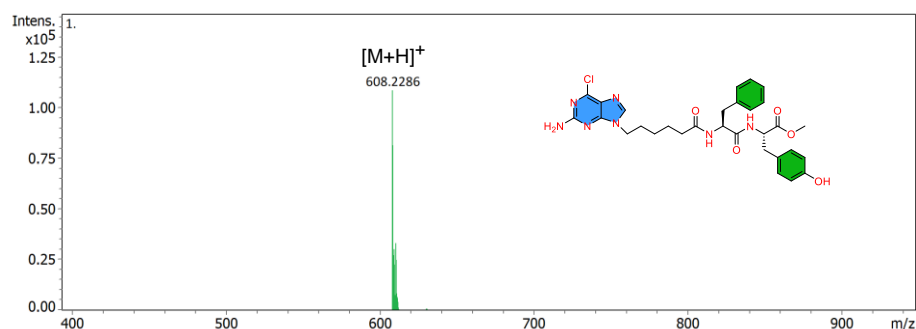


**Figure 4.10** ESI-MS spectrum of **7b**.

#### 4.2.10 Synthesis of **7c**:

$^1\text{H}$  NMR ( $\text{DMSO}-d_6$ , 500 MHz): 1.04-1.11 (m, 2H), 1.36-1.42 (m, 2H), 1.66-1.71 (m, 2H), 1.99-2.02 (d, 2H,  $J = 5, 10$  Hz), 2.81-2.92 (m, 4H), 3.57 (s, 3H), 3.94-3.97 (t, 1H,  $J = 5, 10$  Hz), 4.37-4.41 (m, 1H), 4.45-4.49 (m, 1H), 6.62-6.66 (m, 4H), 6.91 (s, 2H), 6.98-7.02 (m, 4H), 7.88-7.89 (d, 2H,  $J = 5$  Hz), 8.10 (s, 1H), 8.29-8.30 (d, 1H,  $J = 5$  Hz), 9.15 (s, 1H), 9.23 (s, 1H). (ESI-MS,  $m/z$ ):  $[\text{M}+\text{H}]^+$  calculated for  $\text{C}_{30}\text{H}_{35}\text{ClN}_7\text{O}_6$  624.2259; found 624.2375.

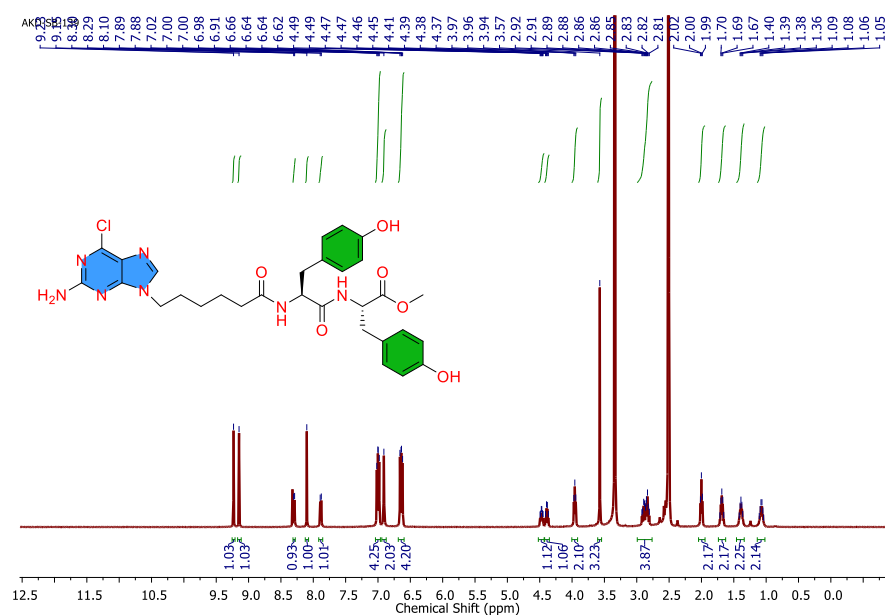


**Figure 4.11.**  $^1\text{H}$  NMR (500 MHz,  $\text{DMSO}-d_6$ ) spectrum of **7c**.

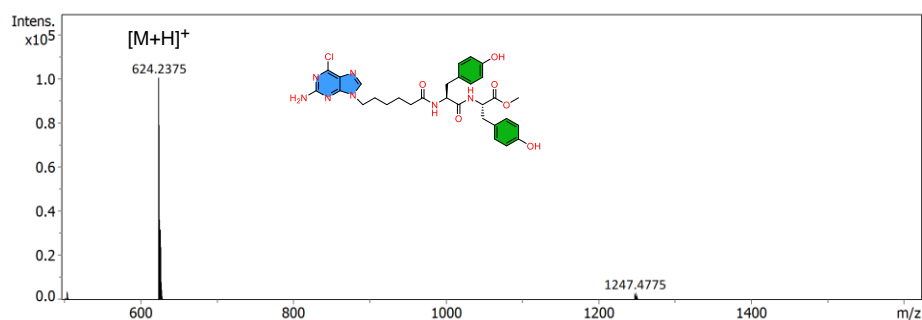


**Figure 4.12** ESI-MS spectrum of **7c**.

#### 4.2.11 General procedure for the synthesis of compound NP5-7:

These compounds were synthesized based on the previously reported synthetic procedure. These compounds were dissolved in the TFA:  $\text{H}_2\text{O}$  (3:1) 5 mL. Then, the reaction was left for stirring for a period of 48 h at room temperature. The progress of the reaction was monitored by HPLC. After the completion of the oxidation reaction, TFA was evaporated under vacuum. Then the residue was dissolved in MeOH, dropwise 1(N) NaOH was added to get the completely hydrolysed product. The progress of the hydrolysis was also monitored by HPLC. After the completion of the hydrolysis, MeOH was evaporated under vacuum, and then it was dissolved in water, and also washed with diethyl ether. Then, after washing the pH of the solution was slowly decreased

to obtain the white precipitate. Then it was recrystallized in MeOH to obtain the pure product.

#### 4.2.12 Synthesis of NP5:

$^1\text{H}$  NMR (DMSO- $d_6$ , 500 MHz): 0.93-1.00 (m, 2H), 1.26-1.32 (m, 2H), 1.51-1.59 (m, 2H), 1.89-1.96 (m, 2H), 2.54-2.63 (m, 1H), 2.83-2.93 (m, 2H), 3.00-3.03 (m, 1H), 3.74-3.77 (t, 2H,  $J = 5, 10$  Hz), 4.30-4.35 (m, 1H), 4.40-4.46 (m, 1H), 6.45 (s, 1H), 7.09-7.20 (m, 10H), 7.57 (s, 1H), 7.92-7.93 (d, 1H,  $J = 5$  Hz) 8.04-8.05 (d, 1H,  $J = 5$  Hz), 10.57 (s, 1H).  $^{13}\text{C}$  NMR (DMSO- $d_6$ , 125 MHz):  $\delta$  25.06, 25.84, 29.64, 35.42, 37.35, 37.82, 42.91, 54.58, 54.84, 116.97, 126.48, 128.41, 129.93, 137.76, 138.73, 151.54, 154.32, 157.41, 171.32, 172.34, 173.39. (ESI-MS,  $m/z$ ):  $[\text{M}+\text{Na}]^+$  calculated for  $\text{C}_{29}\text{H}_{33}\text{N}_7\text{O}_5\text{Na}$  582.2435; found 582.2407.

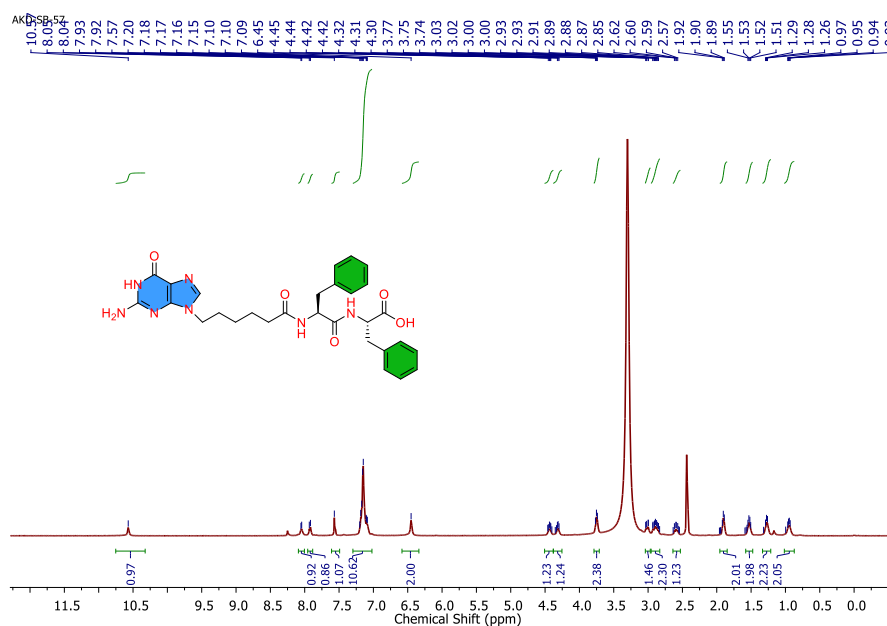


**Figure 4.13.**  $^1\text{H}$  NMR (500 MHz, DMSO- $d_6$ ) spectrum of NP5.

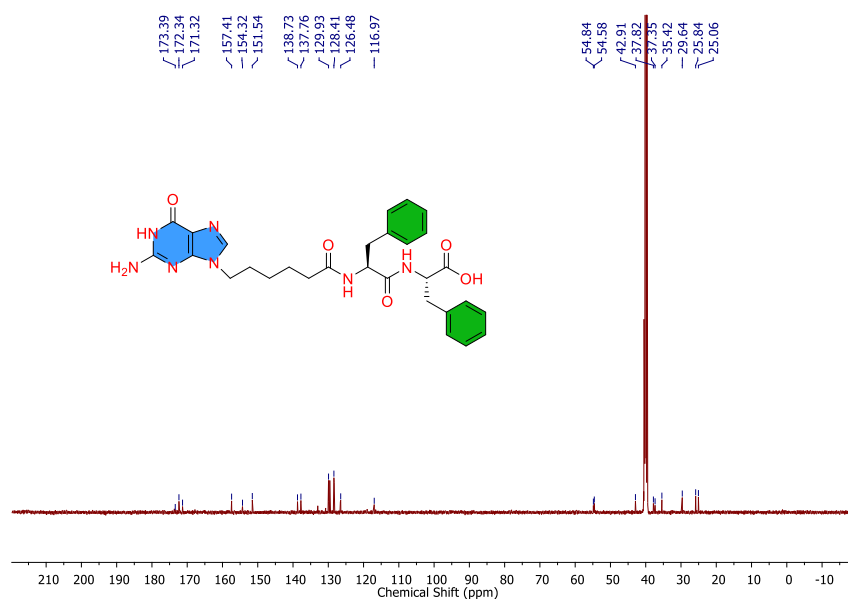


**Figure 4.14**  $^{13}\text{C}$  NMR (125 MHz,  $\text{DMSO}-d_6$ ) spectrum of NP5.

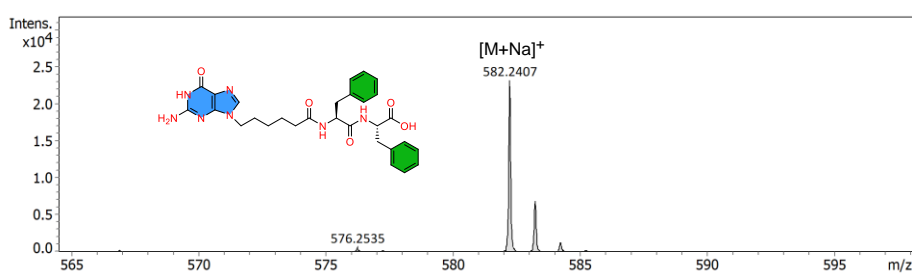


**Figure 4.15** ESI-MS spectrum of NP5.

#### 4.2.13 Synthesis of NP6:

$^1\text{H}$  NMR ( $\text{DMSO}-d_6$ , 500 MHz): 0.98-1.07 (m, 2H), 1.32-1.38 (m, 2H), 1.58-1.64 (m, 2H), 1.97-2.00 (m, 2H), 2.65-2.70 (m, 1H), 2.80-2.84 (m, 1H), 2.93-3.01 (m, 2H), 3.81-3.84 (t, 1H,  $J = 5, 10$  Hz), 4.34-4.38 (m, 1H), 4.52-4.57 (m, 1H), 6.47 (s, 2H), 6.65-6.66 (d, 2H,  $J = 5$  Hz), 7.01-7.02 (d, 2H,  $J = 5$  Hz), 7.15-7.23 (m, 5H), 7.68 (s, 1H), 7.95-7.97 (d, 1H,  $J = 10$  Hz), 8.13-8.14 (d, 1H,  $J = 5$  Hz), 9.23 (s, 1H), 10.56 (s, 1H), 12.70 (s, 1H).  $^{13}\text{C}$  NMR ( $\text{DMSO}-d_6$ , 125 MHz):  $\delta$  25.05, 25.84, 29.62, 35.39, 36.34, 37.92, 42.99, 53.86, 54.24, 115.45, 116.82, 126.62, 127.79, 128.39, 129.64, 130.55, 137.83, 138.46, 151.52, 153.98, 156.42, 157.20,



171.92, 172.25, 173.32. (ESI-MS,  $m/z$ ):  $[M+Na]^+$  calculated for  $C_{29}H_{33}N_7O_6Na$  598.2385; found 598.2380.

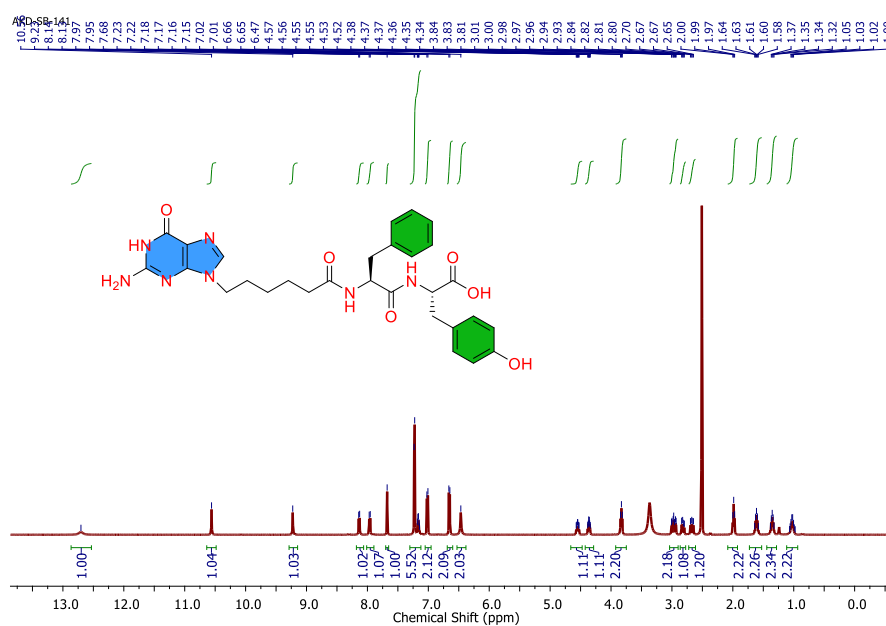


**Figure 4.16.** <sup>1</sup>H NMR (500 MHz, DMSO-*d*<sub>6</sub>) spectrum of NP6.

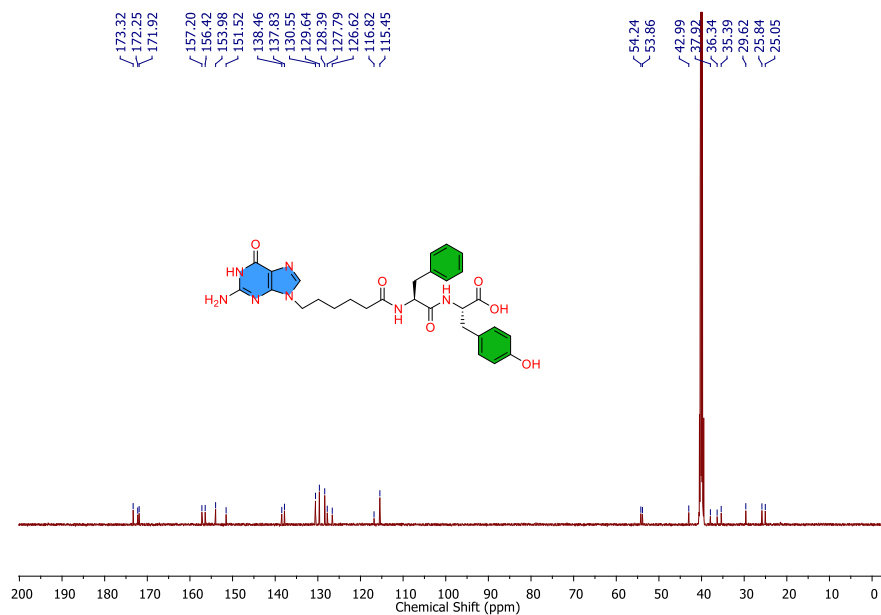


**Figure 4.17** <sup>13</sup>C NMR (125 MHz, DMSO-*d*<sub>6</sub>) spectrum of NP6.

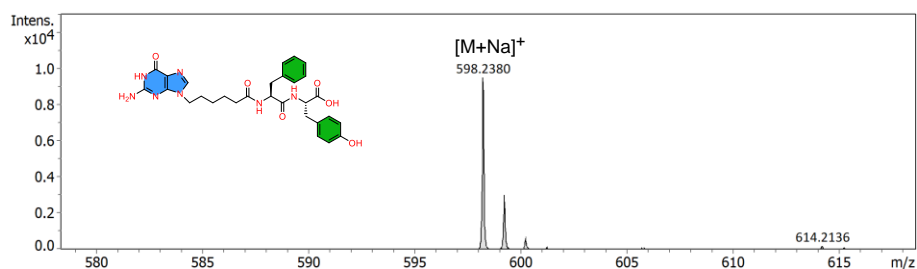


**Figure 4.18** ESI-MS spectrum of NP6.

#### 4.2.14 Synthesis of NP7:

$^1\text{H}$  NMR (DMSO- $d_6$ , 500 MHz): 1.03-1.10 (m, 2H), 1.36-1.39 (m, 2H), 1.59-1.63 (m, 2H), 1.98-2.01 (m, 2H), 2.81-2.98 (m, 4H), 3.82-3.84 (t, 2H,  $J = 5, 5$  Hz), 4.19-4.21 (m, 1H), 4.35-4.38 (m, 1H), 6.61-6.64 (m, 4H), 6.66 (s, 2H), 6.96-7.02 (m, 4H), 7.64 (s, 1H) 7.80-7.81 (d, 1H,  $J = 5$  Hz), 7.98-8.00 (d, 1H,  $J = 10$  Hz), 9.21 (s, 2H), 10.89 (s, 1H).  $^{13}\text{C}$  NMR (DMSO- $d_6$ , 125 MHz):  $\delta$  25.12, 25.93, 29.76, 35.47, 36.42, 37.10, 42.98, 54.83, 54.85, 115.24, 117.00, 130.48, 130.73, 137.82, 151.55, 154.16, 156.14, 156.21, 157.42, 171.53, 172.32, 173.56. (ESI-MS,  $m/z$ ):  $[\text{M}+\text{H}]^+$  calculated for  $\text{C}_{29}\text{H}_{34}\text{N}_7\text{O}_7$  592.2514; found 592.2536.

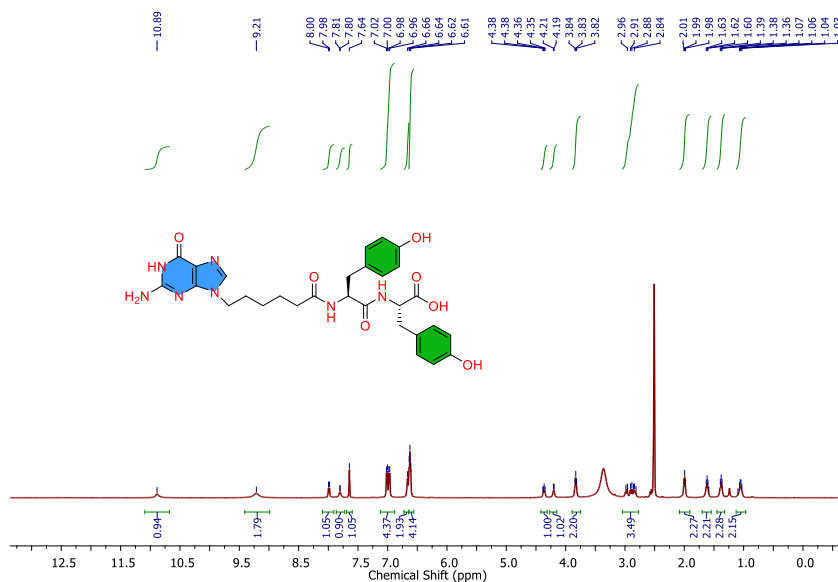


**Figure 4.19**  $^1\text{H}$  NMR (500 MHz, DMSO- $d_6$ ) spectrum of NP7.

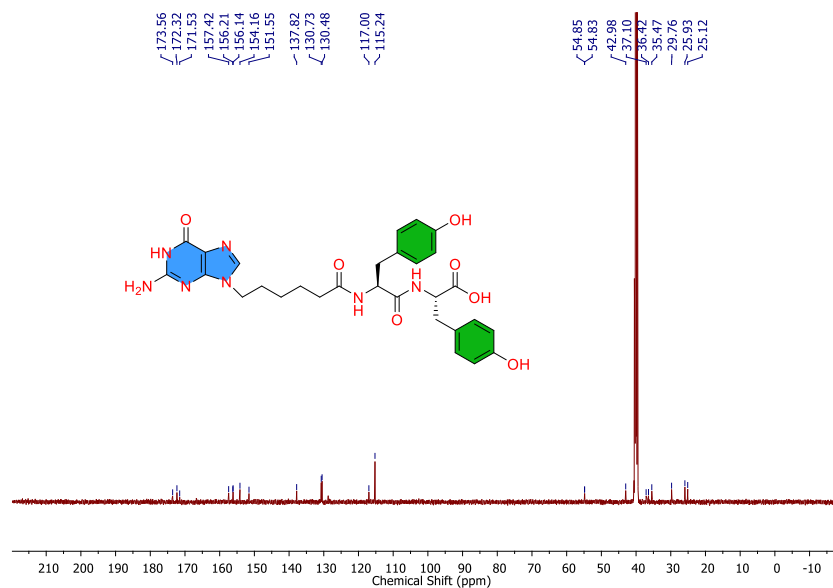


**Figure 4.20**  $^{13}\text{C}$  NMR (125 MHz,  $\text{DMSO}-d_6$ ) spectrum of NP7.

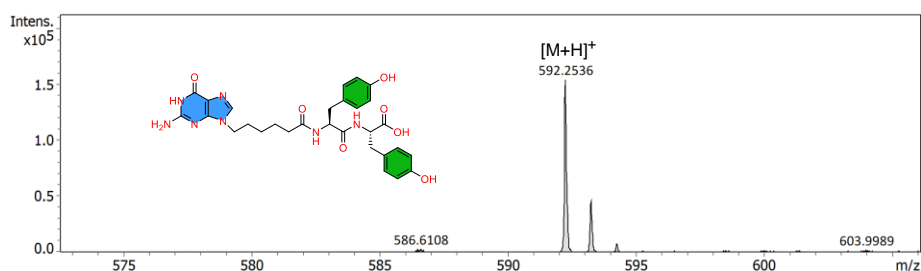


**Figure 4.21** ESI-MS spectrum of NP7.

#### 4.2.15 Molecular Dynamics (MD) Simulation

MD simulation was performed using Amber22. Geometry optimization was carried out before the simulation. AMBERff14SB force field was utilized to apply atom types. AM1-BCC charge set was used. Packmol was used to build the initial system of the simulation. The systems were built with 120 molecules. These molecules were arranged randomly in the simulation box. TIP3P water model was used. General amber force field (GAFF) was used to take care of any missing parameters. Periodic boundary conditions were implemented in each run. Berendsen barostat and Langevin thermostat maintained the constant pressure and temperature. The computational studies were carried out using the following conditions. Initially two minimizations were carried out with 1000 cycles of steepest descent algorithm and 500 cycles of conjugate

gradient algorithm. The temperature of the system was increased to 300K. Then, equilibration was carried out. The Final simulation runs were performed upto 100 ns. The solvent accessible surface area was analyzed by CPPTRAJ.

#### **4.2.16 HPLC Analysis**

The progress of biocatalyst driven reactions was monitored using a Dionex reverse-phase HPLC system, which was connected with a photodiode array detector (Ultimate 3000). A volume of 30 microliters of the sample was injected into a C-18 column with dimensions of 4.6 × 250 mm, which contained fused silica particles measuring 5 micrometres in diameter. The injection was performed at a flow rate of 1 millilitre per minute. The material was eluted using a gradient of water (A) and acetonitrile (B) over a period of 42 minutes (0-4 min %A: 80, %B: 20; 4-35 min %A: 20, %B: 80; 35-40 min %A: 20, %B: 80, 40-42 min %A: 80, %B: 20). The preparation of the sample included dissolving the necessary amount of peptide in a 1 mL solution of acetonitrile and water in a 1:1 ratio.

#### **4.2.17 CD Spectroscopy**

A Jasco J-1500 CD spectrophotometer (Easton, MD, USA) was used to quantify the CD of each peptide hydrogel. CD spectra were recorded with quartz cuvette with a 0.1 mm path length and a maximum chamber capacity of 800 µL. Spectra for of the **NP5** hydrogel was acquired in the 190–300 nm region. The programme JASCO spectra manager was used to analyze the acquired spectra.

#### **4.2.18 FTIR Spectroscopy**

The hydrogel was dried by lyophilizer to obtained powder. ATR-FTIR spectra of the dried hydrogel and the corresponding gelator precursor was acquired using bruker make Vertex 70 instrument. The spectra were recorded from 400 cm<sup>-1</sup> to 4000 cm<sup>-1</sup> at a resolution of 2 cm<sup>-1</sup>, and the

data was processed using OPUS 6.5 software. We used background subtraction to get rid of the atmospheric interference.

#### **4.2.19 ThT Dye Binding Assay**

The method used to conduct the ThT binding test was the same as that which was disclosed in our prior research. The resulting NP5 hydrogel was diluted and exposed to a 0.5 mM thioflavin-T solution for 15 minutes. To investigate the existence of secondary structures in the co-assembled gels, the samples were stimulated at a wavelength of 450 nm, and the emission spectra were recorded using Horiba spectrometer.

#### **4.2.20 Rheological Experiment**

The hydrogels' mechanical rigidity was achieved by using a method similar to that reported in our previous studies. Just before measurement, the hydrogels were quickly demolded in the bottom plate of the rheometer. An Anton Parr MCR301 rheometer was used to measure the mechanical properties of the hydrogels using a parallel plate geometry with a 25 mm diameter (PP25). For the sake of repeatability, the measurements were carried out three times, and the average result is shown.

#### **4.2.21 Scanning Electron Microscopy**

Microscopic methods were used to characterize self-assembled nano structural morphology in the synthesized **NP5** hydrogel. The nano structural morphology inside the hydrogel was visualized by Field-emission scanning electron microscope (FE-SEM model Zeiss Supra55). The **NP5** hydrogel was diluted before taking images. 50  $\mu\text{L}$  of **NP5** hydrogel (20 mM) was diluted with 150  $\mu\text{L}$  of the deionized water. 20  $\mu\text{L}$  of the diluted hydrogel solution was placed on a glass slide. The **NP5** hydrogel on a glass slide was dried twice: once in the air and once under vacuum before being gold-coated.

#### 4.2.22 TEM

Transmission electron microscopy images (TEM) were taken using a field-emission gun TEM (model: Tecnai G2, F30). TEM was operated at a voltage of 200 kV. The **NP5** hydrogel was dilute before taking images. The diluted solution of the **NP5** hydrogel was placed on carbon-coated copper grids. The mesh size of the copper grid was 300. Hydrogel solution on the copper grid was dried at room temperature. **NP5** hydrogel (50  $\mu$ L) was dissolved in 450  $\mu$ L of water. TEM investigations were used to examine the nanostructural shape of hydrogels using 3% phosphotungstic acid as a negative stain.

#### 4.2.23 Wound Healing Assay

The cells were seeded into a 6-well plate and continuously cultured to reach the confluency level of 100% to form a monolayer. A single line wound was formed by scratching the cell through a 1000  $\mu$ l pipette tip and then washed with PBS. Then, the cells were treated with hydrogel. Only PBS was used as control. Thereafter, images were captured through a light microscope (DM21, Leica microsystems, Germany) after an incubation period of 0, 12, 24, 36 and 48 h, and then the wound area was quantified using ImageJ software.

#### 4.2.24 Antibacterial Experiment

##### 4.2.24.1 Bacterial Culture

The microorganisms *Bacillus subtilis* (MTCC 619) and *Escherichia coli* (MTCC 739) were purchased from the Institute of Microbial Technology Chandigarh, India, as a lyophilized powder. Fresh inoculums of the Gram-positive bacteria *B. subtilis* as well as the Gram-negative bacteria *E. coli* were made prior to the tests. A single colony was taken out and afterwards injected into nutrient broth medium that had been autoclaved to promote bacterial growth. Overnight, the bacterial inoculums were incubated at 37 °C in an incubator. Fresh

overnight bacterial suspensions were diluted to a workable concentration of  $1-2 \times 10^8$  colony-forming units (cfu mL<sup>-1</sup>) by diluting them with 0.5 McFarland standards. All cultures had their optical densities evaluated at 625 nm under aseptic circumstances both before and after incubation. Reading was taken using Mutiskan FC plate reader.

#### **4.2.24.2 Culture Media**

The liquid medium used for bacterial culture was called nutrient broth medium, and it was made by combining peptone (10 g), yeast extracts (3 g), and sodium chloride (5 g, NaCl) with 1000 mL of sterile distilled water. Agar-agar powder (15 g) was added to 1000 mL of nutrient broth medium to create the nutrient agar medium. Using NaOH (0.1 N) solution, the pH of the nutrient broth and nutrient agar media was brought to 7.0. In a 25 mL Erlenmeyer flask, the nutrient broth and nutrient agar media were sterilised for 30 minutes at 121 °C and 15 lbs of pressure.

#### **4.2.25 Gelation Method**

The newly developed nucleopeptide molecules 30 mM were placed in a clean 5 mL vial. Then, freshly prepared phosphate buffer (100 mM, pH = 7.4) was added in the vial. Then the resulting solution was vortex for 5 min to homogeneously mix the solution. Finally, the solution was sonicated for 10 min and kept inside the incubator. After 30 min **NP5** formed the hydrogel and the rest of the synthesized **NPs** (**NP6** and **NP7**) formed the precipitate.

#### **4.2.26 Isolation of Blood**

A vacuum tube with the anticoagulant, sodium citrate solution (3.0 w/v%) was used to collect the blood sample. Notably, the blood sample was provided by one of the ambulance drivers as part of a standard physical examination at a medical facility. Blood plasma was then extracted, and the residual cells were used for tests.

#### **4.2.27 Separation of WBCs and Erythrocytes**

By centrifuging blood at 2000 rpm for five minutes under room temperature, erythrocytes were separated out from the blood. With the use of a sterile syringe, WBCs were removed from the buffy coat, and the remaining cells were then washed with 10 mM Phosphate Buffered Saline of pH 7.4 (PBS).

#### **4.2.28 Hemolytic Activity**

A 1% erythrocytes suspension in PBS was employed to assess hemolytic activity. To evaluate the **NP5** hydrogel for hemolysis, the erythrocytes were immediately mixed with different concentration of the hydrogel and left to incubate for 1 hour. PBS was utilized as a negative control and 1% (w/v) Triton X was used as positive control. After that, the mixtures were incubated for 1 hour at 37 °C. After the completion of the incubation period, centrifugation was carried out at 1000 rpm for 10 min at 4 °C.

#### **4.2.29 Antibacterial Properties of the Hydrogel**

The effectiveness of the **NP5** hydrogel against *B. subtilis* and *E. coli* bacteria was examined in vitro. The optical density (OD<sub>625</sub>) technique was used to examine the hydrogels' antibacterial properties. The **NP5** hydrogel with varied concentrations (2 to 0.031 mM) was used for antibacterial study. The control was a bacterial solution in nutrient broth devoid of hydrogels. The absorbances of the test solution and control were estimated at 625 nm.

#### **4.2.30 Animal Cell Culture**

Mouse fibroblast cells (McCoy) and human lung epithelial cells (A549) were procured from NCCS Pune and cultured as per standard protocol. Briefly, the cells were grown in Dulbecco's Modified Eagle Medium (Himedia, Mumbai, India) with standard amount of FBS (Gibco, New York, USA) and penicillin/streptomycin (Himedia, Mumbai, India). The



culture was maintained in a CO<sub>2</sub> incubator (Forma, Steri-cycle i160, Thermo Scientific, Waltham, USA).

#### **4.2.31 Cytotoxicity of the Hydrogel**

The cytotoxicity determination was done by MTT assay. For these, an approximate 10<sup>3</sup> cells were placed in each well of 96 well plate. The plate was incubated for 24 h. Treatment of hydrogel was given for 24 h with concentrations ranging from 2mM to 0.03 mM. After completion of the incubation period the media was aspirated and 50µl of 0.5mg/ml MTT solution was added to each well of the 96 well plate, followed by incubation at 37°C for 3 h. Post incubation the solution was aspirated and DMSO was added to dissolve the formazan and kept on orbital shaker for 1.5 h. The reading was taken in microplate reader (Biotek Synergy H1) at 570 and 590 nm wave length. The IC<sub>50</sub> of the hydrogel could not be determined due to minimal toxicity of the hydrogel. For all further experiments involving animal cell 0.1mM concentration of hydrogel was used.

#### **4.2.32 ROS Estimation by DCFDA Assay**

To understand the ROS scavenging activity of the hydrogel. Cells were seeded in 12 well cell culture plate and kept under incubation for overnight. Then, the cells were treated with 100 µM of H<sub>2</sub>O<sub>2</sub> for 1 h followed by treatment of hydrogel for 12 h after completion of the treatment period. The DCFDA staining, imaging and data analysis was done as described earlier [45].

#### **4.2.33 RNA Isolation and qRT PCR**

To determine the transcript level of inflammatory markers, 1 million cells were seeded in 60 mm dish and allowed to settle, further treated with 100 ng/µL of lipopolysaccharides (Cat# L8880 ANJ Biologicals, NJ, USA) for 12 hrs followed by treatment of hydrogel for 12 h. For positive control equivalent amount of LPS was treated and untreated cells were also kept as negative control. After completion of the

incubation period cells were harvested by scraping and centrifuged at 2500 rpm for 5 min. The pellets were washed with PBS and RNA extraction reagent (Himedia, Mumbai, India) was added and RNA was isolated as mentioned previously [46]. The isolated RNA was quantified by nanodrop and cDNA was prepared from 2 µg of RNA by using cDNA synthesis kit. qRT PCR of IL6, TNFα and NFκB was done using gene specific primers. For McCoy cell mouse specific primers were used.

#### **4.2.34 Western Blot**

To understand the expression of specific markers at protein levels western blotting was performed as mentioned in our earlier work [47]. Briefly post completion of treatment time (LPS + hydrogel treatment) cells were harvested and protein was isolated by RIPA buffer and equal amount of protein was loaded in each well for running gel. The separated proteins were then transferred to 0.45 µM pore size nitrocellulose membrane and after blocking, incubated with primary antibody followed by incubation with secondary antibody and visualization. Analysis and quantification of blots were done using Image J software (National Institutes of Health, USA). Antibodies for NF-κB p65 (#8242, 1:1000) was from Cell Signaling Technology, Danvers, USA. GAPDH (#MA5-15738, 1:2000) was from Invitrogen, Waltham, USA.

#### **4.2.35 Wound Healing Assay**

The cells were seeded into a 6-well plate and continuously cultured to reach the confluency level of 100% to form a monolayer. A single line wound was formed by scratching the cell through a 1000 µl pipette tip and then washed with PBS. Then, the cells were treated with hydrogel. Only PBS was used as control. Thereafter, images were captured through a light microscope (DM21, Leica microsystems, Germany) after an incubation period of 0, 12, 24, 36 and 48 h, and then the wound area was quantified using ImageJ software.

### 4.3 Results and Discussion

The nucleobase, guanine was conjugated with a peptide moiety to synthesize a new class of nucleopeptide (**NP**) moiety. The nucleopeptide was synthesized using a solution phase synthetic procedure. In a previous report, we enhanced the gelation property of the synthesized **NPs** by increasing their hydrophobicity by introducing a long fatty acid chain [48]. In this report, we aim to demonstrate the gelation property in the synthesized nucleopeptide by increasing its hydrophobicity through the introduction of an aromatic amino acid into the synthesized nucleopeptide.

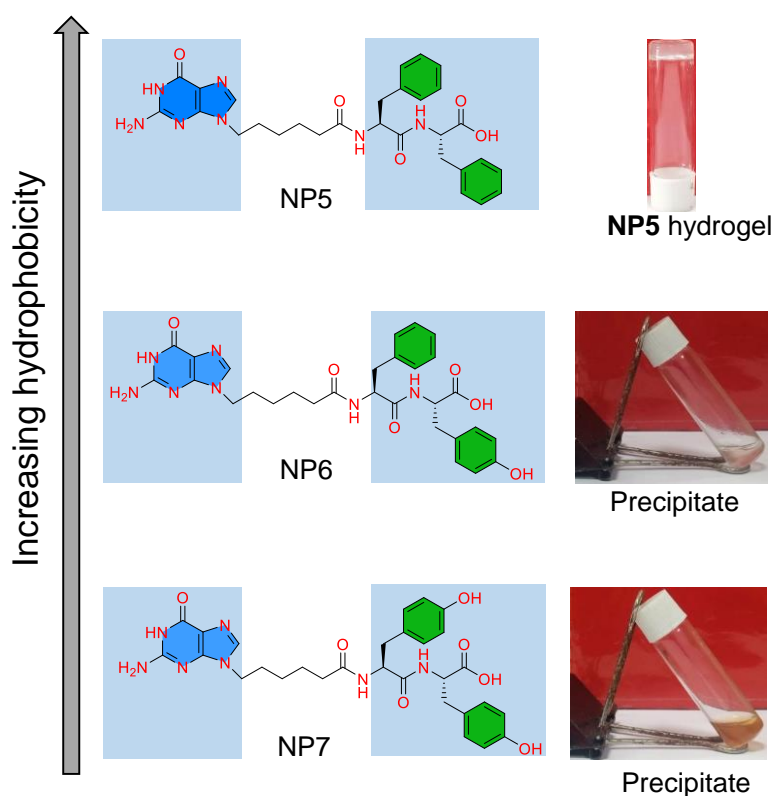
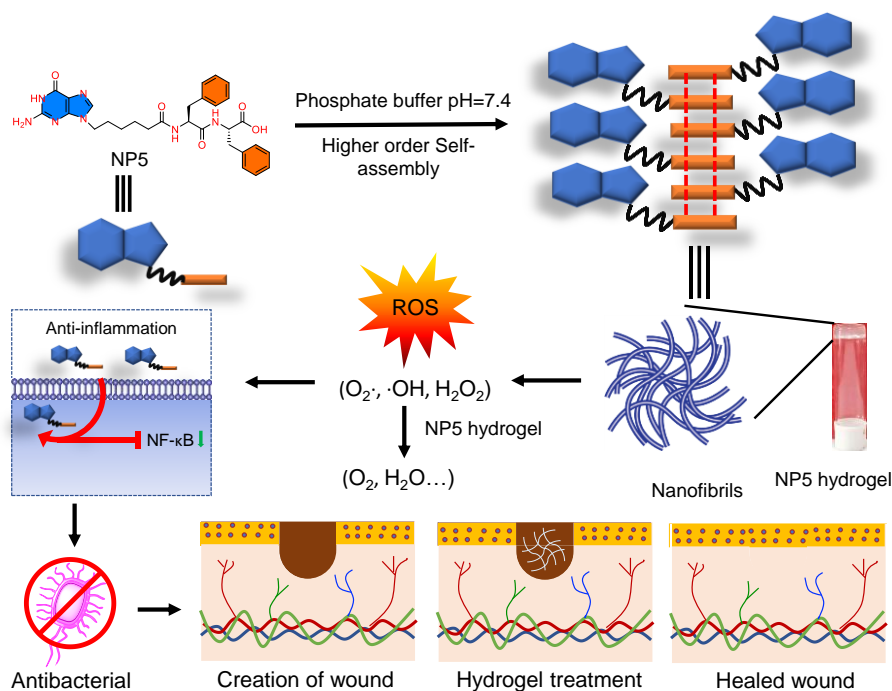


**Figure 4.22** The formation of the hydrogel by NP5. The formation of the precipitate in presence of the phosphate buffer pH = 7.4 by **NP6** and **NP7** respectively.

We have designed three different nucleopeptides (**NP5**, **NP6**, **NP7**) and synthesized them according to the reported solution phase synthetic procedure [49,50]. To form a self-assembled hydrogel, 30 mM of the synthesized **NP5** was taken in a vial, then 500  $\mu$ l of phosphate buffer

with a pH of 7.4 was added. After the buffer was added, the solution was ultrasonicated vigorously for 10 min. The solution was then left at room temperature for 15 min. The formation of the hydrogel was verified by inverting the vial. The minimum gelation concentration was 30 mM. In a similar manner, we attempted to prepare the hydrogel with the other two synthesized NPs. A viscous solution was appeared for the remaining two NP (Figure 4.22).



**Scheme 4.2** Schematic illustration demonstrates the formation of the **NP5** hydrogel, which effectively decreases the inflammation, is efficient against bacterial infection and exhibits excellent activity for the invitro wound healing.

Therefore, only **NP5** formed a stable, self-supported **NP5** hydrogel in phosphate buffer (**Scheme 4.2**). The formation of a stable hydrogel by **NP5** can be attributed to the proper balance of hydrophobicity and hydrophilicity. In a previous report, we demonstrated that increasing hydrophobicity through the introduction of variable chain lengths of the fatty acid led to the gelation property in the synthesized nucleopeptides [48]. In this instance, the increase in hydrophobicity due to the aromatic amino acid plays a crucial role in inducing gelation in the synthesized

**NPs.** The CLogP values for the synthesized **NP5**, **NP6** and **NP7** are 1.488, 0.821, 0.154, respectively. These values clearly indicate that the increased hydrophobicity, brought about by the introduction of aromatic amino acid in the synthesized **NPs**, significantly contributes to the induction of the gelation property. The difference in the aggregation behavior of the synthesized **NPs** is attributed to the variation in the CLogP value. Further, the aggregation behavior of the synthesized nucleopeptides is determined by simulation studies. All the synthesized **NPs** were subjected to simulation studies using Amber22. The simulation was conducted over a time period of 100 ns. Over time, the synthesized **NPs** begin to aggregate. The rate of aggregation increases with the duration of the simulation. Among the **NPs**, **NP5** shows a higher rate of aggregation compared to **NP6** and **NP7** (**Figure. 4.19a**). The solvent accessible surface area (**SASA**) analysis is used to determine the supramolecular aggregation propensity [51]. A decrease in the **SASA** implies the aggregation behavior of the **NPs**. It has been observed that the decrease in **SASA** is more significant for **NP5** as compared to **NP6** and **NP7** (**Figure 4.23b**). Consequently, the increased aggregation in **NP5** leads to a higher order of self-assembly, which helps in the formation of the hydrogel [52,53]. The simulation results support the experimental observation (**Figure 4.24a-c**).

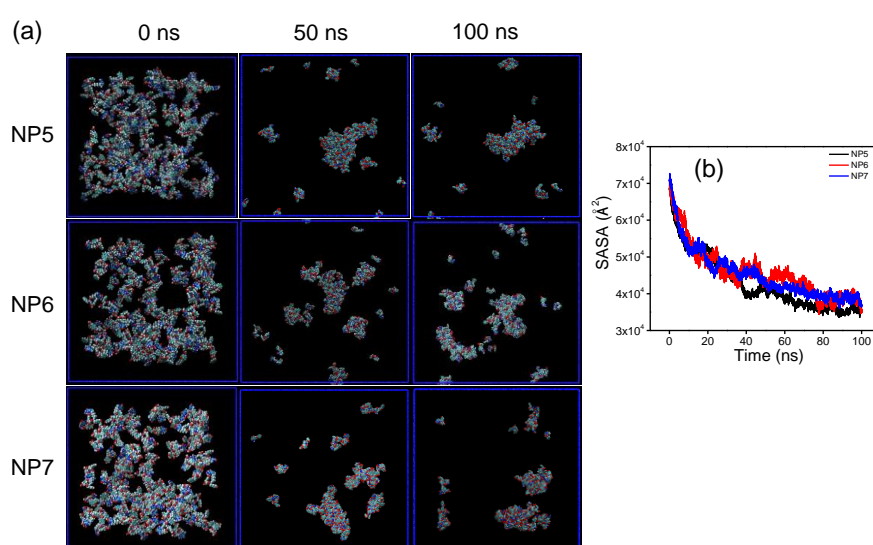


**Figure 4.23** (a) Self-aggregation of the synthesized **NPs** at 0 ns, 50 ns and 100 ns. (b) The decrease of the solvent accessible surface area (SASA) with time.

To further support the aggregation observation from the simulation studies, we conducted Diffusion Ordered NMR Spectroscopy (DOSY) of the synthesized **NPs**. The size of the aggregates, formed by the **NPs**, was determined through the DOSY NMR experiment. This experiment helps in determining the diffusion co-efficient of the supramolecular aggregates. The diffusion constant ( $\text{m}^2/\text{s}$ ) for the C8 proton of the synthesized **NP5**, **NP6** and **NP7** are  $2.03 \times 10^{-13}$ ,  $1.91 \times 10^{-9}$ ,  $3.15 \times 10^{-10}$ , respectively. Among the synthesized **NPs**, **NP5** has the lowest diffusion constant compared to the other **NPs**, indicating a higher tendency to form aggregates.

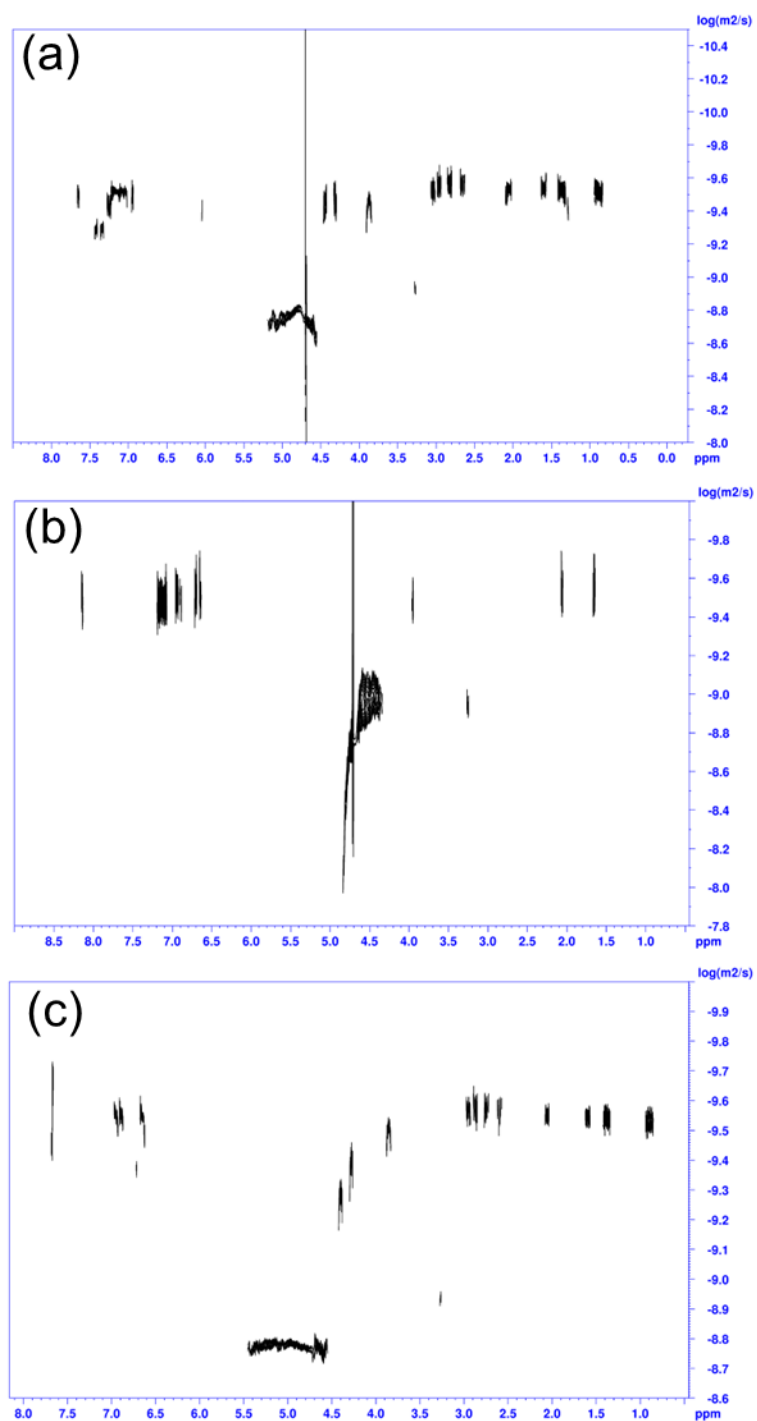


**Figure 4.24** DOSY NMR spectrum of 10 mM (a) NP5 (b) NP6 (c) NP7 in D<sub>2</sub>O at 298K.

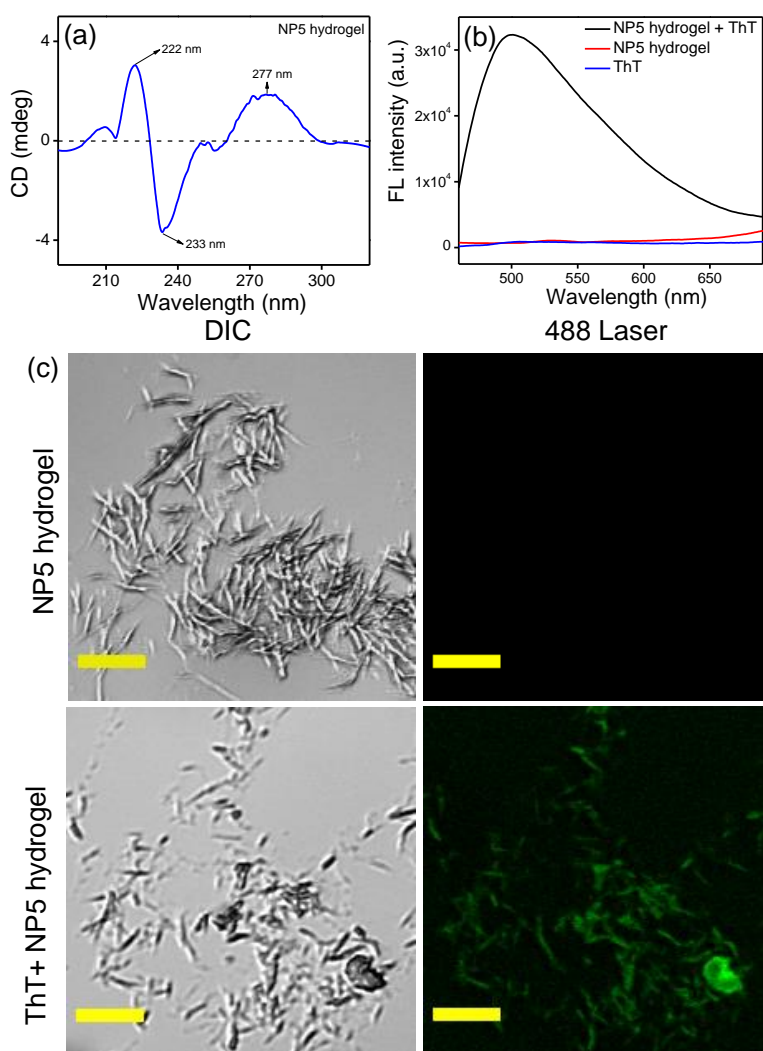


**Figure 4.25** (a) Circular dichroism spectrum of the **NP5** hydrogel. (b) Fluorescence spectrum of the ThT solution (blue line), **NP5** hydrogel (red line) and **NP5** hydrogel with ThT, the excitation wavelength was 450 nm. (c) CLSM images show non fluorescent supramolecular assemblies ( $\lambda_{\text{ex}} = 488$  nm) in the **NP5** hydrogel, upon binding with the ThT, it becomes fluorescent (Scale bar in all images are 5  $\mu\text{m}$ ).

Guanine, which has several H-bonding donor and acceptor site, can participate in H-bonding interactions among themselves to form the secondary structure of DNA. This helps in the formation of hydrogel [54]. Circular dichroism spectroscopy (CD) is an important technique used to determine the presence of secondary structures and the folding of proteins and other biomacromolecules. Therefore, CD spectroscopy was used to investigate whether a secondary structure is present or not.



The **NP5** hydrogel (30 mM) was diluted to 400  $\mu$ M using water. The spectra were recorded and showed a positive peak at 277 nm and a negative peak at 233 nm. These peaks indicate the presence of the DNA secondary structure within the hydrogel [55]. A peak at 222 nm is due to the  $\pi$ -  $\pi^*$  transition for the phenyl moieties in the synthesized **NP5** (**Figure 4.25a**) [56]. Therefore, the CD spectrum suggests that the DNA secondary structure is present within the hydrogel components.

Thioflavin T (ThT) is a benzothiazole-derived fluorophore, typically used to identify the secondary structure of nucleic acids. Although ThT is not fluorescent in water by itself, it displays strong fluorescent emission maxima when it binds with macromolecules like DNA and RNA. ThT is composed of a benzothiazole ring and benzyl amine, which are connected by a C-C bond. Theoretical studies suggest that the free rotation around this C-C single bond results in fluorescence quenching in the solution. When ThT molecules are added to biomolecules, they attach and restrict free rotation, resulting in strong fluorescence [57]. The ThT solution was added to the **NP5** hydrogel during its formation. The fluorescence spectrum was recorded for the ThT incorporated hydrogel, the blank hydrogel, and the blank ThT. The excitation wavelength was set at 450 nm. No prominent peak was observed for the **NP5** hydrogel and the blank ThT solution. However, a strong fluorescence maximum at 494 nm clearly suggests the presence of secondary structures of nucleic acid which facilitate the formation of **NP5** hydrogel (**Figure 4.25b**). A microscopic evaluation was carried out to corroborate the spectroscopic result. In this process, the hydrogel was incubated with a ThT solution [58]. The dye bounded strongly with the supramolecular nano-architecture within the hydrogel, displaying fluorescence that was clearly visible under a confocal laser scanning microscope (CLSM) (**Figure 4.25c**).

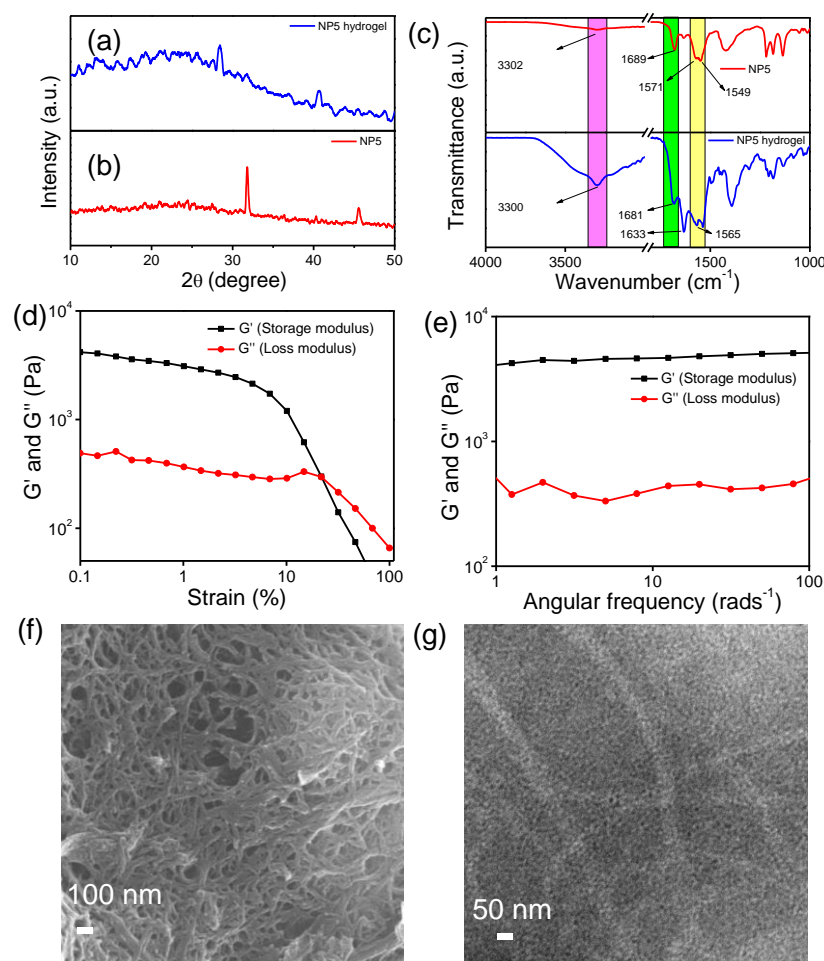


**Figure 4.26** PXRD spectrum of (a) **NP5** hydrogel and (b) the synthesized gelator precursor **NP5**. (c) FT-IR spectra of the **NP5** (red line) and **NP5** hydrogel (blue line). (d) Amplitude sweep experiment of the **NP5** hydrogel. (e) Frequency sweep experiment of the **NP5** hydrogel. (f) SEM and (g) TEM images show the presence of the nano-fibrillar morphology in the **NP5** hydrogel.

The wide-angle powder X-ray diffraction experiment (PXRD) was conducted to examine the self-assembly in the **NP5** hydrogel. PXRD spectra were recorded for the xerogel (made from the **NP5** hydrogel) and the synthesized **NP5**. A peak was observed at  $2\theta=28.36$  which corresponds to a distance of  $3.15 \text{ \AA}$ . This is attributed to the  $\pi$ - $\pi$  stacking distance (**Figure 4.26a**) [59]. The spectra were also recorded for **NP5**, and its crystalline nature was observed (**Figure 4.26b**). Therefore, the PXRD experiment was also revealed the presence of supramolecular stacking within the **NP5** hydrogel which helps in forming a stable, self-

assembled **NP5** hydrogel. To gain more detailed information about the molecular interactions in the self-assembled stable **NP5** hydrogel, we performed FT-IR spectroscopy. The spectra for both the **NP5** hydrogel and the synthesized **NP5** were recorded. We used FT-IR spectroscopy to investigate the existence of amide I and amide II bands. Amide I represent the stretching frequencies of the C=O bond, while amide II represents the stretching frequencies of N-H bond [60]. The peaks at  $1681\text{ cm}^{-1}$  and  $1633\text{ cm}^{-1}$  correspond to the -C=O stretching frequencies. Other peaks at  $1570\text{ cm}^{-1}$  and  $3300\text{ cm}^{-1}$  represent the N-H bending and O-H stretching (**Figure 4.26c**). In the spectrum, the shift of the -C=O stretching frequency in amide I region and the change of N-H bending in the amide II region of the hydrogel from its corresponding gelator precursor may be attributed to the participation of the carbonyl group in the hydrogen bonding interactions. The increase in intensity and shift of the O-H stretching indicate that the O-H of the carboxylic acid is involved in the H-bonding interaction. Therefore, the FTIR spectra clearly indicate that the H-bonding interaction in **NP5** contributes to the formation of the supramolecular aggregate, which in turn facilitate the formation of **NP5** hydrogel. The mechanical properties of the newly developed **NP5** hydrogel were estimated with the help of rheological studies [61]. The area of deformation was investigated using an amplitude sweep experiment, keeping a constant value of frequency of 10 rad/s throughout the entire experiment. The values of the storage modulus ( $G'$ ) and loss modulus ( $G''$ ) was constant at lower strain levels. However, the storage modulus values gradually decreased from 4133 Pa as the strain increased (**Figure 4.26d**). This experiment reveals that the microstructure deforms at higher strain, resulting in the transformation of the hydrogel into a solution. Subsequently, a frequency sweep experiment was conducted at a constant strain of 0.5%. This experiment also demonstrated that the storage modulus values consistently exceed the loss modulus values across all frequency ranges (**Figure 4.26e**). Therefore, the rheological experiment reveals the formation of a stable and stiff **NP5** hydrogel. The morphological characterization of the synthesized **NP5** hydrogel was carried out using various electron

microscopy techniques [62,63]. The SEM images showed the presence of densely entangled nanofiber structures within the **NP5** hydrogel (**Figure 4.26f**). The average width of these nanofiber is 29 nm. Additionally, a transmission electron microscopy experiment was also performed. The TEM images also suggest the presence of nanofiber within the hydrogel (**Figure 4.26g**). The nanofiber within the hydrogel has an average width of 25 nm. Therefore, microscopic images also indicate the existence of dense nanofibers within the hydrogel. Consequently, the nanofiber within the **NP5** hydrogel contributes to the development of a stable **NP5** hydrogel.

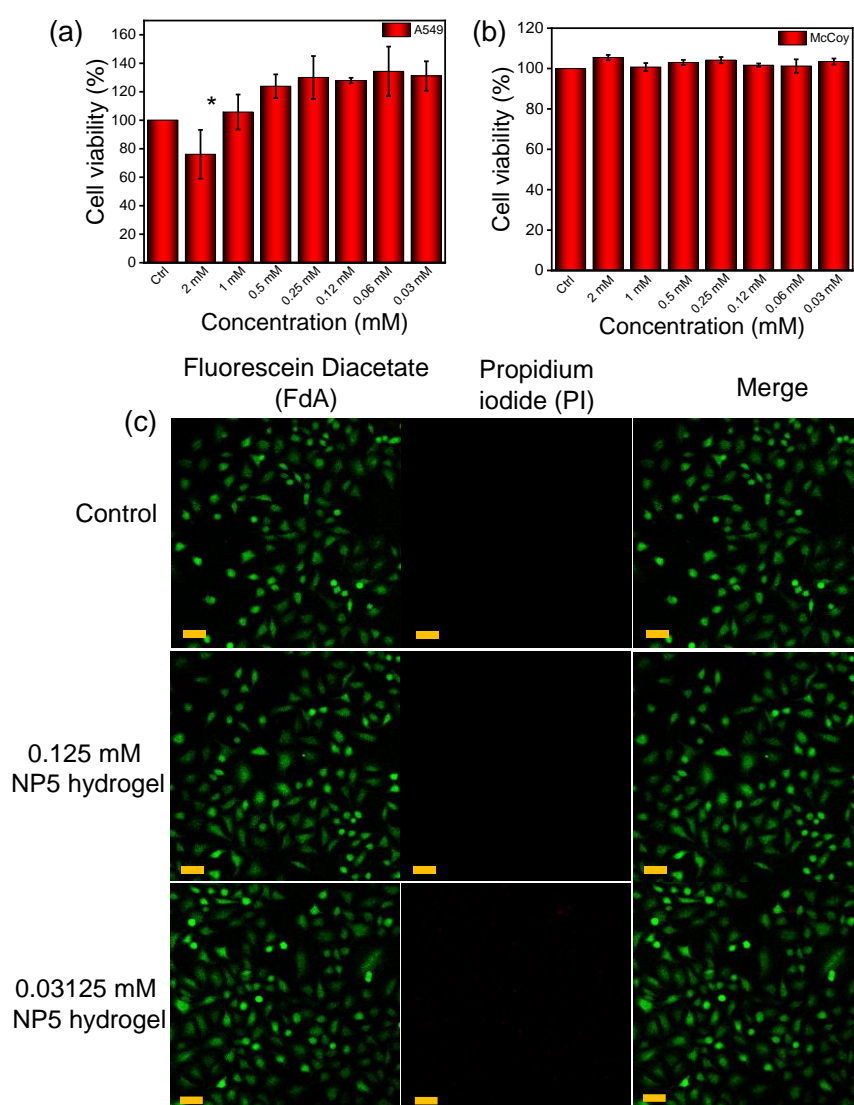


**Figure 4.27** The MTT assay to check cell viability of **NP5** hydrogel on (a) fibroblasts McCoy cell line and (b) epithelial A549 cell line.

Unpaired *t*-tests were conducted for the statistical analysis of the data using graphpad prism trial version. *p*-values of <0.05, <0.001 and <0.0001 were represented with \*, \*\* and \*\*\* respectively as compared to the control. (c) Live-dead cell imaging shows excellent viability of the **NP5** hydrogel towards epithelial A549 cell line. Fluorescein Diacetate (FdA) was used to detect the presence of the live cells after the incubation with different concentration of the **NP5** hydrogel and Propidium iodide (PI) was used for the visualization of the dead cells (scale bar 20  $\mu$ m).

Recent studies have shown that peptide based nanofibrous hydrogels are used in fields such as tissue engineering, stem cell proliferation and drug delivery. This is because they are biocompatible and can hold a large amount of water molecules. Therefore, biocompatibility is a primary requirement for using this soft functional material in biomedicine [64]. The colorimetric MTT experiment was conducted using the synthesized stiff, nanofibrous, **NP5** hydrogel to evaluate its impact on cells. The cells were incubated with the hydrogel for a duration of 24 h. We selected two different cell lines to determine the number of metabolically active cells after the incubation period. The cancerous cell line A549 and the fibroblast cell line (McCoy) were used to evaluate biocompatibility. The cells were treated with varying concentrations of the synthesized nanofibrous **NP5** hydrogel. For the A549 cell, the synthesized **NP5** hydrogel demonstrated minimal toxicity when higher concentrations (2 mM, 1 mM) were applied to the cells, compared to the control experiment (**Figure 4.27a**). The control experiment was carried out using only the media (the composition of the media is mentioned in the experimental section). For the McCoy cell, the hydrogel showed no toxicity. Instead, proliferation was observed with the McCoy cell line (**Figure 4.27b**). Previous studies have also reported minimal cytotoxicity of hydrogels [65]. Based on the MTT data, we used a 0.1 mM concentration in our subsequent cell-based experiments.

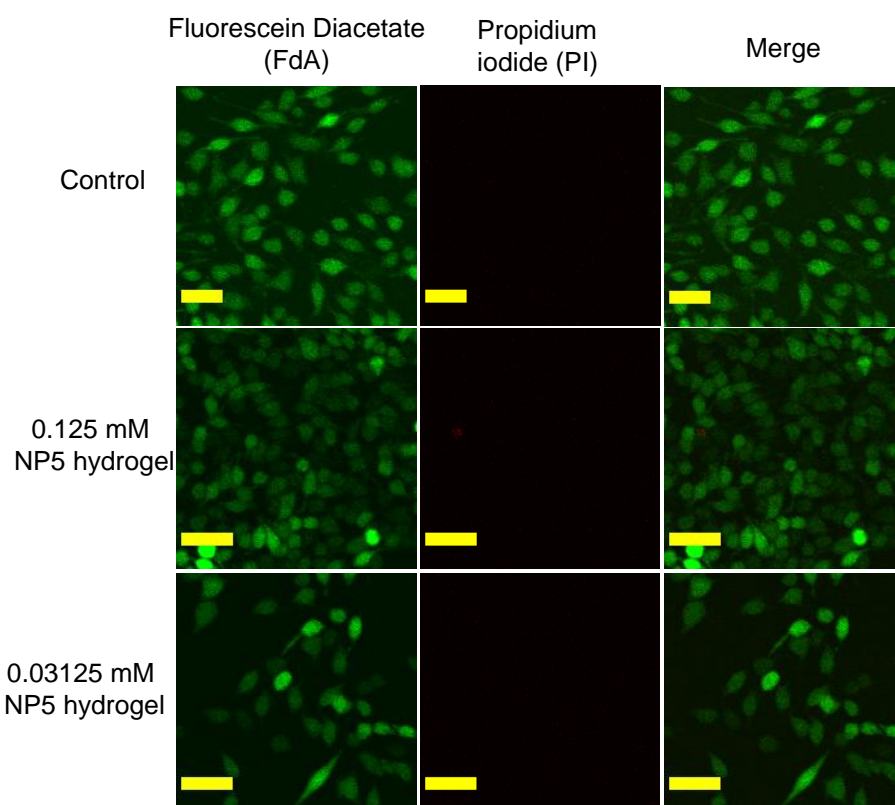


**Figure 4.28** Live-dead cell imaging on the fibroblast McCoy cell by the newly developed **NP5** hydrogel. The scale bar in all the images is 20  $\mu\text{m}$ .

To further confirm the findings from the MTT assay, we performed live-dead cell imaging. This imaging was conducted using the **NP5** hydrogel on the McCoy fibroblast cell line and the A549 epithelial cell line. Different concentrations of the hydrogel (0.125 mM and 0.03125 mM) were used for the live-dead cell imaging experiment. The hydrogel was left to incubate in the cells for a period of 24 h. After the incubation period ended, the cells were stained with fluorescein diacetate (FdA). The bipolar side chains in FdA can help to permeate through the cell membrane. FdA is a non-fluorescent dye. The esterases, which are enzymes that catalyze the hydrolysis of ester bonds, transform the nonfluorescent FdA into fluorescein by non-specific cleavage of the acetate groups present in the FdA. Those cells which are metabolically active and have undamaged cell membranes could be observed under laser light. Dead cells were visualized by staining them with propidium iodide [66]. In both cell lines, no red fluorescence was observed (**Figure**

**4.27c and Figure 4.28).** This clearly indicated, the biocompatible nature of the hydrogel. As a result, this biocompatible hydrogel could potentially be used for wound healing. The results of this experiment are also consistent with our MTT data, which shows minimal cell death due to cytotoxicity.

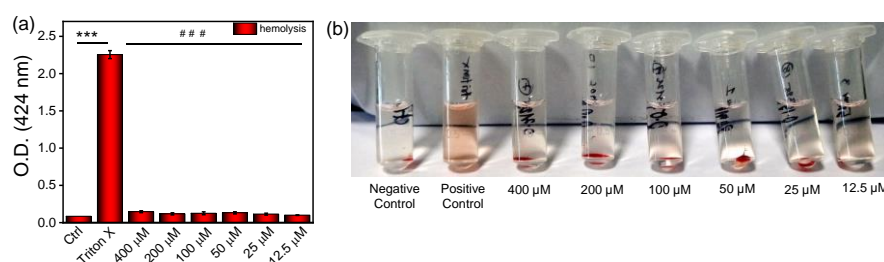


**Figure 4.29** (a) Quantitative measurement of the hemolysis by the **NP5** hydrogel (b) optical image shows the hemolytic activity of the **NP5** hydrogel. Unpaired *t*-tests were conducted for the statistical analysis of the data using graphpad prism trial version. *p*-values of < 0.05, < 0.001 and < 0.0001 were represented with \*, \*\* and \*\*\* respectively for significant upregulation and #, ##, and ### for significant downregulation with respect to the control.

Inflammation, proliferation, and reorganization of tissue layers are all components of the complex and dynamic process of wound healing. This process involves step-by-step, time-consuming restoration of damaged cellular structures [67]. Hemolysis occurs when the hydrogel comes into contact with blood cells. This happens when the blood cell membrane ruptures, releasing hemoglobin and other internal components into the surrounding fluid. The presence of a pink to crimson red color in the serum can be used to visually identify it. This color change can be caused by a variety of medical issues, including microbial infections, autoimmune and genetic diseases, and low solute concentration. The term ‘hemolytic potential’ refers to the ability of a substance to cause hemolysis, or the breakdown of red blood cells, to a certain extent when it comes into contact with blood. The hemolysis experiment demonstrated that the nanofibrous supramolecular

nucleopeptide hydrogels were nonhemolytic. **Figure 4.29a** displays the hemolysis of blood cells when exposed to different hydrogel samples for an hour at 37 °C. TritonX was used as a positive control, while only a buffer was used as a negative control. An optical image shows the hemolytic activity of the **NP5** hydrogel (**Figure 4.29b**). All tested concentrations of the hydrogel were found to be nonhemolytic, with hemolysis levels below the acceptable standard. These findings demonstrate the high compatibility of the supramolecular nucleopeptide hydrogels with blood.

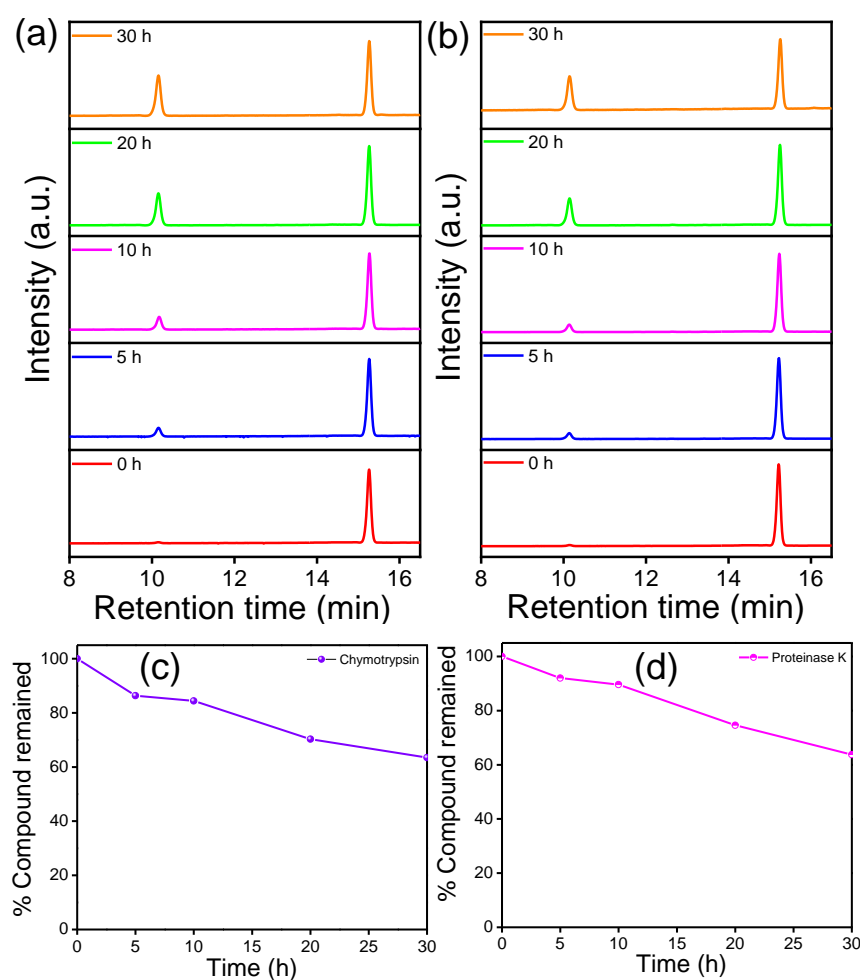


**Figure 4.30** HPLC chromatograms depicts the degradation of the **NP5** hydrogel in the presence of the proteolytic enzymes (a)  $\alpha$ -chymotrypsin (b) proteinase-K. The (%) of the compound remained after the degradation by the proteolytic enzymes (a)  $\alpha$ -chymotrypsin (b) proteinase-K.



Nucleopeptide gelator consisting of amino acids tends to undergo hydrolysis when exposed to proteolytic enzymes, which is associated with a significant rise in proteolytic enzymes in chronic wounds. Therefore, the stability of the nucleopeptide hydrogel was tested in the presence of the proteolytic enzymes. The biostability was tested in the presence of the proteolytic enzymes  $\alpha$ -chymotrypsin and proteinase K [68]. The breakdown of the peptide by enzymes was evaluated at different time intervals using RP-HPLC analysis (**Figure 4.30a and 4.30b**). The proportion of the nucleopeptide that remained undecomposed was estimated by measuring the area under the curve. The nucleopeptide hydrogel showed a degradation of 30-35% at 30 h (**Figure 4.30c and 4.30d**).

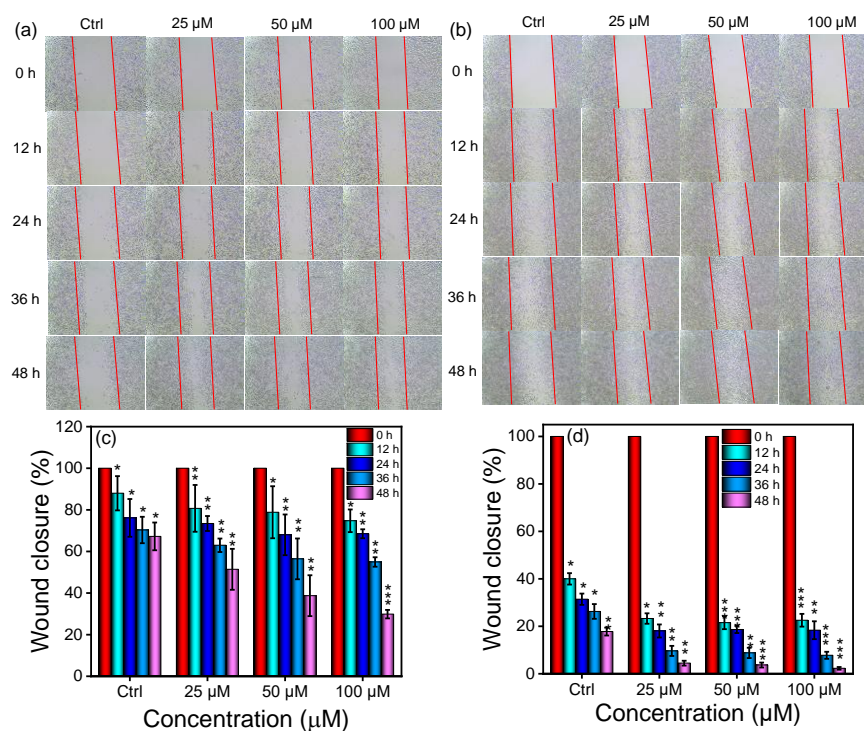


**Figure 4.31** The invitro wound healing experiment on the (a) A549 cell 'and' (b) fibroblasts McCoy cell. The quantification of the wound closure by the (c) A549 cell (d) McCoy cell at 0 h, 12 h, 24 h, 36 h, and 48 h. Unpaired *t*-tests were conducted for the statistical analysis of the data using graphpad prism trial version. *p*-values of < 0.05, < 0.001 and

< 0.0001 were represented with \*, \*\* and \*\*\* respectively as compared to the respective 0 h of each group.

In addition, we examined the impact of **NP5** hydrogel on cell migration by performing a scratch wound test, as cell proliferation and migration are crucial factors in the wound healing process. After making a small scratch on the cell layer, we then incubated them with **NP5** hydrogel. The concentration dependent effect of the hydrogel was studied. Images of the scratch were captured at different times, revealing that the cells treated with a higher concentration of hydrogel showed improved migration, effectively closing the gap within 48 hours (**Figure 4.31a and 4.31b**). When a higher concentration of the hydrogel was applied, about 70-75% of the wounds closed in the A549 cell line, while 95-98% of the scratch wound healed in the McCoy cell line (**Figure 4.31c and 4.31d**). The percentage wound closure was used to represent the amount of wound closure in response to our hydrogel. In this method, the width of the wound at 0 h was considered to be 100%, and as time increases and the wound area decreased, the percentage of the wound area also decreased from 100%. The wound area at respective time points were calculated with respect to 0 h of the respective group. The higher migration in the keratinocytes (McCoy) shows **NP5**'s superior wound healing capability in a natural set up. A previous study by Sparks *et al* also reported the enhanced wound healing potential of peptide hydrogels [69].

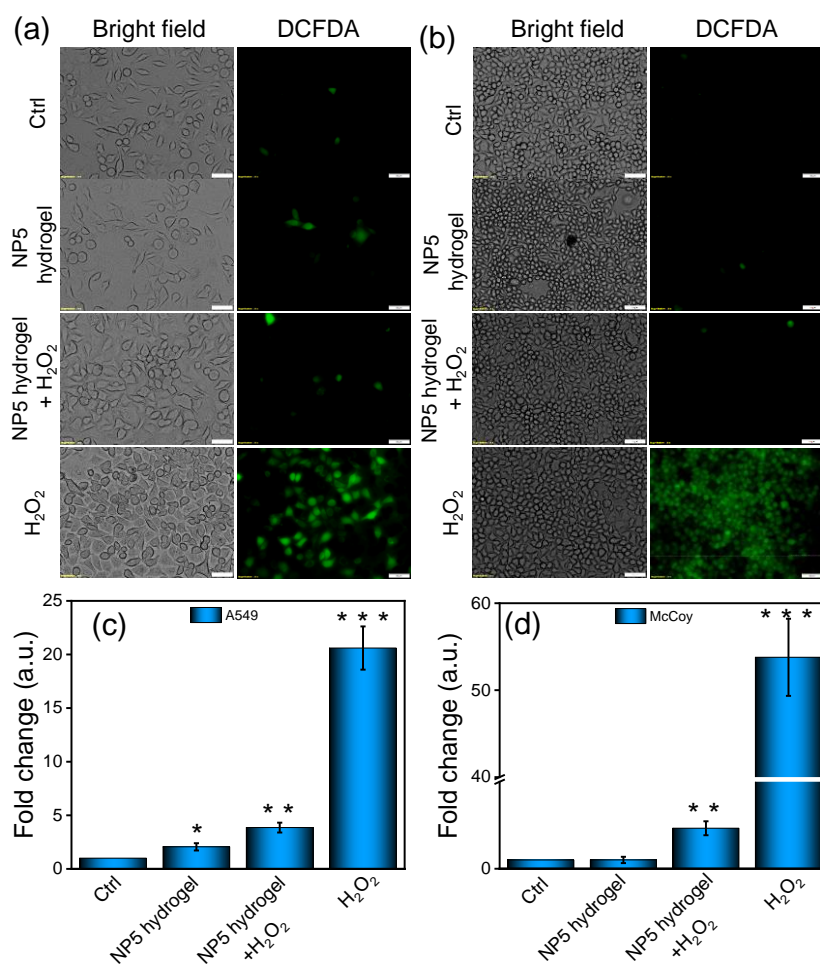


**Figure 4.32** DCFDA assay of the **NP5** hydrogel on the (a) epithelial A549 cell line 'and' (b) fibroblasts McCoy cell line. H<sub>2</sub>O<sub>2</sub> was used to create inflammation in the cell. The scale bar in all images is 50  $\mu$ m. The quantification of the inflammation by the (c) A549 'and' (d) McCoy cell with respect to the control was measured with the ImageJ software. Y-axis was broken at 10. Unpaired *t*-tests were conducted for the statistical analysis of the data using graphpad prism trial version. p-values of <0.05, <0.001 and <0.0001 were represented with \*, \*\* and \*\*\* respectively as compared to the control.

The main barrier to tissue healing in area of a scratch wound is the elevated levels of reactive oxygen species (ROS) [70]. In a study, H<sub>2</sub>O<sub>2</sub> was used to stimulate the production of ROS and induce oxidative stress in McCoy fibroblasts and A549 epithelial cell lines. The objective was to evaluate the effect of the **NP5** hydrogel on the ROS levels in these cell lines when they are under stress from H<sub>2</sub>O<sub>2</sub>. The hydrogel was used

to protect against cellular damage by inhibiting the formation of ROS. The nonfluorescent compound DCFH-DA transforms into the fluorescent compound DCF when it comes into contact with ROS. This transformation was employed as an indirect method to measure the production of ROS within cells. For qualitative analysis, McCoy fibroblasts and A549 epithelial cell lines were examined using a fluorescent microscope to investigate the intracellular location of ROS. The image demonstrates that cells treated with  $H_2O_2$  exhibited a significant amount of green fluorescence, indicating a rise in intracellular ROS levels (**Figure 4.32a and 4.32b**). In contrast, the control and the **NP5** hydrogel alone showed much less green fluorescence in both cell lines. This data suggests that the gel has a significant effectiveness as a free radical scavenger. The measurement of fluorescence intensity also demonstrated a significant increase in intracellular ROS levels after  $H_2O_2$  treatment. However, the use of **NP5** hydrogel effectively mitigated the formation of ROS generated by  $H_2O_2$ . The fluorescence intensity of cells decreased by about 50% after being exposed to hydrogel, compared to cells that were treated with  $H_2O_2$  (**Figure 4.32c and 4.32d**). These results further validated the exceptional ability of the hydrogel to scavenge reactive oxygen species (ROS). After comparing the ROS scavenging capacity of the **NP5** hydrogel with literature, we conclude that our findings are consistent with previously published results. Several groups in previous studies have also demonstrated the ROS scavenging property of various hydrogels, including peptide hydrogels [71]. It is noteworthy to mention that guanine moiety in the **NP5** play a significant role to scavenge free radical. Among the nucleobases, guanine has the lowest reduction potential (1.29 V). Therefore, it is the best electron donor and is preferentially oxidized. Hence, hydroxyl and super oxide radical reacts with guanine that results in decrease in ROS [72].

In addition to the ROS scavenging, wound filling and antibacterial are crucial properties of the gel, it is important to investigate its anti-inflammatory property. This is because the formation of a wound

triggers an inflammatory response. To investigate the anti-inflammatory property of the **NP5** hydrogel, we determined the transcript (IL6, TNF $\alpha$  and NF $\kappa$ B) and protein (NF $\kappa$ B) levels of inflammatory markers using qRT-PCR and western blot methods, respectively (**Figure 4.33**).

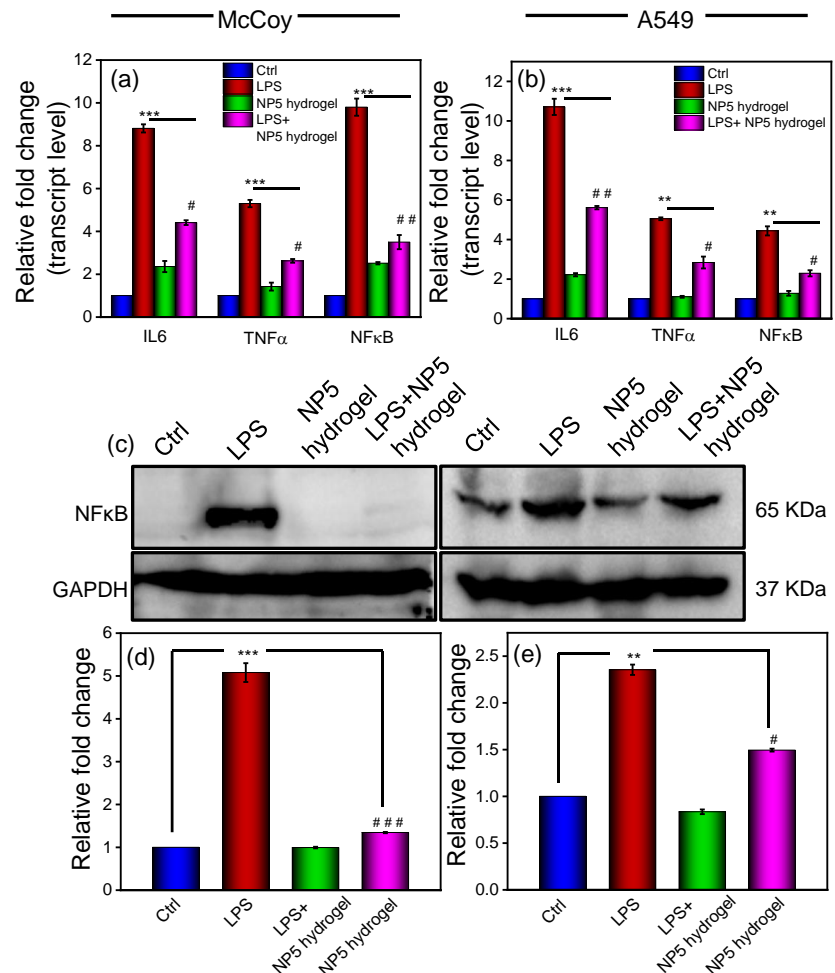


**Figure 4.33 Treatment of hydrogel dampens the inflammatory response in lung and fibroblast cells.** McCoy and A549 cells were treated with bacterial lipopolysaccharide (LPS) for 12 h to induce inflammation followed by treatment of **NP5** hydrogel for another 12 h (LPS+ **NP5** hydrogel group). Only LPS and gel group cells were treated with LPS and **NP5** hydrogel for 12 and 24 h respectively. After completion of the treatment period cells were harvested and transcript and protein level of inflammatory markers were evaluated. Relative transcript level of inflammatory markers (IL6, TNF $\alpha$  and NF $\kappa$ B) in (a) McCoy 'and' (b) A549 cells. (c) Representative western blot image of

NFκB in McCoy (left panel) 'and' A549 (right panel) cells. Relative NFκB protein level in (d) McCoy 'and' (e) A549 cells. The experiment was performed in triplicates, and the results are shown as the mean ± SD of three data points. Statistical significance was determined by Unpaired *t*-tests with 95% confidence interval. \*/#, \*\*/## and \*\*\*/### denotes *p*-values of < 0.05, < 0.001 and < 0.0001 respectively as compared to the control for significant up/down regulation.

Our results indicate that treating cells exposed to LPS with **NP5** hydrogel significantly ( $p < 0.05$ ) reduces the transcript levels of IL6, TNFα and NFκB in the LPS+Gel group compared to the LPS treated group in both fibroblast and lung epithelial cells (**Figure 4.33a and 4.33b**). Furthermore, the gel by itself does not exhibit any inflammatory properties, as evident by the levels of these markers in the gel treatment group (**Figure 4.33a and 4.33b**). We have also evaluated the protein level of NFκB, the primary regulator of inflammation. In the McCoy cell, compared to the LPS treatment group, LPS+Gel group showed a diminished expression of NFκB ( $p < 0.0001$ ). However, in the A549 cell, the decrease is comparatively less compared to the McCoy ( $p < 0.05$ ) (**Figure 4.33c-e**). The results from the anti-inflammatory study suggest that the **NP5** hydrogel possesses anti-inflammatory properties in addition to the other properties mentioned. Previous studies by Chen *et al* have also demonstrated the reduction of IL6 and TNFα in mice treated with hydrogel [73]. Additionally, another study involving a peptide-ibuprofen amphiphile based hydrogel was able to reduce inflammation induced by LPS, as indicated by reduction of IL6, TNFα and NFκB [74].

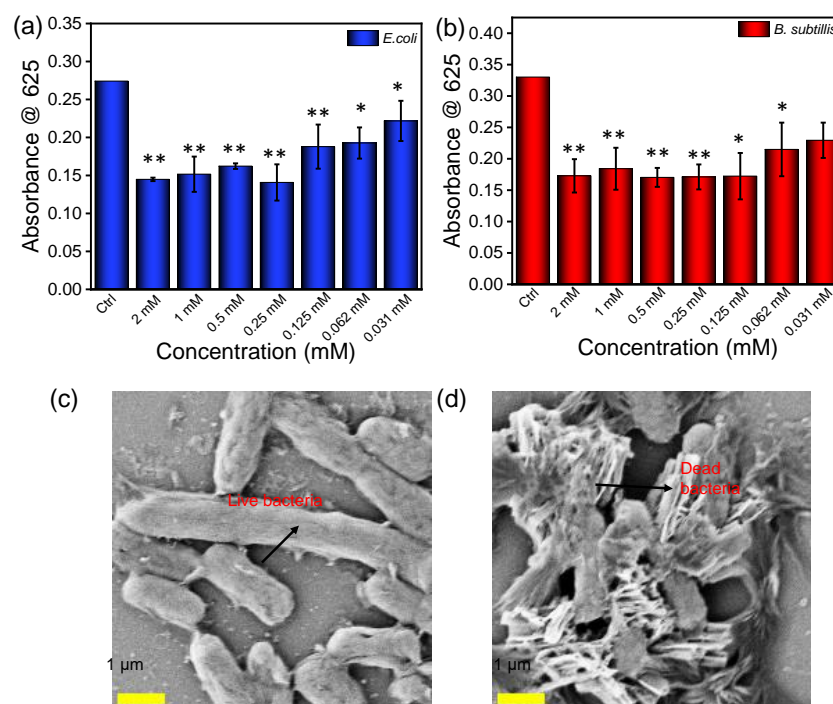


**Figure 4.34** The antibacterial activity of the synthesized **NP5** hydrogel was investigated against (a) Gram-negative *E. coli* (b) Gram-positive *B. subtilis*. All the results were derived from technical triplicate (N = 3). All the data were statistically analyzed by unpaired t-test using graphpad prism trial version. \* $p < 0.05$ , \*\* $p < 0.01$  as compared to the control. FE-SEM images of the *E. coli* bacteria (c) control (without **NP5** hydrogel) (d) in the presence of the **NP5** hydrogel.

Microbial infections and the growth of biofilms on biomaterial surfaces pose significant worldwide challenges and health concerns. Antibacterial hydrogels have inherent properties that effectively hinder bacterial contaminations, making them a viable option in combating drug-resistant pathogens. The bacterial infections in the place of wounds area can lead to chronic conditions and the healing process becomes slow [75]. The effective wound healable biomaterials should effectively eradicate biological contaminations without causing undesirable allergic responses. The inherent propensity of nucleopeptide-based materials to self-assemble confers significant benefits in treating bacterial infections. The intrinsic antibacterial activities of the **NP5** hydrogel were estimated by measuring the optical density at 625 nm against harmful Gram-

positive (*B. subtilis*) and Gram-negative (*E. coli*) bacteria. The results of antibacterial tests indicate that the **NP5** hydrogel effectively suppresses the proliferation of Gram-positive and Gram-negative bacteria. The higher concentration of the **NP5** hydrogel was found to be more effective against the bacteria (**Figure 4.34a and 4.34b**). The FE-SEM images were captured after a 24 h incubation period of the **NP5** hydrogel with the Gram-negative bacteria *E. coli*. The images clearly show the breakdown of the bacterial cell membrane when the hydrogel is applied (**Figure 4.34c and 4.34d**). Therefore, the **NP5** hydrogel potentially be used for wound dressing purposes.

#### 4.4 Conclusion

The nucleopeptide derivatives (**NPs**) were synthesized and the ability of these synthesized **NPs** to form hydrogels were tested. The aggregation behavior of these **NPs** was analyzed using a molecular dynamics simulation study. The DOSY NMR experiment confirmed the higher level of aggregation of the **NP5**. Furthermore, **NP5** hydrogel was characterized using CD, PXRD, ThT-dye binding experiments. SEM, TEM experiments revealed the existence of nanofibers within the **NP5** hydrogel. The **NP5** hydrogel exhibited minimal cytotoxicity, as demonstrated by MTT and cell death studies. The **NP5** hydrogel was also found to be biostable against the proteolytic enzyme proteinase K and  $\alpha$ -chymotrypsin. Furthermore, the **NP5** hydrogel showed the efficacy against *B. subtilis* and *E. Coli* bacteria. It also demonstrated properties of ROS scavenging, antibacterial and anti-inflammatory activity in epithelial cells and keratinocytes. Notably, the hydrogel showed enhanced activity in keratinocytes compared to epithelial cells. In conclusion, the **NP5** hydrogel could be an efficient candidate for wound healing applications. In addition to our findings, the molecular mechanism underlying the wound healing induced by the hydrogel could be studied in more detail.



## 4.5 References

- [1] Kaur G, Narayanan G, Garg D, Sachdev A, Matai I (2022) Biomaterials-Based Regenerative Strategies for Skin Tissue Wound Healing. *ACS Appl Bio Mater* 5:2069–2106. <https://doi.org/10.1021/acsabm.2c00035>.
- [2] Guan T, Li J, Chen C, Liu Y (2022) Self-Assembling Peptide-Based Hydrogels for Wound Tissue Repair. *Adv Sci* 9:2104165. <https://doi.org/10.1002/advs.202104165>.
- [3] Liang Y, He J, Guo B (2021) Functional Hydrogels as Wound Dressing to Enhance Wound Healing. *ACS Nano* 15:12687–12722. <https://doi.org/10.1021/acsnano.1c04206>.
- [4] Togo C, Zidorio AP, Gonçalves V, Botelho P, De Carvalho K, Dutra E (2021) Does Probiotic Consumption Enhance Wound Healing? A Systematic Review. *Nutrients* 14:111. <https://doi.org/10.3390/nu14010111>.
- [5] Tang X, Wang X, Sun Y, Zhao L, Li D, Zhang J, Sun H, Yang B (2021) Magnesium Oxide-Assisted Dual-Cross-Linking Bio-Multifunctional Hydrogels for Wound Repair during Full-Thickness Skin Injuries. *Adv Funct Mater* 31:2105718. <https://doi.org/10.1002/adfm.202105718>.
- [6] Sharifi S, Hajipour MJ, Gould L, Mahmoudi M (2021) Nanomedicine in Healing Chronic Wounds: Opportunities and Challenges. *Mol Pharm* 18:550–575. <https://doi.org/10.1021/acs.molpharmaceut.0c00346>.
- [7] Montazerian H, Davoodi E, Baidya A, Baghdasarian S, Sarikhani E, Meyer CE, Haghniaz R, Badv M, Annabi N, Khademhosseini A, Weiss PS (2022) Engineered Hemostatic Biomaterials for Sealing Wounds. *Chem Rev* 122:12864–12903. <https://doi.org/10.1021/acs.chemrev.1c01015>.

- [8] Huang W, Wang Y, Huang Z, Wang X, Chen L, Zhang Y, Zhang L (2018) On-Demand Dissolvable Self-Healing Hydrogel Based on Carboxymethyl Chitosan and Cellulose Nanocrystal for Deep Partial Thickness Burn Wound Healing. *ACS Appl Mater Inter* 10:41076–41088. <https://doi.org/10.1021/acsami.8b14526>.
- [9] Dong R, Guo B (2021) Smart wound dressings for wound healing. *Nano Today* 41:101290. <https://doi.org/10.1016/j.nantod.2021.101290>.
- [10] Tavakolian M, Munguia-Lopez JG, Valiei A, Islam Md S, Kinsella JM, Tufenkji N, Van De Ven TGM (2020) Highly Absorbent Antibacterial and Biofilm-Disrupting Hydrogels from Cellulose for Wound Dressing Applications. *ACS Appl Mater Inter* 12:39991–40001. <https://doi.org/10.1021/acsami.0c08784>.
- [11] Gurtner GC, Werner S, Barrandon Y, Longaker MT (2008) Wound repair and regeneration. *Nature* 453:314–321. <https://doi.org/10.1038/nature07039>.
- [12] Maia LB, Moura JJG (2014) How Biology Handles Nitrite. *Chem Rev* 114:5273–5357. <https://doi.org/10.1021/cr400518y>.
- [13] Naik S, Larsen SB, Gomez NC, Alaverdyan K, Sandoel A, Yuan S, Polak L, Kulukian A, Chai S, Fuchs E (2017) Inflammatory memory sensitizes skin epithelial stem cells to tissue damage. *Nature* 550:475–480. <https://doi.org/10.1038/nature24271>.
- [14] Ninan N, Forget A, Shastri VP, Voelcker NH, Blencowe A (2016) Antibacterial and Anti-Inflammatory pH-Responsive Tannic Acid-Carboxylated Agarose Composite Hydrogels for Wound Healing. *ACS Appl Mater Inter* 8:28511–28521. <https://doi.org/10.1021/acsami.6b10491>.
- [15] Holzer-Geissler JCJ, Schwingenschuh S, Zacharias M, Einsiedler J, Kainz S, Reisenegger P, Holecek C, Hofmann E, Wolff-Winiski B, Fahrngruber H, Birngruber T, Kamolz L-P, Kotzbeck P (2022) The

Impact of Prolonged Inflammation on Wound Healing. *Biomedicines* 10:856. <https://doi.org/10.3390/biomedicines10040856>.

[16] Pilipenko I, Murzova A, Savin A, Mohamed A-A, Vladimirova E, Koshel E, Shamova O, Kumacheva E (2023) Dual-Function Hydrogel Dressings with a Dynamic Exchange of Iron Ions and an Antibiotic Drug for Treatment of Infected Wounds. *ACS Appl Bio Mater* 6:1896–1905. <https://doi.org/10.1021/acsabm.3c00124>.

[17] Han X, Su Y, Che G, Wei Q, Zheng H, Zhou J, Li Y (2022) Supramolecular Hydrogel Dressing: Effect of Lignin on the Self-Healing, Antibacterial, Antioxidant, and Biological Activity Improvement. *ACS Appl Mater Inter* 14:50199–50214. <https://doi.org/10.1021/acsami.2c15411>.

[18] Giano MC, Ibrahim Z, Medina SH, Sarhane KA, Christensen JM, Yamada Y, Brandacher G, Schneider JP (2014) Injectable bioadhesive hydrogels with innate antibacterial properties. *Nat Commun* 5:4095. <https://doi.org/10.1038/ncomms5095>.

[19] Zhang L, Cao Z, Bai T, Carr L, Ella-Menye J-R, Irvin C, Ratner BD, Jiang S (2013) Zwitterionic hydrogels implanted in mice resist the foreign-body reaction. *Nat Biotechnol* 31:553–556. <https://doi.org/10.1038/nbt.2580>.

[20] Chu B, He J-M, Liu L-L, Wu C-X, You L-L, Li X-L, Wang S, Chen C-S, Tu M (2021) Proangiogenic Peptide Nanofiber Hydrogels for Wound Healing. *ACS Biomater Sci Eng* 7:1100–1110. <https://doi.org/10.1021/acsbiomaterials.0c01264>.

[21] Halder M, Narula M, Singh Y (2023) Supramolecular, Nanostructured Assembly of Antioxidant and Antibacterial Peptides Conjugated to Naproxen and Indomethacin for the Selective Inhibition of COX-2, Biofilm, and Inflammation in Chronic Wounds. *Bioconjugate Chem* 34:645–663. <https://doi.org/10.1021/acs.bioconjchem.3c00014>.

- [22] Liu J, Du C, Huang W, Lei Y (2024) Injectable smart stimuli-responsive hydrogels: pioneering advancements in biomedical applications. *Biomater Sci* 12:8–56. <https://doi.org/10.1039/D3BM01352A>.
- [23] Cheng B, Yan Y, Qi J, Deng L, Shao Z-W, Zhang K-Q, Li B, Sun Z, Li X (2018) Cooperative Assembly of a Peptide Gelator and Silk Fibroin Afford an Injectable Hydrogel for Tissue Engineering. *ACS Appl Mater Inter* 10:12474–12484. <https://doi.org/10.1021/acsami.8b01725>.
- [24] Yang L, Zhang C, Ren C, Liu J, Zhang Y, Wang J, Huang F, Zhang L, Liu J (2019) Supramolecular Hydrogel Based on Chlorambucil and Peptide Drug for Cancer Combination Therapy. *ACS Appl Mater Inter* 11:331–339. <https://doi.org/10.1021/acsami.8b18425>.
- [25] Ghosh T, Das AK (2023) Dynamic boronate esters cross-linked guanosine hydrogels: A promising biomaterial for emergent applications. *Coord Chem Rev* 488:215170. <https://doi.org/10.1016/j.ccr.2023.215170>.
- [26] Mondal S, Das S, Nandi AK (2020) A review on recent advances in polymer and peptide hydrogels. *Soft Matter* 16:1404–1454. <https://doi.org/10.1039/C9SM02127B>.
- [27] Pochan D, Scherman O (2021) Introduction: Molecular Self-Assembly. *Chem Rev* 121:13699–13700. <https://doi.org/10.1021/acs.chemrev.1c00884>.
- [28] Brito A, Kassem S, Reis RL, Ulijn RV, Pires RA, Pashkuleva I (2021) Carbohydrate amphiphiles for supramolecular biomaterials: Design, self-assembly, and applications. *Chem* 7:2943–2964. <https://doi.org/10.1016/j.chempr.2021.04.011>.
- [29] Webber MJ, Appel EA, Meijer EW, Langer R (2016) Supramolecular biomaterials. *Nature Mater* 15:13–26. <https://doi.org/10.1038/nmat4474>.

- [30] Zhou J, Li J, Du X, Xu B (2017) Supramolecular biofunctional materials. *Biomater* 129:1–27. <https://doi.org/10.1016/j.biomaterials.2017.03.014>.
- [31] Carrejo NC, Moore AN, Lopez Silva TL, Leach DG, Li I-C, Walker DR, Hartgerink JD (2018) Multidomain Peptide Hydrogel Accelerates Healing of Full-Thickness Wounds in Diabetic Mice. *ACS Biomater Sci Eng* 4:1386–1396. <https://doi.org/10.1021/acsbiomaterials.8b00031>.
- [32] Uzunalli G, Mammadov R, Yesildal F, Alhan D, Ozturk S, Ozgurtas T, Guler MO, Tekinay AB (2017) Angiogenic Heparin-Mimetic Peptide Nanofiber Gel Improves Regenerative Healing of Acute Wounds. *ACS Biomater Sci Eng* 3:1296–1303. <https://doi.org/10.1021/acsbiomaterials.6b00165>.
- [33] Cui T, Li X, He S, Xu D, Yin L, Huang X, Deng S, Yue W, Zhong W (2020) Instant Self-Assembly Peptide Hydrogel Encapsulation with Fibrous Alginate by Microfluidics for Infected Wound Healing. *ACS Biomater Sci Eng* 6:5001–5011. <https://doi.org/10.1021/acsbiomaterials.0c00581>.
- [34] Sparks HD, Sigaeva T, Tarraf S, Mandla S, Pope H, Hee O, Di Martino ES, Biernaskie J, Radisic M, Scott WM (2021) Biomechanics of Wound Healing in an Equine Limb Model: Effect of Location and Treatment with a Peptide-Modified Collagen–Chitosan Hydrogel. *ACS Biomater Sci Eng* 7:265–278. <https://doi.org/10.1021/acsbiomaterials.0c01431>.
- [35] Hellmund KS, Von Lospichl B, Böttcher C, Ludwig K, Keiderling U, Noirez L, Weiß A, Mikolajczak DJ, Gradzielski M, Kokscha B (2021) Functionalized peptide hydrogels as tunable extracellular matrix mimics for biological applications. *Pept Sci* 113:e24201. <https://doi.org/10.1002/pep2.24201>.
- [36] Giraud T, Hoschtettler P, Pickaert G, Averlant-Petit M-C, Stefan L (2022) Emerging low-molecular weight nucleopeptide-based hydrogels:

state of the art, applications, challenges and perspectives. *Nanoscale* 14:4908–4921. <https://doi.org/10.1039/D1NR06131C>.

[37] Giraud T, Bouguet-Bonnet S, Stébé M-J, Richaudeau L, Pickaert G, Averlant-Petit M-C, Stefan L (2021) Co-assembly and multicomponent hydrogel formation upon mixing nucleobase-containing peptides. *Nanoscale* 13:10566–10578. <https://doi.org/10.1039/D1NR02417E>.

[38] Bakhtiary N, Ghalandari B, Ghorbani F, Varma SN, Liu C (2023) Advances in Peptide-Based Hydrogel for Tissue Engineering. *Polymers* 15:1068. <https://doi.org/10.3390/polym15051068>.

[39] Seah JJ, Wang D-Y (2022) Pushing the frontiers of military medical excellence: updates, progress and future needs. *Military Med Res* 9:27, s40779-022-00388–x. <https://doi.org/10.1186/s40779-022-00388-x>.

[40] Okesola BO, Wu Y, Derkus B, Gani S, Wu D, Knani D, Smith DK, Adams DJ, Mata A (2019) Supramolecular Self-Assembly To Control Structural and Biological Properties of Multicomponent Hydrogels. *Chem Mater* 31:7883–7897. <https://doi.org/10.1021/acs.chemmater.9b01882>.

[41] Du X, Zhou J, Shi J, Xu B (2015) Supramolecular Hydrogelators and Hydrogels: From Soft Matter to Molecular Biomaterials. *Chem Rev* 115:13165–13307. <https://doi.org/10.1021/acs.chemrev.5b00299>.

[42] Biswas A, Malferrari S, Kalaskar DM, Das AK (2018) Arylboronate esters mediated self-healable and biocompatible dynamic G-quadruplex hydrogels as promising 3D-bioinks. *Chem Commun* 54:1778–1781. <https://doi.org/10.1039/C7CC09051J>.

[43] Da Rocha Lapa F, Da Silva MD, De Almeida Cabrini D, Santos ARS (2012) Anti-inflammatory effects of purine nucleosides, adenosine and inosine, in a mouse model of pleurisy: evidence for the role of adenosine A2 receptors. *Purinergic Signal* 8:693–704. <https://doi.org/10.1007/s11302-012-9299-2>.

- [44] Kuno M, Seki N, Tsujimoto S, Nakanishi I, Kinoshita T, Nakamura K, Terasaka T, Nishio N, Sato A, Fujii T (2006) Anti-inflammatory activity of non-nucleoside adenosine deaminase inhibitor FR234938. *Eur J Pharmacol* 534:241–249. <https://doi.org/10.1016/j.ejphar.2006.01.042>.
- [45] Ghosh T, Wang S, Kashyap D, Jadhav RG, Rit T, Jha HC, Cousins BG, Das AK (2022) Self-assembled benzoselenadiazole-capped tripeptide hydrogels with inherent *in vitro* anti-cancer and anti-inflammatory activity. *Chem Commun* 58:7534–7537. <https://doi.org/10.1039/D2CC01160C>.
- [46] Baral B, Kashyap D, Varshney N, Verma TP, Jain AK, Chatterji D, Kumar V, Mishra A, Kumar A, Jha HC (2024) *Helicobacter pylori* isolated from gastric juice have higher pathogenic potential than biopsy isolates. *Genes Dis* 11:34–37. <https://doi.org/10.1016/j.gendis.2023.03.003>.
- [47] Baral B, Saini V, Tandon A, Singh S, Rele S, Dixit AK, Parmar HS, Meena AK, Jha HC (2023) SARS-CoV-2 envelope protein induces necroptosis and mediates inflammatory response in lung and colon cells through receptor interacting protein kinase 1. *Apoptosis* 28:1596–1617. <https://doi.org/10.1007/s10495-023-01883-9>.
- [48] Bhowmik S, Ghosh T, Sanghvi YS, Das AK (2023) Synthesis and Structural Studies of Nucleobase Functionalized Hydrogels for Controlled Release of Vitamins. *ACS Appl Bio Mater* 6:5301–5309. <https://doi.org/10.1021/acsabm.3c00582>.
- [49] Gan KP, Yoshio M, Sugihara Y, Kato T (2018) Guanine–oligothiophene conjugates: liquid-crystalline properties, photoconductivities and ion-responsive emission of their nanoscale assemblies. *Chem Sci* 9:576–585. <https://doi.org/10.1039/C7SC03764C>.

- [50] Datta D (2020) A convenient route to synthesize  $N^2$ -(isobutyryl)-9-(carboxymethyl)guanine for *aeg* -PNA backbone. *Nucleos Nucleot Nucl* 39:530–541. <https://doi.org/10.1080/15257770.2019.1666139>.
- [51] Frederix PWJM, Scott GG, Abul-Haija YM, Kalafatovic, D Pappas, CG, Javid N, Hunt NT, Ulijn RV, Tuttle T (2015) Exploring the sequence space for (tri-)peptide self-assembly to design and discover new hydrogels. *Nature Chem* 7:30–37. <https://doi.org/10.1038/nchem.2122>.
- [52] Misra S, Mukherjee S, Ghosh A, Singh P, Mondal S, Ray D, Bhattacharya G, Ganguly D, Ghosh A, Aswal VK, Mahapatra AK, Satpati B, Nanda J (2021) Single Amino-Acid Based Self-Assembled Biomaterials with Potent Antimicrobial Activity. *Chemistry A European J* 27:16744–16753. <https://doi.org/10.1002/chem.202103071>.
- [53] Noblett AD, Baek K, Suggs LJ (2021) Controlling Nucleopeptide Hydrogel Self-Assembly and Formation for Cell-Culture Scaffold Applications. *ACS Biomater Sci Eng* 7:2605–2614. <https://doi.org/10.1021/acsbiomaterials.0c01658>.
- [54] del Villar-Guerra R, Trent JO, Chaires JB (2018) G-Quadruplex Secondary Structure Obtained from Circular Dichroism Spectroscopy. *Angew Chem Int Ed* 57:7171–7175. <https://doi.org/10.1002/anie.201709184>.
- [55] Del Villar-Guerra R, Gray RD, Chaires JB (2017) Characterization of Quadruplex DNA Structure by Circular Dichroism. *CP Nucleic Acid Chem* 68:17.8.1-17.8.16. <https://doi.org/10.1002/cpnc.23>.
- [56] Amdursky N, Stevens MM (2015) Circular Dichroism of Amino Acids: Following the Structural Formation of Phenylalanine. *ChemPhysChem* 16:2768–2774. <https://doi.org/10.1002/cphc.201500260>.
- [57] Dai Y, Zhang Y, Liao W, Wang W, Wu L (2020) G-quadruplex specific thioflavin T-based label-free fluorescence aptasensor for rapid



detection of tetracycline. *Spectrochim Acta A Mol Biomol Spectrosc* 238:118406. <https://doi.org/10.1016/j.saa.2020.118406>.

[58] Sharma P, Pal VK, Kaur H, Roy S (2022) Exploring the TEMPO-Oxidized Nanofibrillar Cellulose and Short Ionic-Complementary Peptide Composite Hydrogel as Biofunctional Cellular Scaffolds. *Biomacromole* 23:2496–2511. <https://doi.org/10.1021/acs.biomac.2c00234>.

[59] Xie X, Zhang Y, Liang Y, Wang M, Cui Y, Li J, Liu C (2022) Programmable Transient Supramolecular Chiral G-quadruplex Hydrogels by a Chemically Fueled Non-equilibrium Self-Assembly Strategy. *Angew Chem Int Ed* 61:e202114471. <https://doi.org/10.1002/anie.202114471>.

[60] Schwaighofer A, Montemurro M, Freitag S, Kristament C, Culzoni MJ, Lendl B (2018) Beyond Fourier Transform Infrared Spectroscopy: External Cavity Quantum Cascade Laser-Based Mid-infrared Transmission Spectroscopy of Proteins in the Amide I and Amide II Region. *Anal Chem* 90:7072–7079. <https://doi.org/10.1021/acs.analchem.8b01632>.

[61] Raghuwanshi VS, Garnier G (2019) Characterisation of hydrogels: Linking the nano to the microscale. *Adv. Colloid Interface Sci.* 274:102044. <https://doi.org/10.1016/j.cis.2019.102044>.

[62] Kubota R, Tanaka W, Hamachi I (2021) Microscopic Imaging Techniques for Molecular Assemblies: Electron, Atomic Force, and Confocal Microscopies. *Chem Rev* 121:14281–14347. <https://doi.org/10.1021/acs.chemrev.0c01334>.

[63] Onogi S, Shigemitsu H, Yoshii T, Tanida T, Ikeda M, Kubota R, Hamachi I (2016) In situ real-time imaging of self-sorted supramolecular nanofibres. *Nature Chem* 8:743–752. <https://doi.org/10.1038/nchem.2526>.

- [64] Hunt JA, Chen R, Van Veen T, Bryan N (2014) Hydrogels for tissue engineering and regenerative medicine. *J Mater Chem B* 2:5319–5338. <https://doi.org/10.1039/C4TB00775A>.
- [65] Farzanfar J, Farjadian F, Roointan A, Mohammadi-Samani S, Tayebi L (2021) Assessment of pH Responsive Delivery of Methotrexate Based on PHEMA-st-PEG-DA Nanohydrogels. *Macromol Res* 29:54–61. <https://doi.org/10.1007/s13233-021-9007-6>.
- [66] Metzger K, Dannenberger D, Tuchscherer A, Ponsuksili S, Kalbe C (2021) Effects of temperature on proliferation of myoblasts from donor piglets with different thermoregulatory maturities. *BMC Mol and Cell Biol* 22:36. <https://doi.org/10.1186/s12860-021-00376-4>.
- [67] Gavel PK, Dev D, Parmar HS, Bhasin S, Das AK (2018) Investigations of Peptide-Based Biocompatible Injectable Shape-Memory Hydrogels: Differential Biological Effects on Bacterial and Human Blood Cells. *ACS Appl Mater Inter* 10:10729–10740. <https://doi.org/10.1021/acsami.8b00501>.
- [68] Baral A, Roy S, Ghosh S, Hermida-Merino D, Hamley, IW, Banerjee A (2016) A Peptide-Based Mechano-sensitive, Proteolytically Stable Hydrogel with Remarkable Antibacterial Properties. *Langmuir* 32:1836–1845. <https://doi.org/10.1021/acs.langmuir.5b03789>.
- [69] Sparks HD, Mandla S, Vizely K, Rosin N, Radisic M, Biernaskie J (2022) Application of an instructive hydrogel accelerates re-epithelialization of xenografted human skin wounds. *Sci Rep* 12:14233. <https://doi.org/10.1038/s41598-022-18204-w>.
- [70] Xiong Y, Chu X, Yu T, Knoedler S, Schroeter A, Lu L, Zha K, Lin Z, Jiang D, Rinkevich Y, Panayi AC, Mi B, Liu G, Zhao Y (2023) Reactive Oxygen Species-Scavenging Nanosystems in the Treatment of Diabetic Wounds. *Adv Healthc Mater* 12:2300779. <https://doi.org/10.1002/adhm.202300779>.

- [71] Kim YE, Kim J (2022) ROS-Scavenging Therapeutic Hydrogels for Modulation of the Inflammatory Response. *ACS Appl Mater Inter* 14:23002–23021. <https://doi.org/10.1021/acsami.1c18261>.
- [72] Dizdaroglu M, Jaruga P (2012) Mechanisms of free radical-induced damage to DNA. *Free Radical Research* 46:382–419. <https://doi.org/10.3109/10715762.2011.653969>.
- [73] Zhang Y, Kang J, Chen X, Zhang W, Zhang X, Yu W, Yuan W-E (2023) Ag nanocomposite hydrogels with immune and regenerative microenvironment regulation promote scarless healing of infected wounds. *J Nanobiotechnol* 21:435. <https://doi.org/10.1186/s12951-023-02209-2>.
- [74] Deng J, Lin D, Ding X, Wang Y, Hu Y, Shi H, Chen L, Chu B, Lei L, Wen C, Wang J, Qian Z, Li X (2022) Multifunctional Supramolecular Filament Hydrogel Boosts Anti-Inflammatory Efficacy In Vitro and In Vivo. *Adv Funct Mater* 32:2109173. <https://doi.org/10.1002/adfm.202109173>.
- [75] Gavel PK, Kumar N, Parmar HS, Das AK (2020) Evaluation of a Peptide-Based Coassembled Nanofibrous and Thixotropic Hydrogel for Dermal Wound Healing. *ACS Appl Bio Mater* 3:3326–3336. <https://doi.org/10.1021/acsabm.0c00252>.

## **Chapter 5**

# **Enzyme Fueled Dissipative Self-assembly of Guanine Functionalized Molecules and Their Cellular Behaviour**



## 5.1 Introduction

Nucleobases and their analogs play a significant role in the fields of biology as well as chemistry due to their diverse biological function and increasing use as antiviral drugs [1]. The specific hydrogen bonding of nucleobases is involved in important biological processes such as transcription, translation, and replication, which are directly linked with complex biological evolution [2,3]. Amino acid-based supramolecular nanomaterials have gained considerable attention in recent years because of their potential utilization in tissue engineering, drug delivery, enzyme testing, and protein separations as they exhibit notable biological activity and biodegradability [4-7]. Therefore, the development of functional materials by bio-conjugation of nucleobase and peptide offers novel avenues for their assembly. Lipases have a significant impact on biocatalysis due to their wide range of substrate specificity, often strong regio- and enantioselectivity, and capability to operate in both aqueous and organic reaction environments, which make them very adaptable for the polymerization of esters, kinetic resolution, and derivatization. Broadly, an esterase lipase exhibits substrate-specific hydrolysis activity towards esters in aqueous medium. Ester hydrolysis is preferred over esterification in an aqueous environment [8-10]. Here, we plan to harness the equilibrium shifts toward the reverse direction. The formation of the self-assembled building-blocks lowers the activation energy to drive the reaction.

Dissipative self-assembly (DSA) is a ubiquitous process in nature, that occurs far from equilibrium [11]. An example of DSA is the assembly and disassembly of the actin filament, which is driven by the hydrolysis of ATP [12-15]. DSA occurs when non-assembling precursors are activated and transformed into assembling precursors through a continuous supply of energy [16-20]. This is different from molecular self-assembly processes that occur through the thermodynamic equilibrium, where the building-blocks can be exchanged with the surrounding environment. In DSA, the exchange of the building-blocks is balanced and there is no observed involvement or release of energy

[21-25]. This non-equilibrium behavior distinguishes DSA from conventional molecular self-assembly. Therefore, DSA operates far from equilibrium at the expense of energy. The disassembly of molecular building-blocks occurs when the stored energy in the activated building-block dissipates. Thus, two chemical reactions control the assembly and disassembly events that occur in DSA [26-33].

In a chemical fuel driven dissipative self-assembly, a non-assembling building-block dibenzoyl-(L)-cystine (DBC) was activated for self-assembly by the influence of a chemical fuel. The carboxylate groups in the DBC were esterified using methyl iodide. The ester hydrolysis was labile, so when it occurred, it dissipated the energy and caused the activated building-block to disassemble [34]. In living systems, the assembly and disassembly processes driven by fuel are regulated by enzymes [35]. The creation of life on Earth is a mystery to humans. Therefore, researchers have coined the term ‘protocell’, which refers to the primitive or first cell [36]. The term protocell is used to describe cell-like structures that contain self-organized spherical ordered structures. In recent years, research on protocells has mainly focused on designing and developing supramolecular assemblies that contain all the essential ingredients present in cells [37]. Various protocell models are being utilized to explore this mystery, including vesicles [38], colloidosomes [39], microcapsules [40], coacervates [41], water-in-oil emulsions [42], and proteinosomes [43,44]. The main purpose of these models is to compartmentalize molecules and reactions. A lipid-based giant vesicle was used to study the amplification and self-proliferation of DNA [45]. A vesicle made from fatty acids was utilized to study RNA catalysis [46]. In this article, we explore the formation of spheres caused by the biocatalytic inclusion of *p*-hydroxybenzyl alcohol in the synthesized nucleobase functionalized molecules. These spheres could be used as a model for protocells. Cellular organelles are important for maintaining a balanced state in a living cell. Therefore, being able to see the cellular organelles helps us to determine the cell’s health [47]. In recent years, there has been continuous effort to develop fluorophores for visualizing

cellular organelles. Recently, self-assembling biocompatible fluorescent nano architectures have been used to visualize organelles in cells [48]. Herein, the newly developed biocatalytically formed hydrogel has been used to mimic and visualize the organelles. Our main objectives are: (a) to induce dissipative self-assembly of newly design non-assembling building-block called **NP10** using a biocatalyst; (b) to study the self-assembly driven shift of the equilibrium in the reverse direction; (c) to study the morphology inside the biocatalytically formed **NP10** hydrogel; (d) to assess the biocompatibility of a hydrogel derived from **NP10**; (e) to perform live and dead cell imaging and (f) to explore the use of the hydrogel in cell migration.

## 5.2 Experimental Section

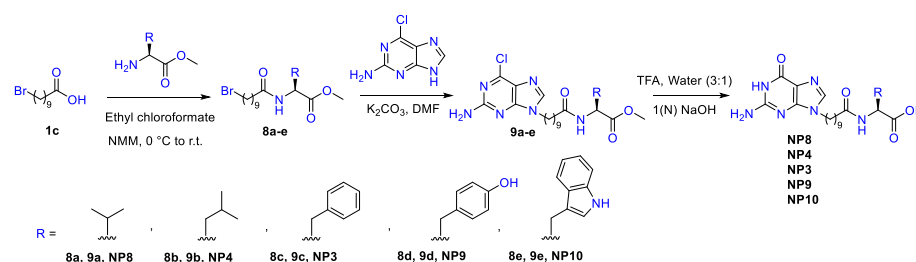
### 5.2.1 Materials and Methods

The used solvents and reagents were purchased from commercially available sources like Alfa Aesar, Sigma Aldrich, Merck and Spectrochem Pvt. Ltd. 2-Amino-6-chloropurine and potassium carbonate ( $K_2CO_3$ ) were obtained from Alfa Aesar. Ethyl chloroformate was purchased from Spectrochem whereas diethyl ether was purchased from Merck. 4-Methylmorpholine was obtained from SRL and 10-Bromodecanoic acid, acid was obtained from TCI. L-Phenylalanine, L-valine, L-Leucine, L-Tyrosine, L-Tryptophan were purchased from SRL. Fetal bovine serum, MTT (3-(4,5-Dimethyl-2-thiazolyl)-2,5-diphenyl-2H-tetrazolium bromide, Dulbecco's Modified Eagle Medium (DMEM) and Streptomycin were obtained from himedia. MitoTracker Green, Hoechst 33342 and Propidium Iodide were obtained from Invitrogen. For moisture sensitive reactions, dry solvent was used in the presence of  $N_2$  or Ar gas. After completion of the reaction, the crude products were purified by column chromatography method using silica as stationary phase and hexane, ethyl acetate or chloroform, methanol as a mobile phase. All  $^1H$  and  $^{13}C$  NMR spectra were set down on Bruker Avance (500 MHz) instrument at 25 °C. ESI-MS spectra were set down on Bruker instrument by using ESI positive mode. The NMR spectra of all intermediates and final products were analyzed by using



MestReNova software. The chemical shift was expressed in the form of ppm ( $\delta$ ) relative to surplus solvents protons as internal standards (DMSO- $d_6$ :  $\delta$  = 2.50 for  $^1\text{H}$  NMR; DMSO- $d_6$ :  $\delta$  39.50 for  $^{13}\text{C}$  NMR,  $\text{CDCl}_3$ :  $\delta$  = 7.26 for  $^1\text{H}$  NMR;  $\text{CDCl}_3$ :  $\delta$  77.50 for  $^{13}\text{C}$  NMR).

## 5.2.2 Synthesis of NPs



**Scheme 5.1** Synthesis of guanine functionalized amino acid derivatives.

### 5.2.3 General procedure for the synthesis of 8a-e:

Under argon atmosphere, 4-methylmorpholine was added in the solution of 10-Bromodecanoic acid in dry chloroform at 0 °C. The solution was left for stirring at this temperature. After 15 minutes, ethyl chloroformate was added into the solution and stirred vigorously at this temperature for additional 45 minutes before the addition of L-amino acids and 4-methylmorpholine. Then the reaction mixture was allowed to stir for 1h at 0 °C and then at room temperature for 16 h. The progress of the reaction was monitored by TLC. After the completion of the reaction, reaction mixture was diluted with water and washed with 1(N) NaOH (3×10) mL and then with brine, 0.5 (N) HCl (3×10) mL and finally with brine. The organic part was dried over  $\text{Na}_2\text{SO}_4$  and concentrate under vacuum. The product was used without further purification.

### 5.2.4 Synthesis of 8a:

The compound **8a** was synthesized as per the above-mentioned general procedure. Yield: 87%.  $^1\text{H}$  NMR ( $\text{CDCl}_3$ , 500 MHz):  $\delta$  0.90-0.91 (d, 3H,  $J$  = 5Hz), 0.93-0.94 (d, 3H,  $J$  = 5 Hz), 1.30 (m, 8H), 1.40-1.42 (m, 2H), 1.63-1.64 (m, 2H), 1.82-1.88 (m, 2H), 2.12-2.19 (m, 1H), 3.39-3.42 (t, 2H,  $J$  = 5, 10 Hz), 3.74 (s, 1H), 4.58-4.60 (m, 1H), 6.00-6.02 (d, 2H,  $J$  = 5 Hz).  $^{13}\text{C}$  NMR ( $\text{CDCl}_3$ , 125 MHz):  $\delta$  17.83, 18.93, 24.69, 25.65,

28.12, 28.68, 29.19, 31.33, 32.79, 34.00, 36.67, 52.17, 56.81, 173.17,  
178.77. (ESI-MS,  $m/z$ ):  $[M+Na]^+$   $m/z$  calcd for  $C_{16}H_{30}BrNO_3Na$ :  
386.1301; found: 386.1297

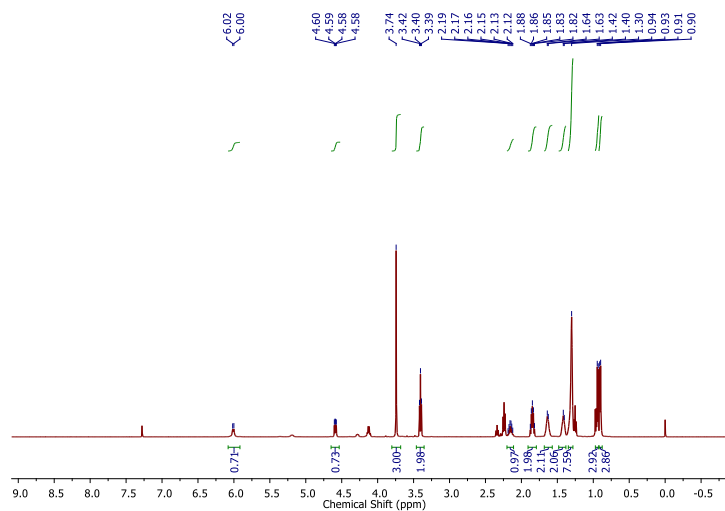


**Figure 5.1**  $^1\text{H}$  NMR (500 MHz,  $\text{CDCl}_3$ ) spectrum of **8a**.

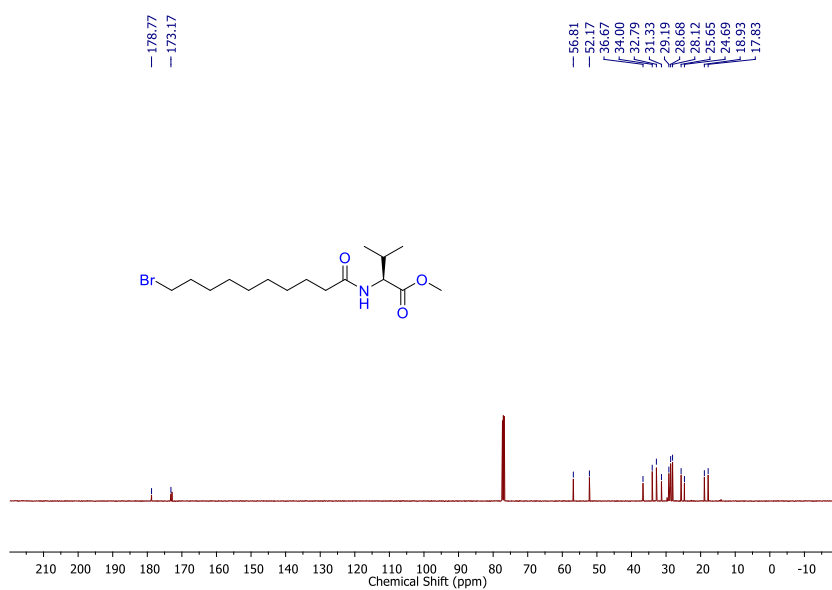


**Figure 5.2**  $^{13}\text{C}$  NMR (125 MHz,  $\text{CDCl}_3$ ) spectrum of **8a**.

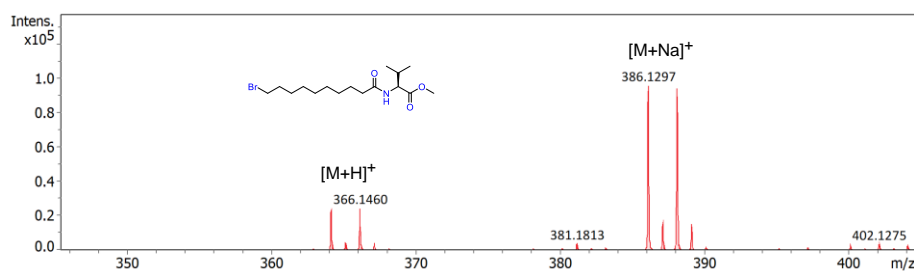


**Figure 5.3** ESI-MS spectrum of **8a**.

### 5.2.5 Synthesis of **8b**:

The compound **8b** was synthesized as per the above-mentioned general procedure. Yield: 88%.  $^1\text{H}$  NMR (DMSO- $d_6$ , 500 MHz):  $\delta$  0.76-0.77 (d, 3H,  $J = 5$  Hz), 0.81-0.83 (d, 3H,  $J = 5$  Hz), 1.18 (s, 8H), 1.27-1.33 (m, 2H), 1.36-1.46 (m, 4H), 1.52-1.57 (m, 1H), 1.69-1.74 (m, 2H), 2.01-2.05 (m, 1H), 3.26 (s, 3H), 3.44-3.46 (t, 2H,  $J = 5, 10$  Hz), 4.18-4.23 (m, 1H), 8.06-8.08 (d, 1H,  $J = 5$  Hz).  $^{13}\text{C}$  NMR ( $\text{CDCl}_3$ , 125 MHz):  $\delta$  21.93, 22.79, 24.85, 25.52, 28.09, 28.65, 29.11, 29.22, 32.77, 33.98, 36.45, 41.66, 50.49, 52.21, 172.92, 173.78. (ESI-MS,  $m/z$ ):  $[\text{M}+\text{Na}]^+$  calculated for  $\text{C}_{17}\text{H}_{32}\text{BrNO}_3\text{Na}$  400.1458; found 400.1459

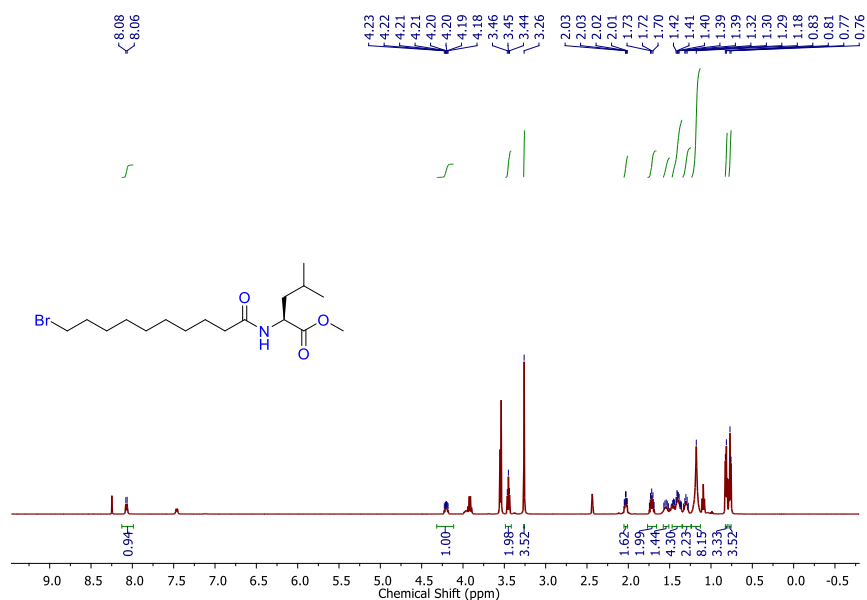


**Figure 5.4**  $^1\text{H}$  NMR (500 MHz,  $\text{CDCl}_3$ ) spectrum of **8b**.

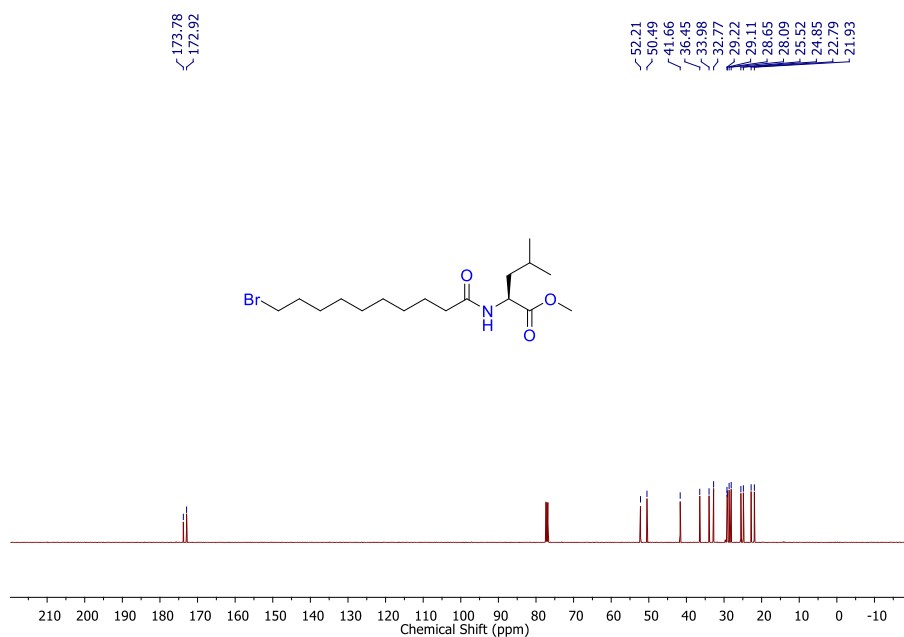


**Figure 5.5** <sup>13</sup>C NMR (125 MHz, CDCl<sub>3</sub>) spectrum of **8b**.

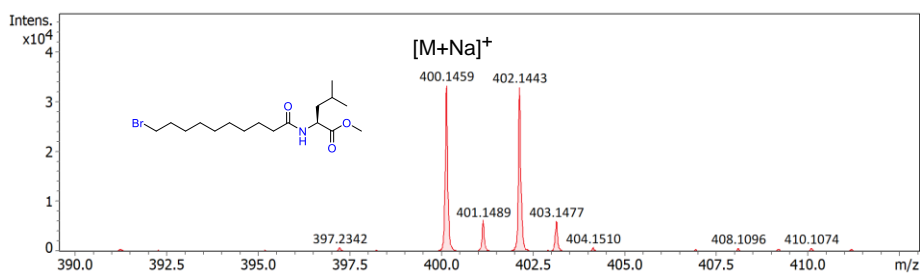


**Figure 5.6** ESI-MS spectrum of **8b**.

### 5.2.6 Synthesis of **8c**:

The compound **8c** was synthesized as per the above-mentioned general procedure. Yield: 90%. <sup>1</sup>H NMR (DMSO-*d*<sub>6</sub>, 400 MHz): δ 1.19-1.27 (m, 8H), 1.44-1.46 (d, 4H), 1.84-1.86 (m, 2H), 2.06-2.11 (m, 2H), 2.91-2.97 (m, 1H), 3.08-3.11 (m, 1H), 3.58-3.60 (t, 2H, *J* = 4, 8 Hz), 3.67 (s, 3H), 4.53 (s, 1H), 7.28-7.34 (m, 5H), 8.30-8.32 (d, 1H, *J* = 8 Hz). <sup>13</sup>C NMR (CDCl<sub>3</sub>, 125 MHz): δ 25.49, 28.13, 28.69, 29.12, 29.19, 29.22, 32.80, 34.03, 36.53, 37.93, 52.33, 52.89, 127.13, 128.57, 129.27, 135.89, 172.20, 172.60. (ESI-MS, *m/z*): [M+Na]<sup>+</sup> calculated for C<sub>20</sub>H<sub>30</sub>BrNO<sub>3</sub>Na 434.1301; found 434.1325.

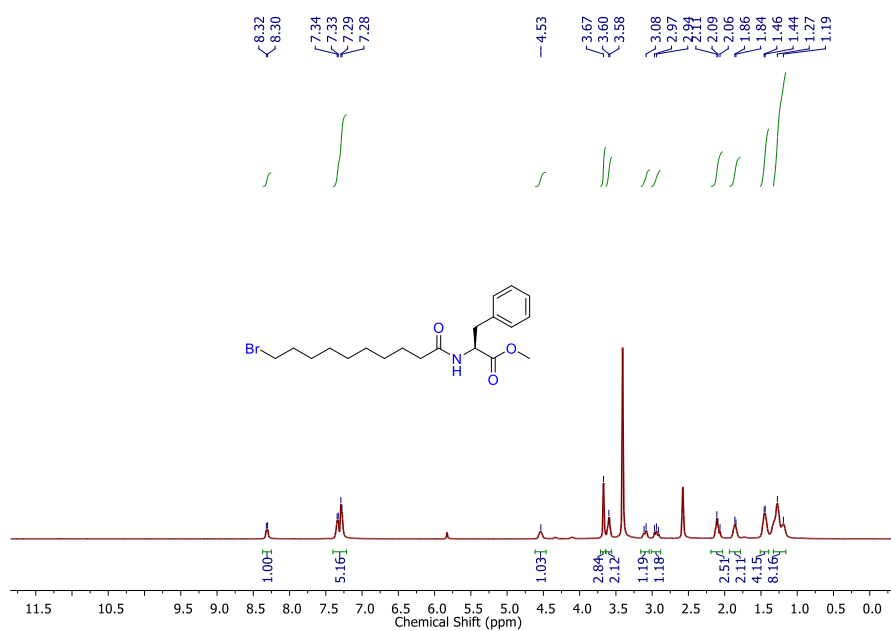


**Figure 5.7** <sup>1</sup>H NMR (500 MHz, CDCl<sub>3</sub>) spectrum of **8c**.

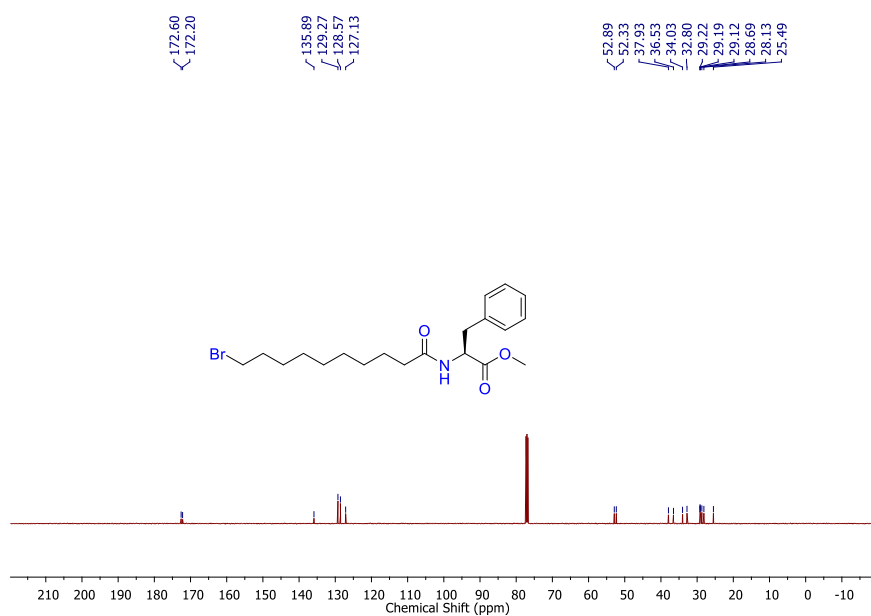


**Figure 5.8** <sup>13</sup>C NMR (125 MHz, CDCl<sub>3</sub>) spectrum of **8c**.

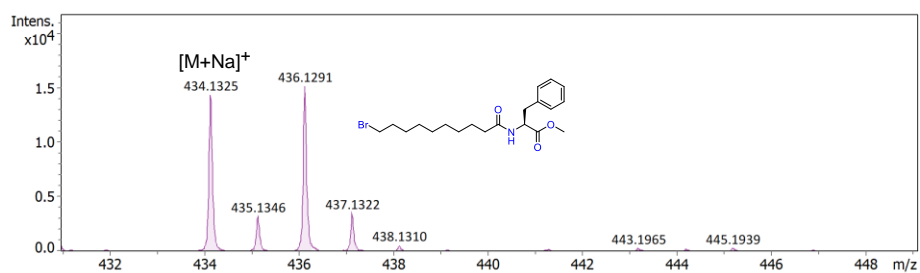


**Figure 5.9** ESI-MS spectrum of **8c**.

### 5.2.7 Synthesis of 8d:

The compound **8d** was synthesized as per the above-mentioned general procedure. Yield: 81%.  $^1\text{H}$  NMR ( $\text{CDCl}_3$ , 500 MHz):  $\delta$  1.27 (8H), 1.38-1.42 (m, 2H), 1.57-1.62 (m, 2H), 1.73-1.87 (m, 2H), 2.16-2.19 (t, 2H), 2.97-3.01 (m, 1H), 3.07-3.11 (m, 1H), 3.51-3.54 (t, 2H), 3.74 (s, 3H), 4.86-4.90 (m, 1H), 5.89-5.91 (d, 2H,  $J = 5$  Hz), 6.72-6.74 (d, 2H,  $J = 5$  Hz), 6.94-6.95 (d, 2H,  $J = 5$  Hz).  $^{13}\text{C}$  NMR ( $\text{DMSO}-d_6$ , 125 MHz):  $\delta$  25.50, 26.83, 28.11, 28.79, 29.09, 29.23, 32.60, 34.08, 36.55, 37.24, 45.21, 53.07, 115.50, 127.45, 130.33, 155.13, 172.38, 172.95. (ESI-MS,  $m/z$ ):  $[\text{M}+\text{Na}]^+$  calculated for  $\text{C}_{20}\text{H}_{30}\text{BrNO}_4\text{Na}$  450.1250; found 450.1251.

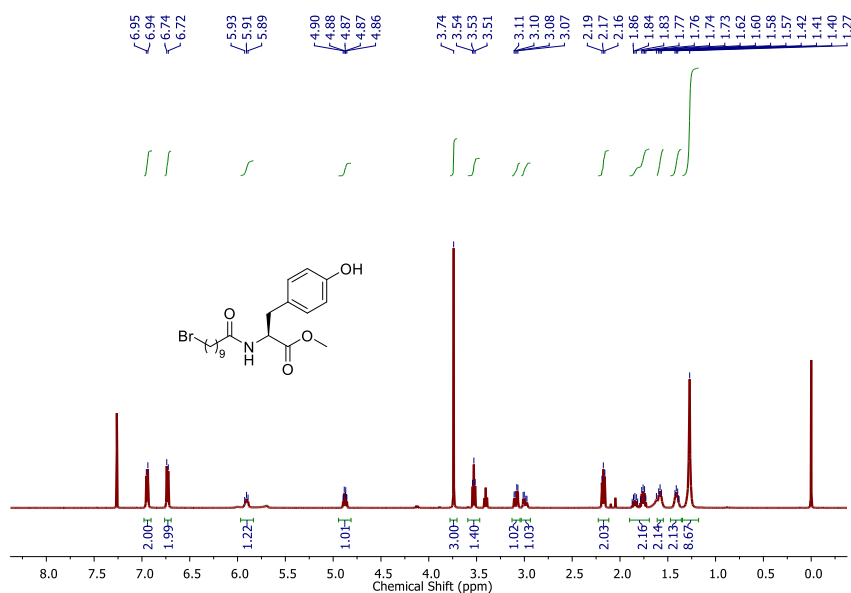


**Figure 5.10**  $^1\text{H}$  NMR (500 MHz,  $\text{CDCl}_3$ ) spectrum of **8d**.

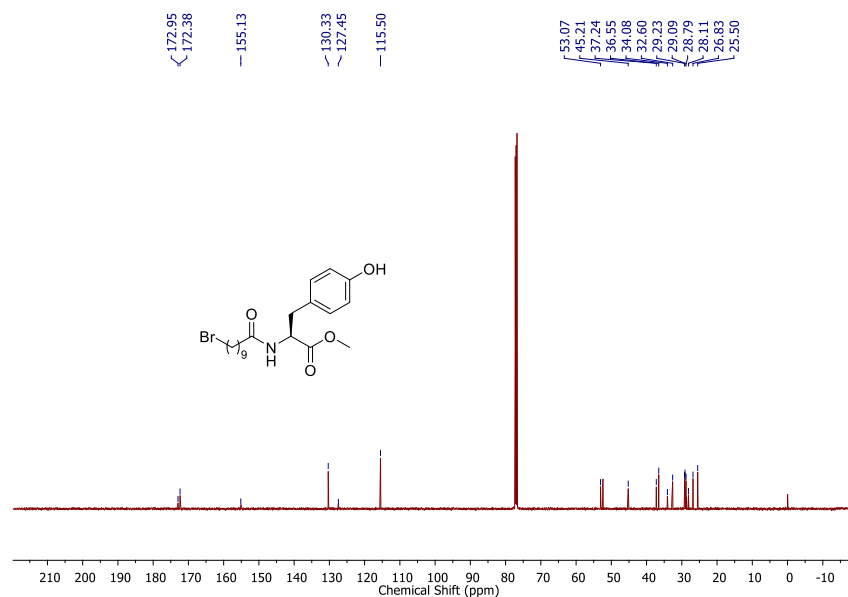


**Figure 5.11** <sup>13</sup>C NMR (125 MHz, CDCl<sub>3</sub>) spectrum of **8d**.

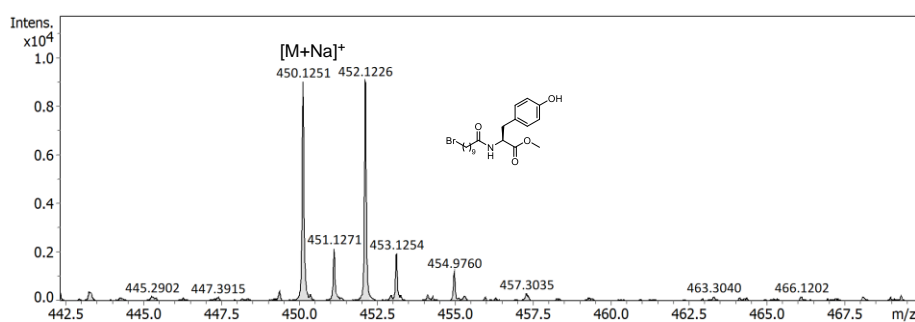


**Figure 5.12** ESI-MS spectrum of **8d**.

### 5.2.8 Synthesis of **8e**:

The compound **8e** was synthesized as per the above-mentioned general procedure. Yield: 85%. <sup>1</sup>H NMR (DMSO-*d*<sub>6</sub>, 500 MHz):  $\delta$  1.09-1.24 (m, 8H), 1.31-1.42 (m, 4H), 1.73-1.79 (m, 2H), 2.03-2.06 (m, 2H), 2.98-3.02 (m, 1H), 3.10-3.14 (m, 1H), 3.48-3.51 (t, 2H, *J* = 5, 10 Hz), 3.56 (s, 3H), 4.46-4.50 (m, 1H), 6.95-6.98 (t, 1H, *J* = 5, 10 Hz), 7.04-7.07 (t, 1H, *J* = 5, 10 Hz), 7.12 (s, 1H), 7.31-7.33 (d, 1H, *J* = 5 Hz), 7.46-7.48 (d, 1H, *J* = 5 Hz), 8.20-8.21 (d, 1H, *J* = 5 Hz), 10.83 (s, 1H). <sup>13</sup>C NMR (DMSO-*d*<sub>6</sub>, 125 MHz):  $\delta$  25.57, 25.91, 27.48, 27.93, 28.48, 28.92, 29.18, 29.34, 29.39, 32.93, 35.42, 52.23, 61.20, 110.02, 111.89, 118.43, 121.44, 124.06, 127.49, 136.54, 172.98, 173.05. (ESI-MS, *m/z*): [M+Na]<sup>+</sup> calculated for C<sub>22</sub>H<sub>31</sub>BrN<sub>2</sub>O<sub>3</sub>Na 475.1393; found 475.1364.

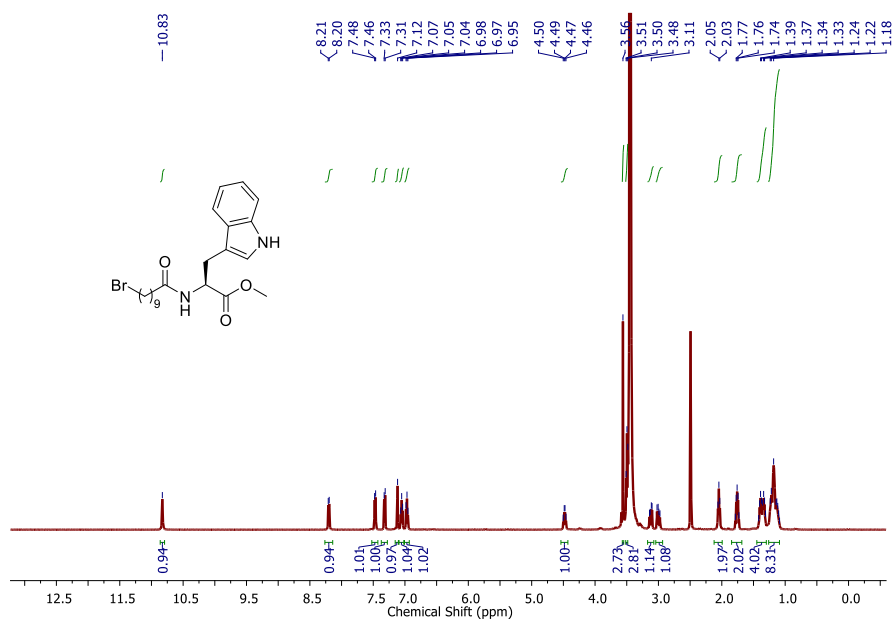


**Figure 5.13** <sup>1</sup>H NMR (500 MHz, CDCl<sub>3</sub>) spectrum of **8e**.

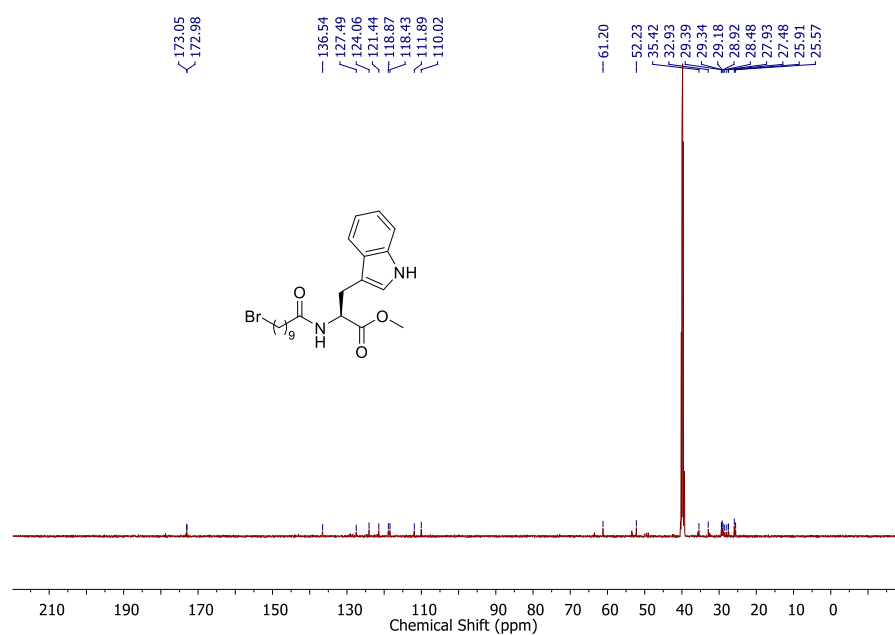


**Figure 5.14** <sup>13</sup>C NMR (125 MHz, CDCl<sub>3</sub>) spectrum of **8e**.

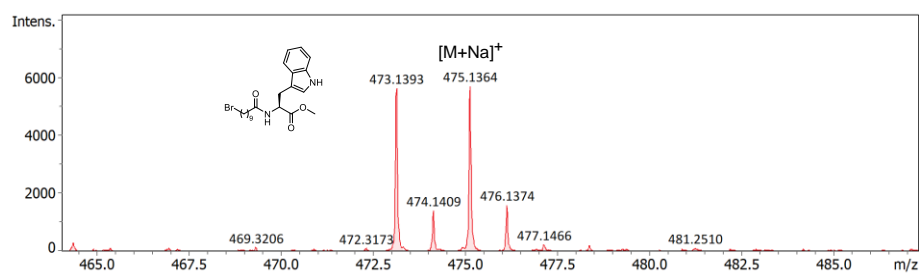


**Figure 5.15** ESI-MS spectrum of **8e**.



### 5.2.9 General procedure for the synthesis of 9a-e:

Here the compounds were synthesized following previously reported synthetic procedure. 2-amino-6 chloro purine was added in the solution of dry DMF (10 ml) under an argon atmosphere. Then  $K_2CO_3$  was added to the solution. Finally, bromoacid was added dropwise into the solution and the reaction was left to stir for 24h. The progress of the reaction was monitored by TLC. After the completion of the reaction, the reaction mixture was diluted with ethyl acetate and washed with water several times, finally with brine and dried over  $Na_2SO_4$ . After the evaporation of the solvent under rota evaporation, the reaction mixture was purified by silica gel column chromatography. The major product was the N9 alkylated product (eluent:  $CHCl_3$ : MeOH = 99:1) and the minor product was the N7 alkylated product (eluent:  $CHCl_3$ : MeOH = 94:6).

### 5.2.10 Compound 9a:

The compound **9a** was synthesized as per the above-mentioned general procedure. Yield: 65%.  $^1H$  NMR ( $DMSO-d_6$ , 500 MHz):  $\delta$  0.90-0.93 (t, 6H), 1.27 (s, 10H), 1.48-1.56 (m, 2H), 1.79-1.84 (m, 2H), 2.02-2.09 (m, 1H), 2.15-2.25 (m, 2H), 3.67 (s, 3H), 4.07-4.10 (t, 2H,  $J = 5, 10$  Hz), 4.19-4.22 (m, 1H), 6.95 (s, 2H), 8.10-8.12 (d, 1H,  $J = 5$  Hz), 8.19 (s, 1H).  $^{13}C$  NMR ( $DMSO-d_6$ , 125 MHz):  $\delta$  18.75, 19.45, 25.73, 26.44, 28.88, 28.95, 29.08, 29.25, 29.38, 30.23, 35.29, 43.47, 52.03, 57.77, 123.81, 143.76, 149.75, 154.53, 160.20, 172.76, 173.14. (ESI-MS,  $m/z$ ):  $[M+Na]^+$  calculated for  $C_{21}H_{33}ClN_6O_3Na$  475.2195; found 475.2202.

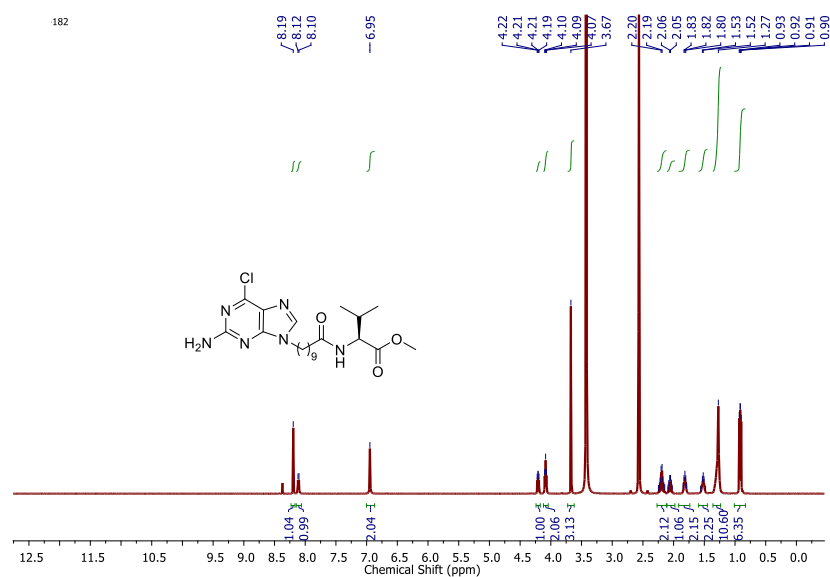


**Figure 5.16** <sup>1</sup>H NMR (500 MHz, DMSO-*d*<sub>6</sub>) spectrum of **9a**.

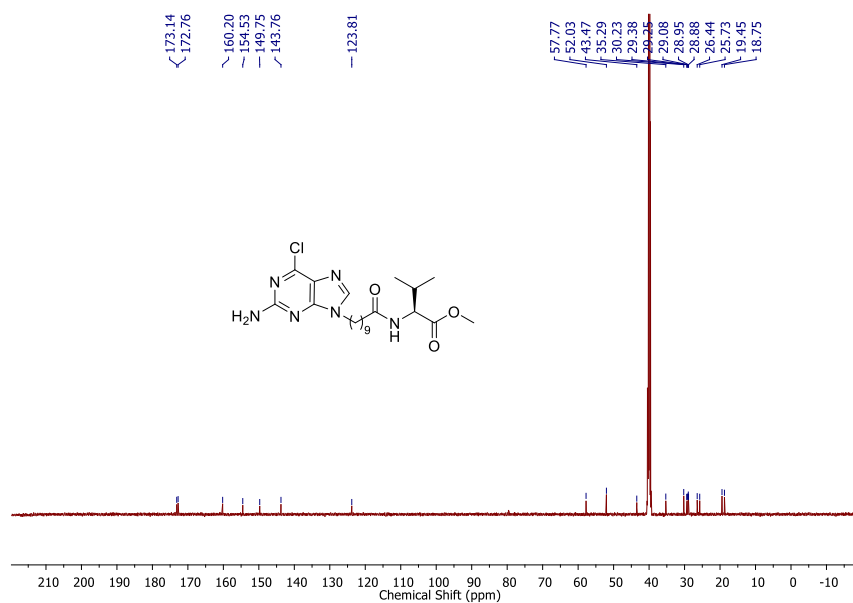


**Figure 5.17** <sup>13</sup>C NMR (125 MHz, CDCl<sub>3</sub>) spectrum of **9a**.

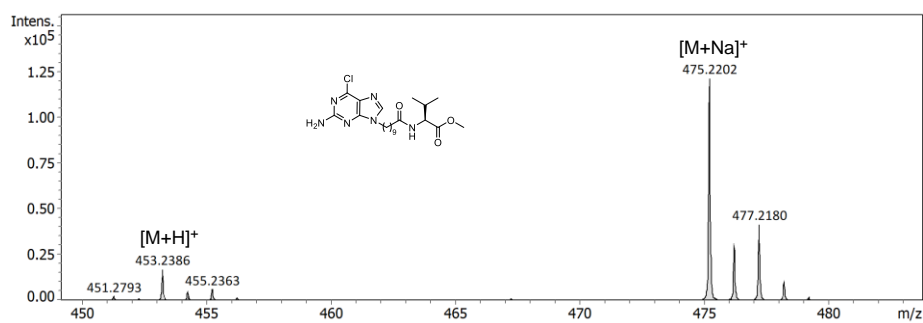


**Figure 5.18** ESI-MS spectrum of **9a**.

### 5.2.11 Compound **9b**:

The compound **9b** was synthesized as per the above-mentioned general procedure. Yield: 61%.  $^1\text{H}$  NMR (DMSO- $d_6$ , 500 MHz):  $\delta$  0.87-0.88 (d, 3H,  $J = 5$  Hz), 0.92-0.94 (d, 3H,  $J = 10$  Hz), 1.27 (s, 8H), 1.48-1.60 (m, 4H), 1.61-1.70 (m, 1H), 1.80-1.85 (m, 2H), 2.10-2.19 (m, 2H), 3.66 (s, 3H), 4.07-4.10 (t, 2H,  $J = 5, 10$  Hz), 4.30-4.34 (m, 1H), 6.95 (s, 2H), 8.18 (s, 1H), 8.20 (s, 1H).  $^{13}\text{C}$  NMR (DMSO- $d_6$ , 125 MHz):  $\delta$  21.62, 23.22, 24.71, 25.64, 26.46, 28.89, 29.08, 29.27, 29.40, 35.38, 43.47, 50.53, 52.19, 123.81, 143.74, 149.75, 154.54, 160.21, 172.87, 173.70. (ESI-MS,  $m/z$ ):  $[\text{M}+\text{Na}]^+$  calculated for  $\text{C}_{22}\text{H}_{35}\text{ClN}_6\text{O}_3\text{Na}$  489.2351; found 489.2358.

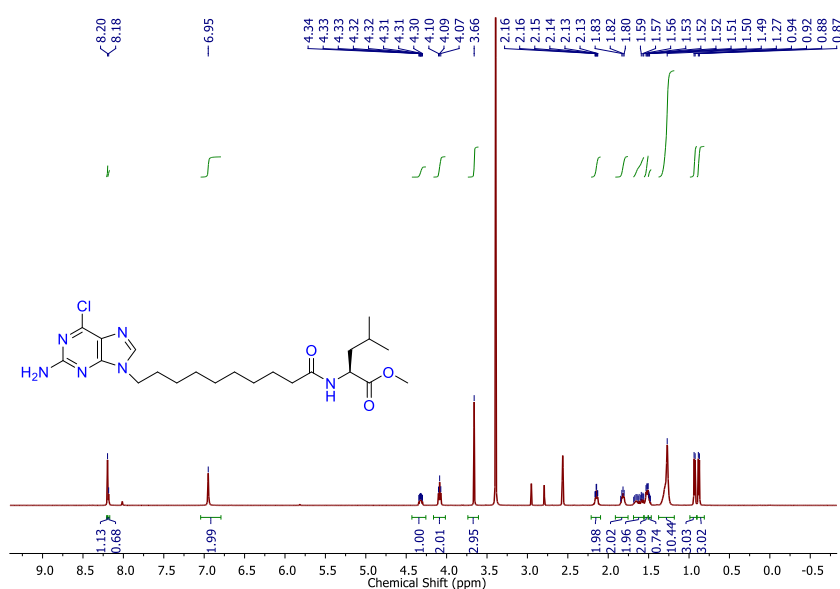


**Figure 5.19**  $^1\text{H}$  NMR (500 MHz, DMSO- $d_6$ ) spectrum of **9b**.

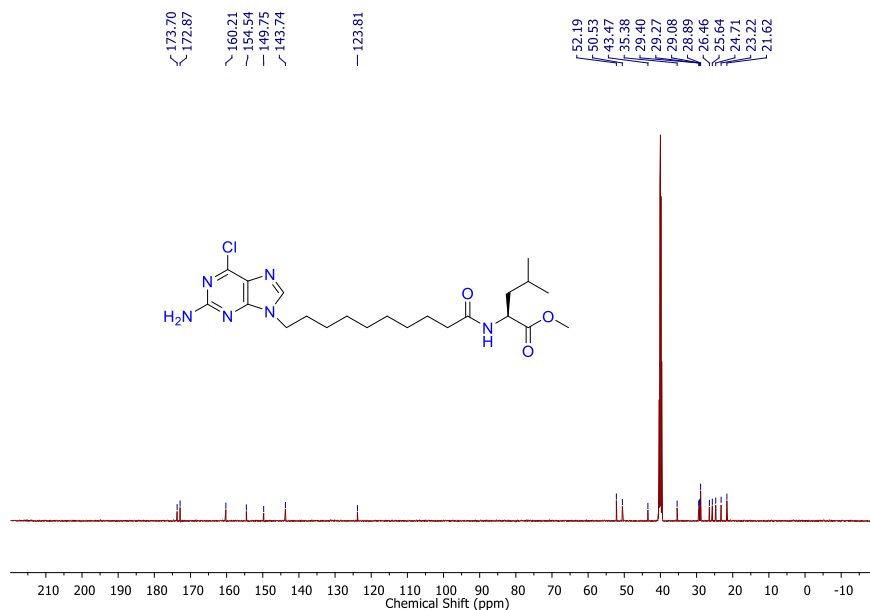


**Figure 5.20**  $^{13}\text{C}$  NMR (125 MHz,  $\text{CDCl}_3$ ) spectrum of **9b**.

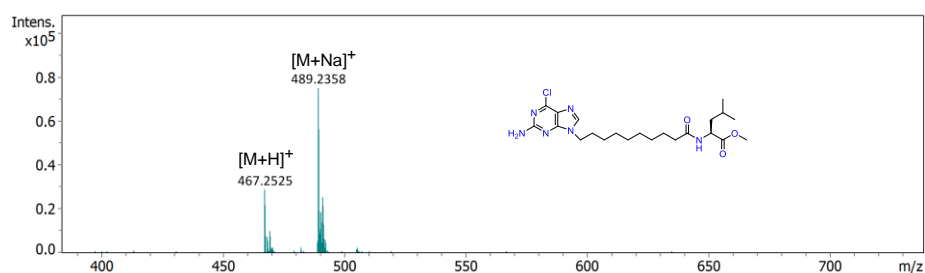


**Figure 5.21** ESI-MS spectrum of **9b**.

### 5.2.12 Compound **9c**:

The compound **9c** was synthesized as per the above-mentioned general procedure. Yield: 67%.  $^1\text{H}$  NMR ( $\text{DMSO}-d_6$ , 500 MHz):  $\delta$  1.09-1.23 (m, 10H), 1.34-1.40 (m, 2H), 1.75-1.79 (s, 2H), 2.01-2.04 (t, 2H,  $J = 5, 10$  Hz), 2.84-2.87 (m, 1H), 3.00-3.04 (m, 1H), 3.59 (s, 3H), 4.02-4.05 (t, 2H  $J = 5, 10$  Hz), 4.44-4.49 (m, 1H), 6.90 (s, 2H), 7.16-7.27 (m, 8H), 8.14 (s, 1H), 8.23-8.24 (d, 1H,  $J = 5$  Hz).  $^{13}\text{C}$  NMR ( $\text{DMSO}-d_6$ , 125 MHz):  $\delta$  25.56, 26.46, 28.81, 28.90, 29.11, 29.21, 29.39, 35.41, 37.11, 43.48, 52.25, 53.82, 123.81, 126.91, 128.62, 128.69, 129.48, 129.52, 137.81, 143.75, 149.75, 154.54, 160.21, 172.72, 172.74. (ESI-MS,  $m/z$ ):  $[\text{M}+\text{Na}]^+$  calculated for  $\text{C}_{25}\text{H}_{33}\text{ClN}_6\text{O}_3\text{Na}$  523.2195; found 523.2193.

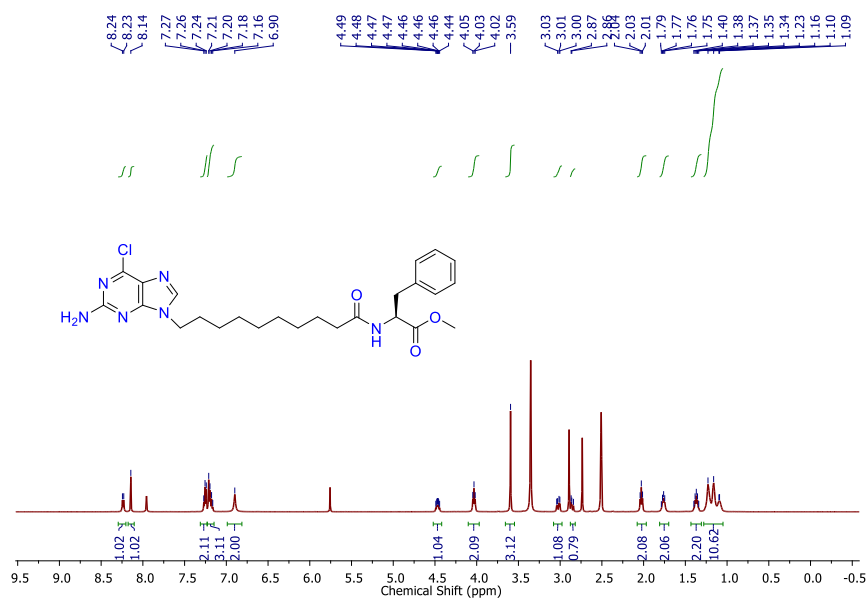


**Figure 5.22** <sup>1</sup>H NMR (500 MHz, DMSO-*d*<sub>6</sub>) spectrum of **9c**.

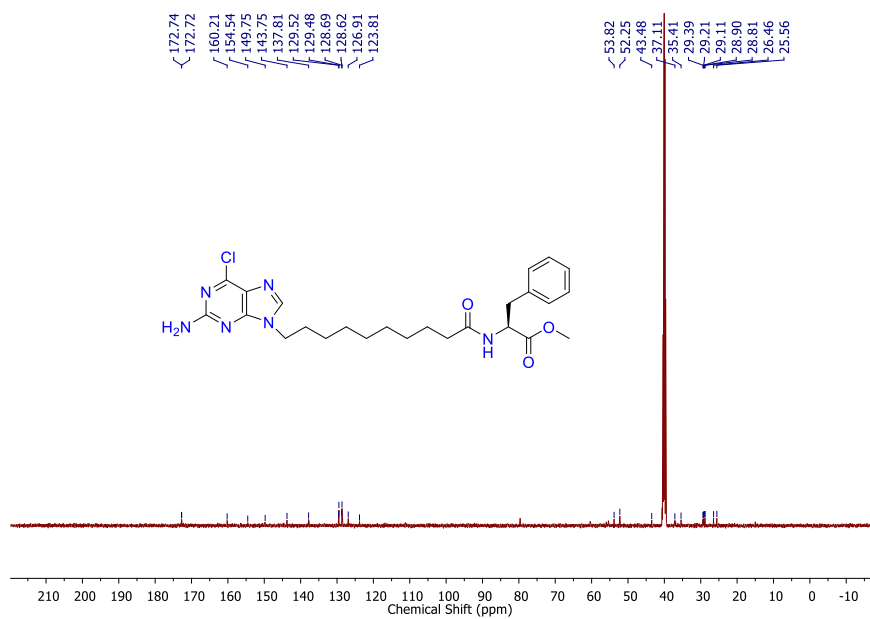


**Figure 5.23** <sup>13</sup>C NMR (125 MHz, CDCl<sub>3</sub>) spectrum of **9c**.

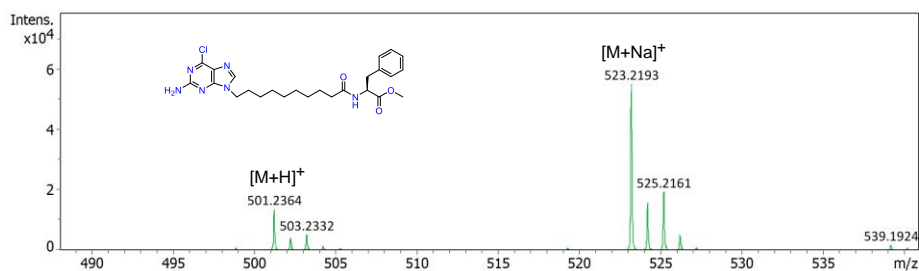


**Figure 5.24.** ESI-MS spectrum of **9c**.

### 5.2.13 Compound **9d**:

The compound **9d** was synthesized as per the above-mentioned general procedure. Yield: 62%.  $^1\text{H}$  NMR (DMSO- $d_6$ , 500 MHz):  $\delta$  1.18-1.30 (m, 10H), 1.42-1.47 (m, 2H), 1.79-1.85 (m, 2H), 2.08-2.11 (t, 2H), 2.78-2.82 (m, 1H), 2.92-2.95 (m, 1H), 3.63 (s, 3H), 4.07-4.10 (t, 2H), 4.40-4.44 (m, 1H), 6.69-6.71 (d, 2H,  $J$  = 10 Hz), 6.95 (s, 1H), 7.03-7.05 (d, 2H,  $J$  = 10 Hz), 8.20 (s, 1H), 8.22-8.23 (d, 1H,  $J$  = 10 Hz), 9.27 (s, 1H).  $^{13}\text{C}$  NMR (DMSO- $d_6$ , 125 MHz):  $\delta$  25.58, 26.45, 28.87, 28.91, 29.13, 29.21, 29.39, 35.41, 36.44, 43.48, 52.16, 54.23, 115.43, 123.81, 127.75, 130.40, 143.74, 149.75, 154.54, 156.41, 160.21, 172.74, 172.86. (ESI-MS,  $m/z$ ):  $[\text{M}+\text{Na}]^+$  calculated for  $\text{C}_{25}\text{H}_{33}\text{ClN}_6\text{O}_4\text{Na}$  539.2144; found 539.2124.

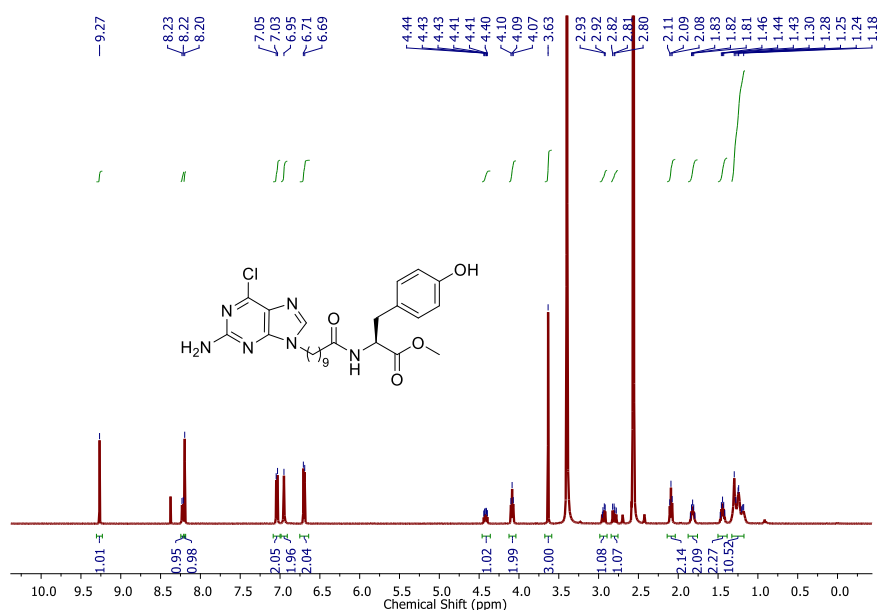


**Figure 5.25**  $^1\text{H}$  NMR (500 MHz, DMSO- $d_6$ ) spectrum of **9d**.

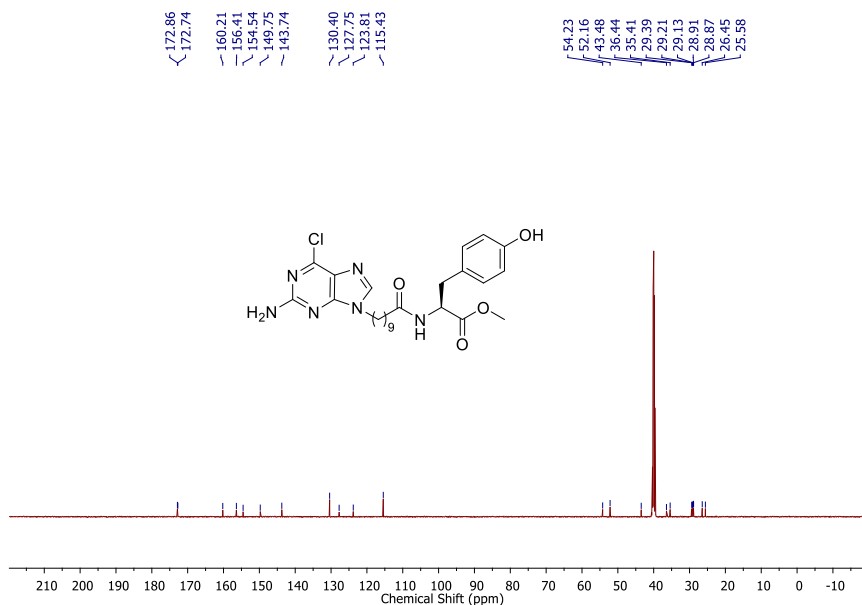


**Figure 5.26** <sup>13</sup>C NMR (125 MHz, CDCl<sub>3</sub>) spectrum of **9d**.

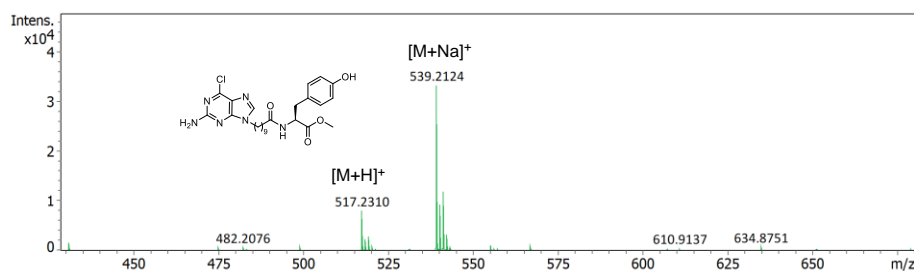


**Figure 5.27** ESI-MS spectrum of **9d**.

#### 5.2.14 Compound **9e**:

The compound **9e** was synthesized as per the above-mentioned general procedure. Yield: 60%. <sup>1</sup>H NMR (DMSO-*d*<sub>6</sub>, 500 MHz): δ 1.17-1.23 (m, 10H), 1.37-1.42 (m, 2H), 1.74-1.78 (m, 2H), 2.04-2.07 (m, 2H), 2.99-3.04 (m, 1H), 3.11-3.15 (m, 1H), 3.57 (s, 3H), 4.01-4.04 (t, 2H), 4.47-4.52 (m, 1H), 6.89 (s, 2H), 6.96-6.99 (t, 1H), 7.04-7.07 (t, 1H), 7.13 (s, 1H), 7.31-7.33 (d, 1H), 7.78-7.49 (d, 1H), 8.14 (s, 1H), 8.19-8.21 (d, 1H), 10.84 (s, 1H). <sup>13</sup>C NMR (DMSO-*d*<sub>6</sub>, 125 MHz): δ 25.54, 26.45, 27.52, 28.90, 29.12, 29.20, 29.38, 35.42, 43.47, 53.45, 63.54, 110.05, 111.87, 118.45, 118.83, 121.40, 123.81, 124.06, 127.52, 136.54, 143.76, 149.76, 154.53, 160.20, 172.81, 173.06. (ESI-MS, *m/z*): [M+Na]<sup>+</sup> calculated for C<sub>27</sub>H<sub>34</sub>ClN<sub>7</sub>O<sub>3</sub>Na 562.2304; found 562.2304.

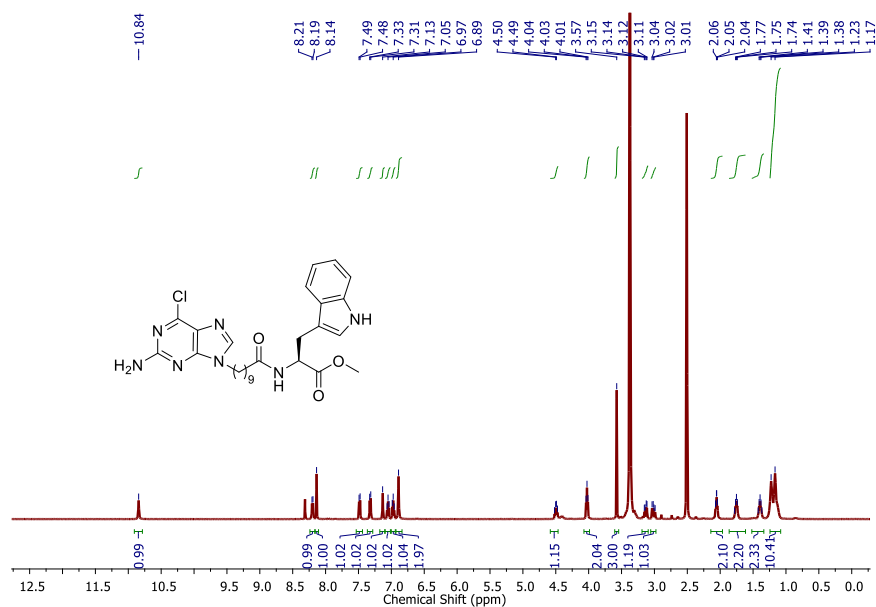


**Figure 5.28** <sup>1</sup>H NMR (500 MHz, DMSO-*d*<sub>6</sub>) spectrum of **9e**.

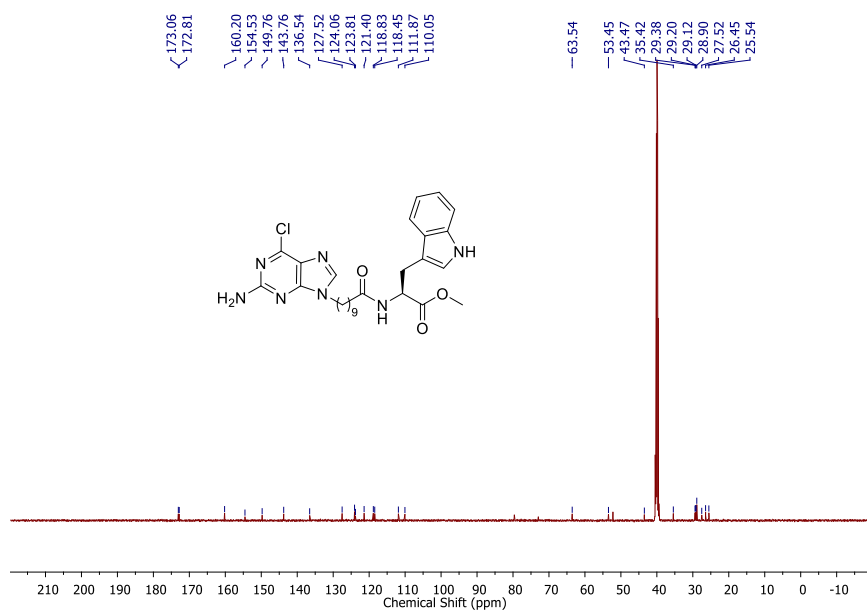


**Figure 5.29** <sup>13</sup>C NMR (125 MHz, CDCl<sub>3</sub>) spectrum of **9e**.



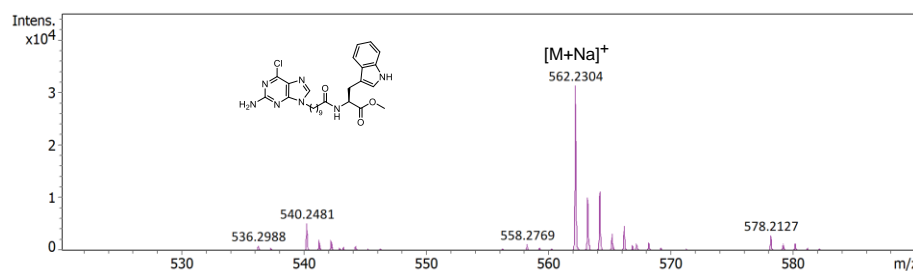


**Figure 5.30** ESI-MS spectrum of **9e**.

### 5.2.15 General procedure for the synthesis of compound NPs:

These compounds were synthesized based on the previously reported synthetic procedure. These compounds were dissolved in the TFA: H<sub>2</sub>O (3:1) 5ml. Then, the reaction was left to stir for 48h at room temperature. The progress of the reaction was monitored by Thin Layer Chromatography (TLC). After the completion of the reaction. TFA was evaporated under vacuums. The reaction was washed with diethyl ether to obtain the white solid.

### 5.2.16 Compound NP8:

The compound **NP8** was synthesized as per the above-mentioned general procedure. Yield: 80%. <sup>1</sup>H NMR (DMSO-*d*<sub>6</sub>, 500 MHz):  $\delta$  0.85-0.87 (dd, 6H), 1.22 (s, 10H), 1.46-1.48 (m, 2H), 1.68-1.73 (m, 2H), 1.99-2.06 (m, 1H), 2.09-2.19 (m, 2H), 3.90-3.93 (t, 2H, *J* = 5, 10 Hz), 4.10-4.13 (m, 1H), 6.48 (s, 2H), 7.67 (s, 1H), 7.83-7.85 (d, 1H, *J* = 5 Hz), 10.64 (s, 1H). <sup>13</sup>C NMR (DMSO-*d*<sub>6</sub>, 125 MHz):  $\delta$  18.58, 19.64, 25.79, 26.43, 28.86, 29.00, 29.07, 29.22, 29.82, 30.34, 35.58, 43.11, 57.76, 117.16, 137.78, 151.66, 153.97, 157.30, 172.84, 173.63. (ESI-MS, *m/z*): [M+Na]<sup>+</sup> calculated for C<sub>20</sub>H<sub>32</sub>N<sub>6</sub>O<sub>4</sub>Na 443.2377; found 443.2383.

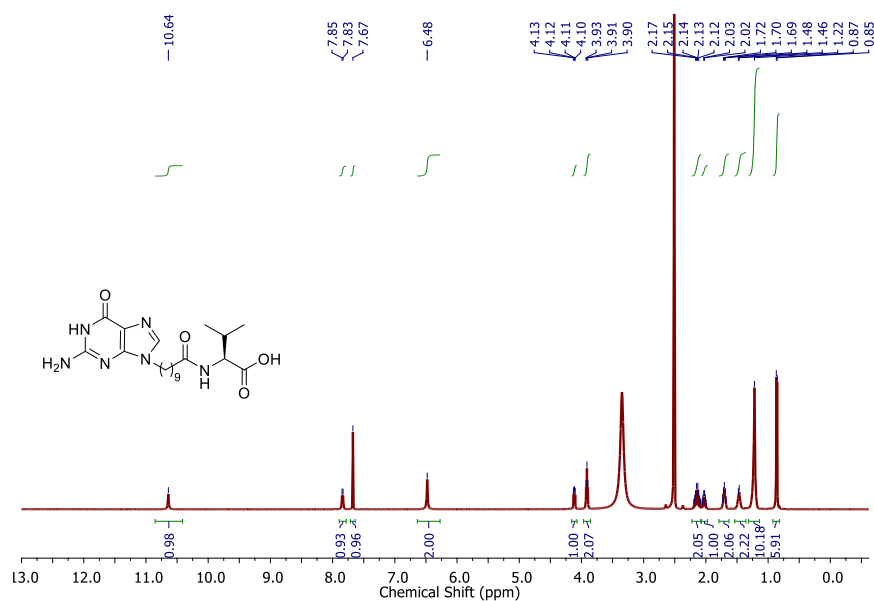


**Figure 5.31** <sup>1</sup>H NMR (500 MHz, DMSO-*d*<sub>6</sub>) spectrum of NP8.

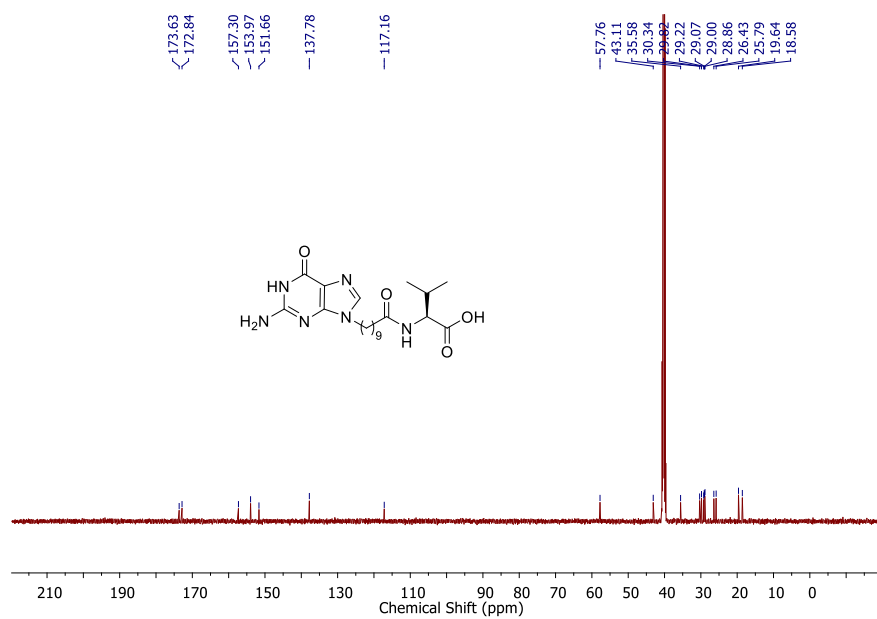


**Figure 5.32** <sup>13</sup>C NMR (125 MHz, CDCl<sub>3</sub>) spectrum of NP8.

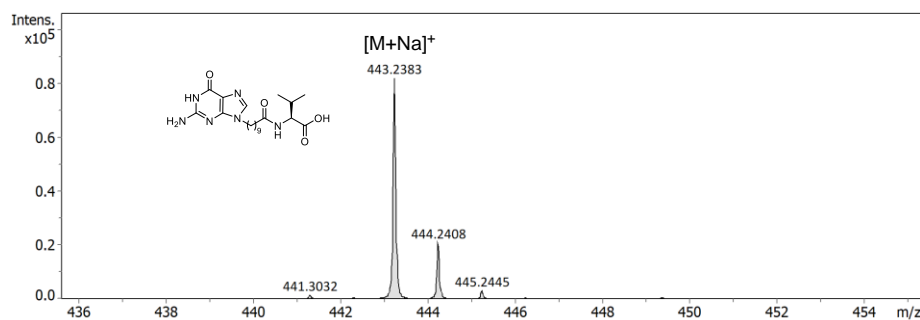


**Figure 5.33** ESI-MS spectrum of **NP8**.

### 5.2.17 Compound NP4:

The compound **NP4** was synthesized as per the above-mentioned general procedure. Yield: 85%.  $^1\text{H}$  NMR (DMSO- $d_6$ , 500 MHz):  $\delta$  0.82-0.83 (d, 3H,  $J = 5$  Hz), 0.87-0.88 (d, 3H,  $J = 5$  Hz), 1.23 (s, 10H), 1.47-1.54 (m, 4H), 1.57-1.64 (m, 1H), 1.76-1.78 (m, 2H), 2.04-2.14 (m, 2H), 4.00-4.03 (t, 2H,  $J = 5$ , 10 Hz), 4.18-4.23 (m, 1H), 6.90 (s, 2H), 8.00-8.01 (d, 1H,  $J = 5$  Hz), 8.56 (s, 1H), 11.22 (s, 1H), 12.47 (s, 1H).  $^{13}\text{C}$  NMR (DMSO- $d_6$ , 125 MHz):  $\delta$  21.65, 23.34, 24.78, 25.69, 26.34, 28.89, 28.94, 29.12, 29.26, 29.45, 35.48, 43.97, 50.46, 113.13, 137.71, 150.98, 154.79, 155.85, 172.72, 174.79. (ESI-MS,  $m/z$ ):  $[\text{M}+\text{H}]^+$  calculated for  $\text{C}_{21}\text{H}_{35}\text{N}_6\text{O}_4$  435.2714; found 435.2720.

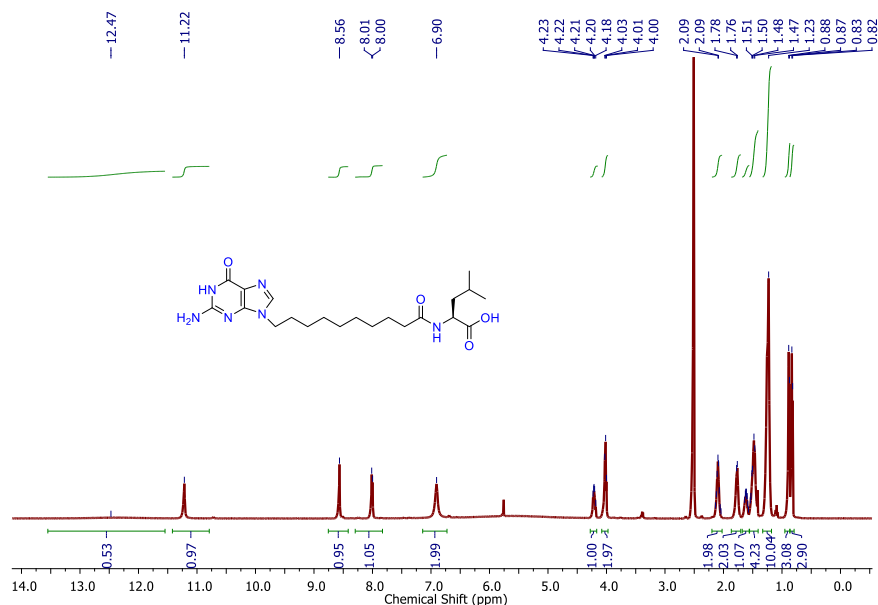


**Figure 5.34**  $^1\text{H}$  NMR (500 MHz, DMSO- $d_6$ ) spectrum of **NP4**.

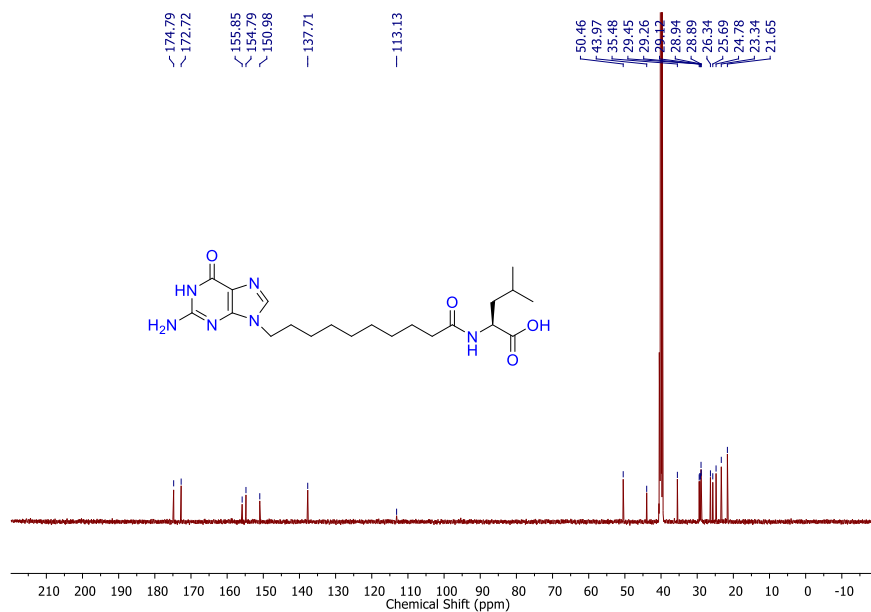


**Figure 5.35**  $^{13}\text{C}$  NMR (125 MHz,  $\text{CDCl}_3$ ) spectrum of **NP4**.

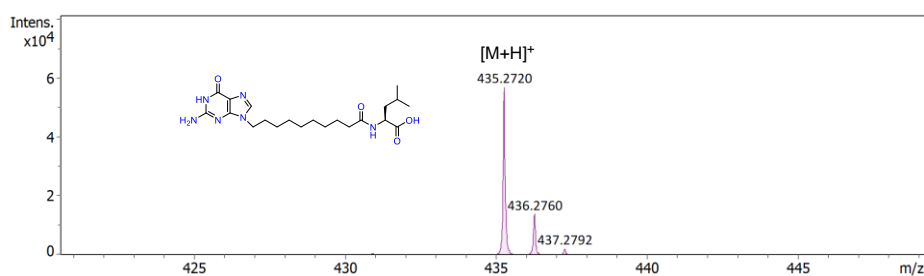


**Figure 5.36** ESI-MS spectrum of **NP4**.

### 5.2.18 Compound **NP3**:

The compound **NP3** was synthesized as per the above-mentioned general procedure. Yield: 83%.  $^1\text{H}$  NMR ( $\text{DMSO}-d_6$ , 500 MHz):  $\delta$  1.08-1.22 (m, 10H), 1.34-1.39 (m, 2H), 1.68-1.73 (s, 2H), 2.00-2.03 (t, 2H,  $J = 5, 10$  Hz), 2.81-2.86 (m, 1H), 3.04-3.07 (m, 1H), 3.90-3.93 (t, 2H  $J = 5, 10$  Hz), 4.37-4.41 (m, 1H), 6.50 (s, 2H), 7.16-7.26 (m, 8H), 7.68 (s, 1H), 8.01-8.03 (d, 1H,  $J = 10$  Hz) 10.65 (s, 1H).  $^{13}\text{C}$  NMR ( $\text{DMSO}-d_6$ , 125 MHz):  $\delta$  25.60, 26.31, 28.84, 28.90, 29.14, 29.19, 29.34, 35.51, 37.19, 44.18, 53.69, 112.27, 126.77, 128.55, 129.51, 137.68, 138.25, 150.83, 155.01, 155.53, 172.61, 173.71. (ESI-MS,  $m/z$ ):  $[\text{M}+\text{H}]^+$  calculated for  $\text{C}_{24}\text{H}_{33}\text{N}_6\text{O}_4$  469.2558; found 469.2555.

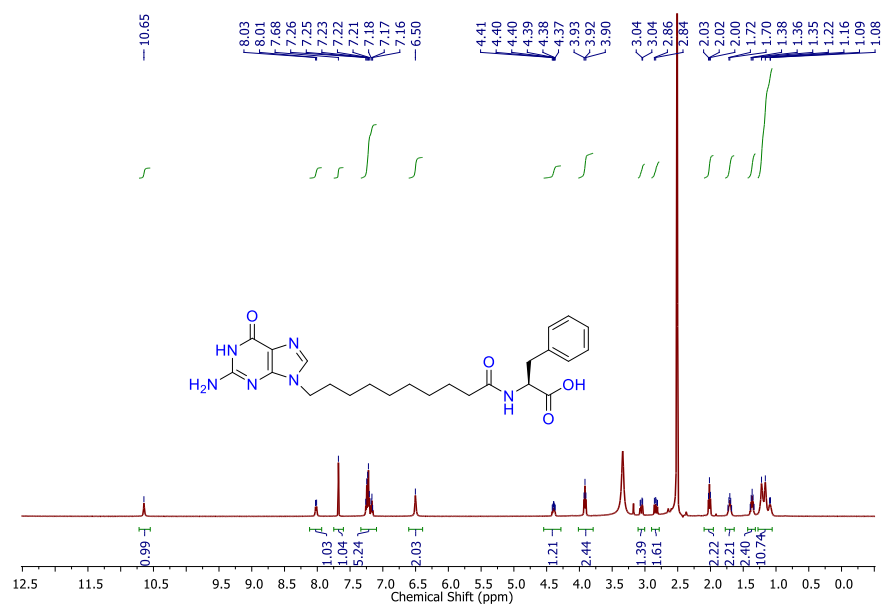


**Figure 5.37** <sup>1</sup>H NMR (500 MHz, DMSO-*d*<sub>6</sub>) spectrum of NP3.

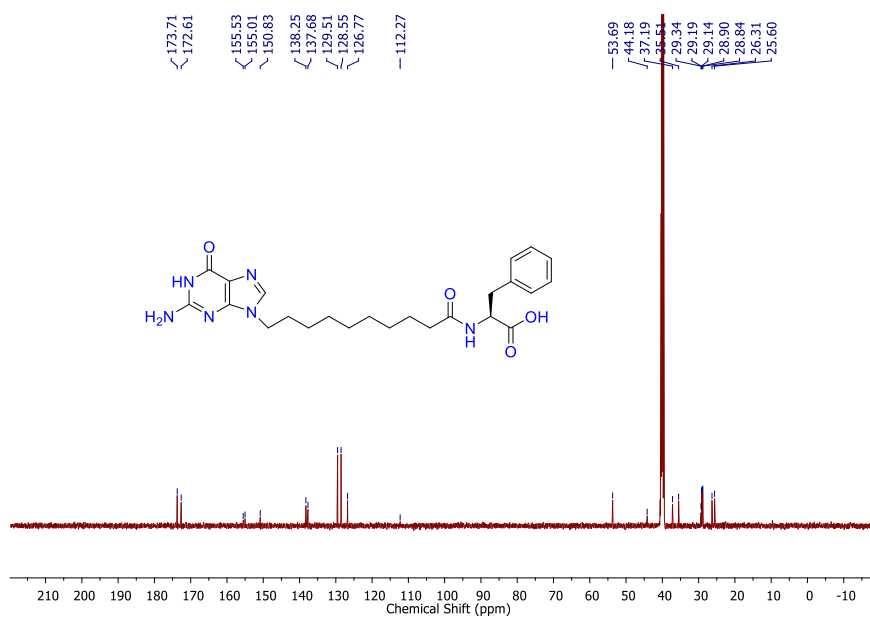


**Figure 5.38** <sup>13</sup>C NMR (125 MHz, CDCl<sub>3</sub>) spectrum of NP3.

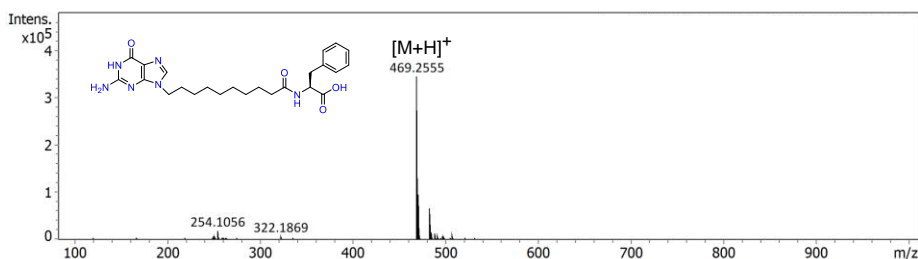


**Figure 5.39** ESI-MS spectrum of **NP3**.

### 5.2.19 Compound **NP9**:

The compound **NP9** was synthesized as per the above-mentioned general procedure. Yield: 88%.  $^1\text{H}$  NMR (DMSO- $d_6$ , 500 MHz):  $\delta$  1.13-1.23 (m, 10H), 1.36-1.41 (m, 2H), 1.68-1.74 (m, 2H), 2.02-2.05 (t, 2H), 2.69-2.74 (m, 1H), 2.90-2.93 (m, 1H), 3.90-3.93 (t, 2H,  $J = 5, 10$  Hz), 4.30-4.35 (m, 1H), 6.50 (s, 2H), 6.63-6.65 (d, 2H,  $J = 10$  Hz), 6.99-7.01 (d, 2H,  $J = 10$  Hz), 7.70-7.71 (d, 1H,  $J = 5$  Hz), 8.01-8.03 (d, 1H,  $J = 10$  Hz), 9.21 (s, 1H), 10.6 (s, 1H), 12.57 (s, 1H).  $^{13}\text{C}$  NMR (DMSO- $d_6$ , 125 MHz):  $\delta$  25.64, 26.45, 28.90, 28.93, 29.15, 29.25, 29.87, 35.52, 36.46, 43.14, 54.10, 115.36, 116.86, 128.20, 130.42, 137.91, 151.57, 153.99, 156.33, 157.22, 172.64, 173.84. (ESI-MS,  $m/z$ ):  $[\text{M}+\text{Na}]^+$  calculated for  $\text{C}_{24}\text{H}_{32}\text{N}_6\text{O}_5\text{Na}$  : 507.2326; found: 507.2325.

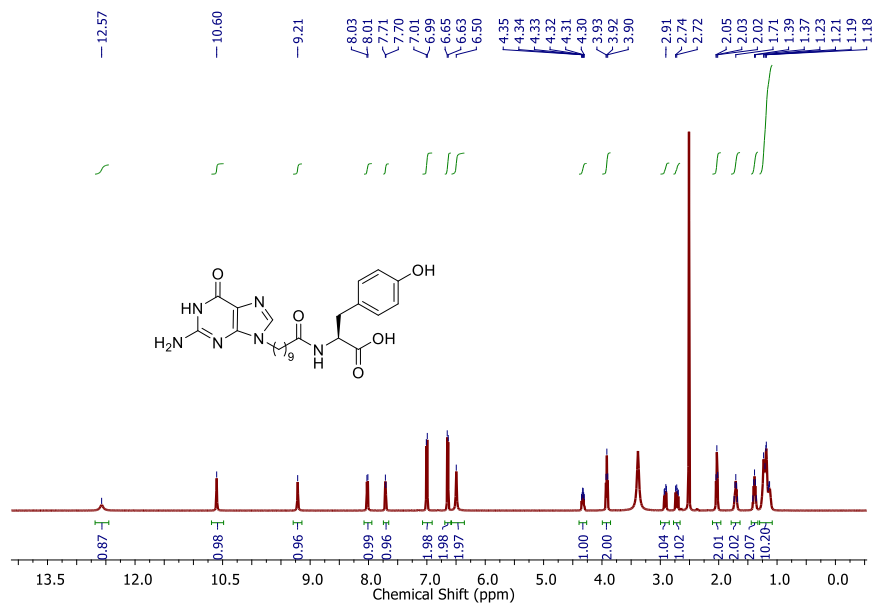


**Figure 5.40**  $^1\text{H}$  NMR (500 MHz, DMSO- $d_6$ ) spectrum of **NP9**.

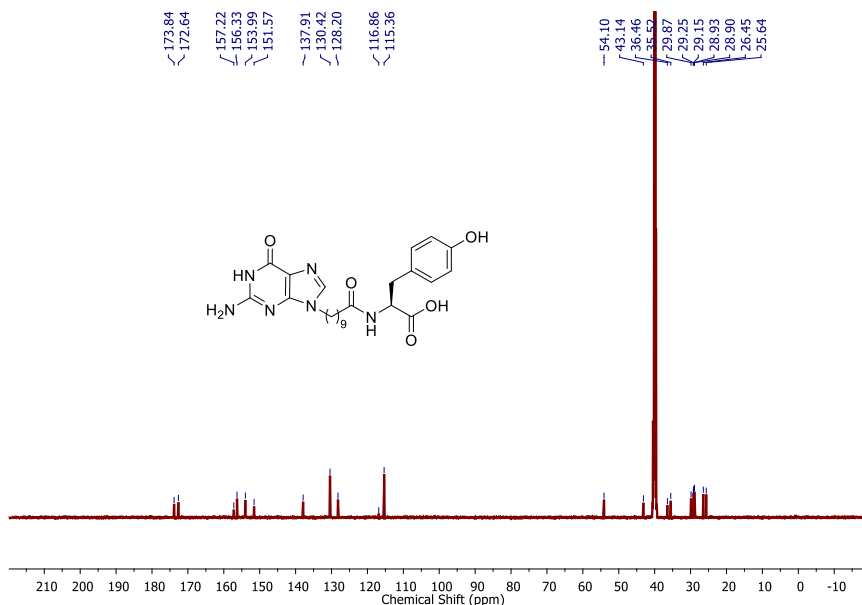


**Figure 5.41** <sup>13</sup>C NMR (125 MHz, CDCl<sub>3</sub>) spectrum of NP9.

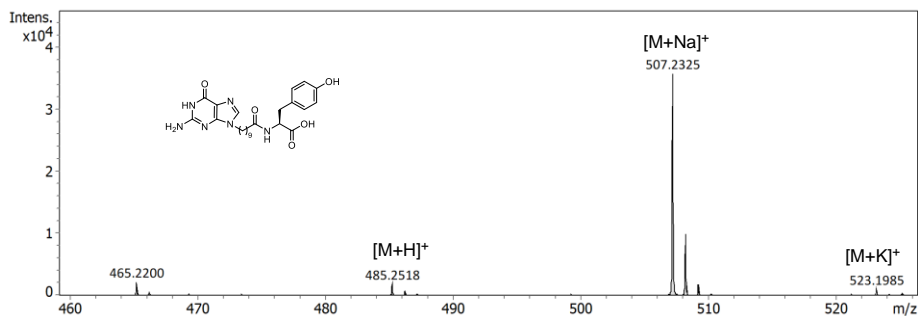


**Figure 5.42** ESI-MS spectrum of NP9.

### 5.2.20 Compound NP10:

The compound **NP10** was synthesized as per the above-mentioned general procedure. Yield: 82%. <sup>1</sup>H NMR (DMSO-*d*<sub>6</sub>, 500 MHz): δ 1.12-1.21 (m, 10H), 1.35-1.41 (m, 2H), 1.66-1.72 (m, 2H), 2.02-2.06 (m, 2H), 2.96-3.01 (m, 1H), 3.13-3.17 (m, 1H), 3.89-3.92 (t, 2H, *J* = 5, 10 Hz), 4.43-4.47 (m, 1H), 6.46 (s, 2H), 6.95-6.98 (t, 1H, *J* = 5, 10 Hz), 7.03-7.06 (t, 1H, *J* = 5, 10 Hz), 7.12 (s, 1H), 7.31-7.32 (d, 1H, *J* = 5 Hz), 7.51-7.53 (d, 2H, *J* = 10 Hz), 7.68 (s, 1H), 8.03-8.04 (d, 1H, *J* = 5 Hz), 10.59 (s, 1H), 10.83 (s, 1H). <sup>13</sup>C NMR (DMSO-*d*<sub>6</sub>, 125 MHz): δ 25.59, 26.42, 27.56, 28.84, 28.91, 29.12, 29.21, 29.84, 35.54, 43.10, 53.34, 110.50, 111.81, 116.97, 118.61, 118.77, 120.75, 121.34, 123.95, 127.65, 136.52,

137.99, 151.61, 153.92, 157.34, 172.75, 174.12. (ESI-MS,  $m/z$ ):  
 $[M+Na]^+$  calculated for  $C_{26}H_{33}N_7O_4Na$  530.2486; found 530.2478.

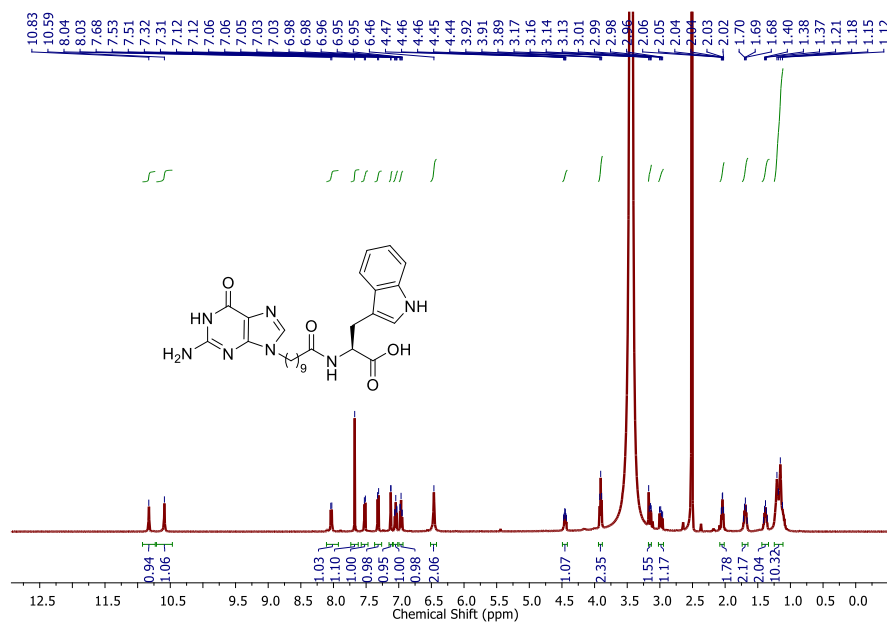


**Figure 5.43** <sup>1</sup>H NMR (500 MHz, DMSO-*d*<sub>6</sub>) spectrum of NP10.

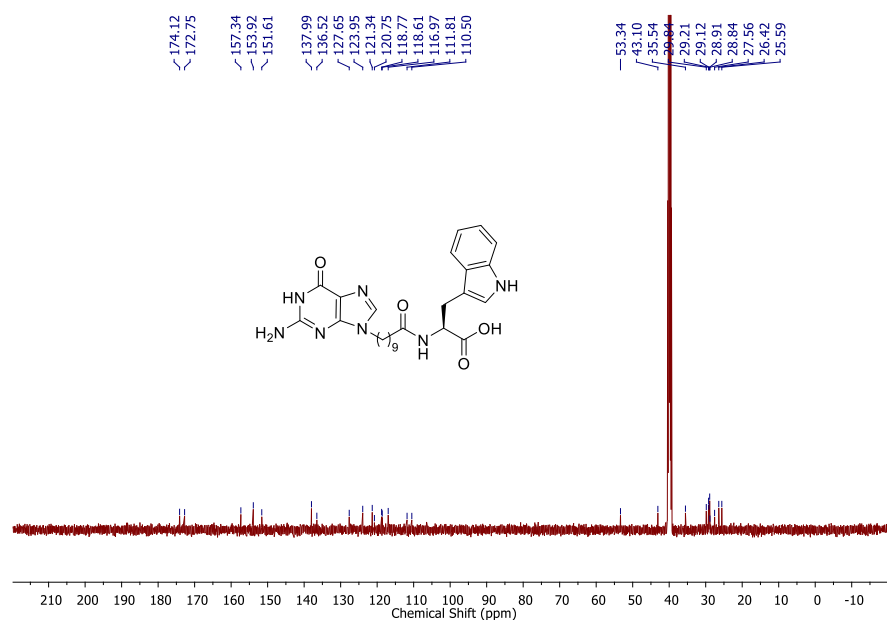


**Figure 5.44** <sup>13</sup>C NMR (125 MHz, CDCl<sub>3</sub>) spectrum of NP10.



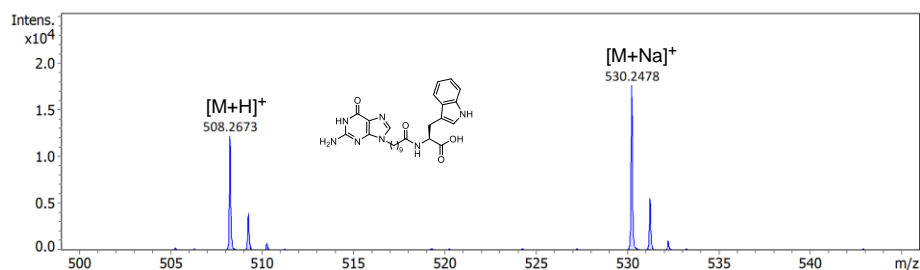


**Figure 5.42** ESI-MS spectrum of **NP10**.

### 5.2.15 HPLC Analysis

The progress of biocatalyst-driven reactions was monitored using a Dionex reverse-phase HPLC system, which was connected to a photodiode array detector (Ultimate 3000). A volume of 30 microliters of the sample was injected into a C-18 column with dimensions of 4.6 × 250 mm, which contained fused silica particles measuring 5 micrometers in diameter. The injection was performed at a flow rate of 1 milliliter per minute. The material was eluted using a gradient of water (A) and acetonitrile (B) over 42 minutes (0-4 min %A: 80, %B: 20; 4-35 min %A: 20, %B: 80; 35-40 min %A: 20, %B: 80, 40-42 min %A: 80, %B: 20). The preparation of the sample included dissolving the necessary amount of peptide in a 1 mL solution of acetonitrile and water in a 1:1 ratio.

### 5.2.16 Computational Molecular Docking

Molecular docking studies of the synthesized **NPs** with lipase (PDB 1CRL) were accomplished in Autodock-Vina software (version 1.1.2) to detect the binding region and mode of interaction of these **NPs** in lipase. Docking analysis was executed after placing a grid box of volume 40 × 40 × 40 on the receptor lipase protein. Docking images were visualized and prepared in UCSF chimera.

### 5.2.17 Circular Dichroism Spectroscopy

The presence of the secondary structures of DNA G-quadruplex inside the hydrogel was analyzed by circular dichroism (CD). The CD spectra

of all peptide hydrogels were obtained through a Jasco J-815 CD spectrophotometer at ambient temperature. The spectra were acquired using a scan rate of  $20 \text{ nm min}^{-1}$  and a bandwidth of  $1 \text{ nm}$  within the wavelength range of  $230\text{--}300 \text{ nm}$ . A quartz cuvette with a thickness of  $(10 \times 10 \text{ mm}^2) \text{ mm}$  was used to conduct three repeated scans, which were then combined to provide average spectra. Before conducting the sample run, the baselines were corrected with the solvent which was used for the experiment. The data analysis was conducted with the Jasco spectra manager. spectrometer.

#### **5.2.18 FT-IR**

FTIR spectra were obtained by analyzing dried samples of **NP10**, **NP10** hydrogel and corresponding **NP10** xerogel. The spectral range analyzed in this study spanned from  $400 \text{ cm}^{-1}$  to  $4000 \text{ cm}^{-1}$ , with a resolution of  $2 \text{ cm}^{-1}$ . To obtain individual spectra, 64 accumulations were averaged using a Bruker spectrometer. The spectra were processed with OPUS 6.5 software.

#### **5.2.19 UV-Vis Spectroscopy**

The ultraviolet-visible (UV-Vis) spectra of the hydrogel were measured using a Jasco V 750 spectrophotometer in a quartz cell with a path length of  $1 \text{ mm}$ . The spectra were recorded within the wavelength range of  $700\text{--}200 \text{ nm}$  with a data interval of  $0.1 \text{ nm}$ . The bandwidth was configured to a value of  $1 \text{ nm}$ , the scanning speed was set to  $200 \text{ nm min}^{-1}$ , and the response time was measured to be  $1 \text{ s}$ .

#### **5.2.20 Fluorescence Spectroscopy**

The fluorescence spectra were obtained by using a Horiba spectrofluorometer (model no. The hydrogel, at a concentration of  $20 \text{ mM}$  in the gel state, was placed in a quartz cuvette with dimensions of  $10 \times 4 \text{ mm}$ . The spectra were acquired using an excitation and emission bandwidth of  $2 \text{ nm}$ , with a data pitch of  $2 \text{ nm}$ . The samples were subjected to excitation at a wavelength of  $375 \text{ nm}$ . The emission spectra were measured throughout the wavelength range of  $385\text{--}730 \text{ nm}$  for

both the sol and gel phases of the peptides, with an average of 3 accumulations.

#### **5.2.21 ThT Dye Binding Experiment**

The Thioflavin T (ThT) stock solution was generated anew by dissolving 1 mg of ThT in 1 mL of Milli-Q water and thereafter passing it through a 0.2  $\mu\text{m}$  syringe filter. The fluorescence spectrum of ThT without any sample was obtained by using the Horiba spectrofluorometer. The excitation wavelength used was 450 nm, and the emission spectra were measured throughout the wavelength range of 460 nm to 800 nm. A volume of 100  $\mu\text{L}$  of a gel sample with a concentration of 20 mM was combined with 1900  $\mu\text{L}$  of a Thioflavin T (ThT) working solution. The resulting mixture was incubated at room temperature for a duration of 15 minutes. Subsequently, the emission spectra of the solution were recorded. This experimental procedure aimed to investigate the interaction between ThT and the secondary structure contained within the gel.

#### **5.2.22 Rheological Behavior of the Hydrogel**

The biocatalytically formed nucleobase functionalized amino acid hydrogel was subjected to rheological investigations utilizing an Anton Parr MCR301 rheometer equipped with a 25 mm parallel plate geometry. In the frequency sweep experiment, the storage modulus ( $G'$ ) and loss modulus ( $G''$ ) were plotted as a function of frequency. The range of frequency was 0.1–100  $\text{rad s}^{-1}$ . The thixotropic properties of the synthesized hydrogel were determined by step-strain experiments. Throughout the experiment, a constant frequency of 10  $\text{rad/s}$  was maintained. The hydrogel was carefully removed from the vial and placed onto the bottom plate of the rheometer just before the measurement. This process ensures that the hydrogels retain their original form and dimensions throughout the experiment. The temperature was consistently maintained at 25  $^{\circ}\text{C}$  during the duration of the experiment. An amplitude sweep experiment was performed to know

the linear viscoelastic region. The frequency sweep experiment was carried out at a constant frequency of 10 rad/s.

### 5.2.23 Morphological Study of the Hydrogel

The presence of fiber-enclosed spheres formed by biocatalysis was characterized using various microscopic techniques such as scanning electron microscopy (SEM), transmission electron microscopy (TEM), and confocal laser scanning microscopy (CLSM). Zeiss field emission scanning electron microscope (model no Supra55 Zeiss) was used to capture SEM images. 50  $\mu\text{L}$  of the hydrogel was taken and placed in an Eppendorf. Then, it was thoroughly crashed with a gel crusher. After that, it was dispersed in 450  $\mu\text{L}$  of water. Then 5  $\mu\text{L}$  of the hydrogel solution was drop-cast on a glass slide. The samples were dried under the air. Then, the samples were kept under vacuum to dry. The gold coating was performed before imaging. JEOL microscope was used to capture TEM images (model no: JEM-2100) with an operating voltage of 200 kV. The TEM images were taken after the formation of the hydrogel at day 30. A volume of 20  $\mu\text{L}$  of the bio-catalytically formed nucleobase functionalized hydrogel was dispersed in 800  $\mu\text{L}$  water. Then 5  $\mu\text{L}$  of the hydrogel solution was placed on a carbon-coated copper grid. The copper grid was then dried by slow evaporation in the air. A phosphotungstic acid solution (1% w/v) was used for negative staining. For the CLSM experiment, 20  $\mu\text{L}$  of the reaction mixture was taken in an Eppendorf. Then, the reaction mixture was dispersed in 200  $\mu\text{L}$  of deionized water. Finally, the solution was diluted with 200  $\mu\text{L}$  of water in the Eppendorf tube. Then, 5  $\mu\text{L}$  of the diluted mixture was placed on a confocal slide. The solution on the slide was dried before taking images. The images were taken using an Olympus Fluoview microscope (Model no FV1000) with a 100x object.

### 5.2.24 MTT Cell-viability Assay

The toxicity of biocatalytically formed **NP10** hydrogel on different cell types was evaluated using the MTT assay. Concisely, a total of  $5 \times 10^3$  cells were introduced into each well of 96-well plates. Then, the plates

were kept under incubation at 37 °C in a 5% CO<sub>2</sub> incubator. After the completion of incubation, the cells were treated with different concentrations of the hydrogel ranging from (0.0078-1 mM) for 24 h. Following the treatment, a solution of 3-(4,5-dimethylthiazol-2-yl)-2,5-diphenyltetrazolium bromide (MTT) was added to the cell. Further cells were incubated for 4 hours. This process allows the MTT dye to be reduced, resulting in the synthesis of formazan. Formazan has high solubility in dimethyl sulfoxide (DMSO). The amount of formazan produced was quantified by recording the optical density of the solution at 570 nm by a plate reader (model no: Thermo Fisher Scientific Multiskan FC). The experiments were conducted in triplicate and presented as the mean  $\pm$  standard deviation (SD).

#### **5.2.25 Live/Dead Cell Imaging**

Live-dead staining was conducted using Hoechst and propidium iodide (PI). Live-dead cell imaging was performed on the HEK 293 and A549 cell lines. The cells were grown on the confocal glass slides. The biocatalytically formed **NP10** hydrogel was added after reaching 70% confluence. Then, the cells were placed in a CO<sub>2</sub> incubator for 24 hours. After 24 h, the cells were stained with the nuclear staining dye Hoechst (10  $\mu$ g/mL) and incubated for 20 min. Then, cells were washed with freshly prepared phosphate buffer solution. Finally, the cells were stained with propidium iodide (5  $\mu$ g/mL) and incubated for 20 min. After the incubation period, the cells were again washed with phosphate buffer. The confocal glass slides were placed on another glass slide with mounting media for imaging. A 405 nm laser for Hoechst and a 559 nm laser for PI were used.

#### **5.2.26 Scratch Assay**

The scratch-wound test was conducted on mice fibroblasts McCoy cell line to study cellular migration. In a 24-well plate,  $5 \times 10^4$  cells per well were placed. Subsequently, cells were attached to the surface and established a monolayer. Subsequently, the cells were incubated in a medium of 1% fetal bovine serum (FBS) for 24 hours. A scratch mark

was created at the center of each well. The scratch experiment was performed using a bio-catalytically formed hydrogel. The gel was sterilized using UV and then mixed with a cell culture medium to prepare a stock solution of concentration 5 mM. The stock solutions were mixed with the cells. The final concentration of NP10 hydrogel was 0.5 mM and 0.25 mM, respectively. The plates were kept inside an incubator and images were taken at various time periods (0 h, 12 h, and 24 h) using a Radicon inverted microscope at a magnification of 10 $\times$ . The analysis of wound closing was carried out by ImageJ software.

### 5.3 Results and Discussion

Herein, the guanine functionalized amino acid derivatives were synthesized following the solution phase protocol (see SI for details). We used aliphatic and aromatic amino acids to conjugate with the nucleobase. Guanine has multiple H-bonding donor and acceptor sides resulting in a greater tendency to form hydrogels. Additionally, use of a C10 lipid chain is expected to offer flexibility for easy folding of the secondary structure. These synthesized nucleobase functionalized molecules were used to study the formation of a hydrogel driven by a biocatalyst lipase, derived from *Candida rugosa* [49,32]. In this experiment, the guanine functionalized gelators (NPs, 20 mM) and *p*-hydroxybenzyl alcohol (PHBA, 80 mM) were taken in 3 mL vials. Then 0.5 mL of phosphate buffer with a pH of 7.4 was added. The concentration of the buffer solution was 50 mM. Then, the reaction mixture was placed in ultra sonication bath for 10 min to dissolve the compounds. Finally, the biocatalyst, lipase (1 mg/ mL), was added to achieve the transformation. The reaction mixture containing vial was incubated at 37 °C (**Scheme 5.2**).

$$\text{R}-\text{O}-\text{C}(=\text{O})-\text{CH}_2-\text{CH}(\text{O}-\text{C}(=\text{O})-\text{R})-\text{CH}_2-\text{O}-\text{C}(=\text{O})-\text{R} \rightleftharpoons \text{HO}-\text{CH}_2-\text{CH}(\text{OH})-\text{CH}_2-\text{OH} + \text{R}-\text{C}(=\text{O})-\text{OH}$$

**Figure 1.** Schematic representation of the self-assembly of a hydrogel. The inactivated building block (1) is activated by the reaction with the hydroxybenzyl alcohol derivative (2) in the presence of lipase, forming the activated building block (3). The activated building block (3) then undergoes self-assembly through H-bonding and hydrophobic interactions to form the hydrogel (4). The hydrogel (4) can be converted back to the inactivated building block (1) by hydrolysis.

**Legend:**

- R=**
  - NP8:** CC(C)C
  - NP4:** CC(C)C
  - NP3:** Cc1ccccc1
  - NP9:** Oc1ccccc1
  - NP10:** c1ccc2c(c1)c3ccccc3n2

The progress of the reaction was monitored using HPLC on a weekly basis. After 4 weeks, 50% of the conversion of **NP10** is observed and the solution turns into a self-assembled hydrogel. Interestingly, other synthesized **NPs** (**G10VOH**, **G10CLOH**, **G10CFOH**, **G10CYOH**) failed to form visible hydrogel. The HPLC data for **NPs** with phenylalanine, leucine, tyrosine and valine indicated <10% conversion (**Figure 5.43a-g**). Often, biocatalysts are highly specific to the substrate structure. This may explain the low conversion observed in the remaining four nucleobase conjugates **NP1-4**. Furthermore, we performed molecular docking to investigate the selectivity of the lipase towards the ligand **NP10**. The details of the docking study are mentioned in the supporting information. The H-bonding and hydrophobic interactions allow **NP10** to fit nicely in the binding pocket (**Figure 5.43h**) of the lipase. The docking image illustrates tight binding of **NP10** to the lipase (**Figure 5.43i**). The binding energy of **NP10** is -7.5 kcal mol<sup>-1</sup>, while for **NP9**,

**NP3, NP4, NP8**, the binding energies are  $-6.6 \text{ kcal mol}^{-1}$ ,  $-6.6 \text{ kcal mol}^{-1}$ ,  $-6.8 \text{ kcal mol}^{-1}$  and  $5.8 \text{ kcal mol}^{-1}$ , respectively.

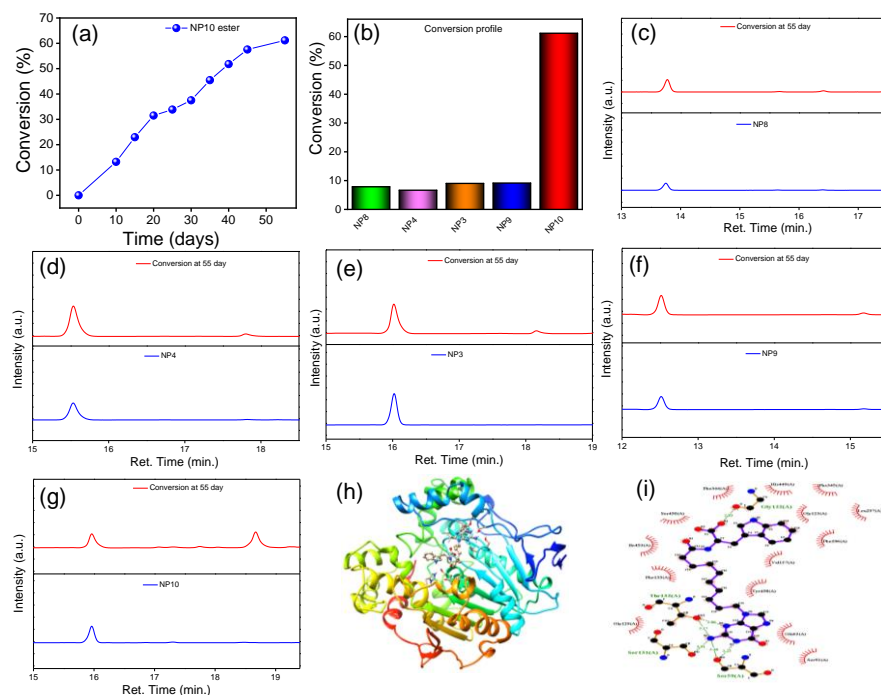


**Figure 5.43** (a) Ester conversion (%) of **NP10** with time (days). (b) Ester conversion histogram of **NPs** at 55 days by the lipase. HPLC chromatograms of (c) **NP8**, (d) **NP4**, (e) **NP3** (f) **NP9** (g) **NP10** (blue line) and biocatalytic conversion to ester (red line) at 55 days. (h) Docking image shows the binding region of the **NP10** in lipase. (i) Protein-ligand interaction diagram of 1CRL and **NP10**.

This indicates that **NP10** has a stronger binding affinity to the active site compared to other **NPs** (**Figure 5.44a-d**). Therefore, the computational study supports the binding selectivity of **NP10** towards lipase. Lipase favors hydrolysis over esterification in aqueous medium. The reaction could occur in the reverse direction when the activated building-blocks undergo higher order self-assembly. The self-assembly is expected to drive the reaction in the reverse direction. As a result, the equilibrium shift is observed in the reverse direction. In this case, the activated building-blocks are produced through enzyme fueled reverse hydrolysis, and they undergo higher order self-assembly leading to the shift of the equilibrium in the reverse direction.



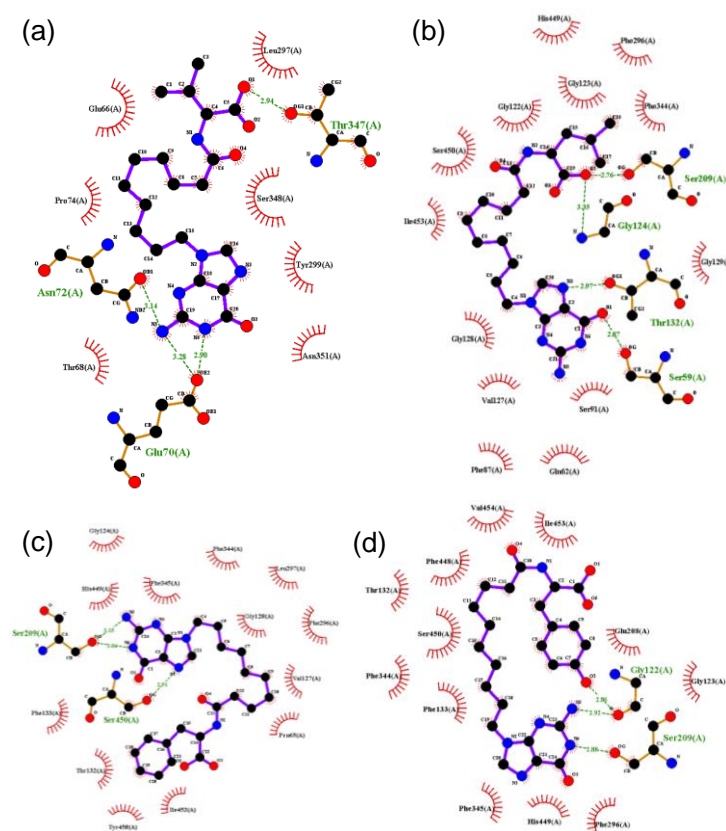


**Figure 5.44** Protein-ligand interaction diagram of 1CRL (a) NP8 and (b) NP4 (c) NP3 and (d) NP9.

It is evident from the kinetic data that the rate of esterification at the initial stage of the reaction was faster than the rate of hydrolysis. The ester obtained using the lipase-catalyzed esterification reaction were assessed by mass spectrometry (**Figure 5.45**). The hydroxyl group present in PHBA participated in the esterification reaction.

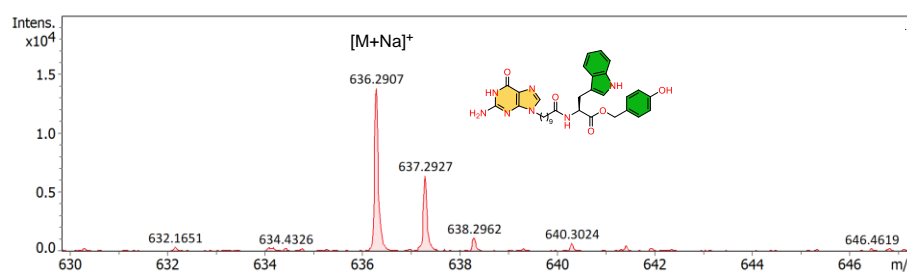


**Figure 5.45** ESI-MS analysis for the biocatalytically formed NP10 hydrogel. The enzymatic reaction between the synthesized nucleobase amino acid conjugate and *p*-hydroxybenzyl alcohol was used to generate NP10 hydrogel.

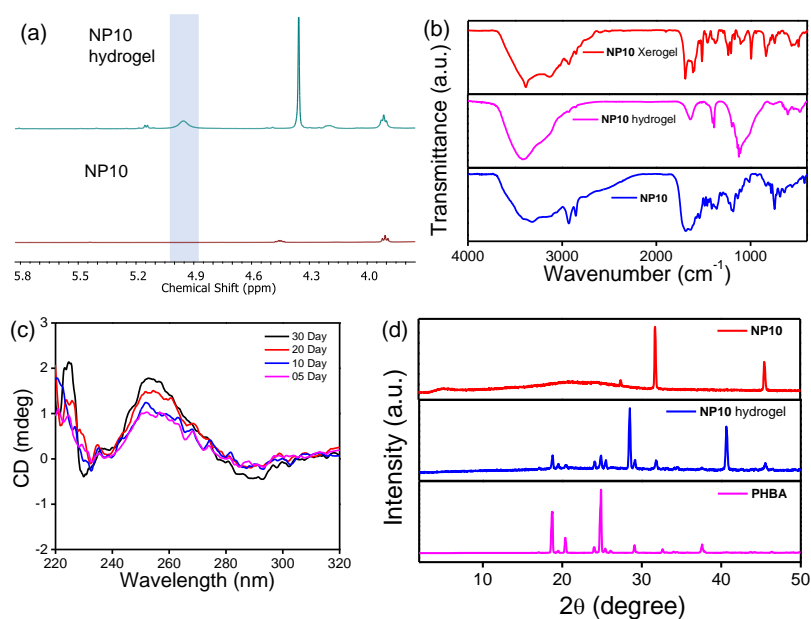


**Figure 5.46** (a) The participation of the aliphatic -OH group of PHBA in the esterification of **NP10** process is confirmed by the  $^1\text{H}$  NMR spectra in  $\text{DMSO}-d_6$ . (b) FT-IR Spectra of **NP10** xerogel (red line), **NP10** hydrogel (pink line) and **NP10** (blue line). (c) CD spectra of the biocatalytically formed **NP10** hydrogel with time (200  $\mu\text{M}$ ). Wide angle PXRD spectrum of **NP10** (red line), **NP10** hydrogel (blue line) and PHBA.

The participation of the hydroxyl group in the lipase-catalyzed dynamic esterification reaction was analyzed by  $^1\text{H}$  NMR spectroscopy. The  $^1\text{H}$  NMR spectrum of **NP10** ester shows a chemical shift at 5.2 ppm, which corresponds to the benzylic protons present in the PHBA (**Figure 5.46a**) [50]. The bio-catalytically synthesized methyl esters participate in the self-assembly process via H-bonding and  $\pi$ - $\pi$  stacking interactions to produce a self-supporting hydrogel. The hydrogel disassembles when the activated esters are subjected to external stimuli, resulting in the production of inactivated building-block nucleobase conjugate and PHBA. The hydrogel breaks apart due to the dissipation of energy in the form of PHBA. The formation of the activated building blocks and their subsequent hydrolysis are irreversible. Therefore, this system can be

considered a dissipative self-assemble system as it fulfills all the necessary criteria required.

The biocatalyst-driven hydrogel was analyzed by several spectroscopic and microscopic techniques. To gain information about the secondary structure, FT-IR spectra were recorded for the synthesized **NP10**, the hydrogel formed through biocatalysis and the xerogel. The amide C=O stretching in **NP10** occurs at  $1638\text{ cm}^{-1}$  and  $1694\text{ cm}^{-1}$  whereas in the xerogel it occurs at  $1612\text{ cm}^{-1}$  and  $1693\text{ cm}^{-1}$ , respectively. This shift in stretching frequency indicates that the amide C=O is involved in H-bonding. The N-H stretching frequency in **NP10** is observed at  $3415\text{ cm}^{-1}$  whereas it is  $3414\text{ cm}^{-1}$  for **NP10** hydrogel and in the corresponding xerogel it is  $3387\text{ cm}^{-1}$  (**Figure 5.46b**) [51,52]. This also suggests that the presence of H-bonding helps to form the nanofibrous hydrogel. Hence, the shift in stretching frequencies is due to the participation of the amide groups in H-bonding. The presence of H-bonding plays a crucial role in the formation of a stable G-quadruplex hydrogel. The presence of a secondary structure within the hydrogel matrices was confirmed by circular dichroism (CD) spectroscopy. The CD spectra were recorded at specific time intervals to characterize the secondary structure present in the hydrogel. The CD spectra of the **NP10** hydrogel shows two bands: a positive band at 260 nm and a negative band at 241 nm (**Figure 5.46c**). The exact folding topology of G-quadruplex is difficult to predict from the CD spectrum. However, the literature reports several G-quadruplex structures, with two basic types differing in their folding. One type is the parallel (head to tail) G-quadruplex where two consecutive G-quartets run parallelly to each other. The other type is the antiparallel (head-to-head) G-quadruplex, where two consecutive G-quartets are oriented in an antiparallel manner. Based on the CD spectra of **NP10** hydrogel, we can conclude that the G-quartet in the **NP10** hydrogel is in parallel orientation [53,54].

The wide-angle powder X-ray diffraction patterns were recorded for both of the xerogel and compounds. The bio-catalytically formed hydrogels were dried using a lyophilizer to obtain solid. The powder

XRD pattern of **NP10** xerogel shows peaks at  $2\theta = 28.48^\circ$ , which corresponds to the  $d$  value of  $3.13\text{\AA}$ , attributed to the stacking distance of consecutive G-quartets. It also shows another peak with  $d$  value of  $2.21\text{\AA}$ , which could be for the  $\pi$ - $\pi$  stacking distance of the indole ring. The X-ray diffraction pattern of **NP10** shows two peaks at  $2\theta = 31.78^\circ$  and  $45.51^\circ$ , whereas the diffraction pattern of PHBA show peaks at  $2\theta = 24.84^\circ$  and  $18.69^\circ$  (**Figure 5.46d**) [55,56]. It is noteworthy to mention that the generation of new peaks and disappearance of substrate peaks in the PXRD pattern of **NP10** xerogel clearly indicate the biocatalytic dynamic esterification of acid.

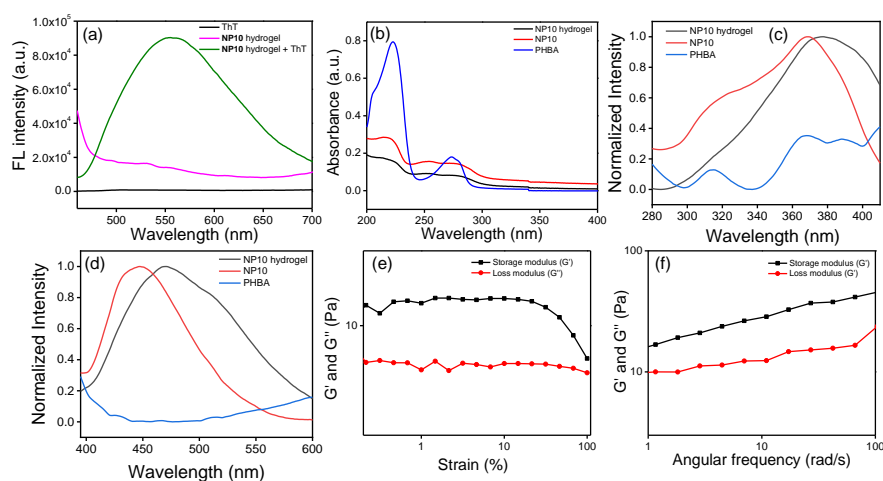


**Figure 5.47** (a) ThT dye binding assay: the excitation spectrum of ThT (black line), **NP10** hydrogel (pink line) and **NP10** hydrogel+ThT (green line) at 450 nm. ThT dye binding experiment was performed after the formation of the hydrogel at 30 days. (b) Absorbance spectra of the synthesized nucleobase functionalized amino acid conjugate **NP10** hydrogel at 30 day, **NP10** and PHBA. (c) Normalised excitation and (d) emission spectra ( $\lambda_{\text{ex}} = 375\text{ nm}$ ) of the **NP10** hydrogel at 30 day, **NP10** and PHBA. Rheological experiments (e) amplitude sweeps and (f) frequency sweep experiment of the biocatalytically formed **NP10** hydrogel.

The extrinsic fluorogenic probes are used to analyze the folding of biomacromolecules like proteins and DNA. These fluorogenic marker are also useful for studying the presence of biological macromolecules

inside cells. Thioflavin T, a cationic fluorogenic marker that contains benzothiazole salt, is utilized to recognize the non-canonical secondary structure of DNA known as G-quadruplex. While ThT is widely used to investigate protein folding in amyloid, it has also been employed for the recognition of G-quadruplex over the past few decades [57]. ThT gives very weak fluorescence when excited at 450 nm, but it becomes fluorescent when it binds to the G-quadruplex. The fluorescent spectrum of the ThT solution was recorded for the catalytically produced hydrogels. The hydrogel solution containing **NP10** and ThT is weakly fluorescent in water when excited at 450 nm. However, after adding ThT to the **NP10** hydrogel solution, it exhibits strong fluorescence at 552 nm (**Figure 5.47a**). Theoretical studies suggest that the fluorescent enhancement of ThT occurs when it binds with biomacromolecules. In the ThT dye, the benzothiazole moiety is attached to the dimethyl benzyl moiety through a C-C bond, allowing for free rotation along the single bond. This rotation causes fluorescence quenching in the ThT solution. However, when ThT binds to macromolecules, the free rotation is restricted, allowing the excited state to be maintained and fluorescence to occur [58]. UV-vis and Fluorescence spectroscopy was used for the study of biocatalytic self-assembly. UV-vis spectra were recorded for the **NP10**, PHBA and **NP10** hydrogel. The peaks were appeared in the range (200-300 nm). The red shift is observed in the **NP10** hydrogel spectra in comparison with the substrate spectra which indicate the presence of higher order assembly in the hydrogel (**Figure 5.47b**) [50]. The fluorescence spectra were recorded for both the substrate solutions and the **NP10** hydrogel formed through biocatalysis. The **NP10** substrate solution gives an emission peak at 450 nm whereas PHBA did not exhibit emission peak upon excitation at 365 nm (**Figure 5.47c**). The red shift is observed upon the conversion of **NP10** (**Figure 5.47d**). The shift towards longer wavelength in the emission maximum of **NP10** is attributed to the formation of the hydrogel through biocatalysis [50].

The mechanical properties of the **NP10** hydrogel formed through biocatalysis were analyzed using a rotational rheometer. An amplitude

sweep experiment was conducted for the **NP10** hydrogel with a constant frequency of 10 rad/s, to determine the linear viscoelastic region. The storage modulus ( $G'$ ) of the **NP10** hydrogel was higher than the loss modulus ( $G''$ ) at lower strain. However, with the increase of strain, the **NP10** hydrogel gradually transformed into a solution, with the loss modulus becoming higher than the storage modulus. This implies that the microstructure inside the hydrogel completely broke down, resulting in the loss of energy at higher strain. The storage modulus and loss modulus were consistently varied at a lower strain ( $<10\%$ ) (**Figure 5.47e**). Further, a frequency sweep test was conducted to assess the mechanical strength of the **NP10** hydrogel at a constant strain of 1%. It was observed that the storage and loss modulus remained almost constant within the frequency range 1-100 rad/s (**Figure 5.47f**) [59].

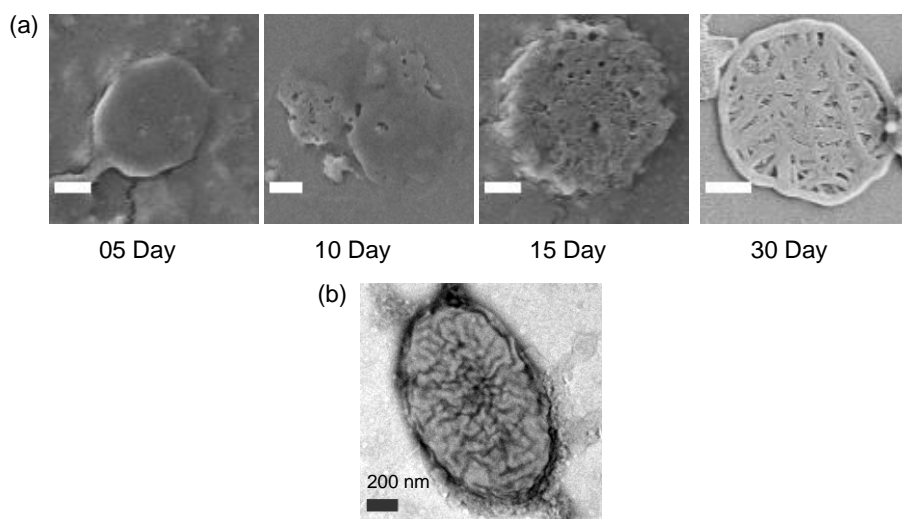


**Figure 5.48** (a) SEM images of nanofiber enclosed sphere, the formation of the fiber enclosed nanosphere on the progress of the reaction has been shown here. (The scale bar in all the images is 1  $\mu\text{m}$ ). (b) TEM image of the biocatalytically formed **NP10** hydrogel at 30 day. The image was taken after the formation of the hydrogel at 30 day.

We conducted morphological characterization by using several microscopic techniques such as SEM, TEM and CLSM. Field emission scanning electron microscopy images show the presence of spheres inside the **NP10** hydrogel (**Figure 5.48a**) formed through biocatalysis.

The images also show the existence of nanofibers inside the spheres. The average diameter of the nanofiber inside the sphere is 159.711 nm [60,61]. The TEM image of the **NP10** hydrogel also clearly reveals the presence of the fiber enclosed spheres (**Figure 5.48b**).

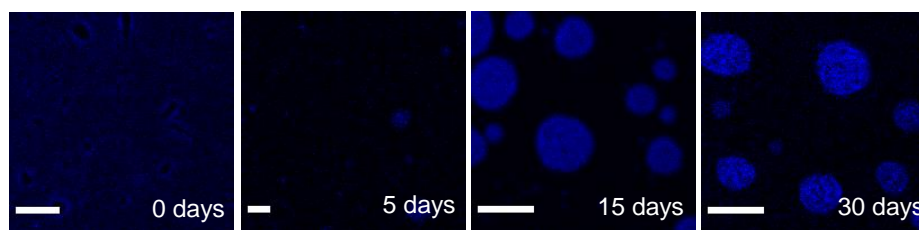
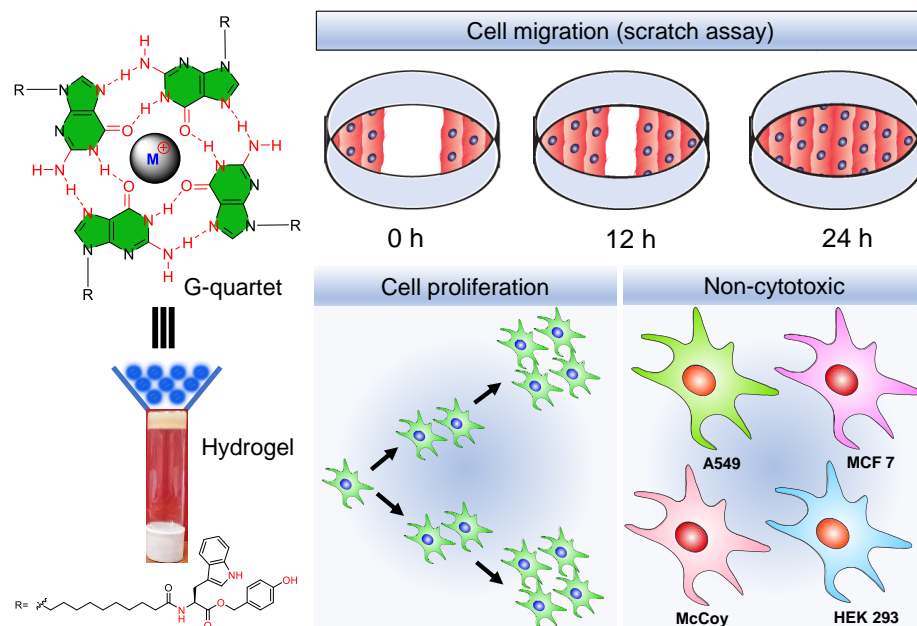


**Figure 5.49** CLSM images show the formation of the fiber enclosed sphere caused by lipase catalyzed esterification of PHBA in **NP10**. (Scale bar in all images are 5  $\mu$ m).

The presence of nanofibers inside the sphere was confirmed by CLSM. The spheres, which contained inherent blue fluorescent fibers, were captured using a 405 nm laser. A small amount of the sample solution (10  $\mu$ L, detail procedure in the SI) was drop casted on the mica foil before imaging. The CLSM images demonstrate the growth of nanofibers inside the spheres (**Figure 5.49**). These phase separated spheres have drawn attention to the researchers due to the similarity between the protoplasm in modern cells and nano fiber enclosed sphere [62]. It is noteworthy to mention that **NP10** forms fibers enclosed spheres, even though it forms a hydrogel. Here, we are reporting that the nanofibers, enclosed within a confined region, undergo higher order self-organization to form the hydrogel. The formation of **NP10** hydrogel, driven by the biocatalyst, was carried out in a phosphate buffer with a pH of 7.4 (buffer concentration was 100 mM). The presence of the salt in the buffer also aids in the formation of the fiber in the confined region. The CLSM images also show the presence of fibers enclosed spheres. The formation and growth of the spheres were studied using CLSM. Therefore, the biocatalyst induces formation of the fibers in a

confined region. Hence, the biocatalytically formed **NP10** hydrogel was used to study cell proliferation and cell migration (**Scheme 5.3**).



**Scheme 5.3** Graphical illustration demonstrating the formation of the bio-catalytically formed **NP10** hydrogel and its use to study cell proliferation and cell migration.

As we mentioned earlier, there is a strong correlation between the fiber enclosed sphere and protocell. Therefore, it is important to investigate the life-like properties integrated within a single sphere. Consequently, we conducted further studies to assess the potential of this hydrogel for use in biomedicine.

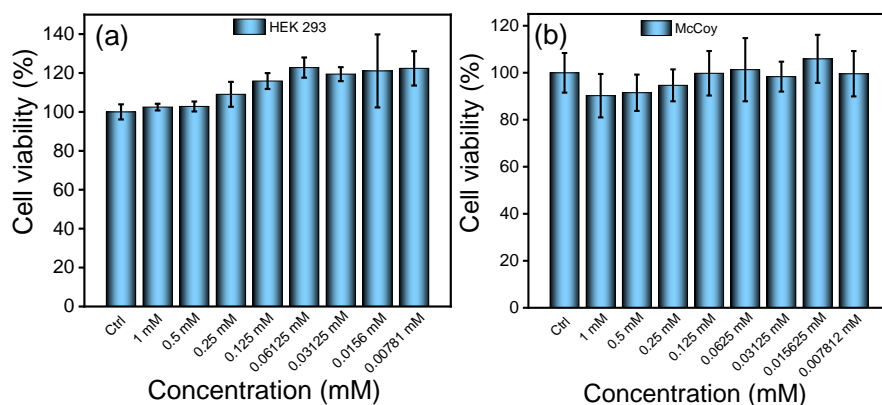




**Figure 5.50** In the cell viability experiment, a range of concentrations (0.00781-1 mM) was applied to check the viability of the cell lines (a) HEK 293 and (b) McCoy.

The evaluation of biocompatibility is necessary to assess whether biocatalytically formed supramolecular hydrogel is suitable as an intelligent biomaterial. In this study, the cytotoxicity and cell proliferation of the biocatalyst-driven hydrogel were checked using in-vitro experiments, specifically the MTT assay. This assay relies on the capability of enzymes called mitochondrial oxidoreductase and dehydrogenase, found in living cells, to break down a pale-yellow compound called MTT into a purple substance called formazan. The formation is impermeable through cell membranes, so it accumulates in healthy cells. Therefore, the colorimetric MTT test was employed for the quantification of healthy cells after treatment compared to control cells. The fibroblast McCoy and epithelial HEK 293 cell lines were chosen for the study. A range of concentrations was used to investigate the biocompatibility of the hydrogel with these cell lines. The MTT cell viability experiment shows that **NP10** hydrogel has more than 92% viability (**Figure 5.50**) for cell lines tested [63]. The data shows the cell proliferation at lower concentrations of the **NP10** hydrogel. Further, we performed live and dead cell imaging on A549 and HEK 293 cell lines. Hoechst dye was used to stain the DNA and nuclei of the live cells. Propidium iodide (PI) was used to stain the double-stranded DNA of the dead cells. In the control experiment, where only buffer was added, a CLSM image shows some red fluorescence after exciting at a 559 nm laser.

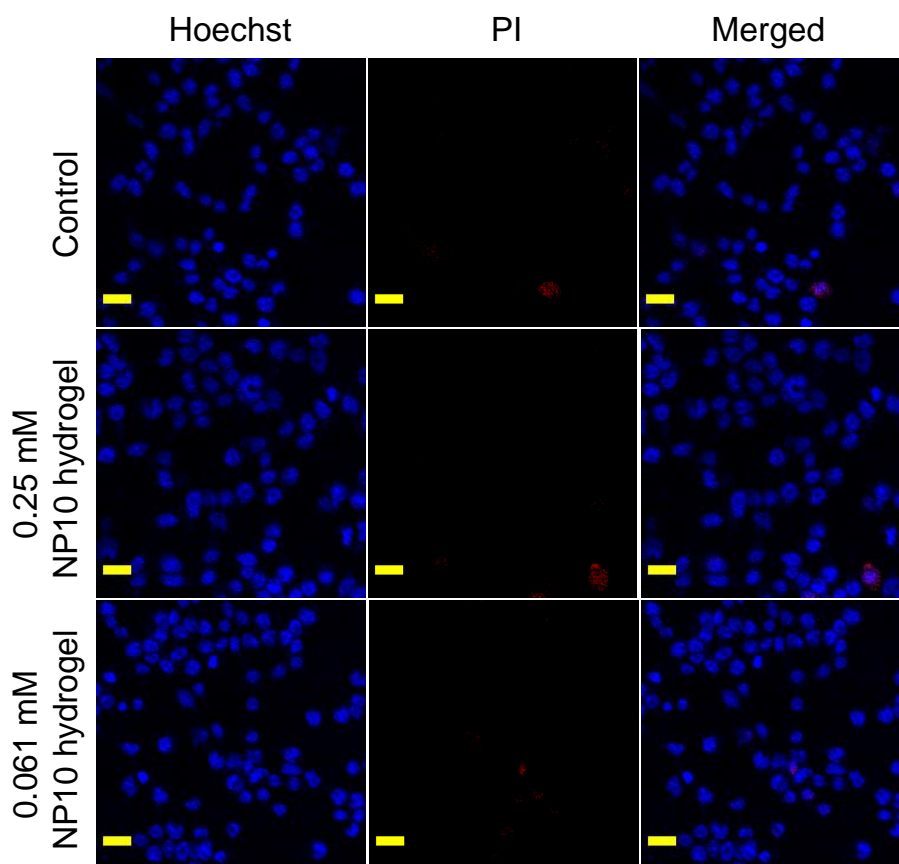


**Figure 5.51** Live and dead cell images on HEK 293 cell lines of (a) control (buffer treated), (b) 0.25 mM and (c) 0.061 mM **NP10** hydrogel. The images were taken using a 10x objective z1.0 (The scale bar in all images is 20  $\mu\text{m}$ ).

Hence, this data indicates the presence of live cells in the sample. There is no prominent red fluorescence observed after treating with the **NP10** hydrogel formed by biocatalysis. The treatment of the hydrogel also increases the cell number as compared to the control. Therefore, the CLSM images clearly show cell proliferation after adding the **NP10** hydrogel (**Figure 5.51**) [64].

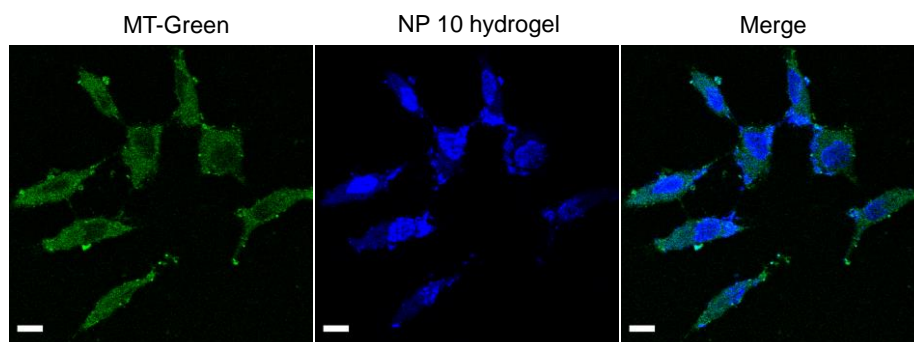


**Figure 5.52** CLSM images (scale bar in all images are 20  $\mu\text{m}$ ) taken after treating of the McCoy cells with **NP10** hydrogel (0.25 mM). The images were taken using 100x objective z1.0.

The biocompatible **NP10** hydrogel formed through biocatalysis was used for the cellular internalization of the hydrogel. Research on fluorescent nanostructures, that can pass through cell membranes for cellular internalization, is an important area of study [65]. Fluorescent-appended peptides have been used to image and monitor self-assembly in the living cells [66]. In biomedical applications, the creation of novel fluorescent peptide-based hydrogels is particularly desired that have the advantage of both fluorescence and self-assembly [67,68]. This is because the use of fluorescence allows for real-time observation of both physiological and pathological processes. Therefore, **NP10** hydrogel was utilized to determine the location within the cell. The hydrogel was introduced into the McCoy cell line, a type of mice fibroblast, and incubated in the cell medium for 2 h at a concentration of 0.125 mM. The cells were washed thrice with the phosphate buffer. Then, the mitochondria staining dye, Mito tracker green (MT-Green), was used to stain the mitochondria. The cell was washed with phosphate buffer prior to imaging. The CLSM images show that the biocatalytically formed G-quadruplex hydrogel specifically binds more with the nucleus than other parts of the cells (**Figure 5.52**).

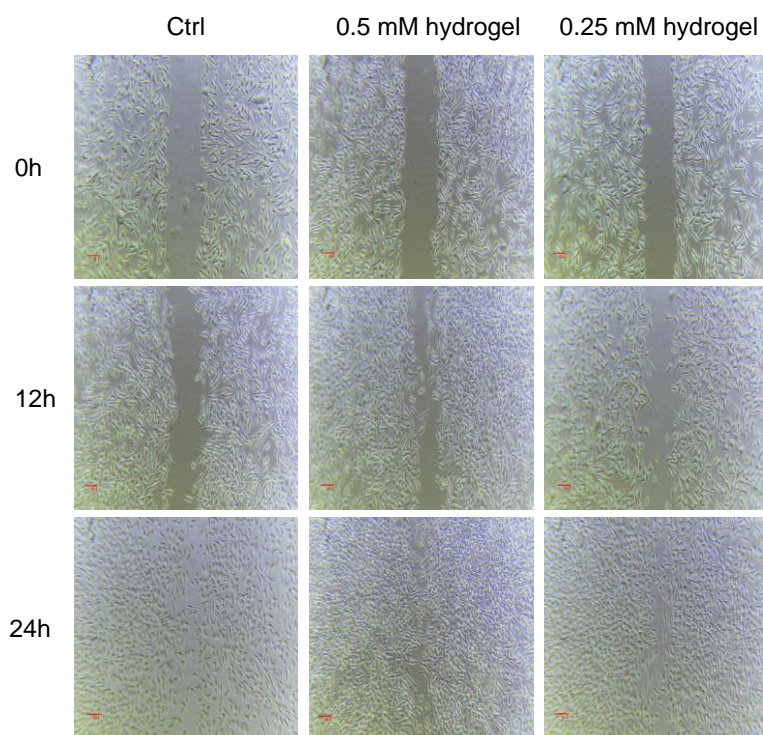


**Figure 5.53** The scratch wound test was used to evaluate the migratory behavior of McCoy cells after the treatment of 0.5 mM and 0.25 mM of **NP10** hydrogel and control. The migration of the cells was at time 0 h, 12 h and 24 h. (Scale bar in all images are 50  $\mu$ m).

Cell migration is a key phenomenon that broadens the variety of biomaterials that can be used to create a synthetic extra cellular matrix (ECM) mimic for the next generation. The ability of cells to interact with the matrix is crucial for their adhesion and migration [64]. The artificial ECM should include bioactive motifs that can promote cell adhesion, survival, and proliferation which would help in wound healing. Having a larger population of cells would help maintain an adequate number of cells that can proliferate and repair the damaged area at the site of injury. Thus, the nucleobase functionalized hydrogel **NP10** formed through biocatalysis can be used to explore its ability to promote cell migration. We employed the scratch wound test, a time-honoured technique, to assess the cell migration capacity. To create a monolayer of cells, cells were cultivated on a 24-well cell culture plate and allowed them to adhere and multiply for 24 h. After that, a scratch was made using a

sterile 200  $\mu$ L tip and treated it with peptides. To assess the migration of cells after hydrogel treatment, we observed the cells under a microscope at different time intervals (**Figure 5.53**).

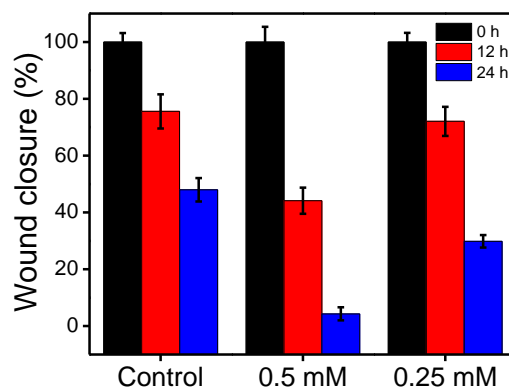


**Figure 5.54** Quantification of the wound closure by **NP10** hydrogel after its formation at 30 day with time after 0 h, 12 h and 24 h.

This study demonstrates the migration of fibroblast cells within the wound area for 24 h after treatment with 0.5 mM and 0.25 mM of the hydrogel formed through biocatalysis, compared to the control (**Figure 5.54**).

#### 5.4 Conclusion

We have explored an enzyme fueled dissipative self-assembly process, which is constructed using nucleobase functionalized biomaterials. These materials were designed and synthesized to create non-covalent polymers that were readily self-assembled using G-quadruplex motif. The dissipative self-assembly system shifted the equilibrium in reverse due to morphological transition over time upon treatment with lipase. The ThT dye binding assay, wide angle PXRD and CD experiments were performed to confirm the presence of G-quadruplex endowed with hydrolysable properties. The fluorescence experiment demonstrated that lipase facilitated the inclusion of PHBA, which in turn induced the self-assembly of the nucleobase functionalized structure starting from **NP10**. The CLSM images clearly indicated that the fiber-enclosed vesicles inside the G-quadruplex hydrogel were fabricated through biocatalysis. The SEM and TEM images further revealed the formation of nano

spheres in a facile manner. The MTT assay demonstrated no observed cytotoxicity of the fiber-enclosed spheres formed in aqueous media. The biocompatibility experiment was performed on HEK 293 and McCoy cell lines. The potential for **NP10** as wound repair dressing was evaluated by scratch assay demonstrating disappearance of the scratch in 24 h following the cell migration after hydrogel treatment. Therefore, the described enzyme fueled approach could potentially be used as self-assembled nature inspired intelligent materials for advanced biological applications in drug delivery, biosensing, cell culture, wound dressing and others.

## 5.5 References

- [1] Qiu L, Patterson SE, Bonnac LF, Geraghty RJ (2018) Nucleobases and corresponding nucleosides display potent antiviral activities against dengue virus possibly through viral lethal mutagenesis. *PLoS Negl Trop Dis* 12:e0006421. <https://doi.org/10.1371/journal.pntd.0006421>.
- [2] Li J, Wang Z, Hua Z, Tang C (2020) Supramolecular nucleobase-functionalized polymers: synthesis and potential biological applications. *J Mater Chem B* 8:1576–1588. <https://doi.org/10.1039/C9TB02393C>.
- [3] Ghosh T, Das AK (2023) Dynamic boronate esters cross-linked guanosine hydrogels: A promising biomaterial for emergent applications. *Coord Chem Rev* 488:215170. <https://doi.org/10.1016/j.ccr.2023.215170>.
- [4] Wang T, Ménard-Moyon C, Bianco A (2022) Self-assembly of amphiphilic amino acid derivatives for biomedical applications. *Chem Soc Rev* 51:3535–3560. <https://doi.org/10.1039/D1CS01064F>.
- [5] Song J, Yuan C, Jiao T, Xing R, Yang M, Adams DJ, Yan X (2020) Multifunctional Antimicrobial Biometallohydrogels Based on Amino Acid Coordinated Self-Assembly. *Small* 16:1907309. <https://doi.org/10.1002/smll.201907309>.

- [6] Xing P, Phua SZF, Wei X, Zhao Y (2018) Programmable Multicomponent Self-Assembly Based on Aromatic Amino Acids. *Adv Mater* 30:1805175. <https://doi.org/10.1002/adma.201805175>.
- [7] Bera S, Xue B, Rehak P, Jacoby G, Ji W, Shimon LJW, Beck R, Král P, Cao Y, Gazit E (2020) Self-Assembly of Aromatic Amino Acid Enantiomers into Supramolecular Materials of High Rigidity. *ACS Nano* 14:1694–1706. <https://doi.org/10.1021/acsnano.9b07307>.
- [8] Qian Z, Lutz S (2005) Improving the Catalytic Activity of *Candida antarctica* Lipase B by Circular Permutation. *J Am Chem Soc* 127:13466–13467. <https://doi.org/10.1021/ja053932h>.
- [9] Kozlov O, Horáková E, Rademacherová S, Maliňák D, Andrýs R, Prchalová E, Líba M (2023) Direct Chiral Supercritical Fluid Chromatography–Mass Spectrometry Analysis of Monoacylglycerol and Diacylglycerol Isomers for the Study of Lipase-Catalyzed Hydrolysis of Triacylglycerols. *Anal Chem* 95:5109–5116. <https://doi.org/10.1021/acs.analchem.3c00053>.
- [10] Choi Y, Chang P-S (2022) Kinetic modeling of lipase-catalysed hydrolysis of triacylglycerol in a reverse micelle system for the determination of integral stereoselectivity. *Catal Sci Technol* 12:2819–2828. <https://doi.org/10.1039/D1CY02182F>.
- [11] Weißenfels M, Gemen J, Klajn R (2021) Dissipative Self-Assembly: Fueling with Chemicals versus Light. *Chem* 7:23–37. <https://doi.org/10.1016/j.chempr.2020.11.025>
- [12] De S, Klajn R (2018) Dissipative Self-Assembly Driven by the Consumption of Chemical Fuels. *Adv Mater* 30:1706750. <https://doi.org/10.1002/adma.201706750>.
- [13] Pollard TD, Blanchoin L, Mullins RD (2000) Molecular Mechanisms Controlling Actin Filament Dynamics in Nonmuscle Cells. *Annu Rev Biophys Biomol Struct* 29:545–576. <https://doi.org/10.1146/annurev.biophys.29.1.545>.

- [14] Hennessey ES, Drummond DR, Sparrow JC (1993) Molecular genetics of actin function. *Biochemical Journal* 291:657–671. <https://doi.org/10.1042/bj2910657>.
- [15] Pantaloni D, Clainche CL, Carlier M-F (2001) Mechanism of Actin-Based Motility. *Science* 292:1502–1506. <https://doi.org/10.1126/science.1059975>.
- [16] Xie X, Zhang Y, Liang Y, Wang M, Cui Y, Li J, Liu C (2022) Programmable Transient Supramolecular Chiral G-quadruplex Hydrogels by a Chemically Fueled Non-equilibrium Self-Assembly Strategy. *Angew Chem Int Ed* 61:e202114471. <https://doi.org/10.1002/anie.202114471>.
- [17] Lu H, Hao J, Wang X (2022) Host-Fueled Transient Supramolecular Hydrogels. *ChemSystemsChem* 4:e202100050. <https://doi.org/10.1002/syst.202100050>.
- [18] Olivieri E, Gasch B, Quintard G, Naubron J-V, Quintard A (2022) Dissipative Acid-Fueled Reprogrammable Supramolecular Materials. *ACS Appl Mater Inter* 14:24720–24728. <https://doi.org/10.1021/acsami.2c01608>.
- [19] Olivieri E, Quintard A (2023) Out of Equilibrium Chemical Systems Fueled by Trichloroacetic Acid. *ACS Org Inorg Au* 3:4–12. <https://doi.org/10.1021/acsorginorgau.2c00051>.
- [20] Dolai G, Shill S, Roy S, Mandal B (2023) Atomic Insight on Inhibition of Fibrillization of Dipeptides by Replacement of Phenylalanine with Tryptophan. *Langmuir* 39:9367–9383. <https://doi.org/10.1021/acs.langmuir.3c00823>.
- [21] Tantakitti F, Boekhoven J, Wang X, Kazantsev RV, Yu T, Li J, Zhuang E, Zandi R, Ortony JH, Newcomb CJ, Palmer LC, Shekhawat GS, De La Cruz MO, Schatz GC, Stupp SI (2016) Energy landscapes and functions of supramolecular systems. *Nature Mater* 15:469–476. <https://doi.org/10.1038/nmat4538>.



- [22] Whitesides GM, Grzybowski B (2002) Self-Assembly at All Scales. *Science* 295:2418–2421. <https://doi.org/10.1126/science.1070821>.
- [23] Lancia F, Ryabchun A, Katsonis N (2019) Life-like motion driven by artificial molecular machines. *Nat Rev Chem* 3:536–551. <https://doi.org/10.1038/s41570-019-0122-2>.
- [24] Needleman D, Dogic Z (2017) Active matter at the interface between materials science and cell biology. *Nat Rev Mater* 2:17048. <https://doi.org/10.1038/natrevmats.2017.48>.
- [25] Rieß B, Grötsch RK, Boekhoven J (2020) The Design of Dissipative Molecular Assemblies Driven by Chemical Reaction Cycles. *Chem* 6:552–578. <https://doi.org/10.1016/j.chempr.2019.11.008>.
- [26] Pezzato C, Cheng C, Stoddart JF, Astumian RD (2017) Mastering the non-equilibrium assembly and operation of molecular machines. *Chem Soc Rev* 46:5491–5507. <https://doi.org/10.1039/C7CS00068E>.
- [27] Cheng C, McGonigal PR, Stoddart JF, Astumian RD (2015) Design and Synthesis of Nonequilibrium Systems. *ACS Nano* 9:8672–8688. <https://doi.org/10.1021/acsnano.5b03809>.
- [28] Noblett AD, Baek K, Suggs LJ (2021) Controlling Nucleopeptide Hydrogel Self-Assembly and Formation for Cell-Culture Scaffold Applications. *ACS Biomater Sci Eng* 7:2605–2614. <https://doi.org/10.1021/acsbiomaterials.0c01658>.
- [29] Van Esch JH, Klajn R, Otto S (2017) Chemical systems out of equilibrium. *Chem Soc Rev* 46:5474–5475. <https://doi.org/10.1039/C7CS90088K>.
- [30] Li X, Wang G, Zhang Q, Liu Y, Sun T, Liu S (2022) Dissipative self-assembly of a dual-responsive block copolymer driven by a chemical oscillator. *J Colloid Interface Sci* 615:732–739. <https://doi.org/10.1016/j.jcis.2022.01.183>.

- [31] Das K, Gabrielli L, Prins LJ (2021) Chemically Fueled Self-Assembly in Biology and Chemistry. *Angew Chem Int Ed* 60:20120–20143. <https://doi.org/10.1002/anie.202100274>.
- [32] Das AK, Maity I, Parmar HS, McDonald TO, Konda M (2015) Lipase-Catalyzed Dissipative Self-Assembly of a Thixotropic Peptide Bolaamphiphile Hydrogel for Human Umbilical Cord Stem-Cell Proliferation. *Biomacromole* 16:1157–1168. <https://doi.org/10.1021/bm501835v>.
- [33] Tan W, Zhang Q, Quiñones-Frías MC, Hsu AY, Zhang Y, Rodal A, Hong P, Luo HR, Xu B (2022) Enzyme-Responsive Peptide Thioesters for Targeting Golgi Apparatus. *J Am Chem Soc* 144:6709–6713. <https://doi.org/10.1021/jacs.2c02238>.
- [34] Boekhoven J, Brizard AM, Kowlgi KNK, Koper GJM, Eelkema R, van Esch JH (2010) Dissipative Self-Assembly of a Molecular Gelator by Using a Chemical Fuel. *Angew Chem Int Ed* 49:4825–4828. <https://doi.org/10.1002/anie.201001511>.
- [35] Rodon-Fores J, Würbser MA, Kretschmer M, Rieß B, Bergmann AM, Lieleg O, Boekhoven J (2022) A chemically fueled supramolecular glue for self-healing gels. *Chem Sci* 13:11411–11421. <https://doi.org/10.1039/D2SC03691F>.
- [36] Gözen I, Köksal ES, Pöldsalu I, Xue L, Spustova K, Pedrueza-Villalmanzo E, Ryskulov R, Meng F, Jesorka A (2022) Protocells: Milestones and Recent Advances. *Small* 18:2106624. <https://doi.org/10.1002/smll.202106624>.
- [37] Schrum JP, Zhu TF, Szostak JW (2010) The Origins of Cellular Life. *cold spring harb perspect biol* 2:a002212–a002212. <https://doi.org/10.1101/cshperspect.a002212>.
- [38] Van Haren, MHI, Nakashima, KK, & Spruijt, E (2020) Coacervate-based protocells: integration of life-like properties in a droplet. *J Syst Chem*, 8:107-120.

- [39] Chen IA, Walde P (2010) From Self-Assembled Vesicles to protocells. *cold spring harb perspect biol* 2:a002170–a002170. <https://doi.org/10.1101/cshperspect.a002170>.
- [40] Li M, Harbron RL, Weaver JVM, Binks BP, Mann S (2013) Electrostatically gated membrane permeability in inorganic protocells. *Nature Chem* 5:529–536. <https://doi.org/10.1038/nchem.1644>.
- [41] Peyratout CS, Dähne L (2004) Tailor-Made Polyelectrolyte Microcapsules: From Multilayers to Smart Containers. *Angew Chem Int Ed* 43:3762–3783. <https://doi.org/10.1002/anie.200300568>.
- [42] Abbas M, Lipiński WP, Wang J, Spruijt E (2021) Peptide-based coacervates as biomimetic protocells. *Chem Soc Rev* 50:3690–3705. <https://doi.org/10.1039/D0CS00307G>.
- [43] Tawfik DS, Griffiths AD (1998) Man-made cell-like compartments for molecular evolution. *Nat Biotechnol* 16:652–656. <https://doi.org/10.1038/nbt0798-652>.
- [44] Huang X, Patil AJ, Li M, Mann S (2014) Design and Construction of Higher-Order Structure and Function in Proteinosome-Based Protocells. *J Am Chem Soc* 136:9225–9234. <https://doi.org/10.1021/ja504213m>.
- [45] Kurihara K, Okura Y, Matsuo M, Toyota T, Suzuki K, Sugawara TA (2015) A recursive vesicle-based model protocell with a primitive model cell cycle. *Nat Commun* 6:8352. <https://doi.org/10.1038/ncomms9352>.
- [46] Chen IA, Salehi-Ashtiani K, Szostak JW (2005) RNA Catalysis in Model Protocell Vesicles. *J Am Chem Soc* 127:13213–13219. <https://doi.org/10.1021/ja051784p>.
- [47] Mukherjee T, Soppina V, Ludovic R, Mély Y, Klymchenko AS, Collot M, Kanvah S (2021) Live-cell imaging of the nucleolus and mapping mitochondrial viscosity with a dual function fluorescent probe.

[48] Mei R, Wang Y, Liu W, Chen L (2018) Lipid Bilayer-Enabled Synthesis of Waxberry-like Core–Fluidic Satellite Nanoparticles: Toward Ultrasensitive Surface-Enhanced Raman Scattering Tags for Bioimaging. *ACS Appl Mater Inter* 10:23605–23616. <https://doi.org/10.1021/acsami.8b06253>.

[49] Davis JT (2004) G-Quartets 40 Years Later: From 5'-GMP to Molecular Biology and Supramolecular Chemistry. *Angew Chem Int Ed* 43:668–698. <https://doi.org/10.1002/anie.200300589>.

[50] Rasale DB, Maity I, Das AK (2014) Lipase catalyzed inclusion of gastrodigenin for the evolution of blue light emitting peptide nanofibers. *Chem Commun* 50:8685–8688. <https://doi.org/10.1039/C4CC02484B>.

[51] Maji K, Abbasi M, Podder D, Datta R, Haldar D (2018) Potential Antileishmanial Activity of a Triazole-Based Hybrid Peptide against *Leishmania major*. *ChemistrySelect* 3:10220–10225. <https://doi.org/10.1002/slct.201802002>.

[52] Moretto V, Crisma M, Bonora GM, Toniolo C, Balaram H, Balaram P (1989) Comparison of the effect of five guest residues on the beta.-sheet conformation of host (L-val)<sub>n</sub> oligopeptides. *Macromole* 22:2939–2944. <https://doi.org/10.1021/ma00197a010>.

[53] Peters GM, Skala LP, Davis JT (2016) A Molecular Chaperone for G4-Quartet Hydrogels. *J Am Chem Soc* 138:134–139. <https://doi.org/10.1021/jacs.5b08769>.

[54] Peters GM, Skala LP, Plank TN, Oh H, Manjunatha Reddy GN, Marsh A, Brown SP, Raghavan SR, Davis JT (2015) G4-Quartet·M<sup>+</sup> Borate Hydrogels. *J Am Chem Soc* 137:5819–5827. <https://doi.org/10.1021/jacs.5b02753>.

- [55] Arnal-Hérault C, Pasc A, Michau M, Cot D, Petit E, Barboiu M (2007) Functional G-Quartet Macroscopic Membrane Films. *Angew Chem Int Ed* 46:8409–8413. <https://doi.org/10.1002/anie.200702605>.
- [56] Ghosh S, Ghosh T, Bhowmik S, Patidar MK, Das AK (2023) Nucleopeptide-Coupled Injectable Bioconjugated Guanosine-Quadruplex Hydrogel with Inherent Antibacterial Activity. *ACS Appl Bio Mater* 6:640–651. <https://doi.org/10.1021/acsabm.2c00912>.
- [57] Mohanty J, Barooah N, Dhamodharan V, Harikrishna S, Pradeepkumar PI, Bhasikuttan AC (2013) Thioflavin T as an Efficient Inducer and Selective Fluorescent Sensor for the Human Telomeric G-Quadruplex DNA. *J Am Chem Soc* 135:367–376. <https://doi.org/10.1021/ja309588h>.
- [58] Ghosh T, Biswas A, Bhowmik S, Das AK (2021) Pt Nanoparticles Supported on a Dynamic Boronate Ester-Based G-quadruplex Hydrogel as a Nanoreactor. *Chem Asian J* 16:215–223. <https://doi.org/10.1002/asia.202001284>.
- [59] Zhong R, Tang Q, Wang S, Zhang H, Zhang F, Xiao M, Man T, Qu X, Li L, Zhang W, Pei H (2018) Self-Assembly of Enzyme-Like Nanofibrous G-Molecular Hydrogel for Printed Flexible Electrochemical Sensors. *Adv Mater* 30:1706887. <https://doi.org/10.1002/adma.201706887>.
- [60] Kubota R, Tanaka W, Hamachi I (2021) Microscopic Imaging Techniques for Molecular Assemblies: Electron, Atomic Force, and Confocal Microscopies. *Chem Rev* 121:14281–14347. <https://doi.org/10.1021/acs.chemrev.0c01334>.
- [61] Rizvi A, Mulvey JT, Carpenter BP, Talosig R, Patterson JP (2021) A Close Look at Molecular Self-Assembly with the Transmission Electron Microscope. *Chem Rev* 121:14232–14280. <https://doi.org/10.1021/acs.chemrev.1c00189>.

- [62] Hyman AA, Weber CA, Jülicher F (2014) Liquid-Liquid Phase Separation in Biology. *Annu Rev Cell Dev Biol* 30:39–58. <https://doi.org/10.1146/annurev-cellbio-100913-013325>.
- [63] Kaur H, Jain R, Roy S (2020) Pathway-Dependent Preferential Selection and Amplification of Variable Self-Assembled Peptide Nanostructures and Their Biological Activities. *ACS Appl Mater Inter* 12:52445–52456. <https://doi.org/10.1021/acsami.0c16725>.
- [64] Sharma P, Pal VK, Kaur H, Roy S (2022) Exploring the TEMPO-Oxidized Nanofibrillar Cellulose and Short Ionic-Complementary Peptide Composite Hydrogel as Biofunctional Cellular Scaffolds. *Biomacromol* 23:2496–2511. <https://doi.org/10.1021/acs.biomac.2c00234>.
- [65] Mazumdar S, Chitkara D, Mittal A (2021) Exploration and insights into the cellular internalization and intracellular fate of amphiphilic polymeric nanocarriers. *Acta Pharmaceutica Sinica B* 11:903–924. <https://doi.org/10.1016/j.apsb.2021.02.019>.
- [66] Chagri S, Ng DYW, Weil T (2022) Designing bioresponsive nanomaterials for intracellular self-assembly. *Nat Rev Chem* 6:320–338. <https://doi.org/10.1038/s41570-022-00373-x>.
- [67] Xue J, Guan Z, Zhu X, Lin J, Cai C, Jin X, Li Y, Ye Z, Zhang W, Jiang X (2018) Cellular internalization of polypeptide-based nanoparticles: effects of size, shape and surface morphology. *Biomater Sci* 6:3251–3261. <https://doi.org/10.1039/C8BM01163J>.
- [68] Mumcuoglu D, Sardan Ekiz M, Gunay G, Tekinay T, Tekinay AB, Guler MO (2016) Cellular Internalization of Therapeutic Oligonucleotides by Peptide Amphiphile Nanofibers and Nanospheres. *ACS Appl Mater Inter* 8:11280–11287. <https://doi.org/10.1021/acsami.6b01526>.

## **Chapter 6**

### **Conclusions and Future Perspectives**





## 6.1 Conclusions

In the past five years our group has made several contributions to the field of supramolecular guanosine and short peptide-based hydrogels. Chapter 6 summarizes the remarkable aspects of the current works and its future perspective. Nucleobases were functionalized with the amino acids to develop G-quadruplex hydrogel. The aggregation propensity of the synthesized compounds was thoroughly studied by DOSY NMR and molecular dynamics simulation experiments. The hydrogels were characterized by performing several experiments such as CD, PXRD, ThT dye binding assay, FT-IR, SEM, TEM and AFM.

The *Chapter 1* described molecular self-assembly and the formation of the hydrogel. The non-covalent interactions behind the hydrogel formation were discussed. The formation of a G-quadruplex structure via Hoogsteen H-bonding interaction was described. The importance of G-quadruplex structure in the replication, transcription, and translation of DNA was mentioned. The role of G-quadruplex in the formation of the hydrogel was outlined. This chapter mainly focused on the formation of the G-quadruplex hydrogel by guanine derivatives. Therefore, this chapter spoke about the recent progress of the guanine-functionalized G-quadruplex hydrogels and their applications.

In *chapter 2*, we successfully synthesized guanine functionalized molecules with variable carbon chain length. The **NP3** formed stable G-quadruplex nanofibrous hydrogel with the support of suitable monovalent alkali metal ions. The Hoogsteen type H-bonding interaction among the guanine moieties and  $\pi$ - $\pi$  stacking were the driving force in the formation G-quadruplex hydrogel. The presence of G-quadruplex inside the hydrogel was demonstrated by circular dichroism spectroscopy, wide angle powder X-ray diffraction study and cationic ThT dye binding study. The effect of monovalent alkali metal ions on the stability of G-quadruplex was also checked. The viscoelastic behaviors of the hydrogel were also determined by the rheological experiments. Hydrogel was thixotropic and found injectable in nature.

The existence of thick and thin nanofibrous morphology inside the hydrogel matrix was characterized with the help of microscopic techniques such as SEM, TEM and AFM. Hydrogel was further utilized for pH responsive sustained delivery of the vitamins like vitamin B<sub>2</sub> and B<sub>12</sub>. The synthesized **NP3** showed excellent biostability towards hydrolytic enzymes proteinase K and chymotrypsin suggesting the improved biostability of this nucleobase amino acid conjugates. The MTT assay clearly revealed that the hydrogel was non-cytotoxic in nature.

In *chapter 3*, the formation of hydrogel by methylation of the synthesized nucleobase amino acid conjugates using the dimethyl sulphate was demonstrated. The dimethyl sulphate activated the gelator precursor to form the hydrogel by higher order self-organization. The formation of the activated gelator molecule was monitored by HPLC. Time dependent <sup>1</sup>H NMR spectroscopy indicated the formation of activated self-assemble building block of **NP3**. Time dependent fluorescence, UV-turbidity experiment, time dependent CD and time dependent rheology depicted the progress of the self-assembly with time. ThT dye binding assay, wide angle powder XRD experiment and CD experiment revealed the nucleic acid secondary structure inside the hydrogel.

*Chapter 4* described the synthesis of nucleopeptide derivatives (**NPs**) and their ability to form hydrogels. The aggregation behavior of these **NPs** was analyzed using a molecular dynamics simulation study. The DOSY NMR experiment confirmed the higher level of aggregation of the **NP5**. Furthermore, **NP5** hydrogel was characterized using CD, PXRD, ThT-dye binding experiments. SEM, TEM experiments revealed the existence of nanofibers within the **NP5** hydrogel. The **NP5** hydrogel exhibited minimal cytotoxicity, as demonstrated by MTT and cell death studies. The **NP5** hydrogel was also found to be biostable against the proteolytic enzyme proteinase K and  $\alpha$ -chymotrypsin. Furthermore, the **NP5** hydrogel showed the efficacy against *B. subtilis* and *E. Coli* bacteria. It also demonstrated properties of ROS scavenging, antibacterial and anti-inflammatory activity in epithelial cells and

keratinocytes. Notably, the hydrogel showed enhanced activity in keratinocytes compared to epithelial cells. In conclusion, the **NP5** hydrogel could be an efficient candidate for wound healing applications.

*Chapter 5* explored an enzyme fueled dissipative self-assembly process, which is constructed using nucleobase functionalized biomaterials. These materials were designed and synthesized to create non-covalent polymers that were readily self-assembled using G-quadruplex motif. The dissipative self-assembly system shifted the equilibrium in reverse due to morphological transition over time upon treatment with lipase. The ThT dye binding assay, wide angle PXRD and CD experiments were performed to confirm the presence of G-quadruplex endowed with hydrolysable properties. The fluorescence experiment demonstrated that lipase facilitated the inclusion of PHBA, which in turn induced the self-assembly of the nucleobase functionalized structure starting from **NP10**. The CLSM images clearly indicated that the fiber-enclosed vesicles inside the G-quadruplex hydrogel were fabricated through biocatalysis. The SEM and TEM images further revealed the formation of nano spheres in a facile manner. The MTT assay demonstrated no observed cytotoxicity of the fiber-enclosed spheres formed in aqueous media. The biocompatibility experiment was performed on HEK 293 and McCoy cell lines. The potential for **NP10** as wound repair dressing was evaluated by scratch assay demonstrating disappearance of the scratch in 24 h following the cell migration after hydrogel treatment.

## **6.2 Future Perspectives**

We have studied a lot about the structural composition, hydrogelation process, and possible uses of these hydrogels made of guanine functional amino acids and peptide derivative. But there are still a lot to learn about this novel method. The field of study on hydrogels formed from biomolecules is very diverse and expansive. In addition to the previously mentioned fields, the hydrogels based on guanine functionalized peptides may have fresh prospects for several additional uses.

In *chapter 2*, we have synthesized synthesized guanine functionalized molecules with variable carbon chain length. The hydrogel is biostable and non-toxic in nature. Therefore, bioinspired newly synthesized hydrogel may be useful in the biomedicine field because of its inherent biocompatible and injectable nature.

In *chapter 3*, the formation of hydrogel by methylation of the synthesized nucleobase amino acid conjugates using the dimethyl sulphate is demonstrated. DNA methylation is an important process in biology. This study is anticipated to pave a new way to mimic the biological processes using methylation with the guanine-based nucleic acids.

In *Chapter 4*, we have synthesized different nucleopeptide derivatives. We have performed various experiments to show the potentiality of the synthesized hydrogel for *in-vitro* wound healing. This hydrogel could be used for the *in-vivo* purposes. In addition to our findings, the molecular mechanism underlying the wound healing induced by the hydrogel could be studied in more detail.

*Chapter 5* we have explored an enzyme fueled dissipative self-assembly process, which is constructed using nucleobase functionalized biomaterials. The hydrogel is biocompatible and facilitate the cell migration. Therefore, the described enzyme fueled approach could potentially be used as self-assembled nature inspired intelligent materials for advanced biological applications in drug delivery, biosensing, cell culture, wound dressing and others.